Calhoun

Institutional Archive of the Naval Postgraduate School

Calhoun: The NPS Institutional Archive

DSpace Repository

Theses and Dissertations

1. Thesis and Dissertation Collection, all items

1974

Comparison of momentum, sensible and latent heat fluxes over the open ocean determined by the direct covariance, inertial and direct dissipation techniques.

Dreyer, Gregory Frank.

http://hdl.handle.net/10945/16926

Downloaded from NPS Archive: Calhoun

DUDLEY KNOX LIBRARY

http://www.nps.edu/library

Calhoun is the Naval Postgraduate School's public access digital repository for research materials and institutional publications created by the NPS community. Calhoun is named for Professor of Mathematics Guy K. Calhoun, NPS's first appointed -- and published -- scholarly author.

Dudley Knox Library / Naval Postgraduate School
411 Dyer Road / 1 University Circle
Monterey, California USA 93943

U. S. NAVAL POSTGRADUATE
SCHOOL, MONTEREY

DUDLEY KNOX LIBRARY
NAVAL POSTGRADUATE SCHOOL
MONTEREY, CALIFORNIA 93940

UNIVERSITY OF CALIFORNIA

San Diego

Comparison of Momentum, Sensible and Latent Heat Fluxes Over the Open Ocean Determined by the Direct Covariance, Inertial and Direct Dissipation Techniques

A dissertation submitted in partial satisfaction of the
requirements for the degree Doctor of Philosophy
in Oceanography

by

Gregory Frank Dreyer

Committee in charge:

Professor Carl H. Gibson, Chairman
Professor Robert S. Arthur
Professor Paul A. Libby
Professor Fred N. Spiess
Professor Siebert Q. Duntley
Doctor Carl A. Friehe

1974

T 161533

Thesis
D7

DUDLEY KNOX LIBRARY
NAVAL POSTGRADUATE SCHOOL
MONTEREY, CALIFORNIA 93940

The dissertation of Gregory Frank Dreyer is approved, and it is acceptable in quality and form for publication on microfilm:

DEDICATION

To Karolyn, Racheal and Gwen, who
... "really know what this means."

TABLE OF CONTENTS

Page

List of Symbols vi

List of Figures xiii

List of Tables xx

Acknowledgment xxi

Vita, Publications and Fields of Study xxii

Abstract xxiv

1. Introduction 1

2. Flux Techniques 4

2.1 Direct Covariance Technique 4
2.2 Dissipation Technique 7
  2.2a Inertial-dissipation technique 9
  2.2b Direct-dissipation technique 11
2.3 Stability Considerations 12
2.4 Budget Equations 15

3. Instrumentation and Data Analysis 24

3.1 Experimental Arrangement 24
3.2 Data Acquisition 31
  3.2a Temperature measurements 34
  3.2b Humidity measurements 35
  3.2c Velocity measurements 39
  3.2d Analog instrumentation 41
3.3 Data Processing 42
3.4 Velocity Pitch Corrections 54

4. Results 58

4.1 Times Series Analysis 58
4.2 Standard Deviations of Turbulent Fluctuations and their Stability Dependence 82
4.3 Pitch Corrected Covariances and Error Analysis 90
4.4 Flux and Correlation Results 98
4.5 Spectra 103
  4.5a Velocity spectra 105
  4.5b Temperature and humidity spectra 137

Page

4.6 Cospectra 162
  4.6a Cospectra of momentum (uw) 163
  4.6b Cospectra of heat and water vapor flux ($w\theta$, wq) 172
    $w\theta$ cospectra 172
    wq cospectra 185
  4.6c Cospectra of horizontal heat and water vapor flux ($u\theta$, uq) 199
  4.6d Cospectra of temperature and humidity (θq) 219
4.7 $k^{5/3}$ Spectra and Comparison of Flux Techniques . . 232
  4.7a Comparison of eddy correlation and inertial dissipation techniques 233
    Momentum flux 233
    Heat and water vapor flux 242
  4.7b Comparison of eddy correlation and direct dissipation techniques 251
  4.7c Scalar variance budgets reeamined 267
4.8 Application of the Bulk Aerodynamic Technique for Estimation of the Turbulent Heat Fluxes 278

5. Summary and Conclusions 282

5.1 Momentum Flux 282
5.2 Latent Heat Flux 286
5.3 Sensible Heat Flux 289
5.4 Model of the Atmospheric Surface Layer Over the Ocean 295
5.5 Recommendations for Further Studies 301

References 304

Appendix 1 312

LIST OF SYMBOLS

a_u	Second order horizontal velocity structure function subrange constant, dimensionless
B	Rate of work done by turbulence on buoyancy forces, cm^2/sec^3
b_γ	Second order scalar structure function subrange constant, dimensionless
C_D	Turbulent drag coefficient, dimensionless
C_p	Specific heat, cal/gm - °C
C_q	Constant in the stability expression for σ_q/q_*, dimensionless
C_T	Constant in the stability expression for σ_θ/T_*, dimensionless
C_W	Constant in the stability expression for σ_w/u_*, dimensionless
D_e	Non-dimensional flux divergence of turbulent kinetic energy transport
D_p	Non-dimensional flux divergence of pressure transport
D_{uu}	Second order horizontal velocity structure function, cm^2/sec^2
D_γ	Scalar molecular diffusivity, cm^2/sec
$D_{\gamma\gamma}$	Second order scalar structure function, $°C^2$, $(\mu gm/cm^3)^2$
db	10 log (Power (1)/Power (2)), dimensionless

e	Kinetic energy per unit mass, cm^2/sec^2
$e_{ij} \equiv \frac{1}{2}(u_{i,j} + u_{j,i})$	Symmetric rate of strain tensor, sec^{-1}
f	Frequency, Hz
f_N	Normalized frequency, $f\,z/\overline{U}$, dimensionless
$G(z/L)$	Stability function for normalized $uw\,f_N$ -cospectrum, dimensionless
g	Acceleration of gravity, 978 cm/sec^2
grad	$\frac{\partial}{\partial x} + \frac{\partial}{\partial y} + \frac{\partial}{\partial z}$, gradient operator, cm^{-1}
H_L	Turbulent latent heat flux, mw/cm^2
H_S	Turbulent sensible heat flux, mw/cm^2
$H_u(z/L)$	Stability function for normalized $u\theta f_N$ -cospectrum, dimensionless
$H_w(z/L)$	Stability function for normalized $w\theta f_N$ -cospectrum, dimensionless
$H_{\theta q}(z/L)$	Stability function for normalized $\theta q\ f_N$ -cospectrum, dimensionless
I	Pressure transport required to balance the kinetic energy budget, cm^2/sec^3
K	von Kármán's constant, 0.4, dimensionless
K_E	Turbulent eddy transfer coefficient for water vapor, dimensionless
K_H	Turbulent eddy transfer coefficient for sensible heat, dimensionless
K_M	Turbulent eddy transfer coefficient for momentum, dimensionless

$K(x)$	Kurtosis of the variable x, $\overline{x^4}/(\overline{x^2})^2$, $\overline{x} = 0$, dimensionless
k	Radian wavenumber, $2\pi f/\overline{U}$, cm^{-1}
L	Monin-Obukhov length, $u_*^3 T_v/Kg\,\overline{w\theta_v}$, dimensionless
L_o	Energy scale, production scale, cm
L_v	Latent heat of vaporization, cal/gm
ℓ	Instrument sensing path length, cm
M	Mean specific humidity, gm/gm
$M_u(z/L)$	Stability function for normalized uq f_N -cospectrum, dimensionless
m	Fluctuating specific humidity, gm/gm
p	Pressure, mb
q	Absolute humidity, μgm/cm^3
R'	Radiation interaction with temperature field, °C/sec
R_B	Bowen ratio, dimensionless
$R_{uw}(f)$	Spectral correlation coefficient, $\Phi_{uw}/(\Phi_{uu}\Phi_{ww})^{1/2}$, dimensionless
r	Separation distance, cm
r_{xy}	Correlation coefficient, $\overline{xy}/\sigma_x\sigma_y$, dimensionless
S_q	General source term of the humidity variance budget equation, $(\mu\text{gm/cm}^3)^2$/sec
S_θ	General source term of the temperature variance budget equation, °C^2/sec

$S(x)$	Skewness of the variable x, $\overline{x^3}/(\overline{x^2})^{3/2}$, $\overline{x} = 0$, dimensionless
$\dot{S}$	Rate of evaporation, μgm/cm^3 - sec
T	Temperature, ° C
T_v	Virtual temperature (includes humidity effects), ° C
t	Time, seconds
U	Horizontal velocity, cm/sec
u	Fluctuating horizontal velocity, cm/sec
u_i	Velocity component in the ith direction, cm/sec
V	Output voltage, volts
v	Fluctuating transverse velocity, cm/sec
v'	Fluctuating output voltage, volts.
W	Vertical velocity, cm/sec
w	Fluctuating vertical velocity, cm/sec
x	Horizontal coordinate, cm
x_i	Spatial coordinate in the ith direction, cm
y	Transverse coordinate, cm
z	Vertical coordinate, height above the mean sea surface, cm

Greek

α_u	Inertial subrange constant for velocity (k-spectrum), dimensionless
α_{xy}	Inertial subrange constant for $\overline{xy}$ covariance (f_N - cospectrum), dimensionless

α_γ	Ratio of turbulent eddy transfer coefficients, dimensionless
β_q	Inertial subrange constant for humidity (k-spectrum), dimensionless
β_θ	Inertial subrange constant for temperature (k-spectrum), dimensionless
γ	Scalar, temperature or humidity, °C and $\mu gm/cm^3$
∂	Differential operator
ϵ	Rate of viscous dissipation of turbulent kinetic energy per unit mass, cm^2/sec^3
η	Dissipation scale, $(\nu^3/\epsilon)^{1/4}$, cm
Θ	Mean potential temperature, ° C
θ	Fluctuating temperature, ° C
λ	Constant in Lyman-alpha humidiometer output equation, $(\mu gm/cm^2)^{-1}$
ν	Molecular kinematic viscosity, cm^2/sec
π	3.14159..., dimensionless
ρ	Density, gm/cm^3
σ_H	Constant in the stability expression for the dimensionless scalar gradient, dimensionless
σ_m	Constant in the stability expression for the dimensionless wind shear, dimensionless
σ_x	Standard deviation of the variable x, (units of x)
τ	Turbulent shear stress, $dynes/cm^2$
τ_0	Turbulent shear stress at the ocean surface, $dynes/cm^2$

Φ_B	Dimensionless humidity gradient
Φ_H	Dimensionless temperature gradient
Φ_M	Dimensionless wind shear
Φ_{xx}(f or k)	Spectrum of x , units of x^2 per Hz or cm^{-1}
Φ_{xy}(f)	Cospectrum of $\overline{xy}$ covariance, units of $x \cdot y$ per Hz
Φ_ϵ	Dimensionless viscous dissipation of kinetic energy
φ	Pitch angle, degrees or radians
φ_s	Sonic anemometer internal misalignment, degrees or radians
χ_q	Dissipation of humidity variance,. $(\mu gm/cm^3)^2$ /sec
χ_θ	Dissipation of temperature variance, $°C^2$/sec
Ω	Resistance, ohms
ξ	Constant in linearized form of dimensionless wind shear expression

Superscripts

$\cdot$	Time derivative
—	Overbar, average, equivalent to ensemble average
~	Normalized quantity (correlation coefficients) or quantity corrected for internal sensor misalignment (vertical velocity, OWAX)

Subscripts

c	Corrected quantity
i	Coordinate direction or spatial derivative if preceded by comma
j	Coordinate direction or spatial derivative if preceded by comma
h	Upper limit
ℓ	Lower limit
m	Measured quantity
o	Initial or reference quantity
γ	Quantity applies to temperature or humidity

Script

$\dot{s}$	Fluctuating evaporation rate, μ gm/cm^3-sec

Bulk Coefficients

C_{wq}	Coefficient for bulk aerodynamic technique of estimating latent heat
$C_{w\theta}$	Coefficient for bulk aerodynamic technique of estimating sensible heat

LIST OF FIGURES

Figure Page

1 Research Platform FLIP in the stable vertical position, with 18 meter port boom and compensating sails on starboard boom 26

2 Instrument package for flux measurements 28

3 Analog instrumentation schematic 33

4 High speed standalone data logger 45

5 Time series analysis system 48

6 Illustrations of techniques for minimizing "leakage" in spectra 52

a. Box car window transform, leakage
b. Derivative pre-whitening
c. Digital pre-whitening
d. Triangular window transform

7 MITOS I-1 time series, u, w, T, q signals measured simultaneously, 12 minutes of continuous data 62

a. First "magnification" of MITOS I time series (x5), 2.5 minutes of data 64
a. 1 Second "magnification" of MITOS I time series (x100), 14 seconds of data 66
a. 2 Third "magnification" of MITOS I time series (x50), 28 seconds data 68

8 OWAX-2 time series, u, w, φ, T, q signals measured simultaneously, 8.5 minutes of continuous data 71

9 OWAX-4 time series, u, w, φ, T, q signals measured simultaneously, 54 minutes of continuous data (φ not included in "magnifications"). 74

b. First "magnification" of OWAX-4 (x10), 5.4 minutes of data 76

Figure Page

b. 1 Second "magnification" of OWAX-4 (x200), 16 seconds of data 78

b. 2 Third "magnification" of OWAX-4 (x100), 32 seconds of data 80

10 Normalized standard deviations of turbulent fluctuations plotted versus $-z/L$ 86

a. σ_u/u_*, σ_w/u_* versus $-z/L$

b. σ_θ/T_*, σ_q/q_* versus $-z/L$

11 MITOS III and average OWAX pitch gyro spectra plotted versus frequency (key to spectral plots Table 6) 93

12 SOMA horizontal velocity spectra plotted versus frequency 107

13 MITOS I horizontal velocity spectra plotted versus frequency 109

14 MITOS III and OWAX horizontal velocity spectra plotted versus frequency 111

15 SOMA vertical velocity spectra plotted versus frequency 113

16 MITOS I vertical velocity spectra plotted versus frequency 115

17 MITOS III vertical velocity spectra plotted versus frequency corrected for pitch (◁) and uncorrected (+) 117

18 OWAX vertical velocity spectra plotted versus frequency 119

19 Average horizontal velocity spectra normalized with u_*^2 plotted versus normalized frequency $(f\,z/\overline{U})$ 122

Figure Page

20 Average vertical velocity spectra normalized with u_*^2 plotted versus normalized frequency . . . 124

21 Average horizontal velocity spectra normalized with u_*^2 and $\Phi_{\epsilon_1}^{2/3}$ (assuming total production = dissipation of kinetic energy) plotted versus normalized frequency 127

22 Average vertical velocity spectra normalized with u_*^2 and $\Phi_{\epsilon_1}^{2/3}$ plotted versus normalized frequency 129

23 Average horizontal velocity spectra normalized with u_*^2 and $\Phi_{\epsilon_2}^{2/3}$ (Wyngaard and Coté)^{61} expression for normalized dissipation plotted versus normalized frequency 131

24 Average vertical velocity spectra normalized with u_*^2 and $\Phi_{\epsilon_2}^{2/3}$ plotted versus normalized frequency 133

25 Spectral ratio Φ_{ww}/Φ_{uu} plotted versus normalized frequency 136

26 SOMA temperature spectra plotted versus frequency 139

27 MITOS I temperature spectra plotted versus frequency 141

28 MITOS III and OWAX temperature spectra plotted versus frequency 143

29 SOMA humidity spectra plotted versus frequency . . 145

30 MITOS I humidity spectra plotted versus frequency 147

Figure Page

31 MITOS III and OWAX humidity spectra plotted versus frequency 149

32 Average temperature spectra normalized with T_*^2 plotted versus normalized frequency 152

33 Average humidity spectra normalized with q_*^2 plotted versus normalized frequency 154

34 Average temperature spectra normalized with T_*^2, Φ_H (dimensionless temperature gradient) and $\Phi_\epsilon^{-1/3}$ plotted versus normalized frequency (comparison with other results) . . . 157

35 Average humidity spectra normalized with q_*^2, Φ_E (dimensionless humidity gradient) and $\Phi_\epsilon^{-1/3}$ plotted versus normalized frequency (comparison with other results) 159

36 MITOS III and OWAX momentum flux (uw) cospectra (corrected for pitch) plotted versus frequency 165

37 Average uw cospectra normalized with u_*^2 plotted versus normalized frequency (comparison with other results) 167

38 Average uw cospectra normalized with u_*^2 plotted linearly versus normalized frequency (comparison with other results) 170

39 SOMA heat flux (wθ) cospectra plotted versus frequency 174

40 MITOS I wθ cospectra plotted versus frequency 176

41 MITOS III and OWAX wθ cospectra plotted versus frequency corrected for pitch 178

Figure Page

42 Average $w\theta$ cospectra normalized with u_*T_* plotted versus normalized frequency (comparison with other results) 181

43 Average $w\theta$ cospectra normalized with u_*T_* plotted linearly versus normalized frequency (comparison with other results) 183

44 SOMA water vapor flux (wq) cospectra plotted versus frequency 187

45 MITOS I wq cospectra plotted versus frequency 189

46 MITOS III and OWAX wq cospectra plotted versus frequency (corrected for pitch) 191

47 Average wq cospectra normalized with u_*q_* plotted versus normalized frequency (comparison with other results) 194

48 Average wq cospectra normalized with u_*q_* plotted linearly versus normalized frequency (comparison with other results) 196

49 MITOS I horizontal heat flux $(u\theta)$ cospectra plotted versus frequency 201

50 MITOS III and OWAX $u\theta$ cospectra plotted versus frequency 202

51 MITOS I horizontal water vapor flux (uq) cospectra plotted versus frequency 205

52 MITOS III and OWAX uq cospectra plotted versus frequency 207

53 Average $u\theta$ cospectra normalized with u_*T_* plotted versus normalized frequency (comparison with other results) 210

54 Average uq cospectra normalized with u_*q_* plotted versus normalized frequency (comparison with other results) 212

Figure Page

55 Average $u\theta$ cospectra normalized with u_*T_* plotted linearly versus normalized frequency . . . 215

56 Average uq cospectra normalized with u_*q_* plotted linearly versus normalized frequency . . . 217

57 SOMA temperature-humidity (θq) cospectra plotted versus frequency 221

58 MITOS I θq cospectra plotted versus frequency . . 223

59 MITOS III and OWAX θq cospectra plotted versus frequency 225

60 Average θq cospectra normalized with T_*q_* plotted versus normalized frequency 227

61 Average θq cospectra normalized with T_*q_* plotted linearly versus normalized frequency 229

62 $k^{5/3}$ average horizontal velocity spectra normalized with $\alpha_u u_*^2 \Phi_{\epsilon_1} (Kz)^{-2/3}$ plotted versus radian wavenumber (ordinate represents agreement between direct covariance and inertial dissipation estimates of u_*^2) 236

63 $k^{5/3}$ average horizontal velocity spectra normalized with $\alpha_u u_*^2 \Phi_{\epsilon_2} (Kz)^{-2/3}$ plotted versus radian wavenumber (ordinate represents agreement between direct covariance and inertial dissipation estimates of u_*^2) 238

64 $k^{5/3}$ average temperature spectra normalized with $2T_*^2 \Phi_H \Phi_\epsilon^{-1/3} (Kz)^{-2/3}$ plotted versus radian wavenumber (ordinate represents β_0 required for agreement between direct covariance and inertial dissipation estimates of T_*^2) 246

Figure Page

65 $k^{5/3}$ average humidity spectra normalized with $q_*^2 \Phi_E \Phi_\epsilon^{-1/3} (Kz)^{-2/3}$ plotted versus radian wavenumber (ordinate represents β_q required for agreement between direct covariance and inertial dissipation estimates of q_*^2) 248

66 MITOS I runs 1 and 7 $k^{-1/3}$ velocity derivative spectra normalized with $\epsilon^{2/3}$ plotted linearly versus normalized wavenumber (ηk) (ordinate represents α_u from direct dissipation estimate) (from McConnell,[50] 1974) 256

67 MITOS I runs 1 and 7 $k^{-1/3}$ temperature derivative spectra normalized with $\chi_\theta \epsilon^{-1/3}$ plotted linearly versus normalized wavenumber (ηk) (ordinate represents β_θ from direct dissipation estimate) (from McConnell,[50] 1974) 258

68 OWAX-4 $k^{-1/3}$ velocity and temperature derivative spectra normalized with $\epsilon^{2/3}$ (velocity) and $\chi_\theta \epsilon^{-1/3}$ (temperature) plotted linearly versus normalized wavenumber (ηk) (ordinate represents α_u or β_θ from direct dissipation estimate) (from McConnell,[50] 1974) . . 260

69 Ramp model for temperature and humidity over the ocean 274

LIST OF TABLES

Page

1. Environmental Conditions 59
2. Flux and Correlation 60
3. Stability Results 83
4. Pitch Angles and Corrected Fluxes 95
5. Normalized Correlation Coefficients 102
6. Spectral and Cospectral Information 104
7. Cospectral Subrange Constants 231
8. Direct Dissipation Results 253
9. Comparison of Eddy Correlation and Direct Dissipation Techniques 263
10. Production and Dissipation of Temperature Variance 268
11. Bulk Aerodynamic Results 280

ACKNOWLEDGMENTS

The author wishes to express his sincere appreciation to Professor Carl H. Gibson for giving direction and purpose to this research. I am most grateful to Drs. Carl A. Friehe and Frank H. Champagne for their encouragement and assistance. A word of thanks is extended to Tom Deaton, Gene Dial and Jerome Dayton for their electronic and computer wizardry. I wish to thank my friends and associates at U. C. S. D., and my colleague, Steve McConnell, for their cooperation and assistance. The author is indebted to Capt. Rich Silva and the crew of FLIP for their invaluable assistance during the research cruises.

A special word of thanks for the professional and heroic accomplishment of Jeri Neuberger, who spent many long and extra hours typing and reviewing the dissertation. To Evelyn Portillo for her work on the figures, I am most grateful. Finally, I wish to express my deepest appreciation to my special friends, wife and family for their help and support during this research.

The author was supported by The Naval Post-graduate School, Monterey, under The Junior Line Officer Advanced Educational Program (BURKE Program), Contract N 66314-70-A-0058.

VITA

October 25, 1945 -	Born - Annapolis, Maryland
1963 - 1967	B.S., Mechanical Engineering, U.S. Naval Academy, Annapolis, Maryland
1967 -	Officer, U.S. Navy, Qualified in Submarines
1969 - 1974	Ph.D., Oceanography, Scripps Institution of Oceanography, University of California, San Diego

PUBLICATIONS

Friehe, C. A., Gibson, C. H. and G. F. Dreyer, "Effects of Temperature and Humidity on Density and Refractive Index Fluctuations Over the Open Ocean," Opt. Soc. Amer. Bull., paper WD-15, p. 13, October, 1972.

Dreyer, G. F., Gibson, C. H. and C. A. Friehe, "Measurements of Temperature and Humidity Fluctuations Over the Open Ocean," Bull. APS, 17, pp. 1102-1103, November, 1972.

Dreyer, G. F. and C. H. Gibson, "The Inertial Subrange of Turbulence Over the Open Ocean," Bull. APS, 16, p. 1306, November, 1971.

FIELDS OF STUDY

Physical Oceanography
Professors Robert S. Arthur, Charles S. Cox, Carl Eckart, Myrl C. Hendershott and Joseph L. Reid

Biological Oceanography
Professors John A. McGowan, Michael M. Mullin and Richard H. Rosenblatt

Marine Chemistry and Nuclear Geochemistry
Professors Harmon Craig and Joris M. T. M. Gieskes

Marine Corrosion
Mr. Frank LaQue

Marine Geology
Professors Joseph R. Curray, Douglas L. Inman and Henry W. Menard

Mathematics
Professors Edward W. Fager and Frank B. Theiss

Meteorology
Professors Daniel B. Olfe and Stanford S. Penner

Fluid Mechanics
Professors Carl H. Gibson, Paul A. Libby and Charles Van Atta

Radiative Transfer in the Sea
Professor Siebert Q. Duntley

FIELD OF RESEARCH

Micrometeorology
Professor Carl H. Gibson

ABSTRACT OF THE DISSERTATION

Comparison of Momentum, Sensible and Latent Heat Fluxes Over the Open Ocean Determined by the Direct Covariance, Inertial and Direct Dissipation Techniques

by

Gregory Frank Dreyer

Doctor of Philosophy in Oceanography
University of California, San Diego, 1974
Professor Carl H. Gibson, Chairman

Measurements of velocity, temperature and humidity were made in the atmospheric surface layer over the open ocean from the Research Platform FLIP, to compare estimates of the fluxes of momentum, sensible and latent heat, using the direct covariance, inertial and direct dissipation techniques. Measurements were made during a series of oceanographic cruises approximately 60 miles off the coast of Baja California, between August 1970 and April 1973. Direct covariance estimates of the fluxes were corrected for instrument tilt using simultaneous measurements of pitch angle, and dissipation estimates were corrected for stability effects.

Agreement was obtained between estimates of momentum

flux by the dissipation techniques and the direct measurements within the uncertainties of the direct estimates (± 25%), applying the assumption that total production of kinetic energy (mechanical + buoyant) equals dissipation. From the direct dissipation technique, the average value determined for the velocity subrange constant was $\alpha_u = 0.53 \pm 0.03$. Trends in the direct dissipation estimates indicate that vertical turbulent transport and pressure transport of kinetic energy cannot be neglected and may be approximately half of the estimates of dimensionless transport measured over land. Comparisons were made between directly measured momentum fluxes corrected for instrument tilt using measured pitch angles, and values obtained using estimates of pitch angle in lieu of measurement. Results of the comparison suggest that large errors in direct momentum flux estimates can be incurred if tilt corrections are based on estimates of pitch angle.

For agreement between inertial dissipation estimates and directly measured latent heat fluxes, an average value of the humidity subrange constant $\beta_q = 0.21 \pm 0.05$ was required. The direct dissipation technique was not applied to estimate latent heat fluxes since the frequency response of the Lyman-alpha humidiometer was not sufficient for direct estimates of the dissipation of humidity variance. Dimensional humidity spectra were similar to horizontal velocity spectra, and water vapor flux cospectra were similar to momentum

flux cospectra.

To obtain agreement between direct estimates of sensible heat flux and inertial dissipation estimates, an average value of the temperature subrange constant $\beta_\theta = 2.2 \pm 0.3$ was required. Estimates of sensible heat flux by the direct dissipation technique were higher than direct measurements by a factor of 2 or more. From direct estimates of the dissipation of temperature variance (± 20%) and sensible heat flux (± 10%), dissipation was greater than production of temperature variance by as much as a factor of 4, not accounted for by uncertainties in the direct estimates, or by temperature flux divergence. Direct dissipation estimates of β_θ varied from 0.7 ± 0.07 to 2.4 ± 0.2. Temperature spectra from different cruises with different environmental conditions did not compare with one another, and were not similar to humidity or velocity spectra. Cospectra of sensible heat flux exhibited similar differences. The differences between production and dissipation of temperature variance, and the behavior of the temperature spectra and sensible heat flux cospectra could be accounted for by consideration of sources of production usually neglected in the temperature variance budget, and attributed to the combined effects of ocean spray evaporation and radiative heating/cooling.

A wide range of bulk coefficients were obtained from comparison of estimates of sensible heat flux by the direct covariance and bulk

aerodynamic techniques, indicating the bulk technique is not reliable for estimates of sensible heat fluxes. A value of $(1.29 \pm 0.36) \times 10^{-3}$ was obtained for the latent heat flux bulk coefficient.

1. INTRODUCTION

Energy and moisture transfer from the oceans to the marine atmosphere are major driving factors of atmospheric and oceanic circulation. Within the last decade a vast amount of scientific investigation and experimentation has been directed toward an understanding of the energy exchanges and physical processes which occur at the atmosphere - ocean interface. Accurate determination of the vertical fluxes of momentum, sensible and latent heat is of prime importance. This research has as its primary objectives the direct measurement of the turbulent fluxes and comparison of various techniques of estimating the fluxes indirectly from related statistical quantities.

Perhaps one of the earliest attempts to estimate the transfer of momentum and heat from the ocean was made by G. I. Taylor in 1913 from a whaling ship using balloon and kite observations of mean temperatures and wind velocities (Taylor, 1970).[1] Due to severe instrument limitations, early methods of estimating the turbulent fluxes have consisted of semi-empirical theories relating mean properties or gradients to the actual fluxes. No direct flux calculation was possible. Many of these methods including the bulk aerodynamic method, integral method, and profile method are discussed by Roll[2] (1965).

With the evolution and development of sophisticated instrumentation and experimental platforms for use on the open ocean, accurate measurements of atmospheric and oceanographic parameters of scales ranging from millimeters to kilometers have become possible. As an outgrowth of the recommendations of the Joint Panel on Sea-Air Interaction of the National Academy of Sciences (1962, 1966)[3,4] the Bardados Oceanographic Meteorological Experiment (BOMEX) was conducted during the summer of 1969. The principal objective in air-sea interaction was the study of the fluxes of momentum, sensible and latent heat described by Davidson (1968)[5] and Kuettner and Holland (1969).[6] Current results from BOMEX have been summarized by Holland (1972).[7] Results of direct flux measurements from the research vessel FLIP obtained using the covariance or eddy correlation method and the well recognized difficulties of the measurement are discussed by Pond et al (1971),[8] Phelps (1971),[9] Phelps and Pond (1971)[10] and Leavitt (1973).[11] The dissipation technique for estimating momentum flux was used by Gibson and Williams (1969)[12] from FLIP in 1968, and for sensible heat flux during BOMEX by Gibson, Stegen and Williams (1970)[13] and Stegen, Gibson and Friehe (1973).[14]

Experimental data for this thesis was obtained from measurements made from the Research Platform FLIP during a series of oceanographic cruises between August 1970 and April 1973 off the

coast of Southern California. Mean and fluctuating components of horizontal and vertical velocity, temperature, humidity, instrument motion, and mean sea surface temperature were measured simultaneously. Fluxes of momentum, sensible and latent heat were obtained by the direct eddy correlation technique corrected for instrument/platform motions and compared with estimates of fluxes by the direct and inertial dissipation techniques. The influence of atmospheric stability on the determination of the fluxes by the latter two methods was determined. Latent and sensible heat fluxes were also determined using the bulk aerodynamic technique (including stability effects) and compared to estimates of the turbulent heat fluxes by the direct covariance technique.

2. FLUX TECHNIQUES

2.1 Direct Covariance Technique

The optimum method of determining the turbulent fluxes of momentum and sensible and latent heat is to measure directly and appropriately average the covariances of vertical velocity with the suitable variable of interest. This method is known as the direct covariance or eddy correlation technique. The technique is based on the definition of the vertical fluxes as given by

$$\begin{aligned} &\text{Momentum Flux} && \tau = -\rho\,\overline{uw} \\ &\text{Sensible Heat Flux} && H_S = \rho\, C_p\, \overline{w\theta} \qquad (1) \\ &\text{Latent Heat Flux} && H_E = L_v\, \overline{wq} \end{aligned}$$

where u, w are the horizontal and vertical fluctuating components of the streamwise velocity vector $\overline{U}$, θ is the fluctuating component of temperature (° C), and q the absolute humidity fluctuation (μgm/cm^3). The constants are ρ density, C_p specific heat capacity, and L_v latent heat of vaporization. Overbars indicate time averages assuming stationary flow. The covariances are obtained by integration of the appropriate cospectrum Φ_{wx} (where x is u, θ, or q) between low and high frequency limits in the same manner as the variances of the individual turbulent components are obtained from the appropriate spectrum Φ_{xx}. The frequency range is determined to include all significant contributions to the integrals

given by

$$\overline{wx} = \int_{f_\ell}^{f_h} \Phi_{wx}(f)\, df \text{ and } \overline{x^2} = \int_{f_\ell}^{f_h} \Phi_{xx}(f)\, df \qquad (2)$$

The low frequency (f_ℓ) or high pass cut-off is normally determined by removal of the record mean on data processing and is thereby set by the length of the data record. The low pass cut-off (f_h) is initially limited by the bandwidth limitations of the instruments used to measure the parameters u, w, θ and q, and is subsequently set by low pass filtering during data analysis, usually adequate to determine the full value of the appropriate flux. Filters are used to reduce high frequency noise and minimize aliasing in analog to digital conversion. In this work the frequency range of the integration was between about 1×10^{-3} and 10 Hz.

Determination of the fluxes directly by this technique is fairly difficult in practice due to the effects of instrument platform motion on the measured turbulent velocity components. Pond et al (1971)[8] obtained values of the covariance $\overline{uw}$ with the eddy correlation technique using a sonic anemometer to measure horizontal and vertical velocity from FLIP during Operation BOMEX. Employing an empirical correction procedure, significant corrections to $\overline{uw}$ were required to account for FLIP motion and effects on the flow field. Rotations of the principal axis of the Reynolds flux tensor were selected to make the spectral correlation coefficient $R_{uw}(f) = \Phi_{uw}/(\Phi_{uu}\Phi_{ww})^{1/2}$

equal to a value of -0.5 for $0.01 < fz/\overline{U} < 0.1$ as suggested by Smith (1967)[15] and Weiler and Burling (1967).[16] Pond et al[8] found typical correction values for $\overline{uw}$ were 13% per degree tilt and 5% and 3% per degree for $\overline{wq}$ and $\overline{w\theta}$ respectively, and it was felt that the measurements were within 1-2° of the correct coordinate system. Contributions to the u , w spectra and $\overline{uw}$ cospectra by wave induced FLIP motion were not included in the integration when determining variances and covariances. Despite the fact that no theoretical assumptions or approximations are required to employ the direct covariance technique, Pond et al[8] assumed that there was no distortion of the Reynolds stress due to the large tilt angles calculated (~ 10°) which would affect the correlation between u and w .

Kaimal and Haugen (1969)[17] have found that the correlation coefficient $r_{uw} = \frac{\overline{uw}}{\sigma_u \sigma_w}$, varies over a wide range from near zero to -0.5 , particularly under unstable conditions. This suggests that the spectral correlation coefficient R_{uw} may also vary with stability. Based on results from the Kansas experiment, Kaimal and Haugen[17] suggest a need for ± 0.1° accuracy in the internal alignment and mounting of sensors used to measure the direct covariance (uw) in the atmospheric boundary layer.

For this research measurements of instrument platform tilt in the u , w plane were made using a vertical gyro located at a known

angle with respect to the velocity sensors. Outputs of the vertical gyro were recorded simultaneously with the fluctuating velocity components and temperature and humidity fluctuations to determine corrected values of the covariances. Description of the instrument package and correction procedures are contained in the instrumentation and data reduction sections.

2.2 Dissipation Techniques

Both the inertial and direct dissipation techniques are somewhat advantageous over the direct covariance method in that they are much less susceptible to errors caused by instrument platform motion. This is due to the fact that the flux estimates are based on measurements of the small scale structure of the velocity and scalar fields. Three variations of the dissipation method differ in the technique used to determine the rates of dissipation of velocity or scalar variance are determined. The dissipation may be measured directly or inferred from the inertial subrange of the appropriate spectra or of the structure function.

The technique for relating the dissipation of velocity and scalar variance to the fluxes of momentum and heat was first suggested by R. J. Taylor (1961).[18] This technique is based on the assumptions discussed in Lumley and Panofsky (1964)[19] that mechanical production is equal to energy dissipation at the same height in the constant flux

layer for near neutral conditions, so that

$$\text{(production)}\quad -\overline{uw}\,\frac{d\overline{U}}{dz} = \overline{\epsilon}\quad \text{(dissipation)} \tag{3}$$

where $\overline{\epsilon}$ = mean rate of viscous dissipation = $2\,\nu\,\overline{e_{ij}^{\,2}}$, and $e_{ij} \equiv (u_{i,j} + u_{j,i})/2$; ν = kinematic viscosity; ρ density, $\overline{U}$ mean streamwise velocity, z = vertical height above the mean sea surface, and u and w are defined as previously.

The same assumption is made for the production and dissipation of scalar variance, i. e.,

$$\text{(production)}\quad -\overline{\gamma w}\,\frac{d\overline{\gamma}}{dz} = \frac{\overline{\chi_{\gamma}}}{2}\qquad \text{(dissipation)} \tag{4}$$

where $\overline{\gamma}$ and γ represent the mean and fluctuating scalars (temperature $(\overline{T}+\theta)$ and humidity $(\overline{q}+q)$), $\overline{\chi_{\gamma}}$ = mean rate of dissipation of scalar variance = $D_{\gamma}\,\overline{|\text{grad}\;\gamma|^{2}}$, and D_{γ}, the molecular diffusivity of the scalar.

Assuming a logarithmic profile for velocity and the scalars, and implicitly invoking conditions of stationarity and horizontal homogeneity, we find

$$\frac{d\overline{U}}{dz} = \frac{u_{*}}{Kz}\;, \qquad u_{*}^{\,2} = -\overline{uw} \tag{5}$$

$$\frac{d\overline{\gamma}}{dz} = \frac{\gamma_{*}}{Kz\,\alpha_{\gamma}}\;, \qquad \gamma_{*} = -\,\frac{\overline{w\gamma}}{u_{*}} \tag{6}$$

where u_* is the friction velocity, K is von Kármán's constant, normally assumed to be 0.4, γ_* the scalar scale, and $\alpha_\gamma = (\overline{\gamma w}\ \partial \bar{U}/\partial z)/(\overline{uw}\ \partial \bar{\gamma}/\partial z) = K_H/K_m$ the ratio of eddy transfer coefficients for the scalars and momentum, assumed unity for neutral conditions (Reynolds analogy). Also assumed is $K_H \simeq K_E$ for humidity. Expressions for the fluxes can be obtained by combining equations (3) and (5), and (4) and (6)

$$u_*^2 = (K \bar{\epsilon} z)^{2/3} \tag{7}$$

$$\gamma_*^2 = \frac{\alpha_\gamma \bar{\chi}_\gamma z}{2 u_* K} \tag{8}$$

2.2a Inertial-dissipation technique

Taylor[18] determined values of $\bar{\epsilon}$ and $\bar{\chi}_\theta$ from the inertial subrange of the second order structure functions for velocity and temperature. From the similarity hypothesis of Kolmogorov (1941)[20] for turbulent velocity fields, and Obukhov (1949)[21] and Corrsin (1951)[22] for turbulent scalar fields assuming local isotropy, the second order structure functions in the inertial subrange are given by

$$D_{uu}(r) = \overline{[U(x+r) - U(x)]^2} = a_u \bar{\epsilon}^{2/3} r^{2/3} \tag{9}$$

$$D_{\theta\theta}(r) = [T(x+r) - T(x)]^2 = b_\theta \bar{\chi}_\theta \bar{\epsilon}^{-1/3} r^{2/3} \tag{10}$$

where U and T (or humidity) are measured at streamwise separation

distance r, between L_o (energy scale) and η (dissipation scale). η is also known as the Kolmogorov scale, defined as $(\nu^3/\bar{\epsilon})^{1/4}$.

Values of $\bar{\epsilon}$ and $\bar{\chi}_\gamma$ can also be determined in the same manner from the inertial subrange of the one-dimensional spectra given by

$$\Phi_{uu}(k) = \alpha_u \bar{\epsilon}^{2/3} k^{-5/3} \tag{11}$$

$$\Phi_{\gamma\gamma}(k) = \beta_\gamma \bar{\chi}_\gamma \bar{\epsilon}^{-1/3} k^{-5/3} \tag{12}$$

where α_u and β_γ are universal constants assumed known, and the radian wavenumber $k = 2\pi f/\bar{U}$ by Taylor's hypothesis. This technique requires accurate values of the constants α_u and β_γ (or a_u and b_γ), and the velocity and scalar spectra and structure functions to follow the $k^{-5/3}$ ($r^{2/3}$) form of the inertial subranges.

In this work, examples of temperature spectra obtained from open ocean atmospheric data are presented which appear to exhibit a very limited, if any, $-5/3$ inertial subrange. Application of Eq.(12) to single frequency (wavenumber) measurements of the spectral function could lead to large errors in the estimation of sensible heat flux if an inertial subrange does not exist. Similar care must be taken when applying Eq. (10) to single separation measurements of the structure function. A substantial portion of the temperature spectrum should be measured (to ~ 100 Hz) to determine if a subrange does exist

before this method is applied. Humidity spectra appear to exhibit a -5/3 inertial subrange behavior over a wider range of frequencies (to ~ 20 Hz) than temperature

2.2b Direct dissipation technique

This technique involves measurement of the mean square values of time derivatives of fluctuating streamwise velocity and temperature to calculate dissipation rates directly. Direct estimates of $\overline{\epsilon}$ and $\overline{\chi}_\theta$ in the atmospheric boundary layer over the ocean from FLIP in 1968 and during Project BOMEX are described by Gibson and Williams (1969),[12] Gibson et al (1970)[13] and Stegen et al (1973).[14] Assuming local isotropy and Taylor's hypothesis ($\overline{U}\, d/dx = -d/dt$), the viscous dissipation may be determined from the relations

$$\overline{\epsilon} = \frac{15\,\nu}{\overline{U}^2} \overline{\left(\frac{\partial u}{\partial t}\right)^2} \tag{13}$$

and

$$\overline{\chi}_\theta = \frac{6 D_\theta}{\overline{U}^2} \overline{\left(\frac{\partial \theta}{\partial t}\right)^2} \tag{14}$$

In practice the appropriate time derivative spectra are integrated to obtain values of the mean square time derivatives. Difficulties in this technique involve the high spatial resolution required of the sensing probes to nearly the Kolmogorov scale (η), of the order of 1 mm in atmospheric flows. High frequency response (~ 2000 Hz) and very

high signal-to-noise ratios are required in the sensor and associated circuitry. At the present writing a humidity sensor with sufficient frequency response was not available to measure adequately mean square humidity time derivatives to calculate the humidity dissipation. As a result, the direct dissipation technique is applied only to estimates of the momentum and sensible heat fluxes.

The direct dissipation technique does offer several advantages over the other techniques. Estimates of the fluxes require relatively simple instrumentation and data analysis, and are not affected by sensor motion because of the high frequency response and fine scale spatial resolution of the sensors used. Measurement of spectra over the entire range of frequencies (wavenumbers) are readily obtainable to determine spectral shapes. The spectra combined with dissipation measurements provide a means of accurately determining the universal constants.

2.3 Stability Considerations

Application of the dissipation techniques using Eqs. (7) and (8) does not account for effects of stability on the flux estimates. These equations are modified by consideration of the turbulent budget equations for kinetic energy and scalar variance, and the flux-profile relationships in the surface layer, within the framework of the Monin-Obukhov surface-layer similarity theory (Obukhov, 1946[23] and Monin-Obukhov, 1954).[24]

In the first tens of meters of the atmospheric boundary layer, the fluxes of momentum and heat are assumed constant. Recent experimental support for this assumption has been given by Haugen et al (1971)[25] and Dyer and Hicks (1972).[26] In this "constant flux layer," according to similarity theory, the turbulence structure is determined by the surface shear stress τ_o, the surface heat flux H_s, the buoyancy parameter g/T, and z the vertical height. The latent heat flux H_L is included to account for humidity effects on buoyancy in the boundary layer over the ocean. From these parameters characteristic scales for velocity (u_*), and scalars $(\gamma_* = T_*, q_*)$ are defined (as in Eqs. (5) and (6)). The length scales are z and the Monin-Obukhov length, defined as

$$L = - \frac{u_*^3 \, T_v}{K g \, \overline{w \theta_v}} \tag{15}$$

where the mean and fluctuating virtual temperature, T_v and θ_v, as given by Lumley and Panofsky (1964),[19] include humidity contributions to buoyancy. They are written as

$$T_v = T\,(1.0 + 0.61\,M) \tag{16}$$

and

$$\theta_v \simeq \theta + 0.61\,Tm \tag{17}$$

where M and m are mean and fluctuating specific humidity (gm/gm). The scale L is a key independent variable of similarity theory and

determines the thickness of the surface layer above which buoyancy factors are not significant.

Applying the scaling parameters to the vertical gradients of velocity and the scalars (temperature, humidity), Eqs. (5) and (6) are rewritten as

$$\frac{d\overline{U}}{dz} = \frac{u_*}{Kz} \Phi_m(z/L) \tag{18}$$

$$\frac{d\overline{\gamma}}{dz} = \frac{\gamma_*}{Kz\alpha_\gamma} \Phi_H(z/L) \quad . \tag{19}$$

The functions Φ_m, the dimensionless wind shear, and Φ_H, the dimensionless scalar gradient, are evaluated empirically. It is generally assumed that $\Phi_H = \Phi_E$ for temperature and humidity. Monin and Yaglom (1971)[27] conclude that the forms of Φ_m and Φ_H for unstable conditions (the prevalent condition over the open ocean) are best given by

$$\Phi_m = (1 - \sigma_m z/L)^{-1/4} \quad \text{for} \quad -1 \leq z/L \leq 0 \tag{20}$$

$$\Phi_H = (1 - \sigma_H z/L)^{-1/2} \quad . \tag{21}$$

A review of the constants σ_m and σ_H has recently been given by Busch et al (1973)[28] and fairly good agreement appears to exist for the value of σ_m. Businger et al (1971)[29] suggests $\sigma_m = 15$,

while Paulson (1970),[30] Badgley et al (1972),[31] and Dyer and Hicks (1970)[32] find $\sigma_m = \sigma_H = 16$. Miyake et al (1970)[33] use $\sigma_m = \sigma_H = 16$, also used by Pond et al,[8] Phelps and Pond,[10] and Leavitt,[11] to obtain results from BOMEX data. For neutral conditions $\left(\Phi_m = \Phi_H = 1\right)$, Businger et al (1971)[29] find values of $\alpha_\gamma = 1.35$ and $K = 0.35$ as compared to the often used values of $\alpha_\gamma = 1.0$ and $K = 0.4$, and suggest $\sigma_H = 9$.

2.4 Budget Equations

If horizontal homogeneity and stationarity are assumed and the effects of humidity on buoyancy are included, the budget equation for kinetic energy per unit mass, $\overline{e^2} = \overline{u^2} + \overline{w^2} + \overline{v^2}$ may be written as (Lumley and Panofsky, 1964)[19]

$$- \overline{uw} \frac{\partial \overline{U}}{\partial z} + \frac{g}{\overline{T}_v} \left[\overline{w\theta} + 0.61 \, \overline{T} \, \overline{wm}\right] - \frac{1}{2} \frac{\partial}{\partial z} \overline{we^2} - \frac{1}{\rho} \frac{\partial}{\partial z} \overline{pw} - \overline{\epsilon} = 0 \quad (22)$$

The non-dimensional form of the budget equation is obtained by multiplying Eq. (22) by $K z / u_*^3$ and employing Eqs. (15) and (18) so that Eq. (22) can be written as

$$\Phi_m - z/L - D_e - D_p - \Phi_\epsilon = 0 \quad . \qquad (23)$$

The terms represent the turbulent shear production, buoyant production, the flux divergence of turbulent kinetic energy, the flux divergence of pressure transport and viscous dissipation

respectively.

Three approaches to simplification of Eqs. (22) and (23) have been suggested. The first approach, given by Eq. (13), is the assumption that production and dissipation of mechanical energy are equal for near neutral conditions. For $|z/L| < 0.5$ Busch and Panofsky (1968)[34] suggest that dissipation is balanced by the sum of buoyant and mechanical production, and that the flux divergence terms may be neglected so that Eq. (23) simplifies to

$$\Phi_m - z/L = \Phi_\epsilon \quad . \tag{24}$$

McBean, et al (1971)[35] conclude from measurements over land that for near neutral conditions ($|z/L| < 0.2$) Eq. (24) is a good approximation. However, for more unstable conditions, $-z/L > 0.3$, dissipation appears to exceed production, and for $z/L \simeq -0.5$ the sum $\Phi_m - z/L - \Phi_\epsilon$ is about 30% of shear production and more than half of buoyant production. Miyake et al (1970)[33] and Pond et al (1971)[8] apply Eq. (24) to calculate momentum flux, however, they do not include stability effects on the mean velocity profile as given by Eq. (18). Hicks and Dyer (1972)[36] include buoyancy effects from Eqs. (18) and (24) to calculate the momentum flux by the inertial dissipation technique.

A recent approach to simplification of the turbulent energy budget has been suggested by Wyngaard and Coté (1971)[37] based upon

measurements in the surface layer over land. From measurements of $\overline{we^2}$ at three different heights the turbulent flux divergence of $\overline{e^2}$ was estimated and found to approximately balance buoyant production in the stability range $-1.0 \leq z/L \leq 0$. Eq. (23) reduces to

$$\overline{uw}\ \frac{\partial \overline{U}}{\partial z} + \overline{\epsilon} + I \simeq 0 \tag{25}$$

where the imbalance I, is attributed to pressure transport divergence. Under stable conditions the imbalance may not be substantial and under strongly unstable conditions $(z/L = -2)$ dissipation and total production did balance. Empirically, the expression for the imbalance term is written as

$$\frac{Kz}{u_*^3}\ I = (1-15\ z/L)^{-1/4} - (1 + 0.5\ |z/L|^{2/3})^{3/2} \tag{26}$$

where the first term on the right-hand side is the Businger formula for dimensionless shear production (Eq. (20), $\sigma_m = 15$), and the second term is the empirical expression determined by Wyngaard and Coté[37] for unstable dissipation data. Using this approach, momentum flux corrected for stability effects may be calculated using the empirical expression for unstable dissipation written as

$$\frac{Kz\overline{\epsilon}}{u_*^3} = (1 + 0.5\ |z/L|^{2/3})^{3/2}\ . \tag{27}$$

This expression for the dissipation was employed by Stegen et al (1973)[14] to calculate momentum flux by the direct dissipation technique.

In recent work employing data from Operation BOMEX, Leavitt (1973)[11] found that total production approximately balanced dissipation in the stability range $-0.2 \geq z/L \geq -1.5$, and that dimensionless turbulent transport as estimated from measurements at two heights was only about half of the dimensionless buoyant production as measured by Wyngaard and Coté (1971).[37]

In general the budget of temperature variance (θ^2) may be written (Monin and Yaglom, 1971)[27]

$$\frac{\partial \overline{\theta^2}}{\partial t} + \bar{u}_i \frac{\partial \overline{\theta^2}}{\partial x_i} + 2\,\overline{u_i\theta}\,\frac{\partial \Theta}{\partial x_i} + \frac{\partial}{\partial x_i}\left(\overline{u_i\theta^2} - D_\theta \frac{\partial \overline{\theta^2}}{\partial x_i}\right) =$$

$$- 2 D_\theta \overline{\left(\frac{\partial\theta}{\partial x_i}\right)^2} + 2\,\overline{\theta R'} + \frac{2\,\overline{\theta \epsilon}}{C_p} + S_\theta \quad , \qquad (28)$$

where repeated indices are summed and u_i and x_i may be replaced by (u, v, w) and (x, y, z) respectively. Here Θ is the mean potential temperature. The temperature variance budget can be simplified by invoking the assumptions of stationarity and horizontal homogeneity; Eq. (28) can then be written as

$$\overline{w\theta}\,\frac{\partial \Theta}{\partial z} + \frac{1}{2}\frac{\partial}{\partial z}\,\overline{w\theta^2} + \frac{1}{2}\,\overline{\chi}_\theta - 2\,\overline{\theta R'} - \frac{2\,\overline{\theta\epsilon}}{C_p} - S_\theta = 0 \qquad (29)$$

where the dissipation of temperature variance $\overline{\chi}_\theta$ is defined as

$$\overline{\chi}_\theta = 2\, D_\theta \overline{\left(\frac{\partial \theta}{\partial x_i}\right)^2} \quad . \tag{30}$$

In a similar manner, the budget of humidity variance $(\overline{q^2})$ may be written as (Coantic and Leducq, 1969)[38]

$$\frac{\partial \overline{q^2}}{\partial t} + \overline{u}_j \frac{\partial \overline{q^2}}{\partial x_j} + 2\, \overline{u_j q} \frac{\partial \overline{q}}{\partial x_j} + \frac{\partial}{\partial x_j} \left(\overline{u_j q^2} - D_q \frac{\partial \overline{q^2}}{\partial x_j} \right) =$$

$$2\, D_q \overline{\left(\frac{\partial q}{\partial x_j}\right)^2} + S_q \tag{31}$$

which simplifies under the same assumptions of stationarity and horizontal homogeneity to

$$\overline{wq} \frac{\partial \overline{q}}{\partial z} + \frac{1}{2} \frac{\partial}{\partial z} \overline{wq^2} + \frac{1}{2} \overline{\chi}_q - S_q = 0 \tag{32}$$

and the dissipation of humidity variance is defined as

$$\overline{\chi}_q = 2\, D_q \overline{\left(\frac{\partial q}{\partial x_j}\right)^2} \quad . \tag{33}$$

The first three terms of the simplified budget equations for temperature and humidity variance (29) and (32), represent production of scalar variance, transport of scalar flux divergence, and scalar variance dissipation due to the smoothing action of molecular

diffusivity respectively. The temperature variance budget contains additional source or sink terms not included in the humidity budget. The term $2\overline{\theta R'}$ represents the effects of heat transfer due to radiation on the temperature variance, $\frac{\overline{2\theta\epsilon}}{C_p}$ the effects of viscous dissipation on the temperature field due to the internal friction of the fluid, and S_θ and S_q represent generalized source or sink terms to account for any phase changes of water vapor or interactions of the temperature and humidity fields due to radiation.

Monin and Yaglom (1971)[27] and Plate (1971)[39] suggest by hypothesis that the viscous internal heating term $\overline{2\theta\epsilon}/C_p$ is insignificant and may be neglected. Friehe (1973)[40] suggests that this term may not be negligible and that there may be a positive correlation of $\overline{\theta\epsilon}$ due to an increase in θ produced by local, rapid adiabatic heating by viscous dissipation. Although a mean value for viscous dissipation $\overline{\epsilon}$ may be estimated from the mean square of the velocity derivative $\overline{(\frac{du}{dt})^2}$ (see Eq. (13)), a positive correlation of $\overline{\theta(\frac{du}{dt})^2}$ may not accurately reflect the actual correlation between fluctuating temperature and the instantaneous viscous dissipation $\overline{\theta\epsilon}$; $\overline{(\frac{du}{dt})^2}$ is only one component of dissipation, used to calculate $\overline{\epsilon}$ by the assumption of isotropy.

In general, the effect of radiative heat transfer is to reduce the value of the mean square temperature fluctuation (Goody (1956),[41] Townsend (1958),[42] Plate (1971)[39]). For internal radiative transfer

Townsend[42] indicates that maximum destruction of $\overline{\theta^2}$ occurs at very small scales of the temperature fluctuations since the most pronounced radiative transfer occurs over the shortest path interval. For atmospheric conditions with high humidity content and strong radiative transfer, Phelps and Pond (1971)[10] suggest that more absorption of long wave radiation occurs at larger scales resulting in a more homogeneous large-scale temperature field and suppression of low frequency temperature fluctuations. Plate[39] also indicates that partial absorption of long-wave radiation by atmospheric water vapor could cause a change of state (conversion to sensible heat) which would influence the temperature field. It is not clear whether this absorption and change of state of water vapor would act as a source or sink in the temperature and humidity variance budgets, and could be included in the generalized source terms.

Coantic and Seguin (1971)[43] have shown that radiative flux divergence due to absorption of infared radiation (long-wave) by water vapor and carbon dioxide always acts in such a way to increase the absolute value of the turbulent heat flux. They conclude that the constant heat flux hypothesis for the surface layer may not be valid, especially for conditions of moderate wind and high moisture content, even for heights above 1 meter.

The generalized source term may also include the effects of ocean

spray on the temperature and humidity fields and possible convective conditions in the upper boundary of the surface layer as suggested by Phelps and Pond (1971).[10]

To further simplify the budget equations of temperature and humidity variance it has been common practice (Miyake et al (1970),[33] Hicks and Dyer (1972),[36] Pond et al (1971),[8] Phelps and Pond (1971),[10] Wyngaard and Coté (1971),[37] Stegen et al (1972)[13] and Paulson et al (1972)[44]) to assume production of scalar variance is equal to the dissipation of scalar variance (Eq. (4)). Neglecting source terms in the temperature variance budget and assuming the transport terms may also be neglected Eqs. (29) and (32) reduce to

$$-\overline{w\theta}\,\frac{d\overline{T}}{dz} = \frac{1}{2}\,\overline{\chi}_\theta \tag{34}$$

and

$$-\overline{wq}\,\frac{d\overline{q}}{dz} = \frac{1}{2}\,\overline{\chi}_q \quad . \tag{35}$$

R. J. Taylor (1961)[18] justifies the assumption of production of temperature variance equal to the dissipation based on negligible values of the flux divergence term $\frac{1}{2} C_p \rho \overline{w\,\theta^2}$ and the viscous heating term $\overline{\theta\epsilon}$ as compared to the production term. Panofsky (1969)[45] also suggests omission of the transport term in the temperature variance budget and that in general, this term is of the order of 10% of the production or dissipation terms. Similar results were obtained by

Wyngaard and Coté (1971)[37] based on measurements of the transport term over land. Wyngaard[37] suggests that the transport term is an order of magnitude smaller than the production for moderately unstable conditions $-1 \le z/L \le 0$. Recent studies by Leavitt (1973)[11] and results presented in this work indicate that in the atmospheric boundary layer over the ocean, dissipation of temperature variance can greatly exceed production for moderately unstable conditions. Leavitt[11] finds that the mean value of turbulent transport in the temperature variance budget is about 25% of the production (representing a loss) for $.25 \le -z/L \le .75$ and a trend similar to Wyngaard's[37], suggesting that for highly unstable conditions the transport may become a gain, supporting Deardorff's (1966)[46] suggestion that for a counter-gradient of potential temperature, positive heat flux can be supported due to turbulent transport.

3. INSTRUMENTATION AND DATA ANALYSIS

3.1 Experimental Arrangement

Data for this thesis was obtained from measurements made from the Research Platform FLIP during a series of oceanographic expeditions in August 1970 (SOMA), September 1971 (MITOS I), February 1972 (MITOS II), April 1972 (MITOS III), and April 1973 (OWAX). For each cruise FLIP was towed to an operating area in the vicinity of 31° 40′ North latitude, 118° 00′ West longitude, approximately 60 miles west of Ensenada, Baja California. After a stable vertical position had been attained, FLIP drifted freely with keel orientated upwind. Wind direction during each cruise was predominately out of the north and northwest so that open ocean conditions were achieved.

The configuration of FLIP employed for the MITOS III and OWAX cruises is shown in figure 1. In this configuration an instrument package was located at the end of the 18.3 meter port boom. The 10.7 meter starboard boom was used to mount a fixed and a trimmable sail to maintain FLIP in an upwind orientation and compensate for the drag on the port boom. The instrument package used for measurements of turbulent velocity, temperature, humidity, and instrument motion is shown in figure 2. It was possible to mount the package rigidly at the boom height of 12.5 meters or to heights

FIGURE 1

Research Platform FLIP in the stable vertical position, with 18 meter port boom and compensating sails on starboard boom

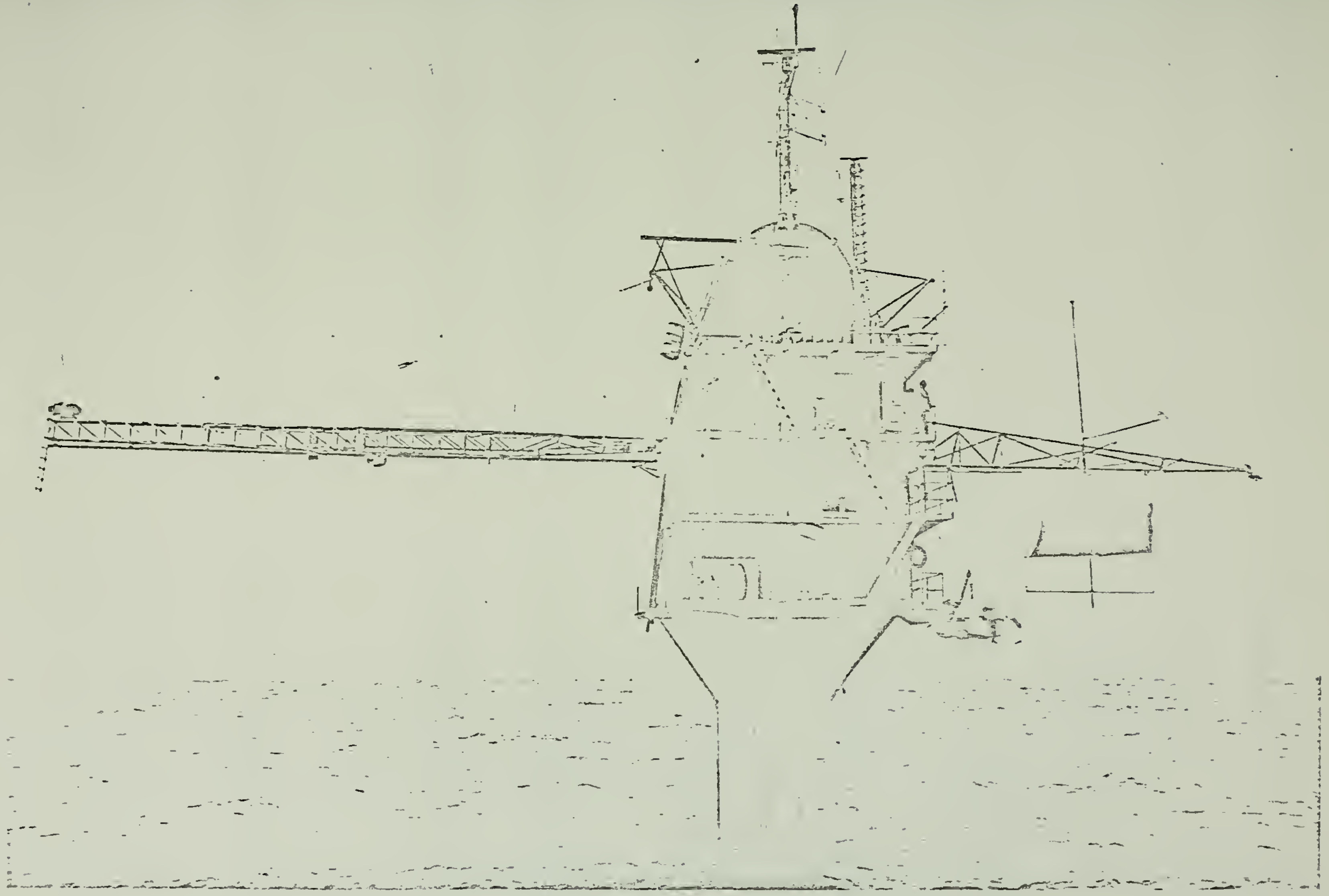

1.6.5.114(j)

FIGURE 2

Instrument package for flux measurements

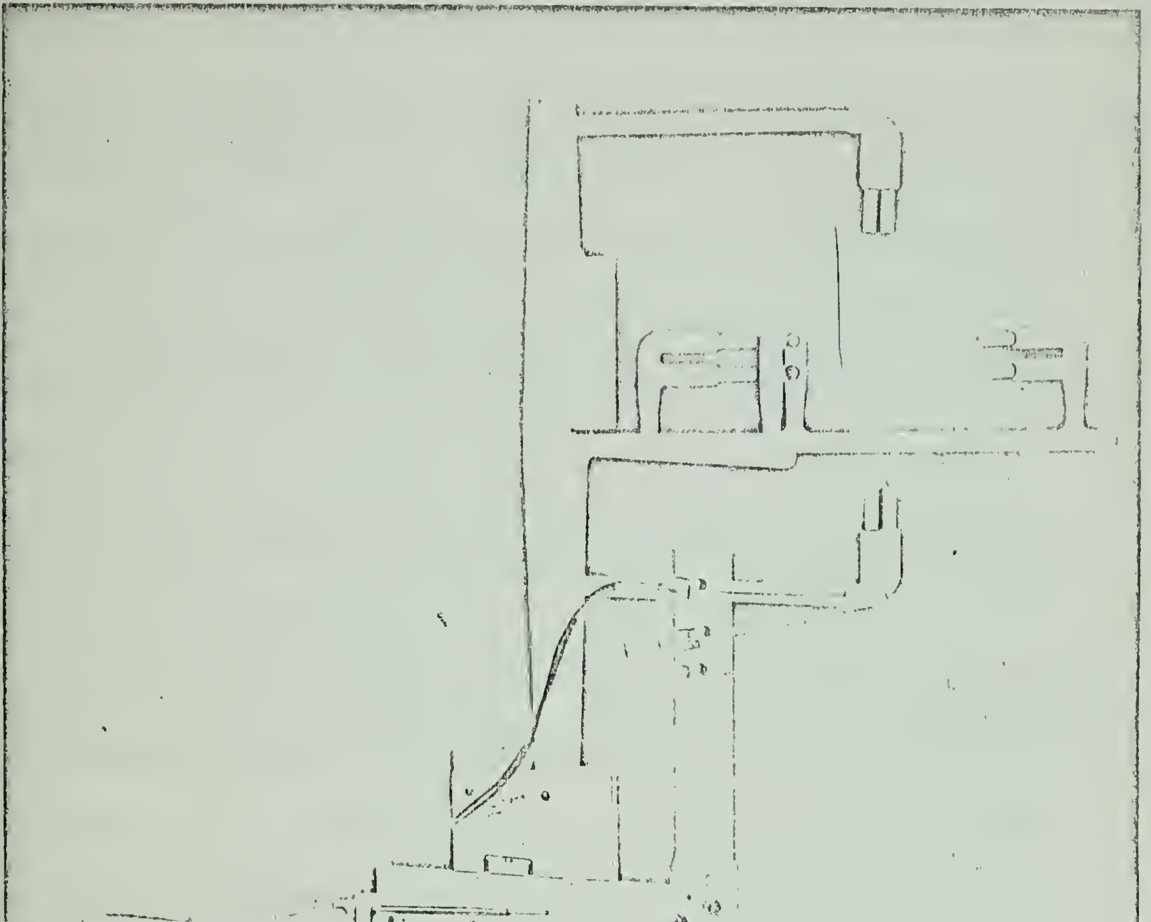

1.6.5.341

of 3 meters by means of a rigid extension pole connected to the end of the boom. Relative positions of the sensors on the instrument package for the MITOS III and OWAX cruises is shown in figure 2. The sonic anemometer used for measurements of three velocity components and shown mounted to the instrument package in figure 2 was employed only for the MITOS III and OWAX cruises. Other velocity sensors included TSI or DISA hot wire and hot film anemometers for high frequency measurements. Cup anemometers were used to measure mean velocity on the instrument package. High frequency temperature measurements were made using thermistors and cold wire probes. A Lyman-Alpha humidiometer was employed for small scale humidity measurements. Precision Hg thermometers and quartz thermometers were used to measure mean air and sea temperature and wet bulb temperature for calculation of mean absolute humidity. All instruments on the package were mounted rigidly and aligned in the laboratory so that any tilt sensed by the gyro would represent instrument tilt.

During the February 1972 cruise (MITOS II) a failure of the large boom necessitated removing the sails from the 10.7 meter boom and using the shorter boom on the starboard side to mount the instrument package approximately 8 meters from FLIP. Due to the proximity of the instrument package to FLIP during the MITOS II cruise and rearrangement of sensors, package motion was not

measured and only a limited amount of high frequency temperature, velocity and humidity data were available for analysis.

The experimental configuration of FLIP for the first two cruises of SOMA and MITOS I consisted of two 10.7 meter booms located on each side of FLIP. An instrument package similar to that shown in figure 2 except of lighter construction was attached to a rigid cable at the end of the port boom at heights between 3 and 8 meters. The package was stabilized by guy lines to minimize vibration and maintain instrument orientation into the wind. The cable to which the package was secured was kept rigid by means of a weight attached at the end of the cable and suspended 20 meters below the sea surface. Due to the experimental configuration of FLIP, the location of the instrument package was closer to FLIP for the first three cruises than for the last two cruises. No pitch corrections were applied to direct covariance measurements from the SOMA and MITOS I cruises. It was still possible, however, to obtain high frequency velocity, temperature and humidity data for analysis and calculation of turbulent fluxes by the dissipation methods. Data from the MITOS III and OWAX cruises were used for the comparison of different methods of calculating the turbulent fluxes of momentum, and sensible and latent heat using pitch corrected direct covariances as a basis for the comparisons.

3.2 Data Acquisition

The data acquisition and analysis system developed over the period of the FLIP cruises is shown schematically in figure 3. This figure is originally from Gibson (1973).[47] For each subsequent cruise the sensors and instrumentation were slightly different with changes and improvements made based upon the knowledge gained from the experience and results of previous cruises. The basic system framework, however, remained the same.

Calibration and test facilities included the wind tunnel of the Applied Mechanics and Engineering Sciences Department and a TSI portable calibration air jet for velocity sensor calibration under laboratory conditions and on FLIP at sea. The cup anemometers and sonic anemometer were calibrated in the laboratory wind tunnel before and after each cruise while the hot wire and hot film calibrations were performed on FLIP. The Lyman-Alpha humidiometer was calibrated in a Cambridge Systems humidity test chamber. Thermistor and cold wire sensors were calibrated on FLIP using a calibration feature built into the temperature bridge circuitry. Temperature sensor calibration consisted of changing the current through the sensor in a balanced bridge by an amount which caused the voltage across the sensor to change by the same amount as that resulting from a 1° C temperature change. Prior to and following the recording of data signals a series of calibration signals were recorded for voltage and frequency references.

FIGURE 3

Analog instrumentation schematic

Analog Instrumentation Schematic

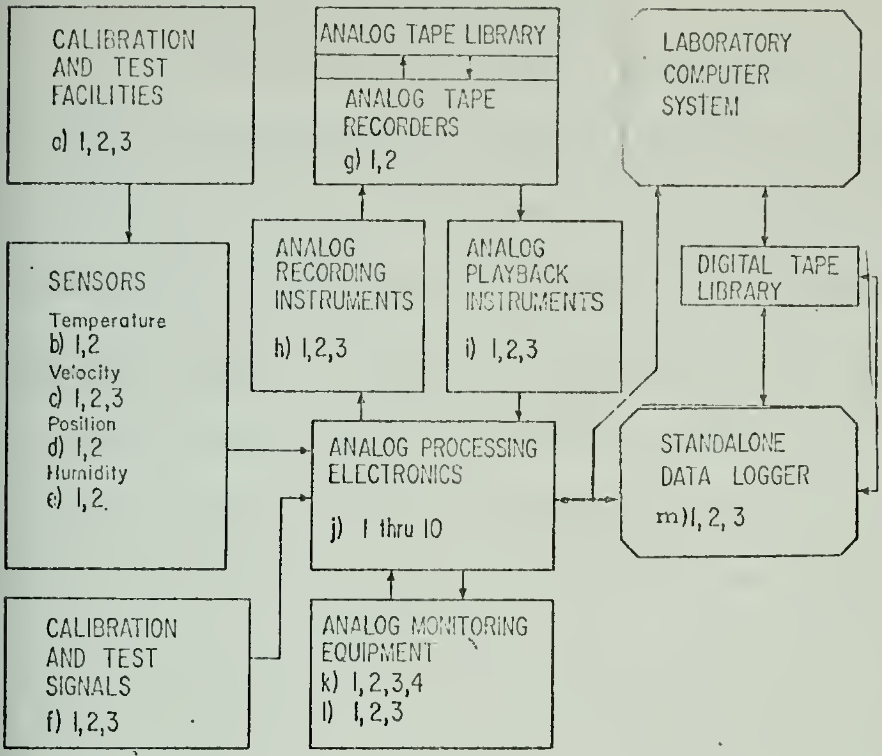

a)
1. Wind tunnel
2. Controlled temperature air jet
3. Portable calibration wind tunnel

b)
1. H-P Quartz thermometer
2. Cold wires & A. C. bridges, thermistors

c)
1. Cup anemometers
2. 3-D sonic anemometer
3. Hot wire and film anemometers

d)
1. Litton inertial guidance platform
2. Pitch gyro

e)
1. Cambridge dew pointer
2. Lyman-Alpha humidiometers

f)
1. Voltage reference
2. Signal generator
3. Noise generator

g)
1. Honeywell 7600
2. Sangamo 3600

h)
1. Pre-emphasis circuits
2. Multiplexer
3. Calibration and input selection patch panel

i)
1. De-emphasis circuits
2. Demultiplexer
3. Flutter compensation

j)
1. Buck and gain amplifiers
2. Multiplier
3. Sum and difference amplifiers
4. Overload indicators
5. Low and high pass filters
6. Differentiators
7. Frequency to voltage converters
8. Square law detector
9. Integrators
10. Voltage to frequency converters

k)
1. Chart recorders
2. Integrating digital voltmeters
3. Frequency counters
4. RMS meters

l) 1. Ubiquitous spectrum analyzer 2. Oscilloscope 3. x-y plotter

m) 1. A/D converter 2. Data buffer 3. Digital tape drive

3.2a Temperature measurements

Temperature fluctuation measurements were made using thermistors and platinum wire sensors (cold wire technique). For atmospheric conditions of very low intensity temperature fluctuations (SOMA cruise) thermistors were ideal since they have high sensitivity with a coefficient of resistance of - 3.2 Ω/Ω/° C. The plantinum wire resistance probes have a coefficient of resistance of 0.3 Ω/Ω/° C. The thermistors used for the temperature measurements are 1000 ohm Veco micro-bead thermistors manufactured by Victory Engineering Corporation of Springfield, New Jersey. The thermistors were of 0.33 and 0.064 mm diameter with a flat frequency response out to 1 and 5 Hz respectively. The platinum resistance wire sensors used for fine structure temperature measurements were of 1 mm length or less, 0.62 μ diameter, with a frequency response to 1.5 KHz. The cold wire sensors were made by Steve McConnell at UCSD employing commercially available TSI probe supports and etched fine platinum wire. For the first FLIP cruise thermistors were used in a Tektronix 3C66 AC bridge circuit. For subsequent cruises the thermistors and cold wires were used in AC or DC (MITOS I only) Wheatstone bridge circuits incorporating a low noise and high gain (80 db) amplifier for amplification of the bridge "error" signal. The bridge amplifier circuits were designed and built by Tom Deaton at UCSD. Equivalent resistance noise level for the resistance circuits was kept below

0.001° C by employing impedence matching transformer coupling for the bridge and amplifier sections of the circuit for the low resistance platinum probes (between 30 and 150 ohms). The entire bridge amplifier circuit was powered by batteries and made small enough to be located physically close to the sensor, reducing the possibility of noise pickup in the cable between sensor and bridge. The short cable length between the sensor and bridge circuits also minimized imbalances in the bridge caused by cable capacitance. By incorporating a cable capacitance balancing circuit in the bridge circuit, any imbalance caused by the cable capacitance was removed from the amplifier, leaving full dynamic range for the temperature signal. The sensor calibration procedure described earlier consisted of changing the wire or thermistor current by 0.3% and 3.2% respectively, corresponding to the coefficient of resistance for each sensor. The calibration signal output from the bridge was a square wave of approximately 40 Hz with peak-to-peak voltage corresponding to 1°C .

3.2b Humidity measurements

Humidity measurements were made with Lyman-Alpha humidiometers purchased from Electromagnetic Research Corporation, College Park, Maryland. The principle of operation of the humidiometer is based on the strong absorption of Lyman-Alpha radiation (1215.6 Å) by water vapor. The radiation is generated from a hydrogen source tube, crosses the measuring path of approximately 1.5 cm

length and enters the detector, a nitrous oxide ionization chamber. The source tube and detector were equipped with special uv windows of magnesium floride for transmission of the sensing beam across the measuring path. These windows were much less susceptible to moisture degradation than the standard lithium flouride windows. Pond et al (1971)[8] and Phelps and Pond (1971)[10] describe successful operation of the Lyman-Alpha humidiometer during Operation BOMEX for humidity fluctuation measurements. During the BOMEX measurements a mechanical flow through path described by Phelps, Pond and Gorner (1970)[48] was employed. For this research no mechanical additions were made to the sensor and the measuring path was open to the mean airflow.

Two different models of the Lyman-Alpha humidiometer were used during the FLIP cruises for this research. The BR model was employed for the first two cruises and the BLR model for the subsequent cruises. The output voltage of the BR model sensor has the form

$$V = V_o e^{-\lambda q \ell} \tag{36}$$

where λ is a constant depending on the absorption coefficient for water vapor and the source current, q the absolute humidity, and ℓ the path length. For humidity measurements with this model the fluctuation calibration was estimated by linearizing the logarithmic relation of (36) in the same manner as was done for the BOMEX measurements by

Pond et al (1971)[8] so that

$$q' \simeq \frac{-v'}{\overline{V}\,(\lambda \ell)} \qquad \text{where} \qquad V = \overline{V} + v' \qquad (37)$$

This method of calibration is probably good to within 10-15% since the fluctuations were very small and the mean humidity during the measurements was in a nearly linear portion of the instrument calibration curve (15° C dew point).

The more recent BLR model humidiometer has a logarithmic amplifier with a 40 db range following the detector amplifier. The exponential variation of the detector output with water vapor is thus converted to a substantially linear variation of output voltage with water vapor concentration. In this model an increased concentration of water vapor gave an increase in output voltage while the opposite was the case for the BR model. Although some source tube aging was noticed, the fluctuation calibration for both models remained fairly constant. Any drift on the instrument was minimized by insuring that the transmission windows were cleaned before each run and the zero point (dry air point for the BLR model) was set.

The humidiometers were calibrated in a Cambridge Systems hygrometric test chamber located at the Naval Electronics Laboratory in San Diego. Due to the limited availability of the chamber only a few absolute calibrations of the sensors were performed. The BR model was calibrated in July and August of 1970 giving a fluctuation

calibration of 11.7 µgm/cm^3/volt used for data from the SOMA cruise (August 1970) and the MITOS I cruise (September 1971). The BLR model sensor was calibrated in March 1972 between the MITOS II and MITOS III cruise and again in February and April, 1973 before and after the OWAX cruise. The calibration results for these three tests were 4.70 µgm/cm^3/volt, 4.81 µgm/cm^3/volt, and 4.75 µgm/cm^3/volt respectively. These results also support the conclusion of Pond et al[8] for the BOMEX results that the fluctuation calibrations were fairly independent of source tube aging for source tube currents which were used (> 0.25 ma). Absolute fluctuation calibration of the instrument for the last three cruises was probably better than 10%. The frequency response of the humidiometer appeared to be flat out to about 5-10 Hz.

Measurements of mean air and sea surface temperature were made with precision Hg thermometers and Hewlett-Packard Model 2801A Quartz thermometers. The quartz thermometers were employed only in the MITOS III and OWAX cruises. Mean temperature data from the MITOS III cruise indicated that the exposed quartz thermometers were subject to radiation heating. For the OWAX cruise the thermometers were equipped with aspirated spirated radiation shielding. Absolute humidity was determined from measurements of dry and wet bulb air temperature using a sling psychrometer. Dew Point temperature was also measured with a Cambridge Systems dew point hygrometer.

3.2c Velocity measurements

Fine scale velocity measurements were made with linearized constant temperature anemometers and hot-wire, x-wire or hot-film sensors. The anemometers were purchased from Thermo Systems Incorporated (Model 1054) and DISA Electronics (Model 55M01). The straight hot-wire, x-wire and hot-film sensors were also purchased from TSI or DISA, constructed of platinum or tungsten, and from 0.4 mm to 1.25 mm in length with frequency response out to 1.5 KHz or better. The hot-film sensors were constructed of a 0.025 mm quartz cylinder over which a 0.5 mm long platinum film was plated with gold leads to the film.

During the first three FLIP cruises, precise measurements of horizontal and vertical velocity with the x-wire sensors often were not obtained due to excessive (~ 30% for MITOS I) drift of the probe calibration in the wind field. The primary source of the calibration drift appeared to be contamination of the hot-wires by salt spray. Use of the hot-film sensors during the last two cruises greatly improved the fine scale velocity measurements and sensor calibration drift was not a significant factor.

A three-component sonic anemometer was also used for velocity measurements during the last two cruises. For the MITOS III cruise (April 1972) an EG&G sonic anemometer was borrowed from Rome Air Development Center for velocity measurements over a band-

width from DC to about 10 Hz. Measurement of velocity with this instrument is based on the principle of Doppler-shift of sound waves by the flow field in the measuring path. Since the instrument is an absolute sensor no calibration was required on FLIP. Unfortunately, due to a failure of a portion of the EG&G associated read-out circuitry only a limited amount of horizontal and vertical velocity data was obtained during the cruise. For the OWAX cruise, a similar EG&G three-component sonic anemometer was purchased, and the sonic anemometer readout system was designed and built by Tom Deaton and Mark Barnum at UCSD. This instrument and readout circuitry were thoroughly tested and calibrated in the 30 inch square, low velocity wind tunnel at UCSD up to a maximum wind speed of 20 meters/sec, and was successfully used during the OWAX FLIP cruise. Some minor distortion of the vertical sensing path of the sonic anemometer was discovered during the testing and calibration procedures. This distortion was due to a slight misalignment of about 1.1° between the vertical sensors but was corrected for in the calculation of momentum and heat fluxes during subsequent data analysis.

Mean velocity during the cruises was also measured with Teledyne-Geotech precision cup anemometers and associated readout circuitry designed and built at UCSD. The cup anemometers were also calibrated in the UCSD wind tunnel and used for comparison to the mean velocity obtained from the sonic, x-wire and hot-film sensors.

3.2d Analog instrumentation

The analog instrumentation employed during the FLIP cruises and for data analysis consisted of analog monitoring, processing, record and playback equipment as shown in figure 3. Data signals were conditioned for FM analog recording by means of amplification and filtering to achieve desired signal levels. Several techniques were employed to improve signal-to-noise ratios and optimize the dynamic range of the tape recorders. These included the use of pre-emphasis (de-emphasis for playback) circuits designed and built by Tom Deaton, and Tektronix 3A8 operational amplifiers as differentiators for analogue pre-whitening of fine scale velocity and temperature signals. Buck and gain amplifers designed by Bruce Williams at UCSD were used for removing known DC levels and subsequent amplification of the bucked signals. The 3A8's were also used for signal amplification. Burr-Brown sum and difference amplifiers were used to obtain horizontal and vertical velocity data from x-wire probes, and also for removing tape recorder flutter noise during playback when necessary. Krohn-Hite and Hewlett-Packard filters with cut-off rates of 12, 24, and 48 db/octave were used to minimize any high frequency noise contamination. Signals were sent through a multiplexer/demultiplexer circuit or directly through a calibration and input selection patch panel for recording on FM analog tape. The patch panel could be used to select either data or calibration

signals for recording, and also used as a signal input monitor terminal during recording and playback.

Two types of tape recorders were used for FM analog data recording. A Sangamo 3500, 1/2 inch, seven channel FM tape recorder was employed for the first four cruises, and a Honeywell 7600, seven/fourteen channel, 1/2 inch/1 inch FM tape recorder for the OWAX cruise. Both tape recorders were adjusted for a 50 db signal-to-noise ratio with a 1 KHz, 5 volt peak-to-peak sine wave. Allowing for signal intermittency and discrete amplification factors available, data signals were recorded as close to ± 2.5 volts peak level as possible without overranging, so that typical signal-to-noise ratios for the data tapes was approximately 40 db. Overload lights on the input selection panel and Krohn-Hite filters, as well as Tektronix storage type oscilloscopes or chart recorders, permitted constant qualitative monitoring of input data signals. A hard-wired Ubiquitous Spectrum Analyzer with oscilloscope and/or x-y plotter output could be used for on-line checks of input signal frequency content and spectral shape. The spectrum analyzer was also used as a valuable tool for determining noise contamination of signals which would have otherwise gone undetected.

3.3 Data Processing

An IBM 1130 digital computer system was employed for data reduction and subsequent data analysis of the analog tapes recorded on

FLIP. A detailed discussion of the laboratory computer system at UCSD and various digital techniques employed for turbulence analysis is given by Gibson (1973)[47] and Clay (1973).[49] Analog-to-digital (A-D) conversion was accomplished with a data acquisition interface to the computer permitting 15 bit samples at up to 100 KHz for single channel operation. Multiplexed sequential sampling of up to 8 channels was also possible at correspondingly slower sampling rates. Digital data could be stored on a 500K data storage disk or on digital tape using a Datum Model 100 digital tape drive unit. The computer system also included an IBM 1442 card reader/punch and a Calcomp 565 plotter for displaying results.

A high speed stand-alone digitizer/data logger system was also developed for A-D conversion shown schematically in figure 4. This system consists of a Tustine Electronics AD 1500 A-D converter-multiplexer, a data buffer, digital oscillator and control circuitry, and a Kennedy 8109 digital tape drive unit. The advantage of this system was that it could be used for double buffered "gapless" sampling at up to 8 KHz for one channel operation or at correspondingly slower rates for up to 16 channel operation. By "gapless" sampling is meant that there was no time delay in sampling the data caused by writing that data on tape. It was then possible to concatenate several tape blocks to make one computer record when analyzing tapes from the data logger system. Computer records consisted of up to 2048 words depending on the number

FIGURE 4

High speed standalone data logger

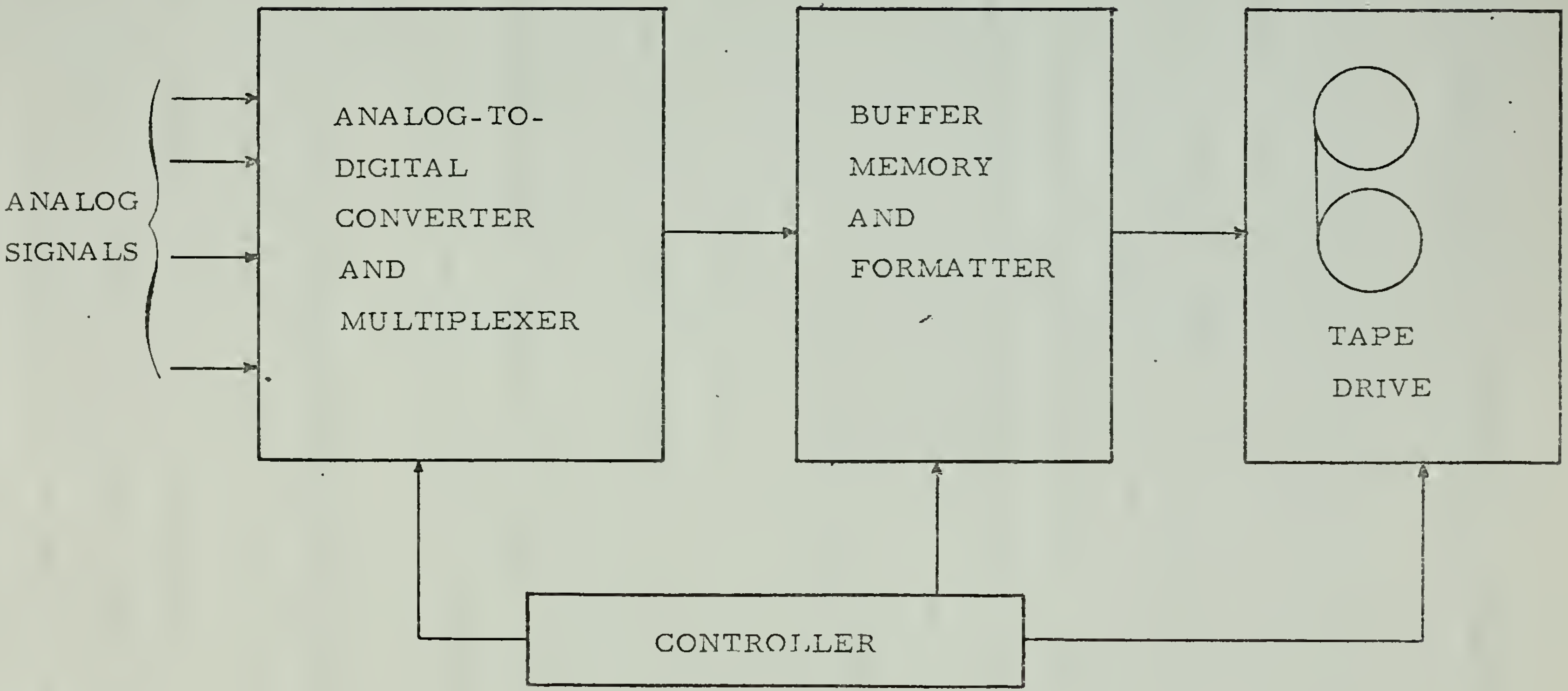

1.6.4.27

HIGH SPEED DATA LOGGER

of channels sampled (typically 4) and the type of analysis programs used.

An extensive, integrated group of time series analysis programs was developed by Gene Dial and Jerome Dayton for analysis of the turbulent data and plotting results. The majority of turbulence data analyzed was input from digital tapes, however, some of the earlier results were obtained from data stored on disk. Figure 5 shows a block diagram of the time series analysis system with programs grouped according to their primary functions: data collection, analysis, and display. This figure is also originally from Gibson (1973).[47] The data collection programs are used for digitizing operations to transfer data from the A-D interface to tape or disk, and for data transfers between tape and disk. Analysis programs permitted examination of raw digital data, statistical analysis, and spectral and cospectral analysis using fast fourier transform techniques. The display programs could be employed for a variety of functions to organize and output analyzed data.

A-D conversion consisted of amplification and filtering of the played back analog signals to make maximum use of the dynamic range of the A-D converter (± 10 volts) or data logger (± 2.5 volts), and prevent aliasing of the output spectral data. Input analog signals were filtered at the Nyquist frequency, i.e., at half of the sampling frequency. The analog instrumentation described earlier was used for

FIGURE 5

Time series analysis system

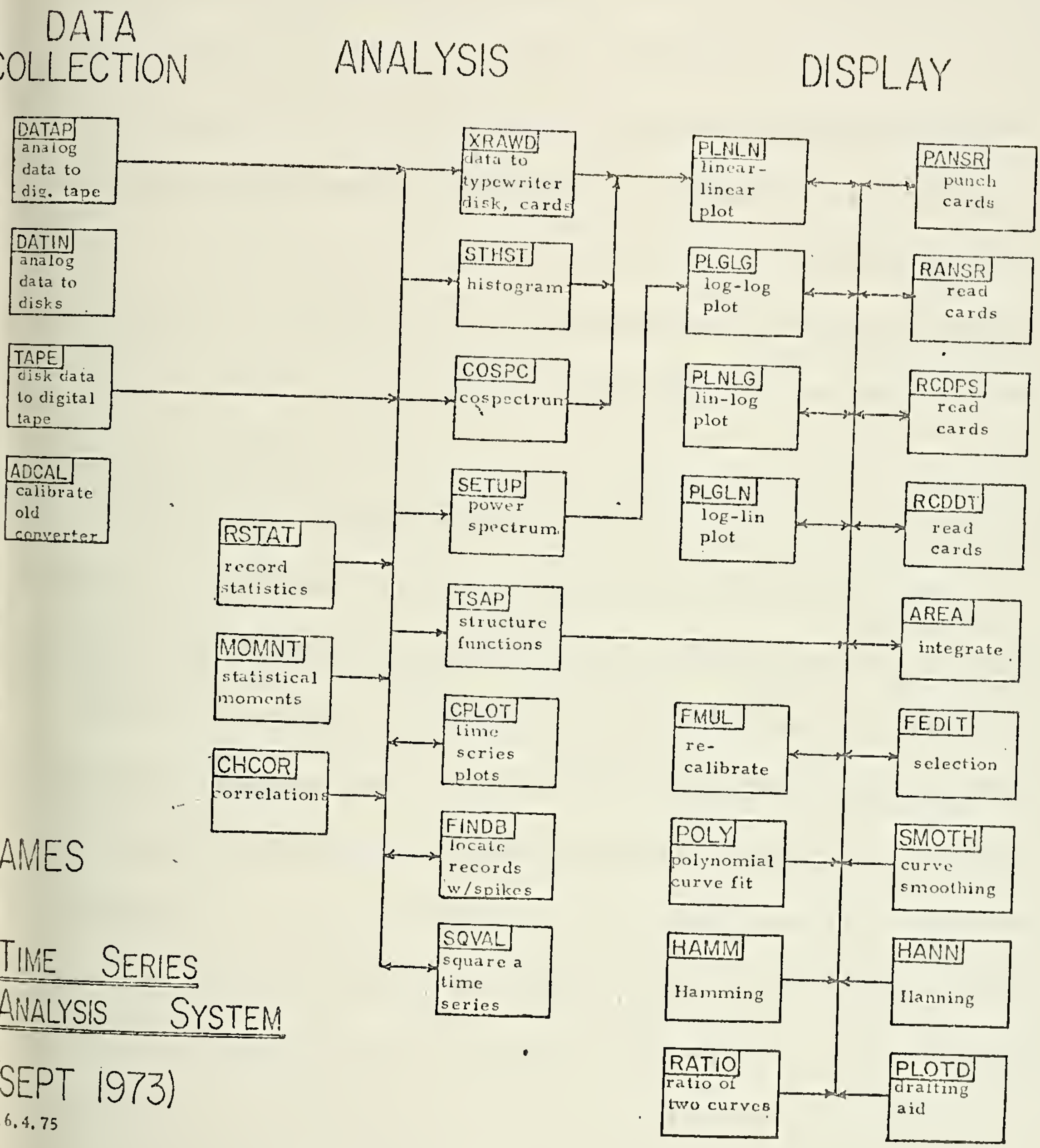

AMES

TIME SERIES ANALYSIS SYSTEM

(SEPT 1973)

1.6.4.75

this off-line analog signal conditioning. The digital tapes were initialized with an alphanumeric tape label at the beginning, consist of many tape records in the middle, and have an end-of-file mark at the end. Specification of the number of channels of input data and the record length was made by control communication to the digitizing programs DATAP and DATIN through the computer keyboard/typewriter. Several realizations over one section of analog data were normally made at different sampling frequencies and corresponding filter frequencies so that spectral estimates could be obtained over a wide range of frequencies.

The primary analysis programs employed for this work included CPLOT for time series plotting and determination of calibration factors; the statistics programs STHST and RSTAT used for calculation of averages, variance, standard deviation, running mean, and maximum and minimum values, and CHCOR and MOMNT for calculation of correlation coefficients and multiple channel moments or covariances; the spectral programs SETUP and COSPC were used for calculation of power spectra and cospectra. The SETUP program included options for boxcar or triangular data windowing and digital pre-whitening/post-darkening. For analysis of signals with steep power spectra and high power at lower frequencies (particularly true for horizontal velocity data) the triangular windowing was found to minimize the possiblity of "leakage" from lower to higher frequencies. Turbulent velocity and

scalar spectra fall off at a rate of slightly less than 6 db/octave. Predicted slopes for log-log plots of turbulent velocity and scalar power spectrum versus frequency would be -5/3 as given in Eqs. (11) and (12). The boxcar window employs a direct transform of the time series while with the triangle window the data is multiplied by factors increasing from zero to one at both ends of the data record to the middle. This means that much less energy is transferred from high to low frequencies in the convolution operation employing the triangular window since the side lobes of the triangle window fall off at 12 db/octave rather than 6 db/octave. Another means of reducing leakage was to flatten the signal spectrum from -5/3 to a + 1/3 slope by analog differentiation or by digital pre-whitening (i.e. transforming the first difference of the digital data).

Effects of leakage on atmospheric velocity data from the MITOS III cruise and subsequent techniques to minimize the leakage are illustrated in figures 6a, 6b, 6c, and 6d. A velocity signal from the hot-film and its analog derivative were simultaneously sampled at 50 and 500 Hz to obtain several hundred 1024 point records which were transformed and averaged. Figure 6a shows effects of leakage on the boxcar window transform of the "straight" signal. The spectral estimates were multiplied by the corresponding frequency (f) raised to the 5/3 power before plotting. Sampling at the two different frequencies

FIGURE 6

Illustrations of techniques for minimizing "leakage" in spectra

a. Box car window transform, leakage

b. Derivative pre-whitening

c. Digital pre-whitening

d. Triangular window transform

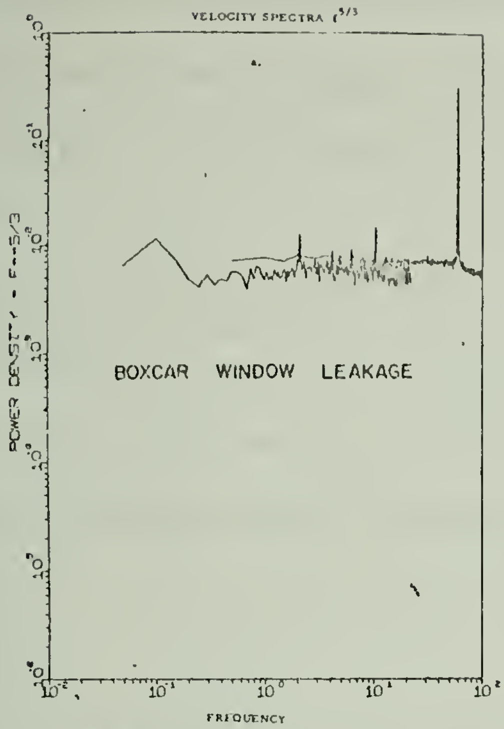

POWER SPECTRA OF VELOCITY SAMPLED AT 50 HZ AND 500 HZ WITH BOXCAR DATA WINDOW
1.6.7.73

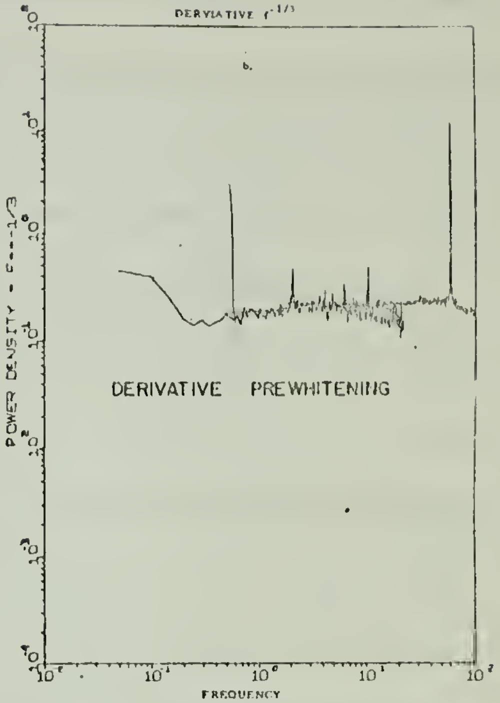

POWER SPECTRUM OF VELOCITY DERIVATIVE SAMPLED AT 50 AND 500 HZ WITH BOXCAR DATA WINDOW
1.6.7.69

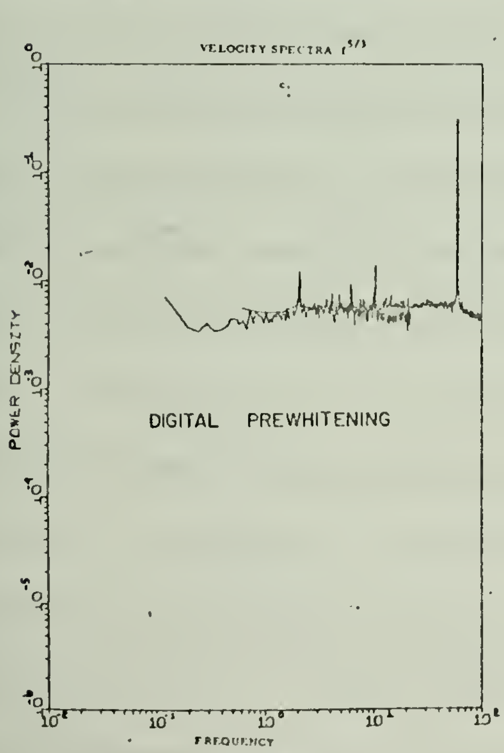

POWER SPECTRA OF VELOCITY SAMPLED AT 50 HZ AND 500 HZ WITH A DIGITAL PREWHITENING
1.5.7.70

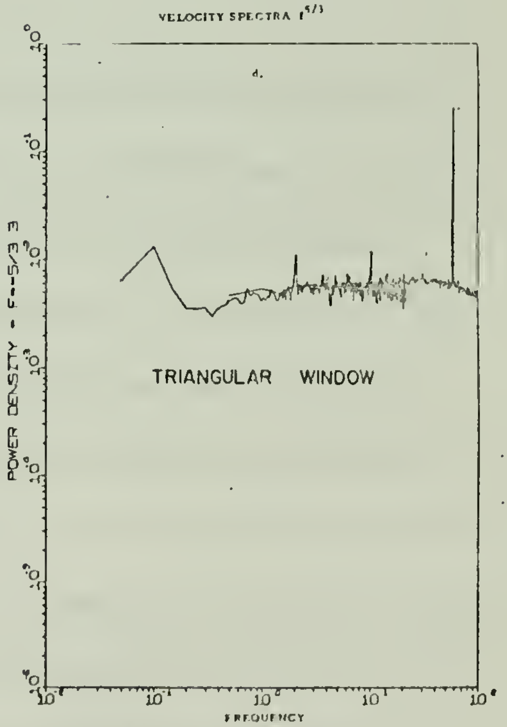

POWER SPECTRUM OF VELOCITY SAMPLED AT 50 HZ AND 500 HZ WITH TRIANGULAR DATA WINDOW
1.6.7.71

accentuates the leakage problem for the high frequency run since the low sampling boxcar window is wider in time and narrower in frequency, so there is less low frequency leakage in the overlap region of the two spectra. Figure 6b shows the effects of analog differentiation of the signal with a boxcar window transform. Spectral estimates were multiplied by f raised to the +5/3 power before plotting. Due to the low energy of the derivative spectrum at low frequencies there is little energy leakage to higher frequencies and consequently good agreement of the high and low spectra in the overlap region. The fall off of the high end of the low frequency spectrum is due to filtering. Figure 6c shows the effects of digital pre-whitening/post-darkening (correcting for the effects of the transfer function of the differencing operation) of the straight velocity signal with the boxcar transform. Results are similar to that of the analog differentiation pre-whitening. Figure 6d shows the straight velocity signal transformed with the triangular window and the spectral estimates multiplied by f raised to the 5/3 power. Again there is very good agreement in the overlap region.

Due to the time consuming nature of the digital pre-whitening technique, the triangular window transform or analog differentiation was employed for minimizing the effects of leakage during spectral analysis of high frequency data. Spectra computed with the boxcar window at sampling frequencies below 100 Hz did not appear to be greatly affected by leakage. However, any leakage effects were minimized by

obtaining several realizations of spectral data at different frequencies and matching the high frequency spectra to the low frequency spectra.

Reduced data from the analysis programs was initially stored in (x, y) lists on a special disk file where it could be modified for plotting or output to punched cards. The plotting routines consist of log-log (PLGLG), semilog (PLGLN), and linear-linear (PLNLN) coordinates. Data could be calibrated before analysis by entering the appropriate computer units per physical units into the analysis program or by modification of the output data with the FMUL program. The FMUL program allows recalibration of the x, y lists by specification of the variables A, B, C, D according to the formulae:

$$\begin{aligned} (\text{new } x) &= A * (\text{old } x)^{B} \\ (\text{new } y) &= C * (\text{old } y) * (\text{new } x)^{D} \end{aligned} \tag{38}$$

Recalibrated values of x and y replace the old values on the disc file allowing for output data of the type shown in figures6a-d. The special disc file may also be reentered by inputing saved data cards with the card read programs RANSR, RCDPS, and RCDDT, each program applicable for a different data card format.

3.4 Velocity Pitch Corrections

Data obtained during the MITOS III and OWAX cruises was used to calculate the turbulent fluxes by the direct covariance technique corrected for instrument tilt. During these two cruises optimum

experimental conditions were achieved, thus making this calculation possible. The instruments were mounted at the end of the long port boom 18 meters from the side of FLIP which substantially eliminated the strong tilt effect experienced during Operation BOMEX. Dirft of horizontal velocity sensors experienced during the first three cruises was substantially eliminated using the hot film velocity sensors. The sonic anemometer was employed for limited horizontal and vertical velocity measurements during the MITOS III cruise and for more extensive measurements during the OWAX cruise. The pitch component of the instrument package due to FLIP motion was measured with a vertical gyro system developed by R. E. Davis of Scripps Institution of Oceanography and used to convert measured vertical velocity for this data during digital analysis. The vertical gyro was calibrated in the laboratory prior to the FLIP cruises and mounted on the instrument package so that its axis was exactly parallel to the vertical axis of the sonic anemometer. Calibration of the pitch gyro was possible to 0.1° using a specially constructed tilt platform, also used for the sonic anemometer calibration.

To correct for instrument platform tilt, the measured horizontal and vertical velocity components were rotated in the x-z plane by an amount equal to the pitch angle measured by the vertical gyro. This correction is not relative to an inertial reference frame and as such does not correct for all components of FLIP motion, but only for

instrument tilt due to FLIP motion. It was also necessary to correct the measured vertical velocity data from the sonic anemometer employed for the OWAX cruise due to a misalignment of the vertical sensing path heads by 1.1° .

Denoting the measured and corrected velocity components by u_m, w_m and u_c, w_c respectively, and making a positive rotation of the vertical axis in the downstream direction by an angle φ (measured), the transformations are written as

$$\left.\begin{aligned}
u_c &= u_m \cos\varphi + w_m \sin\varphi \\
w_c &= w_m \cos\varphi - u_m (\sin\varphi + \varphi_s) \\
\overline{u_c w_c} &= \overline{(u_m w_m)\cos 2\varphi} - \overline{(u_m w_m)(\sin\varphi + \varphi_s)} \\
&\quad + \overline{w_m^2 \sin\varphi \cos\varphi} - \overline{u_m^2 (\sin\varphi + \varphi_s)\cos\varphi} \\
\overline{w_c \gamma} &= \overline{w_m \gamma \cos\varphi} - \overline{u_m \gamma (\sin\varphi + \varphi_s)}
\end{aligned}\right\} \quad (39)$$

where $\gamma = \theta$ or q , and φ_s is the sonic misalignment correction of order $\overline{\varphi}$ ($\varphi_s = 1.1°$ for OWAX). Since the measured gyro angles were typically less than 2° a small angle approximation can be made so that

$$\begin{aligned}
\cos\varphi &\simeq 1 \\
\sin\varphi &\simeq \varphi \text{ (radians)} .
\end{aligned} \qquad (40)$$

The measured and corrected velocities and the measured gyro angle are functions of time and as such consist of mean and fluctuating components. To first order the transfer motions can be rewritten for the fluctuating components and the small angle approximation as

$$\overline{(u\ w)}_c = \overline{(u\ w)}_m + \overline{w_m^2\varphi} - \overline{u_m^2\varphi} - \overline{u_m^2\varphi_s}$$

$$\overline{w_c\gamma} = \overline{w_m\gamma} - \overline{u_m\gamma\,\varphi} - \overline{u_m\gamma\,\varphi_s} \qquad (41)$$

4. RESULTS

Results from the data analysis of the SOMA, MITOS I, MITOS III and OWAX cruises can be identified with two types of meteorological conditions. The SOMA and MITOS I cruises represent warm, humid conditions during late summer with measurements made at night and late afternoon. The MITOS III and OWAX cruises represent colder, less humid conditions with measurements made during late winter/ early spring in the early morning or mid-day. Major environmental conditions and important numerical results are given in Tables 1 and 2. Stability data derived from the data analysis are given in Table 3. It will be shown from time series analysis and spectral and cospectral analysis that the MITOS I cruise represents conditions similar to those experienced during operation BOMEX presented by Pond et al (1971),[8] Phelps and Pond (1971),[10] and Leavitt (1973).[11] The MITOS III and OWAX cruises represent conditions similar to those experienced by the above authors also (cold, less humid conditions).

4.1 Time Series Analysis

Typical signals of horizontal velocity u, vertical velocity w, temperature T, and absolute humidity q, representing the warm, humid conditions of MITOS I are shown in figures 7, 7a, 7a1 and 7a2. Similar signals for the colder, less humid conditions of OWAX are shown in figures 8, 9, 9b, 9b1, and 9b2. Also included in the OWAX

TABLE 1

Environmental Conditions

	Day	Time (local)	Run (min.) Duration	z(cm)	$\overline{U}$(cm/sec)	T(°C) air	T(°C) sea	T(°C) Dew Point	q(μgm/cm^3) air	σ_u (cm/sec)	σ_w (cm/sec)	σ_θ (°C)	σ_q (μgm/cm^3)
SOMA 1	8/25/70	2100 N	52	500	768	19.2	20.9	16.4	14.0	68.7	55.1	.058	.319
2	8/26/70	2140 N	52	500	676	19.0	20.8	15.0	12.8	56.7	31.8	.136	.522
3	8/27/70	2130 N	52	500	687	19.3	20.7	15.6	13.3	80.6	47.3	.104	.390
MITOS 1	9/25/71	2020 N	120	500	703	19.4	21.6	15.0	12.8	63.8	40.4	.095	.540
7	9/28/71	1600 A	120	300	532	18.9	19.7	11.0	10.0	54.0	34.5	.342	.366
MITOS III													
2	4/20/72	1440 D	150	1250	677	14.7	15.4	10.2	9.5	44.6	28.7	.095	.204
OWAX 2	3/24/73	0500 D	340	350	378	13.6	14.6	8.7	8.7	50.7	19.5	.163	.258
3	3/25/73	0130 N/M	340	350	450	13.4	14.6	6.1	7.2	57.0	22.0	.142	.343
4	3/26/73	0330 N/M	85	350	510	13.4	14.5	4.5	6.5	49.0	22.5	.108	.450

Legend:

N	night
D	day
A	afternoon
M	morning

TABLE 2

Flux and Correlation Results

		$\overline{uw}$ (cm²/sec²)	C_D	$\overline{w\theta}$ (°C-cm/sec)	$\overline{wq}$ (μgm/cm²-sec)	$\overline{\theta q} \times 10^2$ (°C-μgm/cm³)	$-\overline{u\theta}$	$-\overline{uq}$	τ (dyne/cm²)	H_S (mw/cm²)	H_L (mw/cm²)	$R_B = \frac{H_S}{H_L}$	$-\frac{z}{L}$	$-r_{uw}$	$r_{w\theta}$	r_{wq}	$-r_{u\theta}$	$-r_{uq}$	$r_{\theta q}$
SOMA	1	(767)	1.3*	0.22	3.52	0.46	-	-	(.91)	0.27	8.7	0.03	0.023	(.203)	.07	.205	-	-	.247
	2	(594)	1.3*	0.28	5.46	1.91	-	-	(.71)	0.28	13.5	0.02	0.05	(.329)	.06	.329	-	-	.269
	3	(613)	1.3*	0.48	5.99	1.68	-	-	(.73)	0.48	14.8	0.04	0.06	(.161)	.10	.325	-	-	.414
MITOS I	1	(642)	1.3*	1.19	10.08	2.42	1.52	27.5	(.76)	1.19	25.0	0.06	0.11	(.249)	.311	.460	.251	.798	.471
	7	(365)	1.3*	3.10	6.12	6.02	3.47	9.65	(.43)	3.10	15.2	0.25	0.23	(.196)	.263	.480	.188	.488	.480
MITOS III																			
	2	455	0.993	1.46	2.96	1.03	2.45	4.83	0.56	1.46	7.37	0.24	0.29	0.355	.535	.588	.349	.531	.531
OWAX	2	163	1.14	1.32	2.46	3.07	1.95	2.64	0.20	1.32	6.12	0.27	0.41	0.165	.415	.489	.236	.201	.729
	3	270	1.33	1.43	3.65	4.44	1.62	4.68	0.33	1.43	9.08	0.29	0.22	0.215	.458	.484	.200	.239	.911
	4	343	1.27	1.20	5.11	3.76	2.87	8.94	0.42	1.20	12.72	0.12	0.17	0.311	.494	.496	.342	.299	.760

( ) calculated assuming $u_*^2 = C_D(\bar{U})^2$
* assumed value

$\tau = -\rho\,\overline{uw}$
$H_S = C_p\,\overline{w\theta}$
$H_L = L\,\overline{wq}$

$\rho_{(T = 19°C)} = 1.19 \times 10^{-3}\ \mathrm{gm/cm^3}$

$\rho_{(T = 13°C)} = 1.22 \times 10^{-3}\ \mathrm{gm/cm^3}$
$C_p = 0.24\ \mathrm{cal/gm°C}$
$L_v = 587_{(19°C)}\ \mathrm{cal/gm}$

$L_v = 588_{(13°C)}\ \mathrm{cal/gm}$

FIGURE 7

MITOS I-1 time series, u, w, T, q signals measured simultaneously, 12 minutes of continuous data

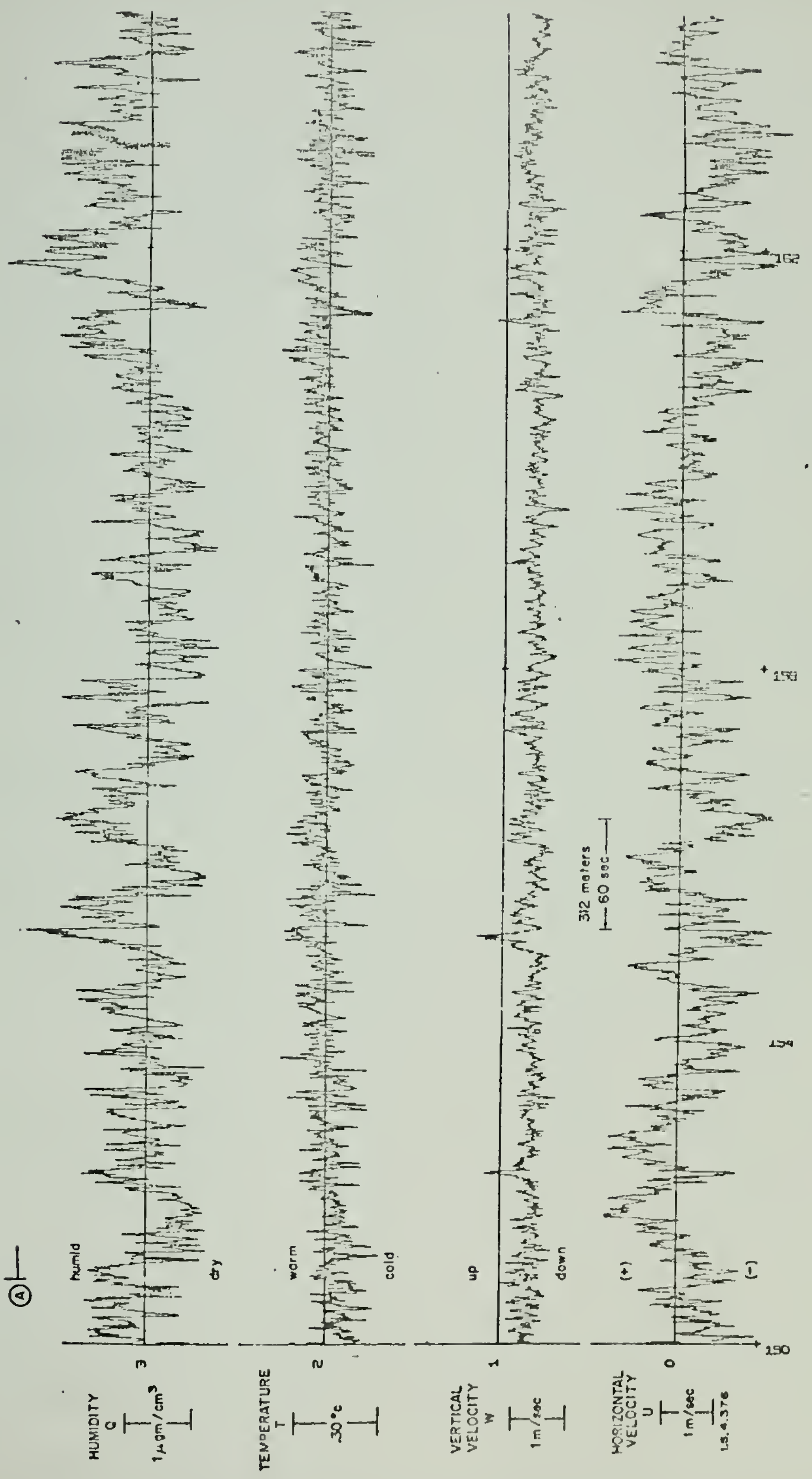
A
HUMIDITY
q
1 μgm/cm³
3
humid
dry
TEMPERATURE
T
.30°c
2
warm
cold
VERTICAL
VELOCITY
W
1 m/sec
1
up
down
HORIZONTAL
VELOCITY
U
1 m/sec
1.5.4.376
0
(+)
(−)
150
154
158
162
312 meters
60 sec

FIGURE 7

a. First "magnification" of MITOS I time series (x5), 2.5 minutes of data

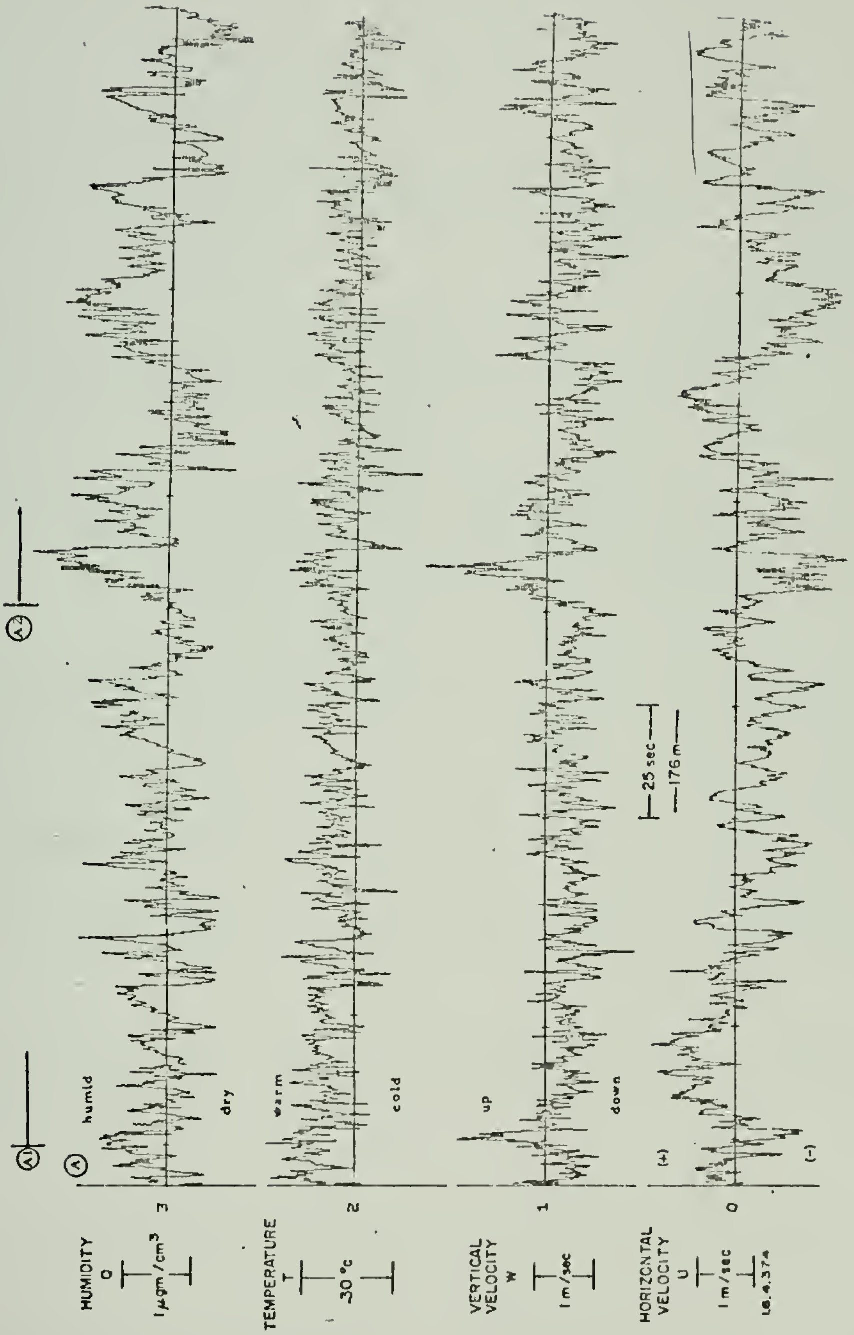
HUMIDITY
Q
1 µgm/cm³
TEMPERATURE
T
.30 °c
VERTICAL VELOCITY
W
1 m/sec
HORIZONTAL VELOCITY
U
1 m/sec
18.4.374
3
2
1
0
A
A1
A2
humid
dry
warm
cold
up
down
(+)
(-)
25 sec
176 m

FIGURE 7

a. 1 Second "magnification" of MITOS I time series (x100), 14 seconds of data

A1

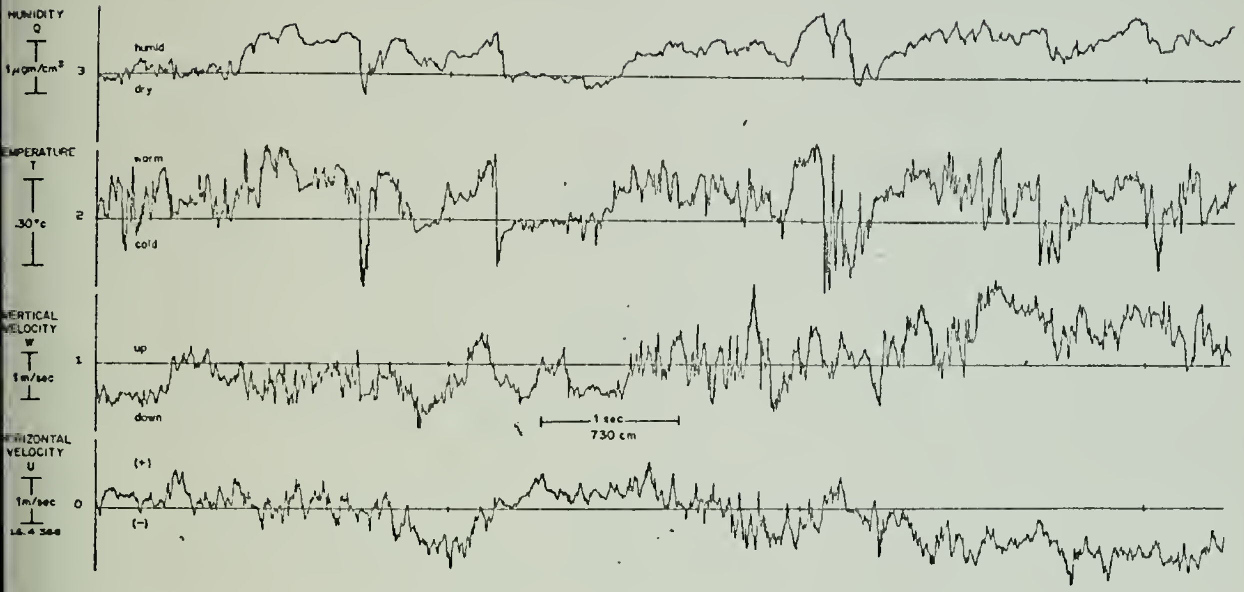
HUMIDITY
Q
1 μgm/cm³
3
humid
dry
EMPERATURE
T
.30°c
2
warm
cold
ERTICAL
ELOCITY
w
1 m/sec
1
up
down
1 sec
730 cm
IZONTAL
VELOCITY
u
(+)
1m/sec
0
(−)
16.4 sec

A1 cont.

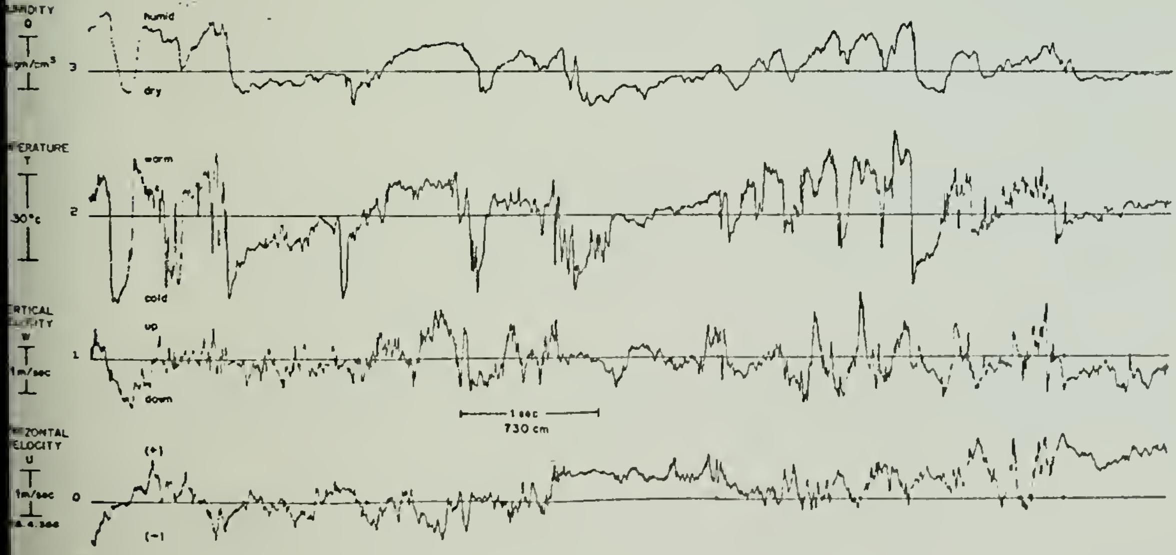
MIDITY
Q
gm/cm³
3
humid
dry
ERATURE
T
.30°c
2
warm
cold
RTICAL
w
1m/sec
1
up
down
1 sec
730 cm
ZONTAL
ELOCITY
u
(+)
1m/sec
0
(−)
8.4 sec

FIGURE 7

a. 2 Third "magnification" of MITOS I time series (x50), 28 seconds of data

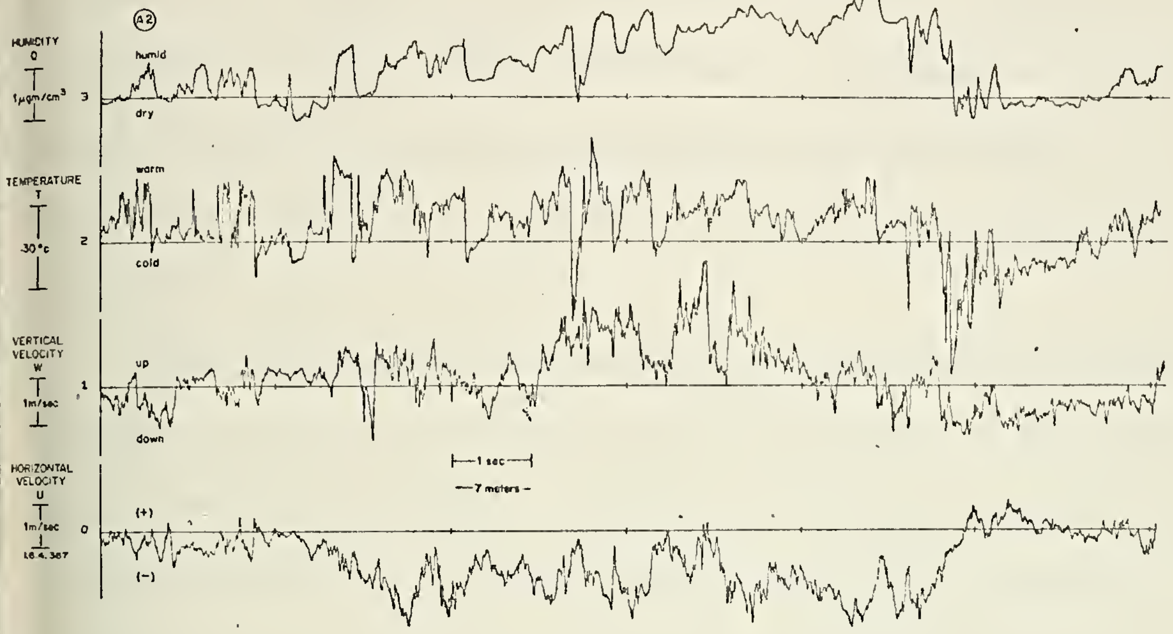
Ⓐ2
HUMIDITY
Q
1μgm/cm³
3
humid
dry
TEMPERATURE
T
.30°c
2
warm
cold
VERTICAL VELOCITY
W
1m/sec
1
up
down
HORIZONTAL VELOCITY
U
1m/sec
0
(+)
(−)
16.4.367
1 sec
7 meters

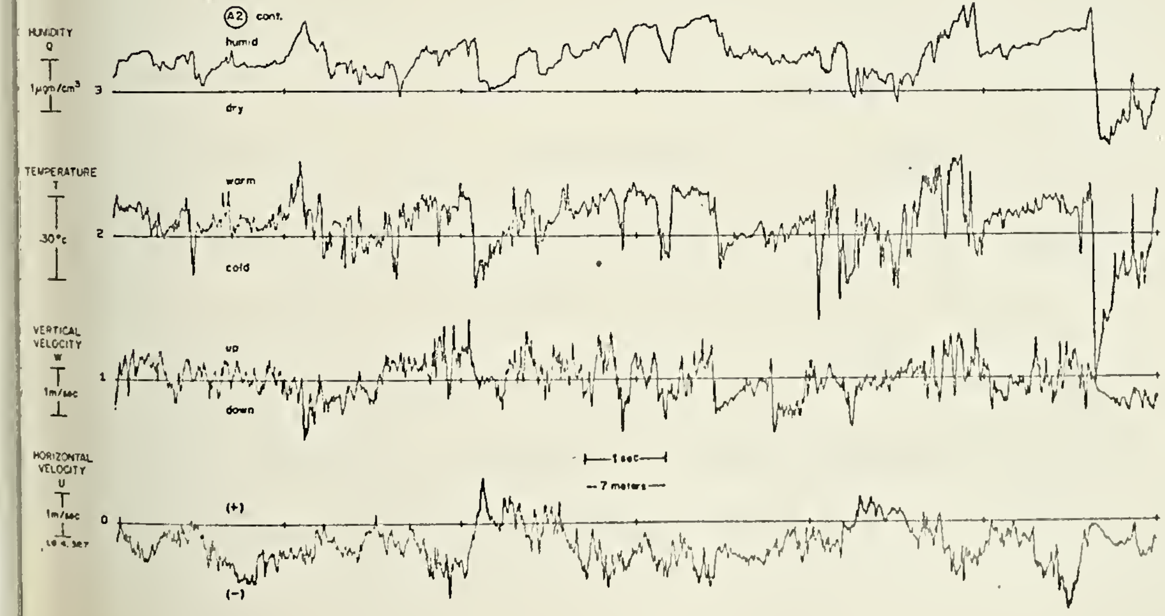
Ⓐ2 cont.
HUMIDITY
Q
1μgm/cm³
3
humid
dry
TEMPERATURE
T
.30°c
2
warm
cold
VERTICAL VELOCITY
W
1m/sec
1
up
down
HORIZONTAL VELOCITY
U
1m/sec
0
(+)
(−)
16.4.367
1 sec
7 meters

time series is the pitch angle measured by the vertical pitch gyro on the instrument package. For each cruise the time series begin with the large scale structure of each signal and show successively smaller scales of the original time series. The gyro pitch is only shown in the largest scale time series for OWAX data. The procedure employed for the time series analysis can be compared to increasing the magnification power of a microscope to look at smaller scales of any particular feature of the object.

Measurements of absolute humidity during the MITOS I and OWAX cruises were made with the Lyman-Alpha humidiometer so the response in both cases will be similar. Temperature was measured with a platinum cold wire for the MITOS I (figure 7) and OWAX 4 (figure 9) data and with a micro-bead thermistor for the OWAX 2 time series (figure 8). The temperature signal for the MITOS I cruise was high-pass filtered at 0.001 Hz (6 db/octave) so that events occurring over a period greater than the time constant of the filtering process (159 seconds) will be attenuated. For this reason the period of time covered by the first figure of the MITOS I series (figure 7) is of smaller scale than the first figure of the OWAX 4 series (figure 9), but can be compared to the OWAX 2 data presented in figure 8.

Horizontal and vertical velocity for the MITOS I data was measured with an x-wire anemometer, while the horizontal and vertical velocity measurements for the OWAX data were made using a

FIGURE 8

OWAX-2 time series, u, w, φ, T, q signals measured simultaneously, 8.5 minutes of continuous data

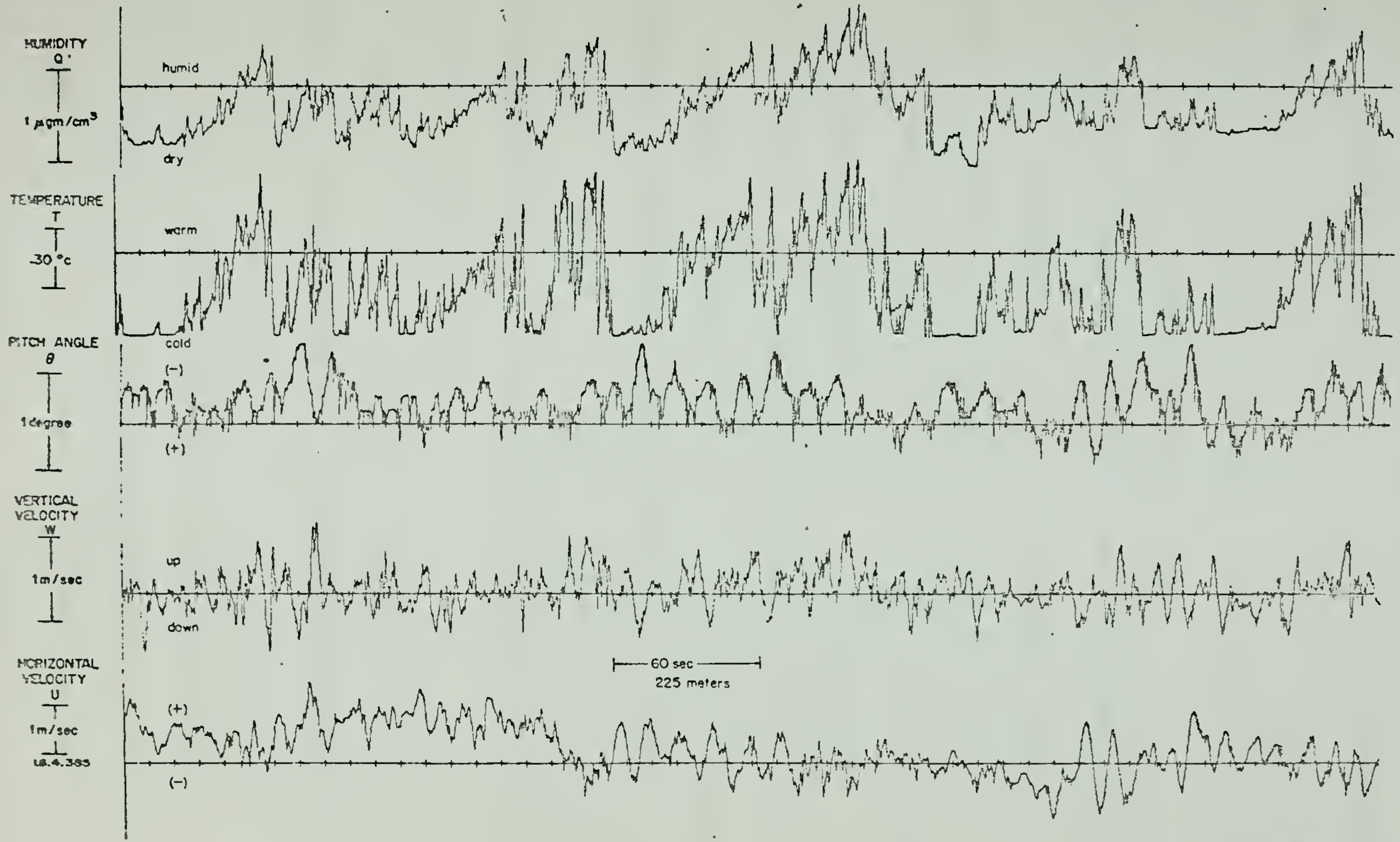
HUMIDITY
Q'
1 μgm/cm³
humid
dry
TEMPERATURE
T
.30 °c
warm
cold
PITCH ANGLE
θ
1 degree
(−)
(+)
VERTICAL
VELOCITY
W
1 m/sec
up
down
HORIZONTAL
VELOCITY
U
1 m/sec
US.4.385
(+)
(−)
60 sec
225 meters

sonic anemometer. Limitations of the frequency response of the sonic anemometer as compared with the x-wire can be seen for the smallest scales represented in OWAX figures 9b1 and 9b2. It should be noted that the centerline of each time series does not necessarily correspond to the zero or mean level of each individual signal.

The large scale trends in the MITOS I and OWAX data are shown in figures 7, 8, 9 representing 12, 8.5 and 54 minutes of data respectively. In general, ramp-like structures of 100-200 m wavelengths can be seen in the temperature and humidity signals with warm humid air associated with upward vertical velocity and negative horizontal velocity changes. Both the temperature and humidity rise gradually to a maximum value and then decrease sharply to a minimum value. The gyro pitch angle is in general out of phase with the horizontal velocity variations and in phase with the vertical velocity variations, with positive gyro angles associated with larger upward excursions of the vertical velocity.

Referrring to the first "magnification" of the time series in figure 7a and 9b representing 3 and 3.5 minutes of real time, the ramp-like structure of the temperature and humidity signals can clearly be seen. The temperature signal for the MITOS I data is more like the BOMEX temperature signals presented by Pond et al[8] and Leavitt.[11] The original filtering process should not have any significant affect at this scale for the MITOS I data. The humidity and temperature

FIGURE 9

OWAX-4 time series, u, w, φ, T, q signals measured simultaneously, 54 minutes of continuous data (φ not included in "magnifications")

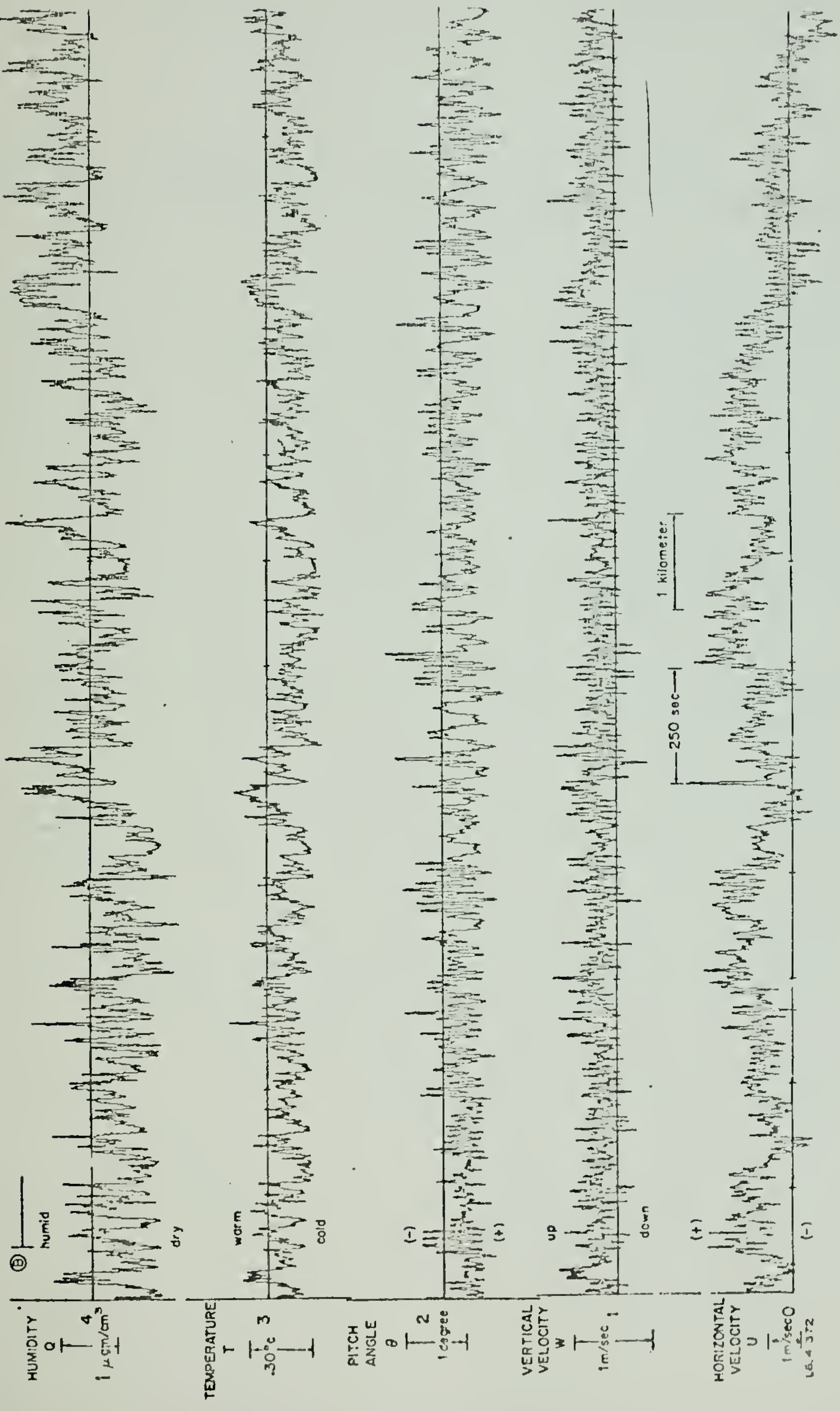
Ⓑ
HUMIDITY
Q
4
1 μgm/cm³
humid
dry
TEMPERATURE
T
3
.30°c
warm
cold
PITCH
ANGLE
θ
2
1 degree
(-)
(+)
VERTICAL
VELOCITY
W
1m/sec
1
up
down
HORIZONTAL
VELOCITY
U
1 m/sec
0
(+)
(-)
250 sec
1 kilometer
L6.4 372

FIGURE 9

b. First "magnification" of OWAX-4 (x10), 5.4 minutes of data

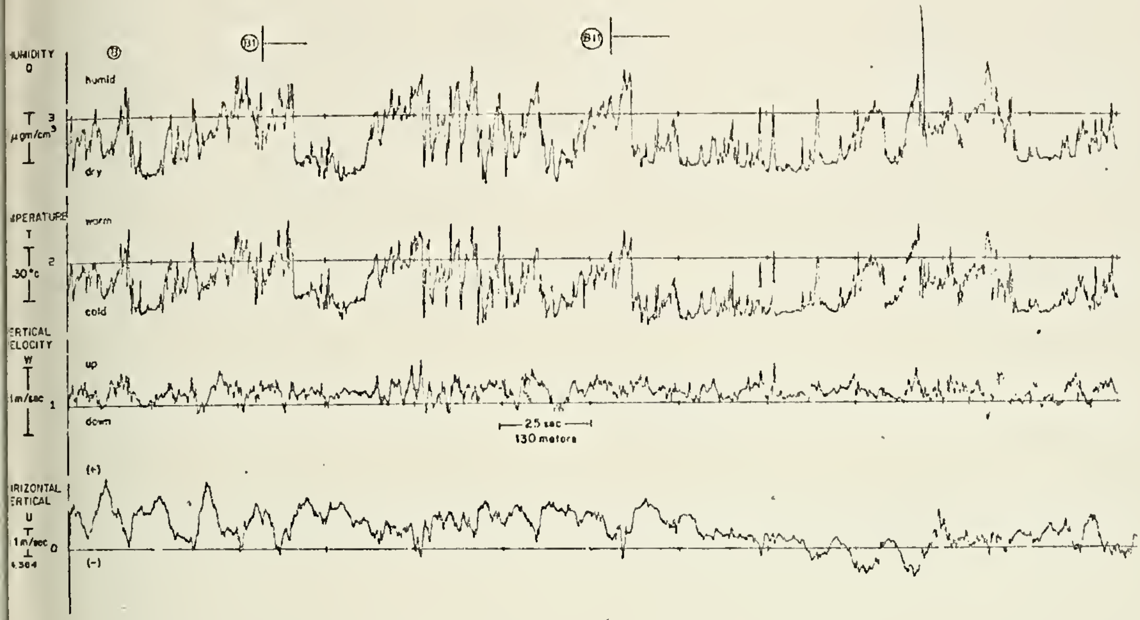
Ⓑ
B1
B11
UMIDITY
Q
humid
3
µgm/cm³
dry
PERATURE
T
warm
2
.30°c
cold
ERTICAL
ELOCITY
W
up
1m/sec
1
down
├─25 sec─┤
130 meters
(+)
RIZONTAL
ERTICAL
U
1m/sec
0
4.384
(-)

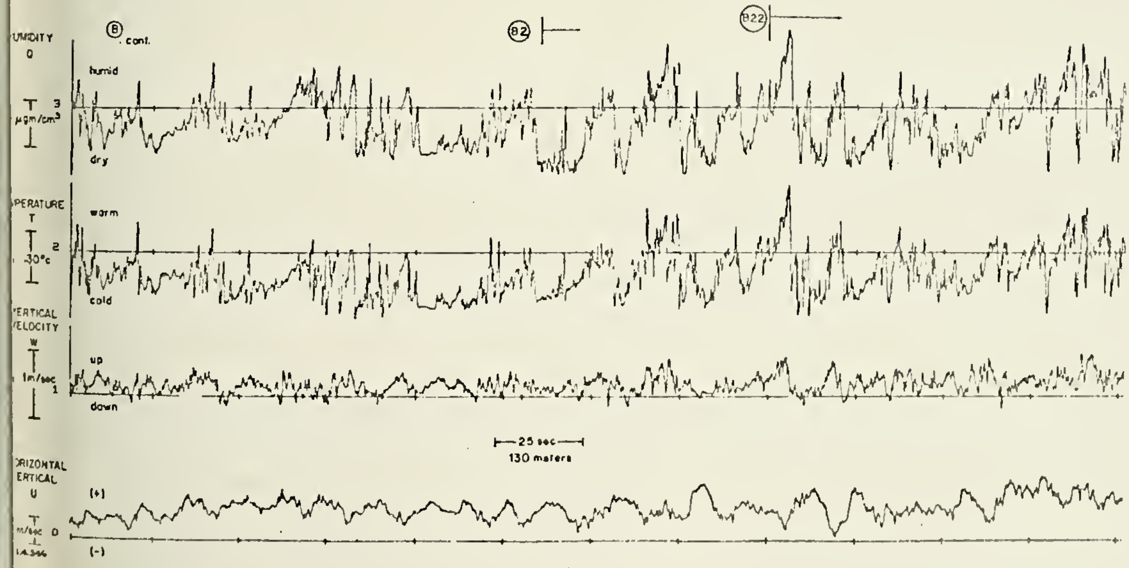
Ⓑ cont.
B2
B22
UMIDITY
Q
humid
3
µgm/cm³
dry
PERATURE
T
warm
2
.30°c
cold
ERTICAL
ELOCITY
W
up
1m/sec
1
down
├─25 sec─┤
130 meters
RIZONTAL
ERTICAL
U
(+)
m/sec
0
14.344
(-)

FIGURE 9

b. 1 Second "magnification" of OWAX-4 (x200), 16 seconds of data

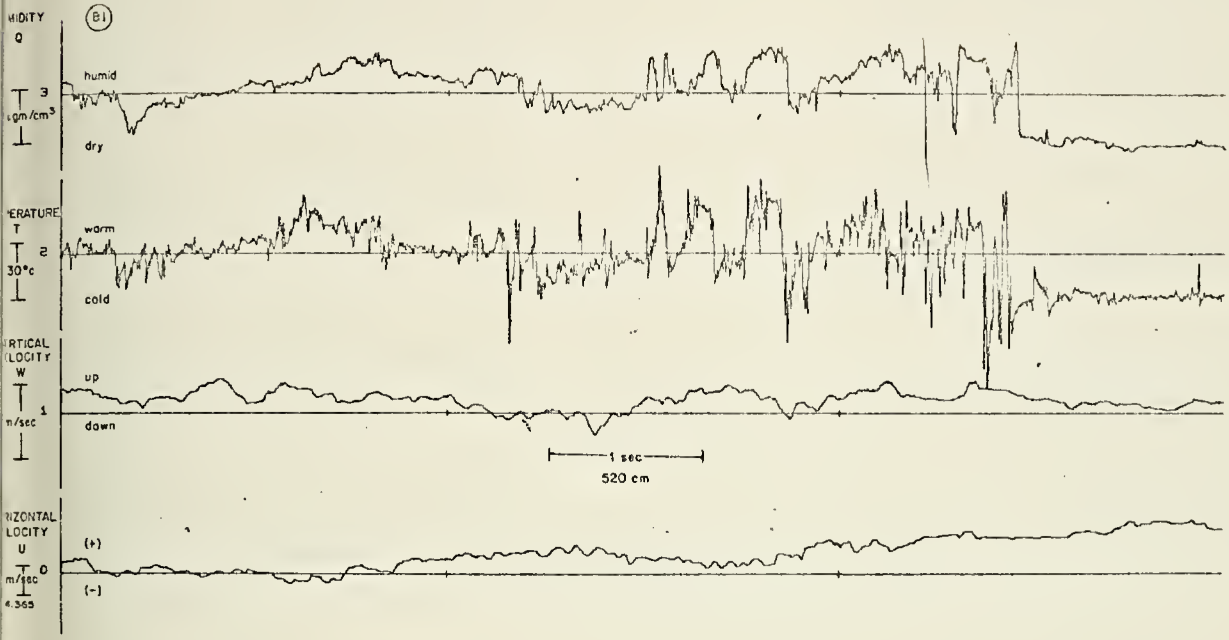
B1
HIDITY
Q
3
gm/cm³
humid
dry
ERATURE
T
2
30°c
warm
cold
RTICAL
LOCITY
W
1
n/sec
up
down
1 sec
520 cm
IZONTAL
LOCITY
U
0
m/sec
(+)
(-)
4.365

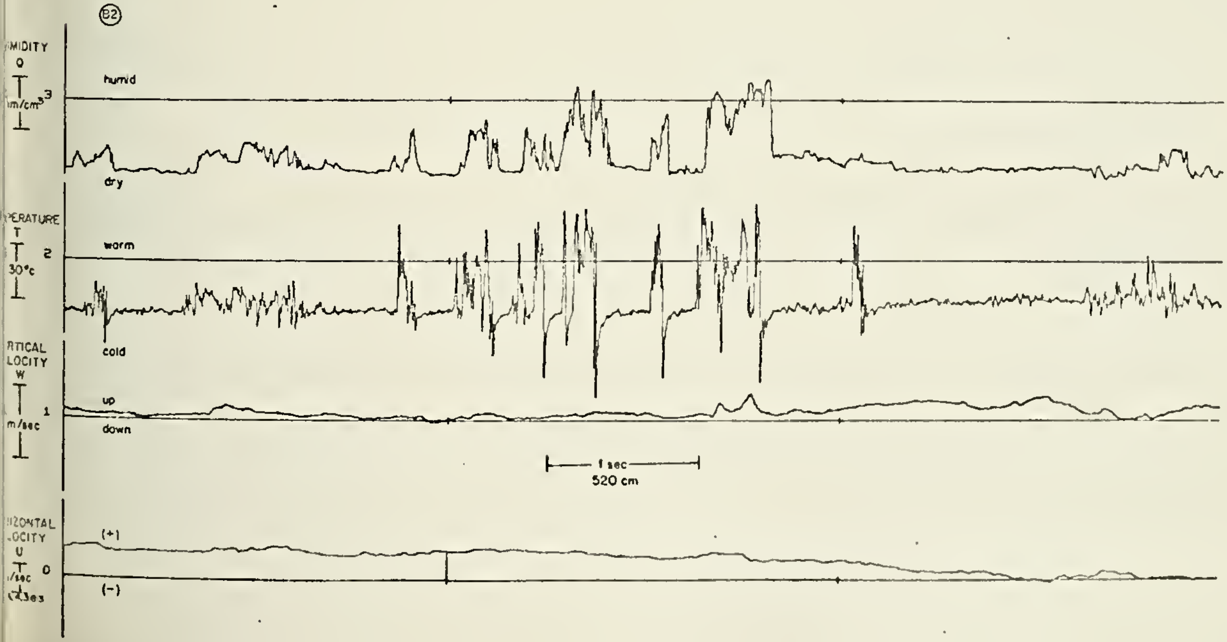
B2
MIDITY
Q
3
m/cm³
humid
dry
PERATURE
T
2
30°c
warm
cold
RTICAL
LOCITY
W
1
m/sec
up
down
1 sec
520 cm
IZONTAL
LOCITY
U
0
/sec
(+)
(-)
4.363

FIGURE 9

b. 2 Third "magnification" of OWAX-4 (x100), 32 seconds of data

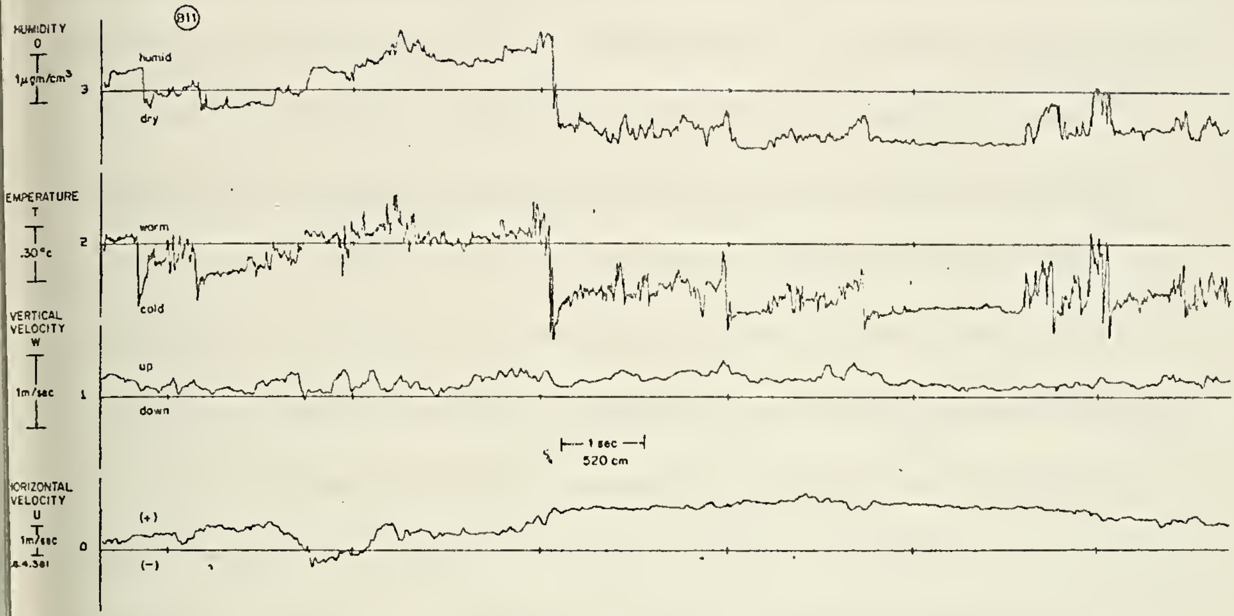
811
HUMIDITY
Q
1μgm/cm³
3
humid
dry
TEMPERATURE
T
.30°c
2
warm
cold
VERTICAL
VELOCITY
W
1m/sec
1
up
down
1 sec
520 cm
HORIZONTAL
VELOCITY
U
1m/sec
0
(+)
(−)
8.4.361

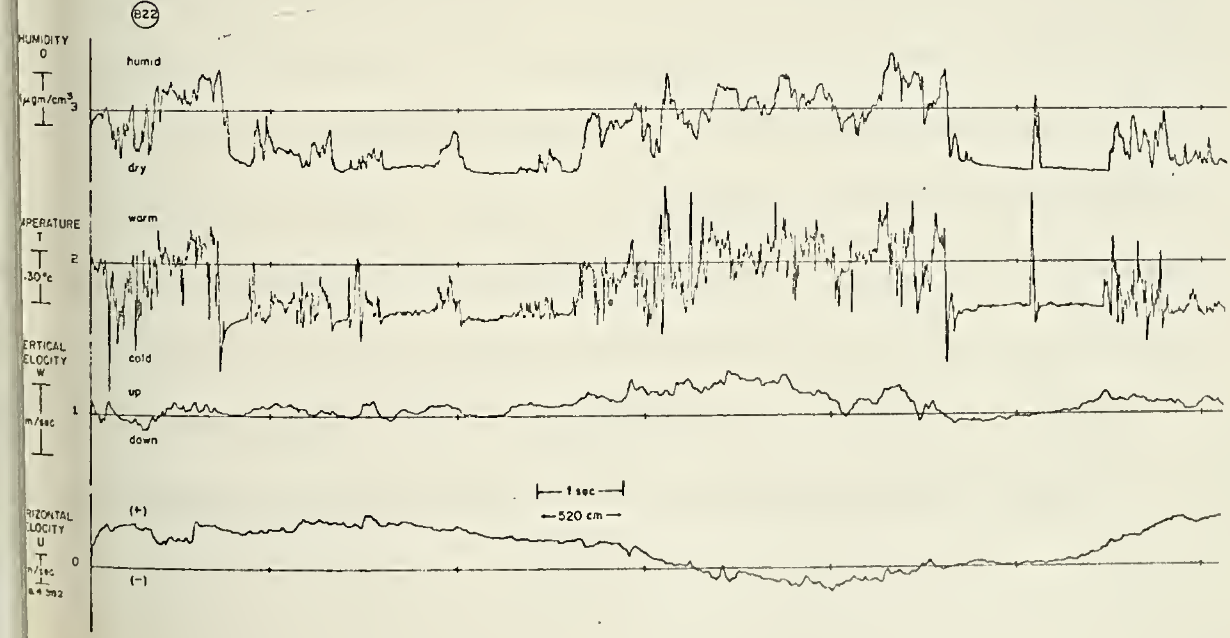
822
HUMIDITY
Q
μgm/cm³
3
humid
dry
PERATURE
T
.30°c
2
warm
cold
ERTICAL
ELOCITY
W
m/sec
1
up
down
1 sec
520 cm
RIZONTAL
LOCITY
U
n/sec
0
(+)
(−)
8.4.362

ramp interfaces are not only associated with maximum values but also with minimum values of temperature and humidity and with what has been termed "cold spikes" in the temperature signals. The cold spikes appear to be more pronounced in the MITOS I temperature signals than in the OWAX temperature signals. The OWAX temperature and humidity signals appear more intermittent than the MITOS I signals, even though the height of the sensors for the OWAX data was 350 cm as compared to 500 cm for the MITOS I data. From concurrent research on BOMEX, MITOS I, MITOS III and OWAX data McConnell (1974),[50] has obtained kurtosis values for dT/dx from MITOS I and BOMEX which are lower by a factor of 2 than similar kurtosis values calculated for OWAX and MITOS III data. This indicates more intermittency in the temperature data for the later cruises.

Figures 7a1 and 9b1 show the smallest scale magnification and each represent approximately 12 seconds of real time. The ramp-like structure of the temperature and humidity fields is still evident at this scale at wavelengths of less than 5 m . The temperature and humidity appear well correlated except at the interfaces of the ramps where the largest cold spikes in the temperature occur. Figure 9b1 shows that cold spikes can occur during relatively quiescent periods between the large scale ramps. There is relatively more activity at higher frequencies and more small scale ramps for the MITOS I data as compared to OWAX data. Another feature peculiar to the temperature

signals for both OWAX and MITOS I data is the occurrence of reverse ramps at scales less than 500 cm. These reverse ramps showing interfaces reversed to the mean flow direction are similar to the large scale ramp structure of temperature in a heated jet as discussed by Gibson, Friche and McConnell (1974).[51] The reduction of frequency response for the sonic anemometer as compared to the x-wire can be seen in figure 9b1 and 9b2.

Figures 7a2 and 9b2 show the existence of cold spikes at ramp interfaces occasionally on the upwind reversed interfaces, and also during more quiescent periods. The OWAX data show more intermittency than the MITOS I data and the occurrence of reverse ramps is in evidence. The MITOS I temperature signal also exhibits a slower warming trend after an interface in which the temperature decreases than the OWAX data exhibits.

The effect of intermittency of the OWAX temperature data and the effect of the different behavior of the OWAX and MITOS temperature signals at larger scales on spectral and cospectral shapes will be discussed in Sections 4.5 and 4.6. Differences between temperature spectra and sensible heat flux cospectra are similar to those obtained by Pond et al,[8] Phelps and Pond,[10] and Leavitt.[11]

4.2 Standard Deviations of Turbulent Fluctuations and Stability Dependence

The measured standard deviations for horizontal and vertical

TABLE 3

Stability Results

		$-z/L$	ϕ_H	$\phi_\epsilon^{2/3}$(Prod - Diss)	$\phi_\epsilon^{2/3}$(Wyngaard)	u_*(cm/sec)	$-T_*$(°C)	$-q_*$(μgm/cm^3)	σ_u/u_*	σ_w/u_*	$-\sigma_\theta/T_*$	$-\sigma_q/q_*$
SOMA	1	0.023	0.855	0.964	1.04	27.7	.008	.127	2.48	1.98	7.25	2.51
	2	0.05	0.795	0.941	1.07	24.4	.011	.224	2.32	1.30	11.97	2.33
	3	0.06	0.714	0.935	1.08	24.7	.019	.242	3.26	1.91	5.35	1.61
MITOS	1	0.11	0.602	0.922	1.13	25.3	.047	.398	2.52	1.60	2.02	1.36
	7	0.23	0.462	0.939	1.19	19.1	.162	.320	2.82	1.81	2.11	1.14
MITOS III		0.29	0.421	0.959	1.22	21.3	.068	.139	2.09	1.35	1.40	1.47
OWAX	2	0.41	0.364	1.01	1.27	12.8	.103	.192	3.96	1.52	1.58	1.34
	3	0.22	0.470	0.935	1.18	16.4	.087	.222	3.48	1.34	1.63	1.54
	4	0.17	0.518	0.925	1.15	18.5	.065	.276	2.65	1.22	1.66	1.66

velocity, and temperature and humidity fluctuations are given in Table 1. Values of the ratios σ_u/u_*, σ_w/u_*, σ_θ/T_* and σ_q/q_* are given in Table 3 for stability results and plotted versus $-z/L$ in figure 10. Figure 10 also compares present results for this work with other current results. For each run the averaging time is given under "run duration" in Table 1. The variances and covariances were obtained by integration under the spectral and cospectral curves. Integration of the u and w spectra to obtain variances for OWAX data did not include the area under the peak at 0.1 Hz due to FLIP induced motion. An approximate correction was made by drawing a faired line through the affected region in a similar manner as was done by Pond et al (1971)[8] and Leavitt (1973).[11] Any resultant error from this procedure can be expected to be small since the peak at 0.1 Hz in the w spectrum for MITOS III data was removed by an instantaneous pitch correction of the w signal using Eq. (39) of Section 3.4. The u and w spectra from SOMA and MITOS I do not show a large peak at 0.1 Hz since a large part of the FLIP motion was removed by the cable suspension system of these two cruises. The u_* values for OWAX and MITOS III were obtained from integration of the uw cospectrum corrected for tilt effects using the transformation equations of Section 3.4. The uw cospectrum for MITOS III was corrected for pitch using Eq. (39) while the OWAX data was corrected for pitch using the mean angle approximations of

FIGURE 10

Normalized standard deviations of turbulent fluctuations plotted versus $-z/L$

a. σ_u/u_* , σ_w/u_* versus $-z/L$

b. σ_θ/T_* , σ_q/q_* versus $-z/L$

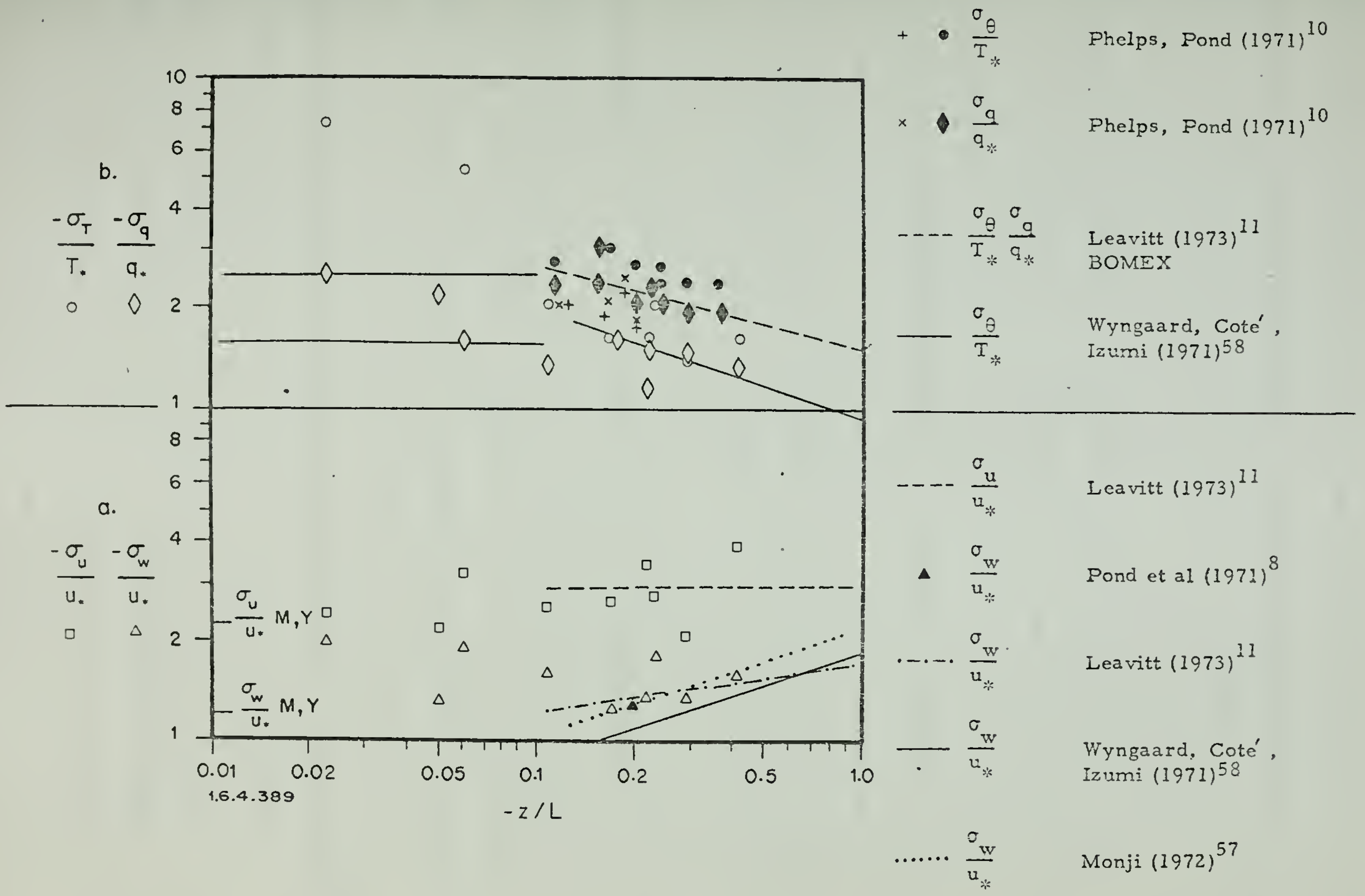
b.
$-\frac{\sigma_T}{T_*}$ ○ $-\frac{\sigma_q}{q_*}$ ◇
a.
$-\frac{\sigma_u}{u_*}$ □ $-\frac{\sigma_w}{u_*}$ △
10
8
6
4
2
1
8
6
4
2
1
$\frac{\sigma_u}{u_*}$ M,Y □
$\frac{\sigma_w}{u_*}$ M,Y
0.01
0.02
0.05
0.1
0.2
0.5
1.0
1.6.4.389
-z/L
+ ● $\frac{\sigma_\theta}{T_*}$ Phelps, Pond (1971)10
× ◆ $\frac{\sigma_q}{q_*}$ Phelps, Pond (1971)10
$\frac{\sigma_\theta}{T_*}$ $\frac{\sigma_q}{q_*}$ Leavitt (1973)11 BOMEX
$\frac{\sigma_\theta}{T_*}$ Wyngaard, Cote', Izumi (1971)58
$\frac{\sigma_u}{u_*}$ Leavitt (1973)11
▲ $\frac{\sigma_w}{u_*}$ Pond et al (1971)8
$\frac{\sigma_w}{u_*}$ Leavitt (1973)11
$\frac{\sigma_w}{u_*}$ Wyngaard, Cote', Izumi (1971)58
$\frac{\sigma_w}{u_*}$ Monji (1972)57

Eq. (41). Any residual peak at 0.1 Hz not removed by the pitch corrections was faired through with a straight line approximation. To obtain the entire covariance from the cospectra, integration was performed between $f = 0.001$ Hz and $f = 10$ Hz. The lowest frequency point obtained from cospectral analysis was between .003 and 0.005 Hz, so that it was assumed that the cospectra went to zero at 0.001 Hz for the integration. The additional area obtained using this integration technique amounted to an average of 7% for the $\overline{uw}$ covariance and 4% for the $\overline{w\gamma}$ covariances. The u_* values for the SOMA and MITOS I runs were calculated from the relation $u_*^2 = C_D \bar{U}^2$ since no correct pitch angle was available to obtain pitch corrected uw cospectra. An assumed value of $C_D = 1.3 \times 10^{-3}$ was used in the calculations of u_*. This value of C_D is an average value obtained from the results of Deacon and Webb (1962)[52] who suggest $C_D = (1.0 + 0.07\,\bar{U}) \times 10^{-3}$ (average 1.47×10^{-3} for SOMA and MITOS I cruises), Hasse (1970)[53] and Miyake et al (1970)[33] who give values of C_D of $(1.21 \pm 0.24) \times 10^{-3}$ and $(1.1 \pm 0.18) \times 10^{-3}$ for slightly unstable conditions similar to the SOMA cruises, Smith (1970)[54] who obtains a value of $(1.35 \pm 0.34) \times 10^{-3}$, Pond et al (1971)[8] who obtains $(1.5 \pm 0.26) \times 10^{-3}$ for BOMEX results, and Mitsuta and Fujitani (1974)[55] who suggest 1.22×10^{-3} from Northwest Pacific Ocean and East China Sea data. Also included in the average is the present result from the MITOS III and OWAX cruises of (1.18 ± 0.20)

$\times 10^{-3}$ for pitch corrected data.

The ratio σ_u/u_* for this work is 2.84 ± 0.53. This ratio historically has shown considerable scatter when plotted versus z/L and values of σ_u/u_* for neutral stability range from 1.8 obtained by Kaimal et al (1972)[56] to 2.3 suggested by Monin and Yaglom (1971).[27] Their value is shown at $-z/L = 10^{-2}$ in figure 10a. Leavitt (1973)[11] obtained a value of 2.8 ± 0.5 for σ_u/u_* from BOMEX data in the stability range of $0.1 < -z/L < 1.0$ which is represented by the dashed line in figure 10a. Mitsuta and Fujitani[55] report a value of $\sigma_u/u_* = 3.30 \pm 0.78$ for $-z/L \simeq 0.2$ from their work in the Northeastern Pacific and East China Sea for measurements taken from a cruising ship corrected for ship motion.

The predicted shape for the behavior of the ratios σ_w/u_*, σ_θ/T_* and σ_q/q_* versus $-z/L$ is given by the relations

$$\begin{aligned} \sigma_w/u_* &= C_w(-z/L)^{1/3} \\ -\sigma_\theta/T_* &= C_T(-z/L)^{-1/3} \\ -\sigma_q/q_* &= C_q(-z/L)^{-1/3} \end{aligned} \tag{42}$$

where C_w, C_T and C_q are constants and u_*, T_*, and q_* are given by Eqs. (5) and (6). Values of the ratio σ_w/u_* for the OWAX and MITOS III runs with pitch corrections show considerably less

scatter than those ratios calculated using an assumed C_D. The pitch corrected values of σ_w/u_* agree well with the results of Pond et al,[8] Leavitt[11] and Monji (1972),[57] are slightly higher than the results of Wyngaard, Coté and Izumi (1971)[58] for Kansas data, and slightly lower than the results of Mitsuta and Fujitani.[55] Leavitt[11] estimates $C_w = 1.7$ although his data show the trend represented by the dashed and dotted line in figure 10a for $0.1 < -z/L < 1.0$. Pond et al[8] from BOMEX data obtain an average value for $\sigma_w/u_* = 1.32 \pm 0.09$ represented by the dark triangle in figure 10a. The dotted line of figure 10a represents a result of $C_w = 2.2$ given by Monji[58] from data obtained at the Bonneville Salt Flats in Utah. The Wyngaard et al[58] and Kaimal et al[56] result of $C_w = 1.9$ from Kansas data is represented by the unbroken line of figure 10a. Mitsuta and Fujitani[55] obtain a value of $\sigma_w/u_* = 1.68 \pm 0.2$ for $-z/L \simeq 0.2$. The ratios σ_u/u_* and σ_w/u_* show that the large scale velocity field is anisotropic. Spectral results will be given in Sections 4.5 and 4.7 illustrating the approach to isotropy for the small scale structure of the velocity field.

The ratios $-\sigma_\theta/T_*$ and $-\sigma_q/q_*$ obtained for this work are shown in figure 10b and follow the prediction of Wyngaard et al[58] for $C_T = 0.95$. Results of Leavitt[11] (dashed line with slope $-1/4$) and Phelps and Pond (1971)[10] from BOMEX data shown in figure 10b are higher than their San Diego data and ratios from this work. The ratios σ_q/q_* for the MITOS I and SOMA data are lower than the results for

the OWAX and MITOS III data. In general for the SOMA and MITOS I cruises the values of σ_θ/T_* are higher than the values of σ_q/q_* as was found by Phelps and Pond[10] for BOMEX results. The OWAX and MITOS III ratios are more nearly equal as was found by Phelps and Pond[10] for pre-BOMEX (San Diego) data which follows the Wyngaard et al[58] prediction more closely than the BOMEX data. The high values of σ_θ/T_* for the SOMA cruise are not surprising due to the uncertainty in the assumed C_D value, the small sensible heat fluxes measured during the cruise, and the possible effects of non-stationarity at low values of $-z/L$. Near $z/L = 0$, σ_θ/T_* versus z/L exhibits a cusp-like behavior which makes the ratio more uncertain and difficult to measure

4.3 Pitch Corrected Covariances and Error Analysis

Covariances determined by the eddy correlation technique are fairly difficult to measure as noted in Section 2.1. In addition to the errors caused by platform (sensor) motion, the measurements are also sensitive to instrument alignment errors and cospectral distortion at high frequencies due to spatial averaging and sensor separation. The covariances obtained for the MITOS III and OWAX cruises were corrected for platform motion errors due to pitch using simultaneous pitch angle measurements of a vertical gyro mounted at a known angle with respect to the velocity sensors (sonic anemometer). Spatial averaging of the sonic anemometer occurs over a path length of 20 cm

so that the smallest wavelength resolved is 1.26 m. Effects of this spatial averaging on the velocity spectra and cospectra occur at $f z/\overline{U}$ values of 10 for MITOS III and 2.8 for OWAX (discussed in Section 4.5a. Distortion of the scalar flux cospectra at high frequencies due to sensor separation is more pronounced since the sonic anemometer and temperature/humidity sensors were separated by ~ 50 cm, reducing the high frequency cut-off to $f z/\overline{U}$ values of $\simeq 1.0$ and 4 for the two cruises. No correction for spatial resolution or sensor separation was made since contributions to the covariances above $f z/\overline{U} = 1$ are small. The resultant error in the covariances is less than 5% for the OWAX cruise and negligible for the MITOS III cruise.

The sonic anemometer used to measure horizontal and vertical velocity during the OWAX cruise had a misalignment of 1.1° in the vertical sensing path which induced u- contamination in the measured vertical velocity. The covariances which include vertical velocity have been corrected to account for this misalignment represented by φ_s in the equations of Section 3.4.

The measured pitch angle spectra of the vertical gyro for MITOS III and OWAX is shown in figure 11 as $\log f\, \Phi_{\varphi\varphi}(f)$ plotted versus $\log f$, where f is frequency in Hertz. The OWAX spectrum is an average from the 3 runs analyzed. Both spectra show a pronounced peak at $f \simeq 0.1$ Hz due to FLIP induced motion. The MITOS III

FIGURE 11

MITOS III and average OWAX pitch gyro spectra plotted versus frequency (key to spectral plots Table 6)

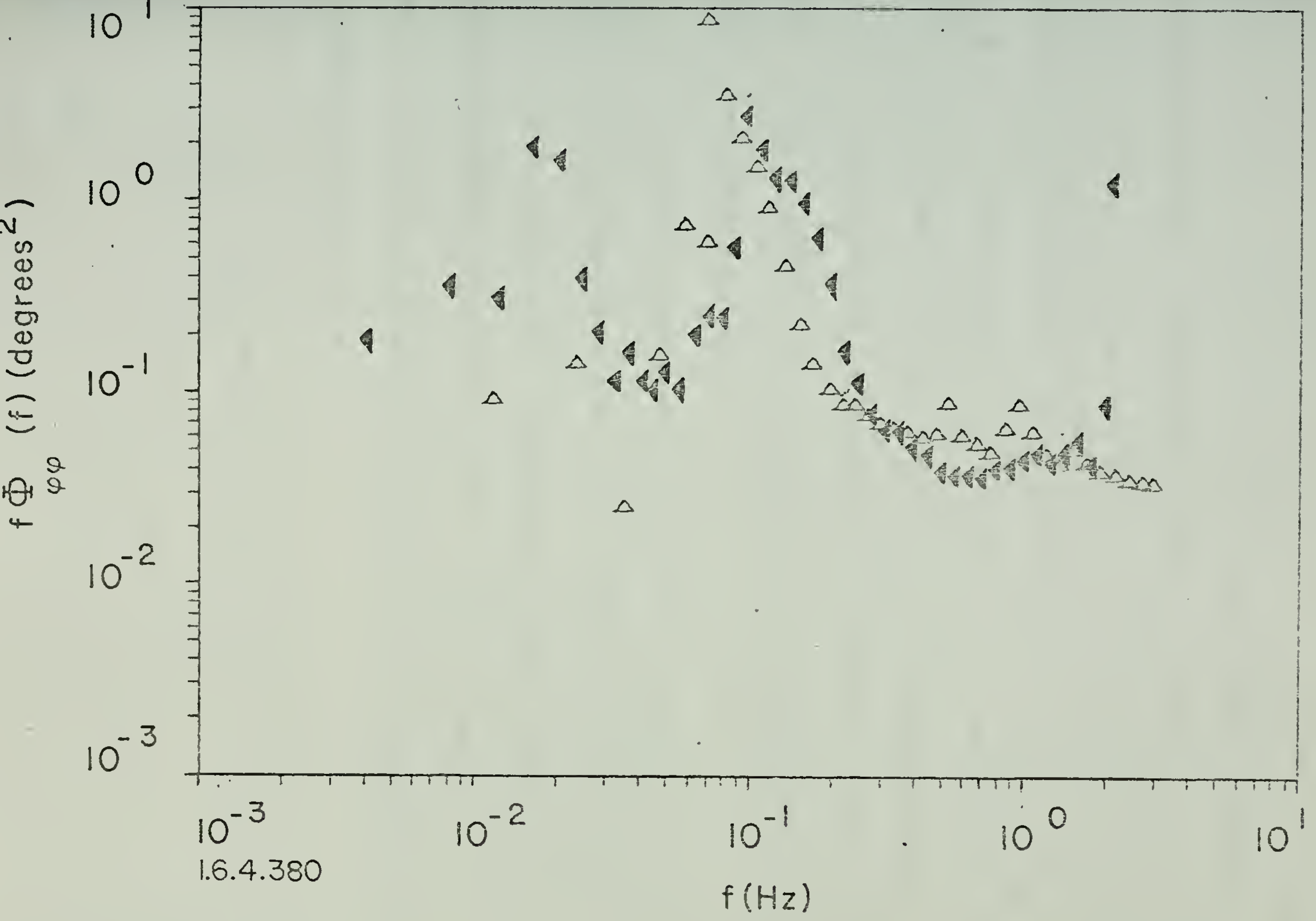
$f\,\Phi_{\varphi\varphi}(f)$ (degrees^2)
10^{1}
10^{0}
10^{-1}
10^{-2}
10^{-3}
10^{-3}
10^{-2}
10^{-1}
10^{0}
10^{1}
1.6.4.380
f (Hz)

spectrum also exhibits a peak at 0.01 Hz and in general has a higher spectral level than the OWAX spectrum for $f < 0.04$ Hz . Mean pitch angles and values of σ_φ for the MITOS III and OWAX cruises are presented in Table 4 . Also given in Table 4 are the measured and corrected vertical velocities (w) , the uncorrected and corrected uw covariances with confidence limits, and values of $-R_{uw}(f) = \Phi_{uw} / (\Phi_{uu} \Phi_{ww})^{1/2}$ in the frequency band $0.01 < f < 0.1$ calculated for each pitch corrected run. A comparison is also made with two other methods of estimating the pitch angle in lieu of actually measuring the angle. Table 4 gives uncorrected and corrected scalar flux covariances with confidence limits.

The mean pitch angle from the MITOS III cruise shows a much greater variation than those from all the OWAX runs, with $\sigma_\varphi > \overline{\varphi}$. For this cruise (MITOS III) an instantaneous point-by-point pitch correction was applied to the measured u and w signals by Drs. Carl Friehe and Frank Champagne using the first two equations of (39) re-written as (for $\varphi_s = 0$):

$$\begin{aligned} u_c(t) &= u_m(t) \cos \varphi(t) + w_m(t) \sin \varphi(t) \\ w_c(t) &= w_m(t) \cos \varphi(t) - u_m(t) \sin \varphi(t) \end{aligned} \qquad (43)$$

where $u(t) = \overline{U} + u'$

$w(t) = \overline{W} + w'$

$\varphi(t) = \overline{\varphi} + \varphi'$

TABLE 4

Pitch Angles and Corrected Fluxes

Pitch Angle (degrees)	MITOS III-2	OWAX 2	OWAX 3	OWAX 4
$\overline{\varphi} \pm \sigma_{\varphi}$	0.61 ± 0.73	0.47 ± 0.23	1.0 ± 0.29	1.41 ± 0.27
From $R_{uw} \simeq -0.5$	3°	6°	4°	3°
From $\sin^{-1} \tilde{W}_m/\overline{U}_m$	4.7°	0°	-0.13°	-1.4°
$\overline{W}$, Vertical Velocity (cm/sec)				
Measured $\overline{W}_m$	54	7.3	7.5	-3.1
Corrected for Misalignment $\tilde{W}_m$	-	0	-1.05	-12.0
Corrected for Pitch $\overline{W}_c$	36	-3.1	-8.9	-21.1
$-uw$ (cm^2/sec)				
Uncorrected	352	96	160	251
Corrected*	455 ± 118	163 ± 37	270 ± 68	343 ± 107
Measured $R_{uw}(f)$	0.42	0.27	0.29	0.43
From $R_{uw} \simeq -0.5$	416	335	453	401
From $\sin^{-1}(\tilde{W}_m/\overline{U}_m)$	447	149	209	239
$\overline{w\theta}$ (° C-cm/sec)				
Uncorrected	1.36	1.26	1.37	1.08
Corrected*	1.46 ± 0.11	1.32 ± 0.16	1.43 ± 0.19	1.20 ± 0.09
$\overline{wq}$ (μ gm/cm^2 -sec)				
Uncorrected	2.79	2.39	3.48	4.72
Corrected*	2.96 ± 0.11	2.46 ± 0.29	3.65 ± 0.54	5.11 ± 0.39

*Measured pitch angle used

and the bars and primes denote mean and fluctuating components. The calculations were performed on the UCSD CDC 3600 computer. The cospectra and covariances were then computed with the corrected u and w. For the OWAX data the corrected covariances were obtained by assuming a mean pitch angle with a small angle approximation and using the equations of (41). This approximation for the OWAX data is probably valid since the measured angles and standard deviations were small. The uncorrected covariances given in Table 4 are those which would have been obtained if no pitch angle or misalignment correction had been made. Corrected covariances (also given in Table 2) include the corrections. The confidence limits given for the covariances include errors incurred from the following sources:

1. Uncertainty in calculating the area under the cospectral curve (11%).
2. Uncertainty of the pitch angle measurement, σ_u, σ_w, and the sonic misalignment correction (OWAX only) (8%).
3. Possible errors incurred by fairing through the effects of FLIP induced motion on the cospectra (9%).

The percentages given are average values for the corrected $\overline{uw}$ covariance, more sensitive to pitch effects and FLIP motion than the scalar covariances. The confidence limits for the scalar covariances amount to an average value of 10% of the corrected covariances.

The mean R_{uw} value of the data is -0.32 ± 0.08 for $0.01 > f > 0.1$. Leavitt[11] obtains a value of $R_{uw} = -0.35$ for his 30 m

data in the same frequency interval using a pitch angle correction calculated from the relation

$$\bar{\varphi} = \sin^{-1}\left(\frac{\tilde{W}_m}{\bar{U}_m}\right) \tag{44}$$

where $\tilde{W}_m$ and $\bar{U}_m$ are the measured mean vertical and horizontal velocities. Values of $\bar{\varphi}$ calculated from this relation and $\tilde{W}_m$ (corrected for sonic misalignment) are shown in Table 4, as well as the $\overline{uw}$ values obtained using this correction. Pond et al[8] use an assumed value of $R_{uw} = -0.50$ to estimate the pitch angle for the covariance corrections. Pitch angles calculated by this method are also given in Table 4 with the resultant $\overline{uw}$ values for this correction. The $\overline{uw}$ corrected value of MITOS III calculated using the instantaneous correction procedure (for large σ_φ) is in fairly good agreement with the values obtained from the other two methods, even though the pitch angles required for the correction are larger than the measured pitch angle. For the OWAX data, the values of $\overline{uw}$ obtained for the correction used by Leavitt[11] are an average of 12% lower than those corrected for with measured mean pitch angle; the values of $\overline{uw}$ calculated using the $R_{uw} = -0.50$ correction are higher than the measured pitch angle corrected $\overline{uw}$ values by as much as a factor of 2 for the OWAX 2 run. In his comparison of 8 m data using the $R_{uw} =$ -0.50 correction and the 30 m data, Leavitt[11] indicates the differences

in mean stresses at the two heights may be due to errors in estimating the pitch angles, and that the differences would be removed by a 2.5° rotation of estimated pitch angles at 30 m, and an opposite rotation for the 8 m data. Although the uncertainties in the corrected $\overline{uw}$ values for this work average ~ 25% the trend of the corrections which estimate (in lieu of measuring) the pitch angle to give higher or lower $\overline{uw}$ results for the OWAX data than obtained for the measured pitch angle procedure, appears to support Leavitt's[11] suggested method for removing the difference between the stresses at the two heights.

4.4 Flux and Correlation Results

Directly measured fluxes of momentum, sensible and latent heat are given in Table 2. The momentum fluxes for SOMA and MITOS I were calculated from $u_*^2 = C_D\overline{U}^2$ as discussed in the previous section. Since the fluxes were calculated for only one height for each run it was not possible to test the validity of the constant flux layer assumption. A general trend in the heat flux results can be discerned by noting that the calculated BOWEN ratio $R_B = H_S/H_L$ is lower for all the night runs than the day runs, implying radiation may affect the amount of sensible heat measured by the eddy correlation method. The lowest value of the BOWEN ratio for the OWAX results (from OWAX 4) was obtained from an early morning run before sunrise. The night run of OWAX 3 extended into the daylight hours and was of longer duration than the OWAX 4 run. The MITOS I-7 run, which had a BOWEN ratio of 0.25, was made

during the late afternoon before sunset. Phelps and Pond (1971)[10] have suggested that radiation may have an affect on the larger scales of temperature fluctuations in air with high concentrations of water vapor, causing more absorption of long wave radiation and a more homogeneous large scale temperature field. This affect may be more pronounced at night when only long-wave radiation emitted from the ocean is present.

Values of the overall correlations between each pair of parameters defined as $r_{xy} = \frac{\overline{xy}}{\sigma_x \sigma_y}$ are given in Table 2. The average overall correlation $-r_{uw}$ for the pitch corrected results of MITOS III and OWAX is 0.26 ± 0.08 (mean and standard deviation), in agreement with the value of $-r_{uw} = 0.262 \pm 0.035$ obtained by Pond et al.[8] The results of Pond et al[8] may be expected to have less scatter than the present results since the procedure used to correct their data for pitch effects assumed that the u and w fluctuations had a $R_{uw}(f) = -0.5$ correlation in the frequency range 0.01 - 0.1 Hz. From Leavitt's[11] 8 meter data the average value of $-r_{uw} = 0.26 \pm 0.06$. To correct for pitch effects, Leavitt determined the angle required to align the sonic anemometers in the manner described in Section 4.3 using measured mean vertical and horizontal velocites. Using this angular rotation the resultant vertical velocity determined by transformation equations similar to those of Eq. (39) had zero mean.

A stability normalization can be applied to the R_{uw} values obtained from the pitch corrected covariances, as suggested by the

results of Kaimal and Haugen (1969)[17] who found that the correlation coefficient may vary with stability. To remove the stability dependence of normalized velocity spectra presented in Section 4.5a, the spectra are normalized with the expression for the dimensionless kinetic energy dissipation Φ_ϵ. If the normalized correlation coefficient is determined by the relation $\tilde{r}_{uw} = \overline{uw}\,\Phi_\epsilon^{2/3} / (\Phi_{uu}\Phi_{ww})^{1/2}$ (see Appendix 1), the average value of $-\tilde{r}_{uw} = 0.25 \pm 0.06$ for the pitch corrected data using $\Phi_{\epsilon_1}^{2/3} = (\Phi_m - z/L)^{2/3}$ (Eq. (24)). For $\Phi_{\epsilon_2}^{2/3} = (1 + 0.5\,|z/L|^{2/3})$, the average value of $-\tilde{r}_{uw} = 0.30 \pm 0.06$. The value of $-\tilde{r}_{uw} = 0.25$ for Φ_{ϵ_1}, agrees with the value obtained by Miyake et al (1970),[59] (0.25) and the standard deviation of the result is reduced.

The overall values of $r_{w\theta}$ (0.48 ± 0.04) for the OWAX and MITOS III data corrected for pitch are higher than those obtained from SOMA and MITOS I runs (0.16 ± 0.11). The pitch correction to the $w\theta$ and wq cospectra is small compared to that for the uw cospectra, so that the trend in the $r_{w\theta}$ values is probably real. Phelps and Pond[10] also obtained higher values of $r_{w\theta}$ for pre-BOMEX (San Diego) data than those obtained from the BOMEX data.

The average value of r_{wq} from all the cruises for this work is 0.43 ± 0.11. There is a slight trend for the values of r_{wq} for OWAX and MITOS III to be higher than the SOMA and MITOS I values, but is not pronounced as the trend in the $r_{w\theta}$ values. The overall correlation coefficient r_{wq} given by Phelps and Pond[10] for BOMEX data (0.33) is

comparable to the average value of r_{wq} for the MITOS I and SOMA cruises ($r_{wq} = 0.36$).

The $r_{u\theta}$ values for each run are lower than the corresponding $r_{w\theta}$ values with the exception of OWAX 4 which shows the opposite behavior. It is difficult to notice any real trends in the $r_{u\theta}$ and r_{uq} values and the $\overline{u\theta}$ and $\overline{uq}$ covariances since they were not determined for the SOMA cruise. The anamolous high value of $-r_{uq} = 0.78$ for run MITOS I-1, which also has the highest $\overline{wq}$ and $\overline{uq}$ values may be due to drift or misalignment of the x-wire in the mean flow since the $r_{\theta q}$ value unaffected by pitch is comparable to that obtained from MITOS I-7. The value of $\overline{uq}$ for MITOS I-1 is comparable to values of $\overline{uq}$ obtained by Phelps and Pond[10] during BOMEX.

Results obtained for $r_{\theta q}$ for this work agree with those obtained by Phelps and Pond[10] from pre-BOMEX ($r_{\theta q} \simeq 0.8$) and BOMEX ($r_{\theta q} = 0.5$) temperature and humidity data. Lower values of $r_{\theta q}$ were obtained for the SOMA and MITOS I cruises (0.38 ± 0.09) than were obtained for the MITOS III and OWAX cruises (0.73 ± 0.13).

The correlation coefficients which include the scalars can also be normalized in a similar manner as was done for the r_{uw} correlation coefficient. The normalization for the $r_{w\gamma}$ and $r_{u\gamma}$ correlation coefficient is $(\Phi_H)^{1/2}\, \Phi_\epsilon^{1/6}$ where γ is equal to θ or q, and the normalization for the $r_{\theta q}$ correlation is $\Phi_H \Phi_\epsilon^{-1/3}$ (see Appendix 1). The normalized correlation coefficients are given in Table 5.

TABLE 5 - Normalized Correlation Coefficients

		$\tilde{r}_{w\theta}$	$\tilde{r}_{wq}$	$\tilde{r}_{u\theta}$	$\tilde{r}_{uq}$	$\tilde{r}_{\theta q}$
SOMA	1	0.06	0.20	-	-	0.21
	2	0.05	0.29	-	-	0.21
	3	0.09	0.27	-	-	0.29
MITOS I	1	0.24	0.36	0.19	0.62	0.28
	7	0.18	0.33	0.13	0.33	0.22
MITOS III	2	0.35	0.38	0.23	0.23	0.22
OWAX	2	0.25	0.29	0.14	0.12	0.26
	3	0.32	0.33	0.14	0.14	0.43
	4	0.35	0.36	0.39	0.29	0.39

$$\tilde{r}_{x\gamma} = \frac{\overline{x\gamma}\ \Phi_H^{1/2}\ \Phi_\epsilon^{1/6}}{\sigma_x\ \sigma_\gamma}$$

$x = u, w$

$\gamma = \theta, q$

$$\tilde{r}_{\theta q} = \frac{\overline{\theta q}\ \Phi_H\ \Phi_\epsilon^{-1/3}}{\sigma_\theta\ \sigma_q}$$

The factors $\Phi_\epsilon^{-1/3}$ and $\Phi_\epsilon^{1/6}$ were not included in the normalizations since the differences between the individual runs amount to less than 4% if $\Phi_\epsilon^{-1/3}$ or $\Phi_\epsilon^{1/6}$ were included. The trends noted for the measured correlation coefficients are still applicable, however, less pronounced. The average $\tilde{r}_{w\theta}$ correlation coefficient for all the data is 0.21 ± 0.1, comparable to the result of Miyake et al (1970b)[59] of $r_{w\theta} = 0.24 \pm 0.2$ for near neutral conditions $(-z/L = 0.04)$. The trend in the $\tilde{r}_{\theta q}$ correlation coefficients for OWAX and MITOS III (0.32 ± 0.08), and the SOMA and MITOS I cruises (0.25 ± 0.04) would not be removed by including the factor $\Phi_\epsilon^{-1/3}$ in the normalization.

4.5 Spectra

In this section horizontal and vertical velocity (u, w), temperature (θ), and specific humidity (q) spectra computed from the four cruises will be presented and discussed. The method of spectral presentation will be to plot initially the individual run spectra in absolute units for each cruise as $\log f\Phi_{xx}(f)$ versus $\log(f)$, where f is frequency in Hertz. The individual runs are then averaged for each cruise and plotted in normalized form as $\log f_N \Phi_{xx}(f_N)/N_{xx}$ $(= f\Phi_{xx}(f)/N_{xx})$, where N_{xx} is the appropriate normalizing quantity (e.g. u_*, T_*, etc.) versus $\log f_N (= fz/\overline{U})$, the normalized frequency, following the trandition of atmospheric spectra presentation.

Table 6 gives the cruises, runs, appropriate plot symbol and

TABLE 6

Spectral and Cospectral Plot Information

Dimensional Absolute Spectra		Plot Symbol	Sampling Frequencies
SOMA	1	+	16, 130, 2000
	2	◁	16, 130, 200
	3	X	16, 130, 200
MITOS I	1	+	2.2, 20, 200
	7	◁	2.2, 20, 200
MITOS III	2*	□	2.0, 20, 200
OWAX	2	+	2.0, 20, 200
	3	◁	2.0, 20, 200
	4	X	2.2, 20, 200

Average Normalized Spectra	
SOMA	+
MITOS I	X
MITOS III	◀
OWAX	▷ ▽

*Figure 17 shows the MITOS III w spectrum corrected for pitch (◁) and uncorrected (+) sampled at 3.0 Hz.

sampling frequencies used to digitize the analog data. The record length for each spectral computation was 512 words/record/channel. Each spectral realization at different sampling frequencies was calibrated in absolute units, 20th decade averaged, and matched to the lower frequency spectra. Not all the points from each spectral realization are shown in order to reduce overlapping points and because the end points of each realization are affected by the filter cut-off (Nyguist frequency).

4.5a Velocity spectra

Absolute horizontal velocity spectra for SOMA, MITOS I and MITOS III/OWAX are shown in figures 12, 13, and 14. The vertical velocity spectra from these cruises are shown in figure 15 - SOMA, figure 16 - MITOS I, figure 17 - MITOS III and figure 18 - OWAX. Only the w-spectrum of MITOS III is shown corrected and uncorrected since an instantaneous pitch correction was employed for this cruise. The averaged u and w spectra are shown in figures 19 and 20 normalized with u_*^2 and plotted versus f_N.

The large peak in the u and w spectra between $0.05 < f < 0.2$ Hz due in large part to wave induced FLIP motion is more pronounced in the OWAX spectra ($z = 350$ cm) than in the spectra from SOMA, MITOS I and MITOS III. For both the OWAX and MITOS III cruises the instrument package was rigidly attached to FLIP, while for the SOMA and MITOS I cruises the instrument package was

FIGURE 12

SOMA horizontal velocity spectra plotted versus frequency

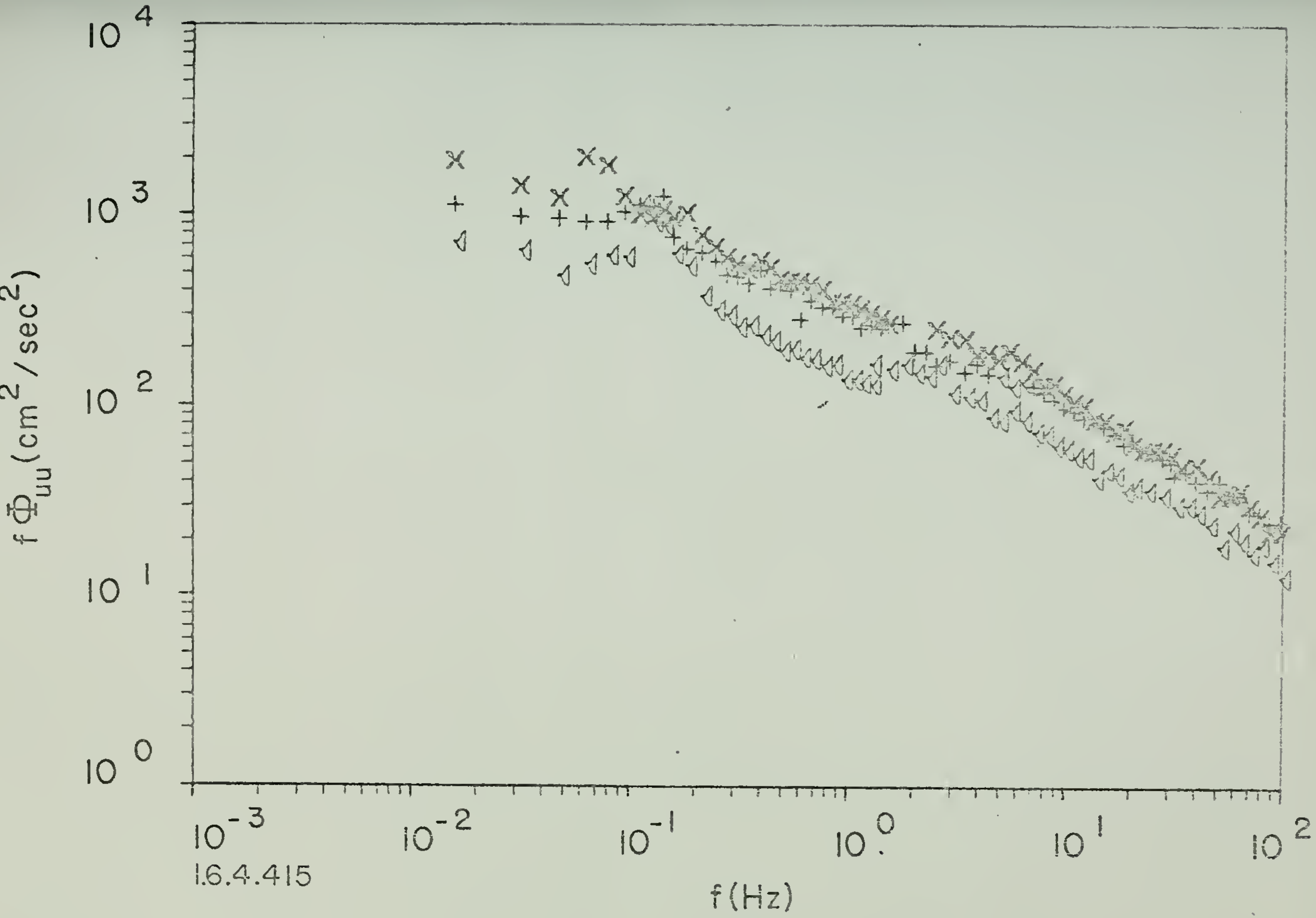
$f\Phi_{uu}(cm^2/sec^2)$
10^4
10^3
10^2
10^1
10^0
10^{-3}
10^{-2}
10^{-1}
10^0
10^1
10^2
1.6.4.415
f(Hz)

FIGURE 13

MITOS I horizontal velocity spectra plotted versus frequency

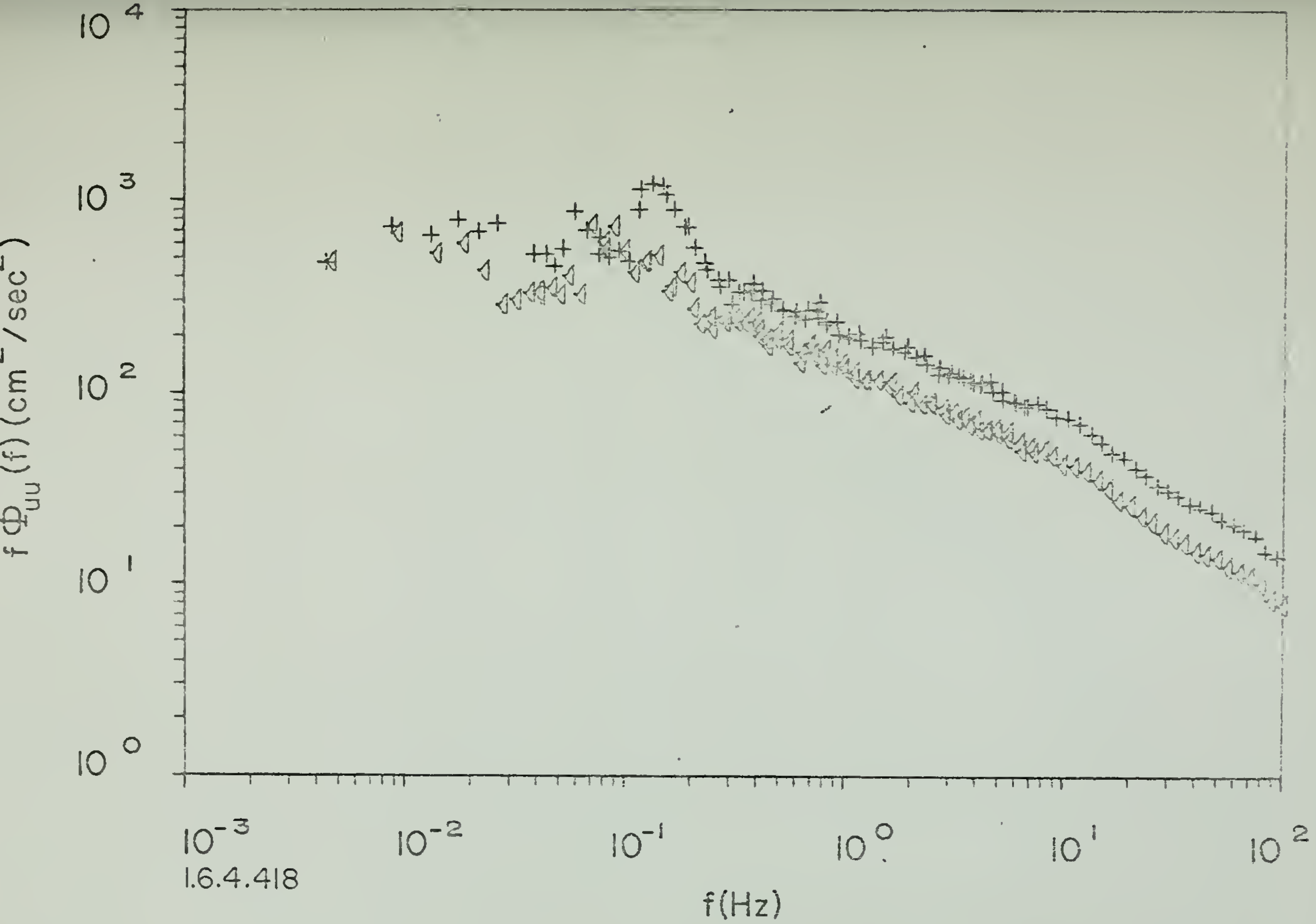
10^4
10^3
10^2
10^1
10^0
$f\,\Phi_{uu}(f)\,(cm^2/sec^2)$
10^{-3}
10^{-2}
10^{-1}
10^0
10^1
10^2
1.6.4.418
f(Hz)

FIGURE 14

MITOS III and OWAX horizontal velocity spectra plotted versus frequency

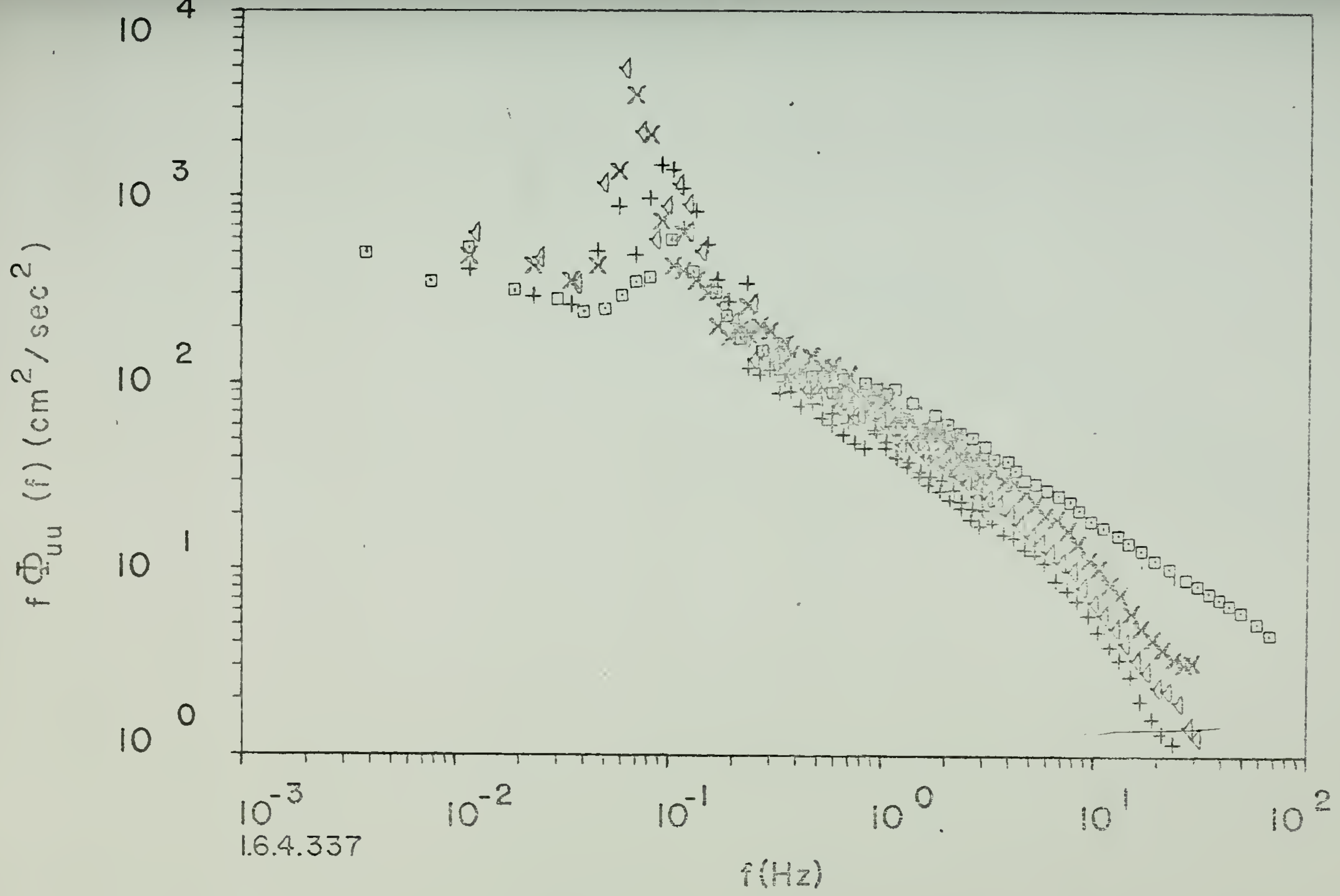
$f\,\Phi_{uu}(f)\ (cm^2/sec^2)$
10^4
10^3
10^2
10^1
10^0
10^{-3}
10^{-2}
10^{-1}
10^0
10^1
10^2
1.6.4.337
f(Hz)

FIGURE 15

SOMA vertical velocity spectra plotted versus frequency

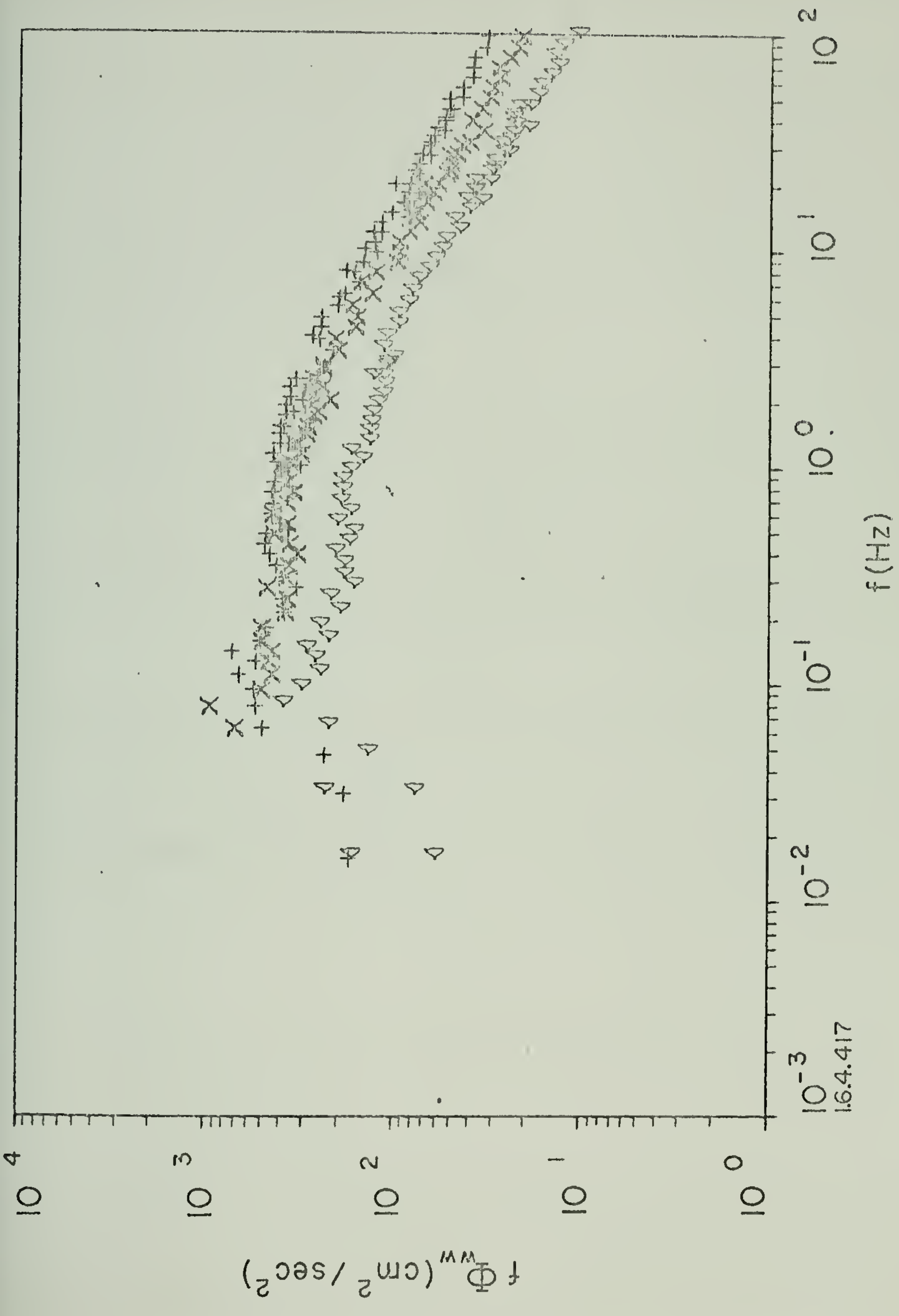
fΦww(cm²/sec²)
10⁰
10¹
10²
10³
10⁴
f(Hz)
10⁻³
10⁻²
10⁻¹
10⁰
10¹
10²
1.6.4.417

FIGURE 16

MITOS I vertical velocity spectra plotted versus frequency

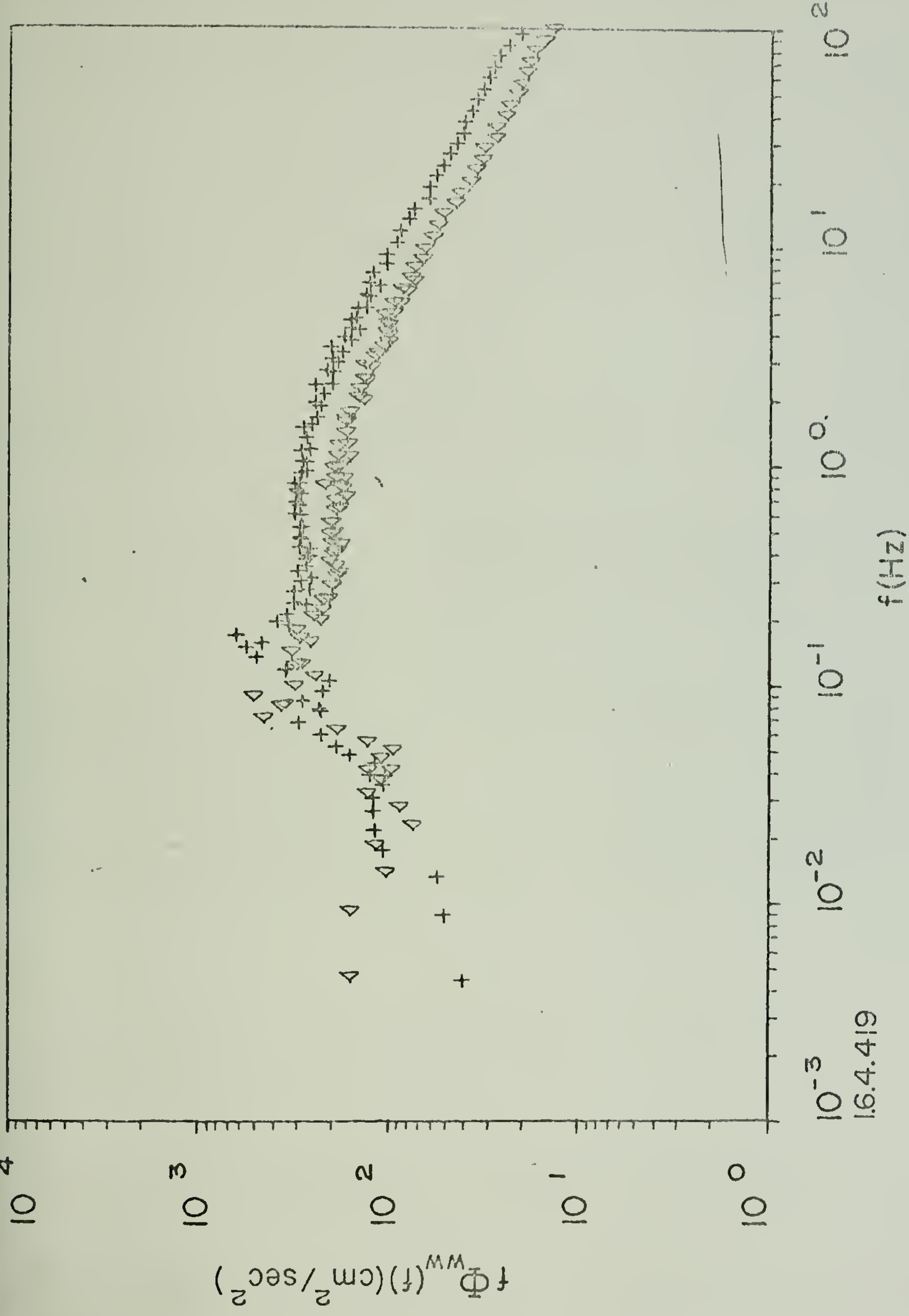
10^{0}
10^{1}
10^{2}
10^{3}
10^{4}
$f\Phi_{ww}(f)(cm^2/sec^2)$
10^{-3}
10^{-2}
10^{-1}
10^{0}
10^{1}
10^{2}
f(Hz)
16.4.419

FIGURE 17

MITOS III vertical velocity spectra plotted versus frequency corrected for pitch (◁) and uncorrected (+)

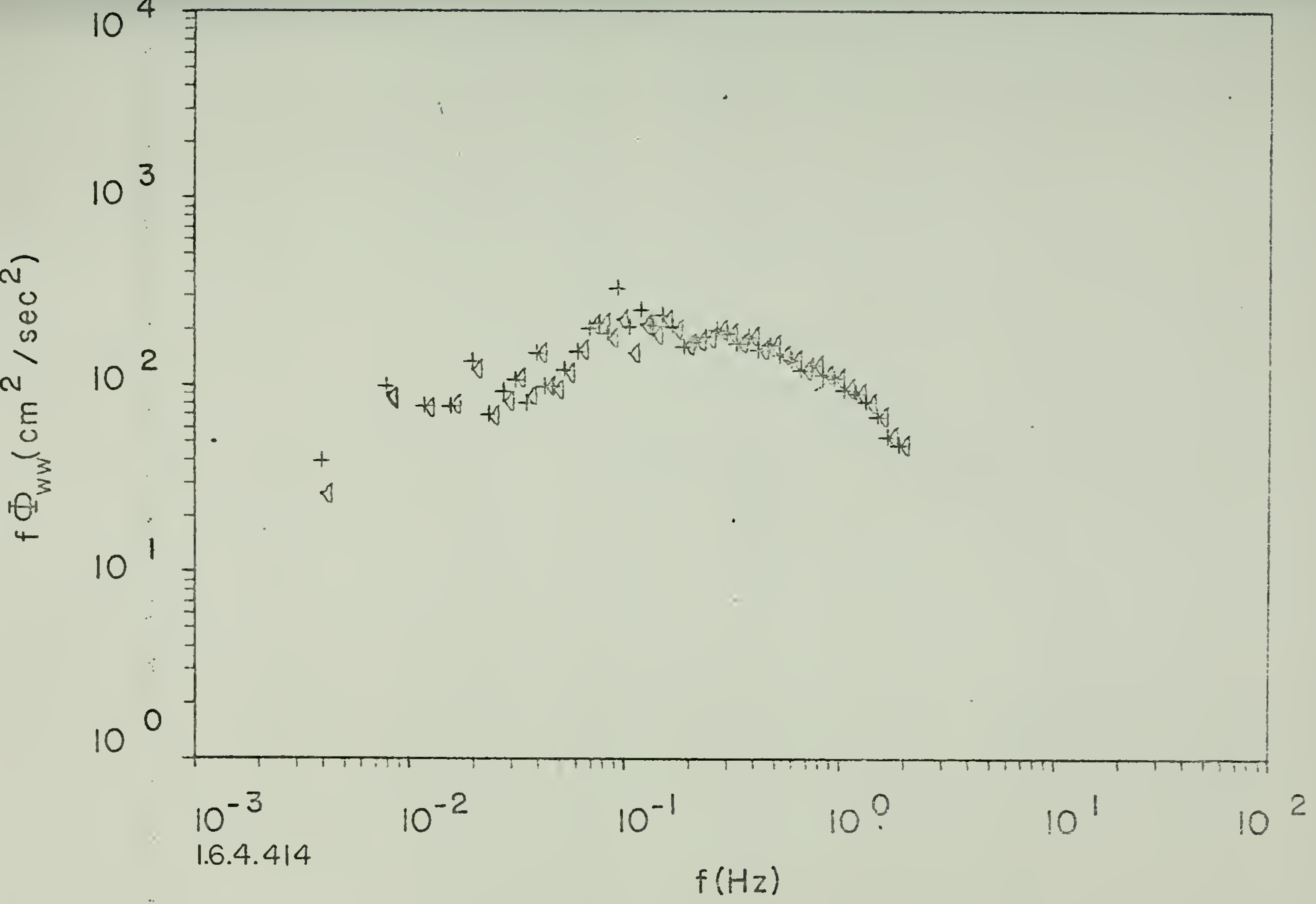
10^4
10^3
10^2
10^1
10^0
$f\Phi_{ww}(cm^2/sec^2)$
10^{-3}
10^{-2}
10^{-1}
10^0
10^1
10^2
1.6.4.414
f(Hz)

FIGURE 18

OWAX vertical velocity spectra plotted versus frequency

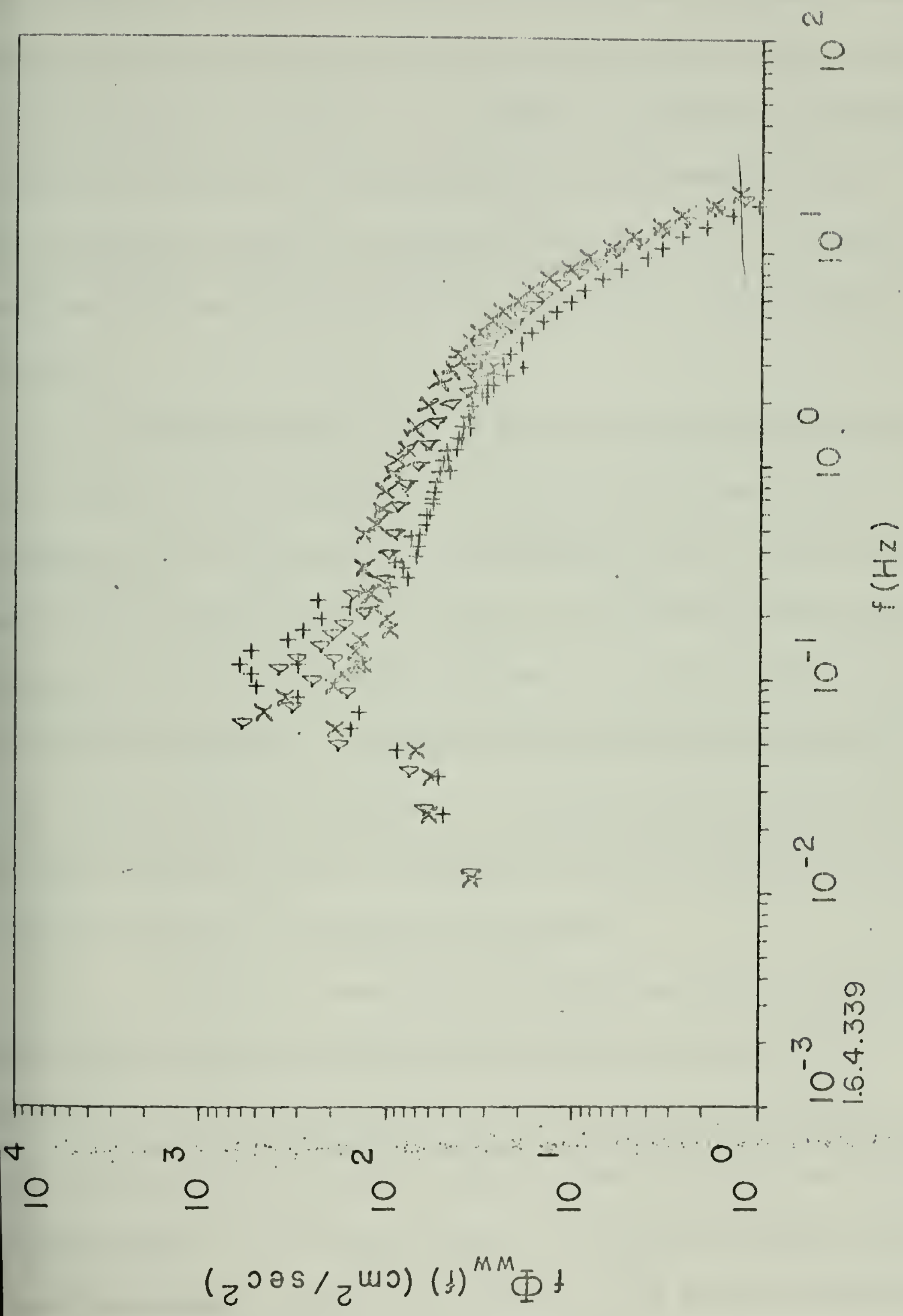
$f\,\Phi_{ww}(f)$ (cm^2/sec^2)
10^0
10^1
10^2
10^3
10^4
f (Hz)
10^{-3}
10^{-2}
10^{-1}
10^0
10^1
10^2
16.4.339

suspended on a cable. This suspension technique did appear somewhat successful in reducing the wave induced FLIP motion effects on the velocity spectra. Figure 17 shows pitch corrected and uncorrected w spectra from MITOS III to illustrate that the instantaneous pitch correction does appear to remove the peak at 0.1 Hz for this data, although only one high uncorrected spectral value at that frequency is shown.

The peak at 0.1 Hz in the velocity spectra may also be due in part to the effects of waves on the turbulent flow field as suggested by the results of Lai and Shemdin (1971).[60] These investigators found that simple mechanically generated water waves had a noticeable effect on the velocity spectra (u, w) and cospectra (uw) at the wave frequency. A maximum percentage increase in σ_u and σ_w of 24% and 9% respectively was found at heights above the water between 10 and 50 cm. The water waves did not appear to have any affect on the spectra in the inertial subrange.

The sonic anemometer horizontal and vertical velocity for the OWAX cruise, and vertical velocity spectra for the MITOS III cruise have not been corrected for spatial averaging and exhibit a fall-off in spectral level at lower frequencies than the x-wire and hot film velocity spectra. With a path length of 20 cm the response of the sonic anemometer should be accurate for $f_N \leqq 10$ for MITOS III and $f_N \leqq 2.8$ for OWAX velocity data according to the relation

FIGURE 19

Average horizontal velocity spectra normalized with u_*^2 plotted versus normalized frequency $(f\,z/\overline{U})$

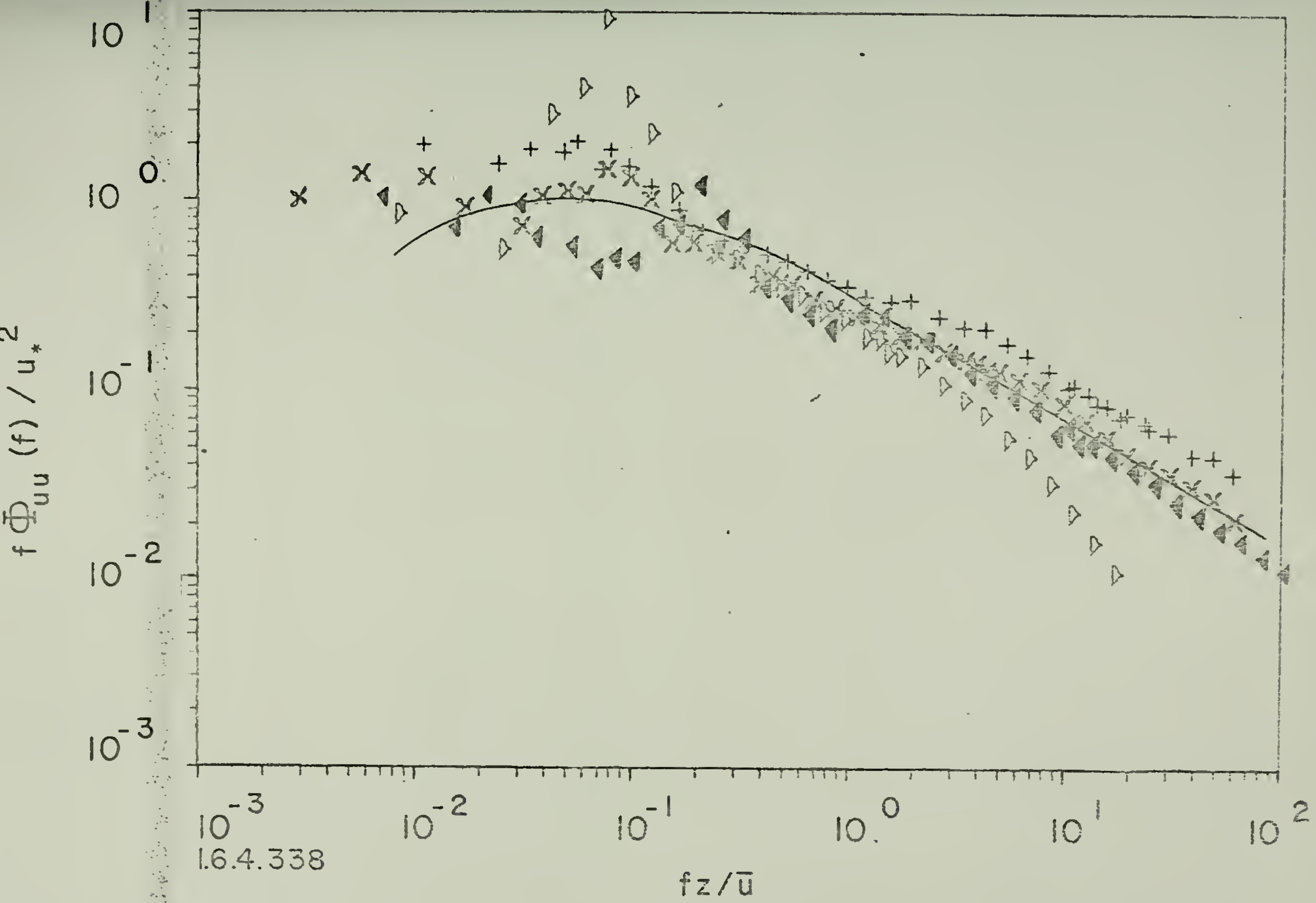
$f\Phi_{uu}(f)/u_*^2$
10^{1}
10^{0}
10^{-1}
10^{-2}
10^{-3}
10^{-3}
10^{-2}
10^{-1}
10^{0}
10^{1}
10^{2}
1.6.4.338
$fz/\overline{u}$

FIGURE 20

Average vertical velocity spectra normalized with u_*^2 plotted versus normalized frequency

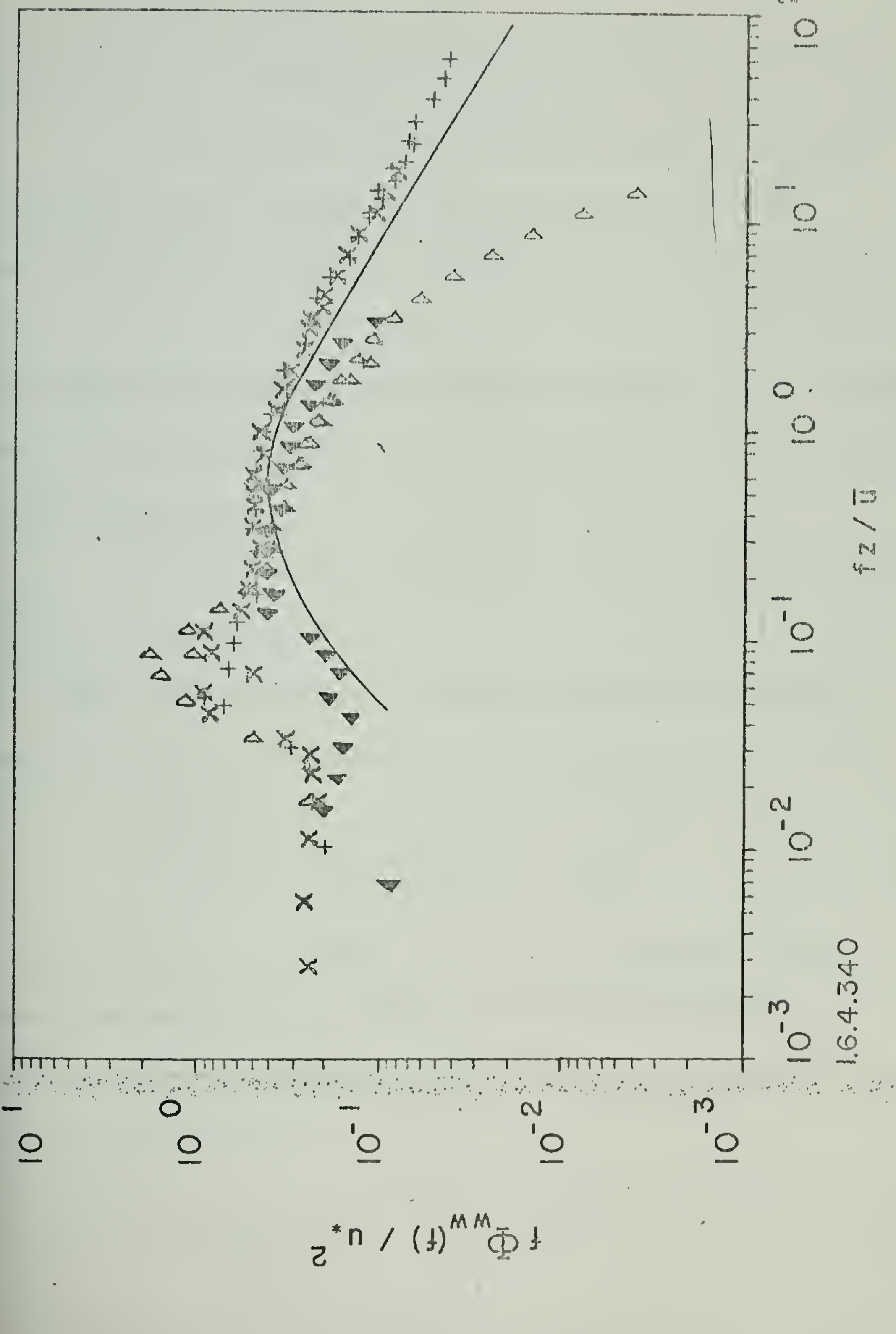
10^{1}
10^{0}
10^{-1}
10^{-2}
10^{-3}
$f\Phi_{ww}(f) / u_*^2$
10^{-3}
10^{-2}
10^{-1}
10^{0}
10^{1}
10^{2}
$fz/\overline{U}$
1.6.4.340

$$fz/\overline{U} = z/2\pi\ell \qquad (45)$$

where $z = 1250$ cm (MITOS III) and 350 cm (OWAX), and $\ell = 20$ cm.

The averaged u and w spectra of figures 19 and 20 normalized with u_*^2 are in fair agreement with the Kansas data of Kaimal et al (1972)[56] represented by the dark line in both figures. In general the spectral values for the SOMA and MITOS I are higher than the OWAX and MITOS III spectra for $f_N > 2$, possibly due to uncertainty in the u_* values and also due to sonic response for the OWAX spectra.

To remove the z/L dependence of the velocity spectra, an additional normalizing factor is required, namely $\Phi_\epsilon^{2/3}$, where $\Phi_\epsilon = \frac{kz}{u_*^3}\epsilon$ from Eq. (23). The inertial subrange form of the u spectra given by Eq. (11) may be rewritten as

$$\frac{f_N \Phi_{uu}(f_N)}{u_*^2} = \frac{\alpha_u}{(2\pi K)^{2/3}} \Phi_\epsilon^{2/3} f_N^{-2/3} \qquad (46)$$

For this work an α_u value of 0.53 was used based upon direct dissipation results from MITOS I, MITOS III and OWAX 4 in the concurrent work of McConnell (1974).[50] For an $\alpha_u = 0.53$ and $K = 0.4$, (46) becomes

$$\frac{f_N \Phi_{uu}(f_N)}{u_*^2 \Phi_\epsilon^{2/3}} = 0.29\ f_N^{2/3} \qquad (47)$$

FIGURE 21

Average horizontal velocity spectra normalized with u_*^2 and $\Phi_{\epsilon_1}^{2/3}$ (assuming total production = dissipation of kinetic energy) plotted versus normalized frequency

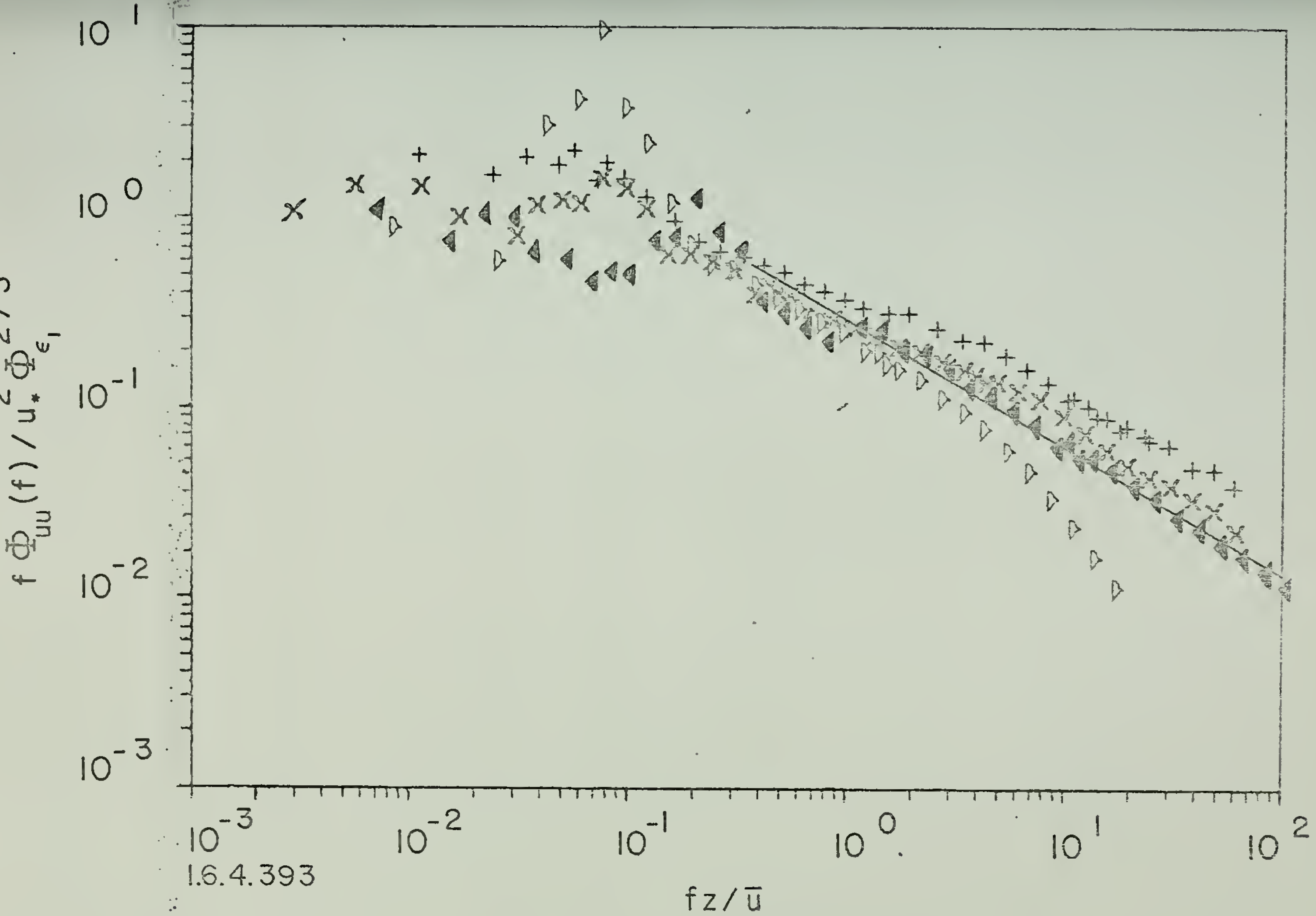
$f\,\Phi_{uu}(f)\,/\,u_*^2\,\Phi_{\epsilon_1}^{2/3}$
10^1
10^0
10^{-1}
10^{-2}
10^{-3}
10^{-3}
10^{-2}
10^{-1}
10^0
10^1
10^2
1.6.4.393
$fz/\overline{u}$

FIGURE 22

Average vertical velocity spectra normalized with u_*^2 and $\Phi_{\epsilon_1}^{2/3}$ plotted versus normalized frequency

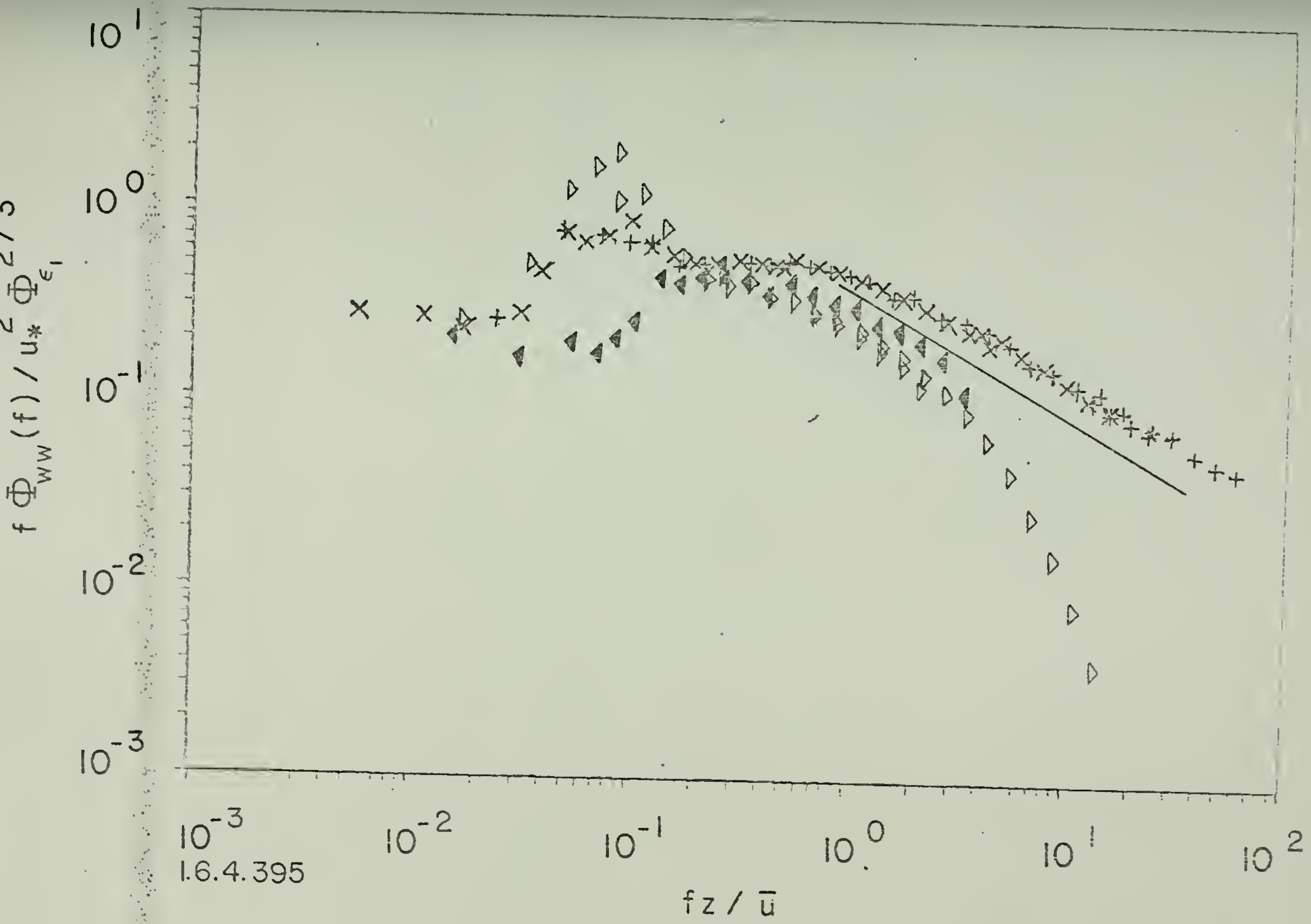
$f\,\Phi_{ww}(f)\,/\,u_*^2\,\Phi_{\epsilon_1}^{2/3}$
10^{1}
10^{0}
10^{-1}
10^{-2}
10^{-3}
10^{-3}
10^{-2}
10^{-1}
10^{0}
10^{1}
10^{2}
1.6.4.395
$fz\,/\,\bar{u}$

FIGURE 23

Average horizontal velocity spectra normalized with u_*^2 and $\Phi_{\epsilon_2}^{2/3}$ (Wyngaard and Coté)[61] expression for normalized dissipation plotted versus normalized frequency

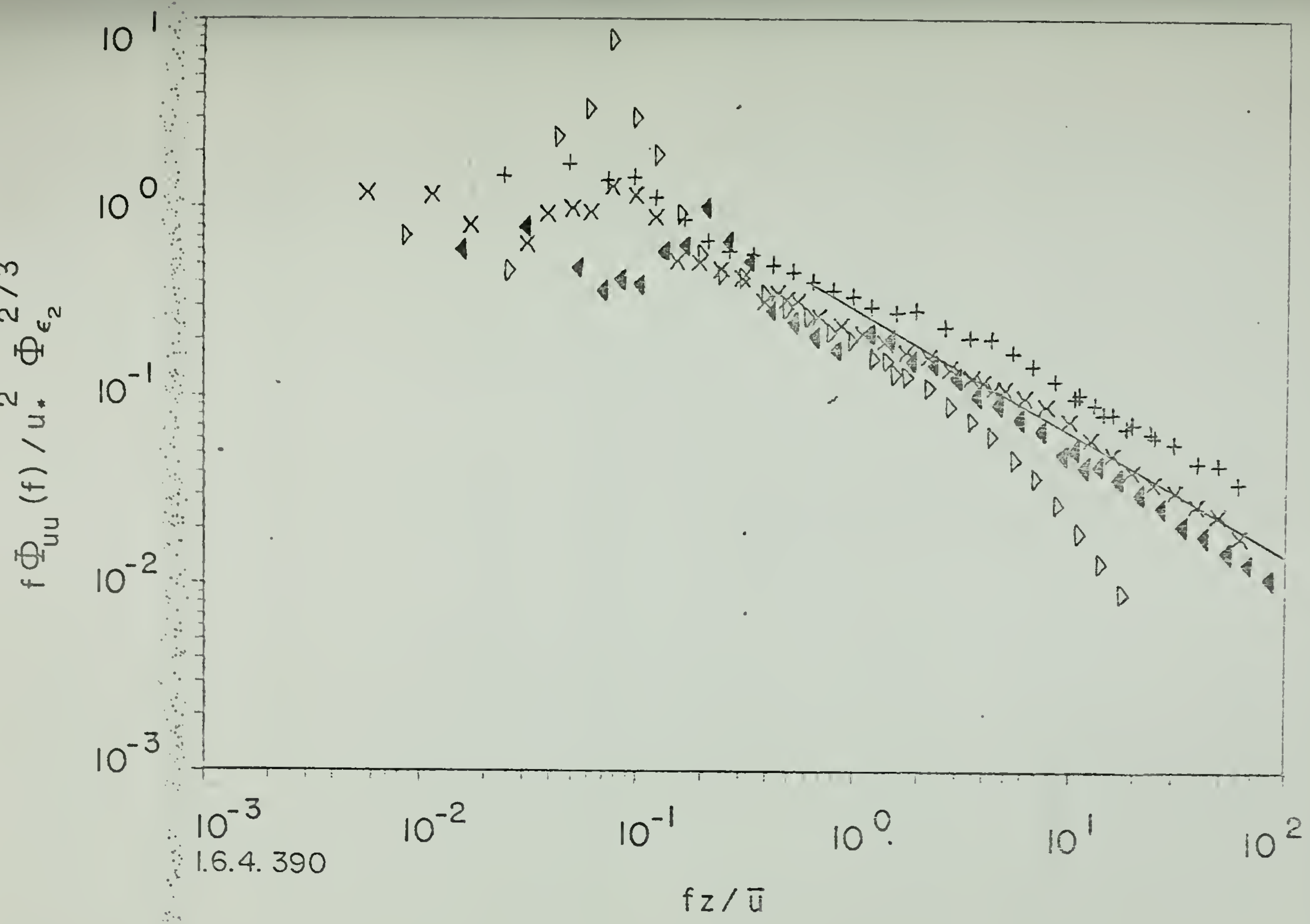
$f\Phi_{uu}(f)/u_*^2\ \Phi_{\epsilon_2}^{2/3}$
10^1
10^0
10^{-1}
10^{-2}
10^{-3}
10^{-3}
10^{-2}
10^{-1}
10^0
10^1
10^2
1.6.4. 390
$fz/\bar{u}$

FIGURE 24

Average vertical velocity spectra normalized with u_*^2 and $\Phi_{\epsilon_2}^{2/3}$ plotted versus normalized frequency

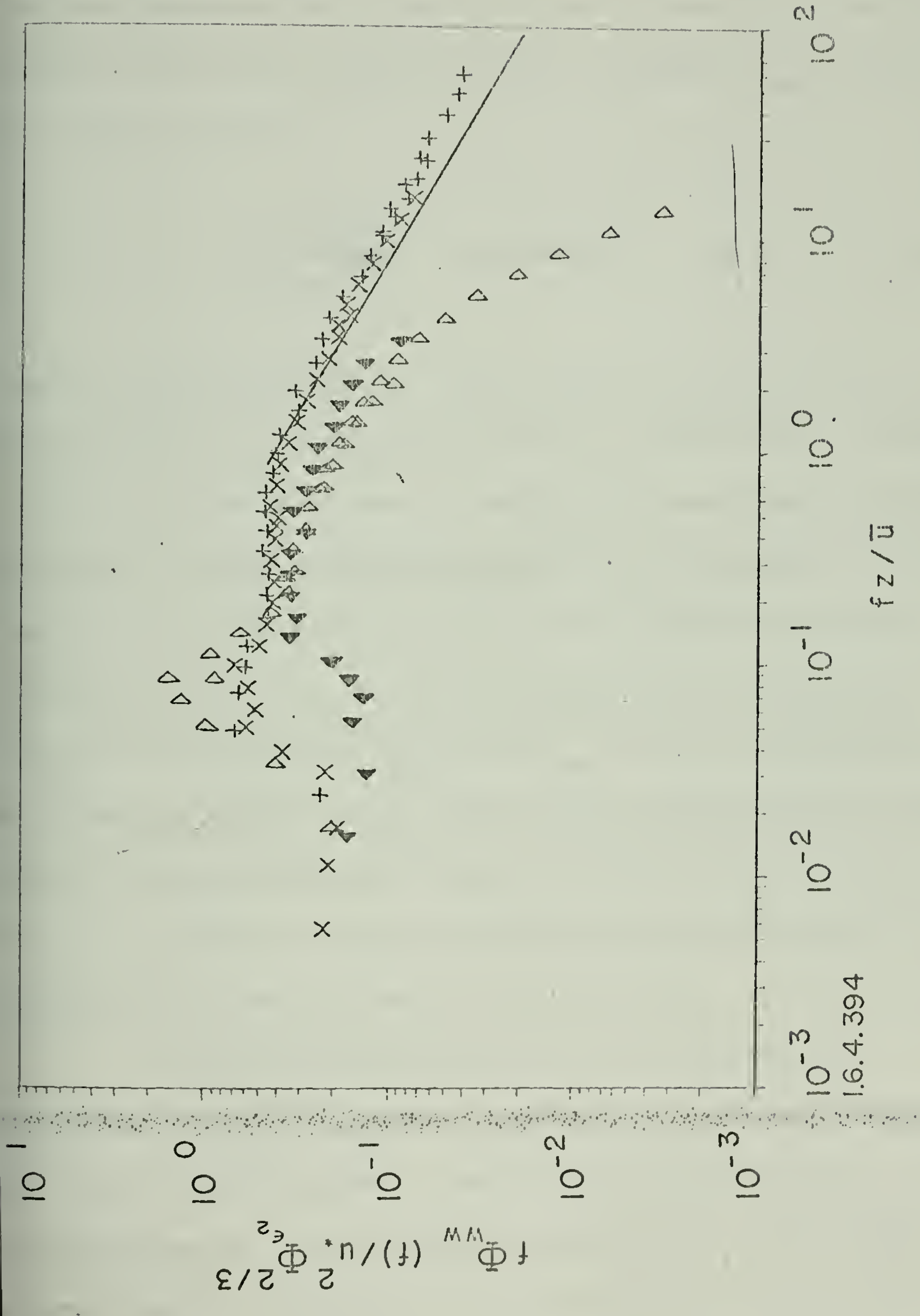
$f\Phi_{ww}(f)/u_*^2\,\Phi_{\epsilon}^{2/3}$
10^{1}
10^{0}
10^{-1}
10^{-2}
10^{-3}
10^{-3}
10^{-2}
10^{-1}
10^{0}
10^{1}
10^{2}
$fz/\bar{u}$
1.6.4.394

A similar relationship can be obtained for the w spectra by assuming isotropic conditions and making use of the relationship $\Phi_{ww} = 4/3\ \Phi_{uu}$ in the inertial subrange:

$$\frac{f_N \Phi_{ww}(f_N)}{u_*^2 \Phi_\epsilon^{2/3}} = 0.39\ f_N^{-2/3} \quad . \tag{48}$$

Figures 21 and 22 show the f_N u and w spectra normalized with the expression $\Phi_{\epsilon_1}^{2/3} = [(1-16\ z/L)^{-1/4} - z/L]^{2/3}$ from Eq. (24), assuming dissipation of mechanical energy is balanced by buoyant and mechanical production. This normalization is compared to the results of Leavitt[11] (dark line figures 21 and 22) who obtains from BOMEX data values of 0.28 ±0.05 and 0.37 ±0.07 for the constants in Eqs. (47) and (48). Figures 23 and 24 show the $f_N\Phi_{uu}$ and Φ_{ww} spectra normalized with the expression $\Phi_{\epsilon_2}^{2/3} = (1 + 0.5|z/L|^{2/3})$ from Eq. (27) based on the results of Wyngaard and Cote'[37] who used values of $\alpha_u = 0.5$ and $K = 0.35$ to obtain their normalized velocity curves with values of the constants for Eqs. (47) and (48) of 0.296 and 0.394.

Constants obtained from this work for Eq. (47) are 0.29 ± 0.06 for $\Phi_{\epsilon_1}^{2/3}$ and 0.23 ± 0.06 for Φ_{ϵ_2} and 0.40 ± 0.09 and 0.32 ± 0.09 for Eq. (48). A more sensitive test of the two expressions for Φ_ϵ will be discussed in Section 4.6. A test of the validity of the inertial subrange relationship $\Phi_{ww} = 4/3\ \Phi_{uu}$ which assumes local isotropy is shown in figure 25. The average ratio

FIGURE 25

Spectra ratio Φ_{ww} / Φ_{uu} plotted versus normalized frequency

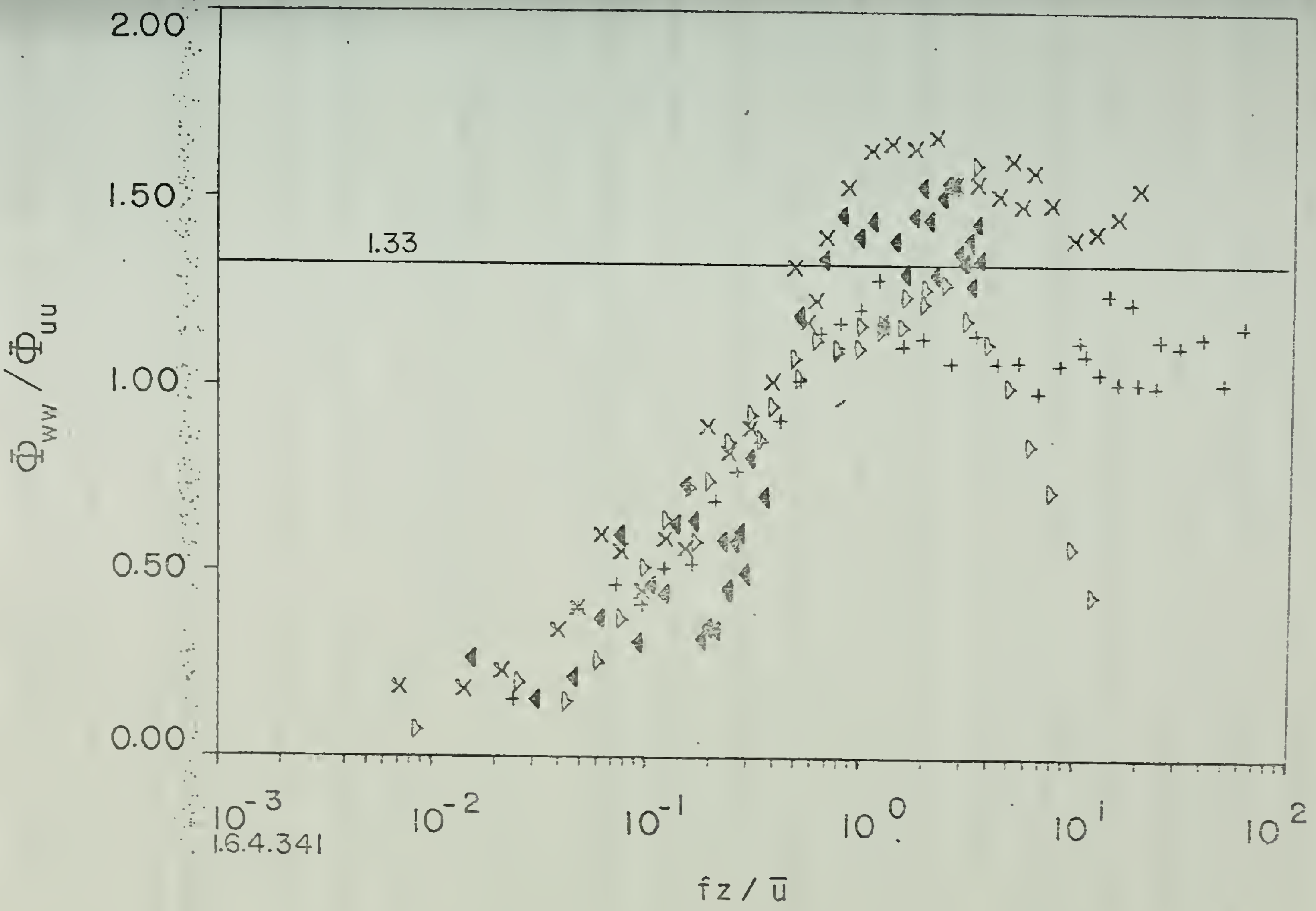
Φ_{ww} / Φ_{uu}
2.00
1.50
1.00
0.50
0.00
1.33
10^{-3}
10^{-2}
10^{-1}
10^{0}
10^{1}
10^{2}
1.6.4.341
$fz / \bar{u}$

Φ_{ww}/Φ_{uu} for each cruise is plotted versus f_N. The OWAX and MITOS III spectra have approximately the required ratio while the MITOS I data is higher and the SOMA data is lower than the required ratio. The high and low ratio values of the MITOS I and SOMA data may in part be due to x-wire drift experienced during the two cruises and discussed in Section 3.2c, due to salt contamination on the probes. Both MITOS I x-wire runs experienced 30% drift in the velocity calibrations but were matched with cup anemometer results which agreed well with the mean of the before and after run calibrations. The SOMA x-wires were calibrated only before each run so that the absolute drift is unknown and only run 1 was matched with a cup anemometer. For this reason the averaged normalized SOMA velocity spectra are probably inordinately high and are not included in the estimates of the constants in Eq. (47).

4.5b Temperature and humidity spectra

Absolute temperature spectra for SOMA, MITOS I, and MITOS III/OWAX are shown in figures 26, 27 and 28; absolute humidity spectra for the cruises are shown in figures 29, 30, and 31. Microbead thermistors were used to measure temperature fluctuations for the SOMA cruise and for OWAX runs 2 and 3. The temperature spectra of MITOS I, MITOS III and OWAX 4 were obtained from cold wire temperature data. Humidity was measured with the Lyman-Alpha humidiometer for all cruises.

FIGURE 26

SOMA temperature spectra plotted versus frequency

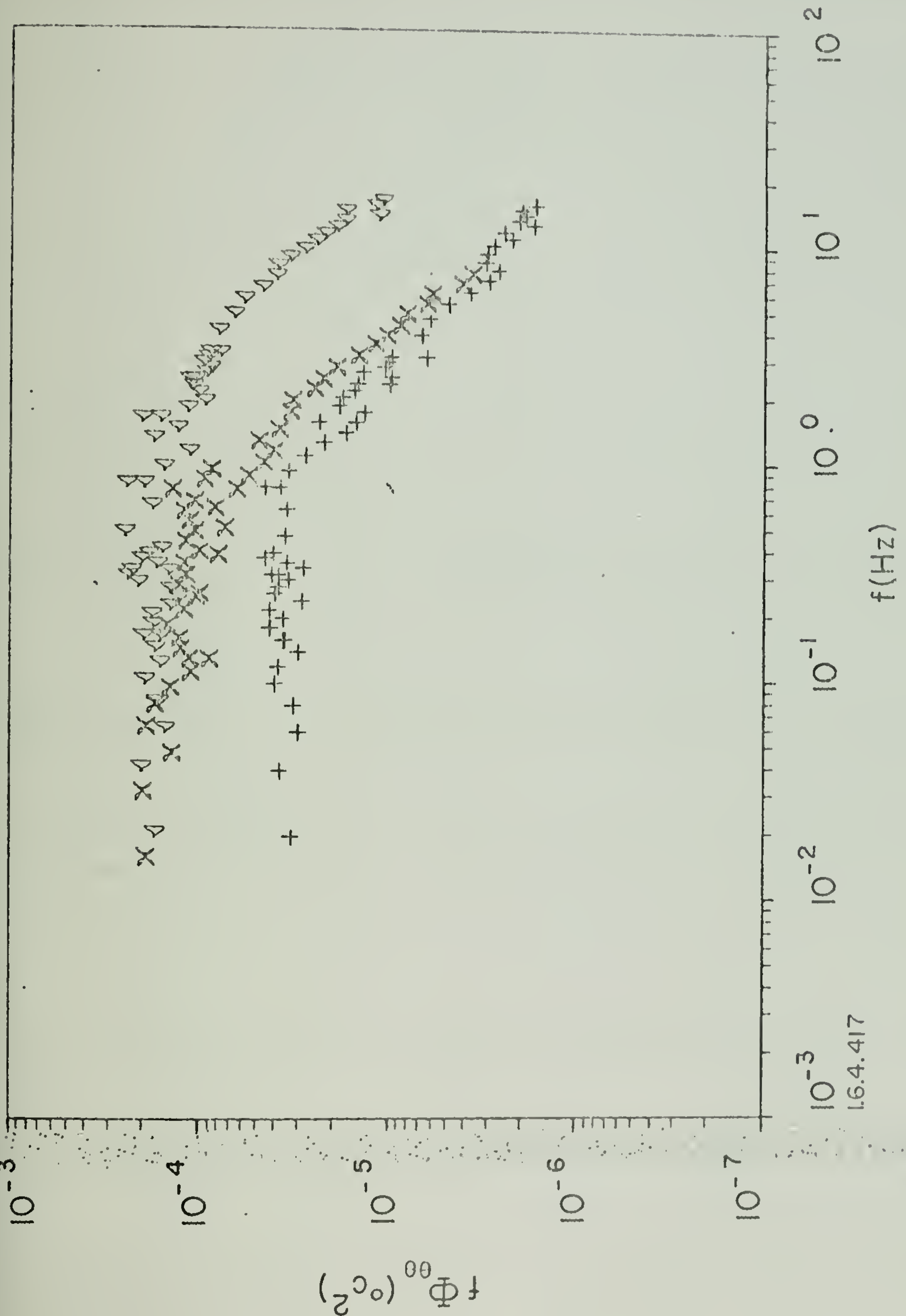
10^{-3}
10^{-4}
10^{-5}
10^{-6}
10^{-7}
$f\Phi_{00}$ (°C^2)
10^{-3}
10^{-2}
10^{-1}
10^{0}
10^{1}
10^{2}
f(Hz)
1.6.4.417

FIGURE 27

MITOS I temperature spectra plotted versus frequency

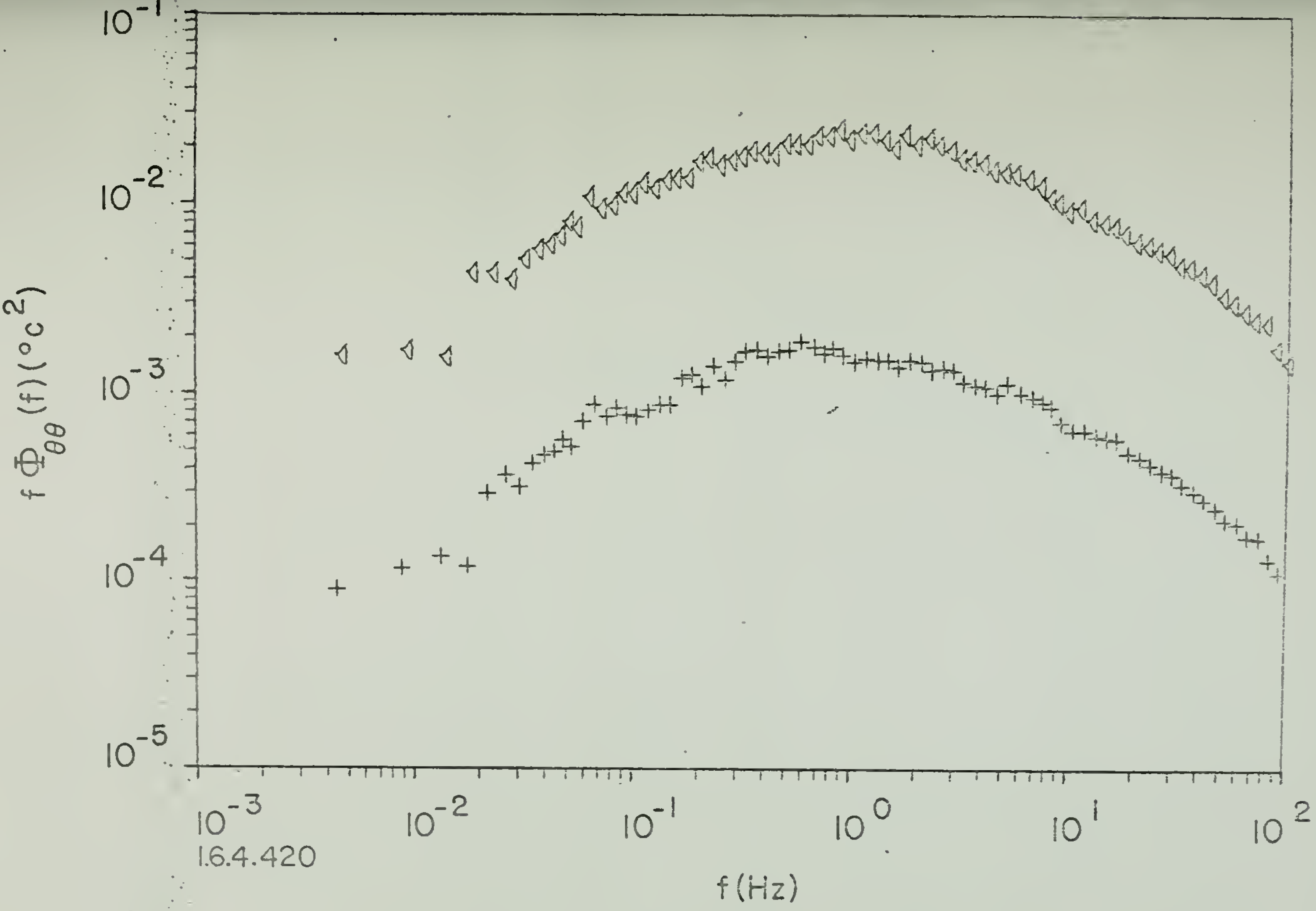
$f\Phi_{\theta\theta}(f)(°c^2)$
10^{-1}
10^{-2}
10^{-3}
10^{-4}
10^{-5}
10^{-3}
10^{-2}
10^{-1}
10^{0}
10^{1}
10^{2}
1.6.4.420
f(Hz)

FIGURE 28

MITOS III and OWAX temperature spectra plotted versus frequency

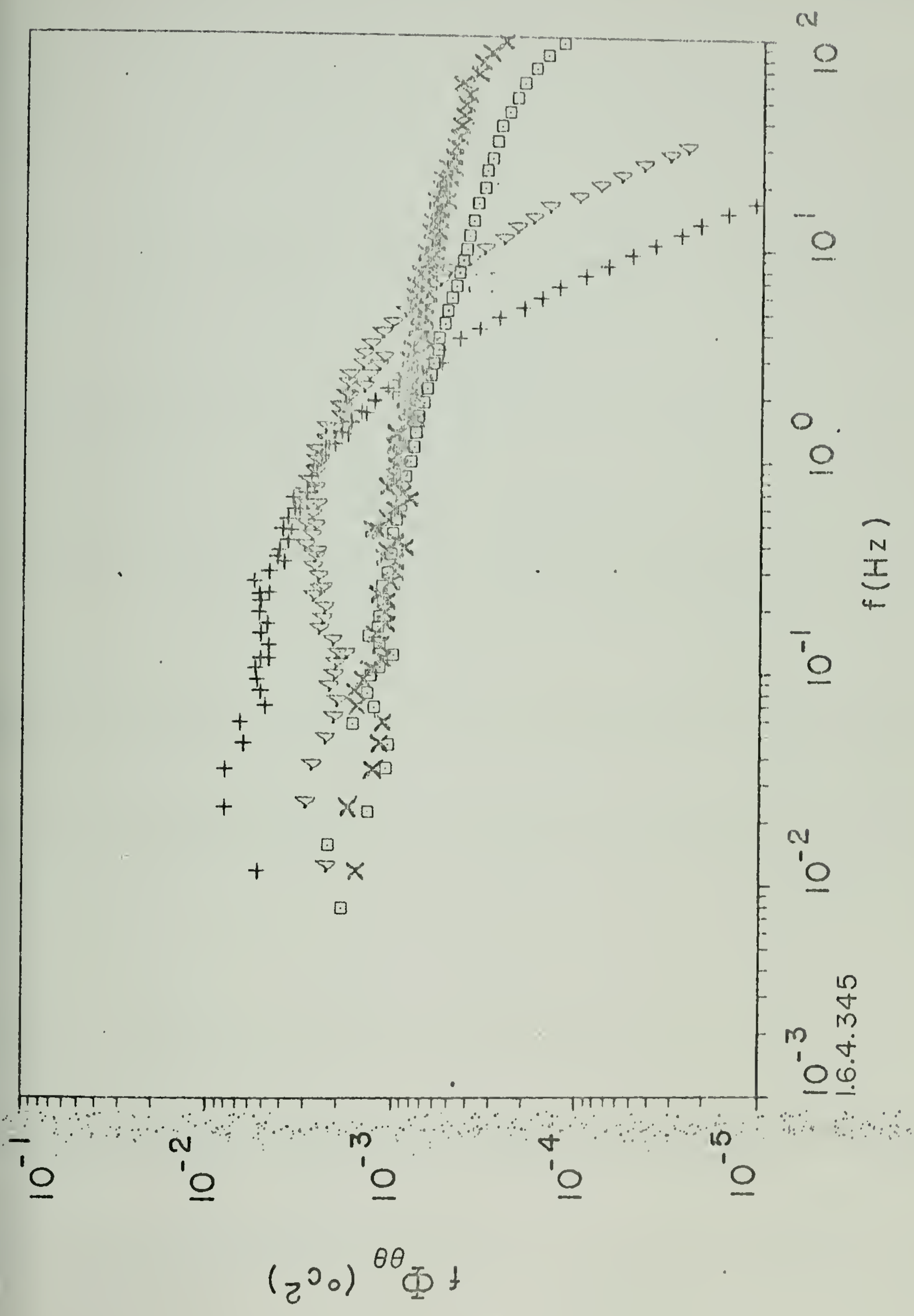
$f\,\Phi_{\theta\theta}$ ($^{\circ}C^2$)
10^{-1}
10^{-2}
10^{-3}
10^{-4}
10^{-5}
10^{-3}
10^{-2}
10^{-1}
10^{0}
10^{1}
10^{2}
f(Hz)
1.6.4.345

FIGURE 29

SOMA humidity spectra plotted versus frequency

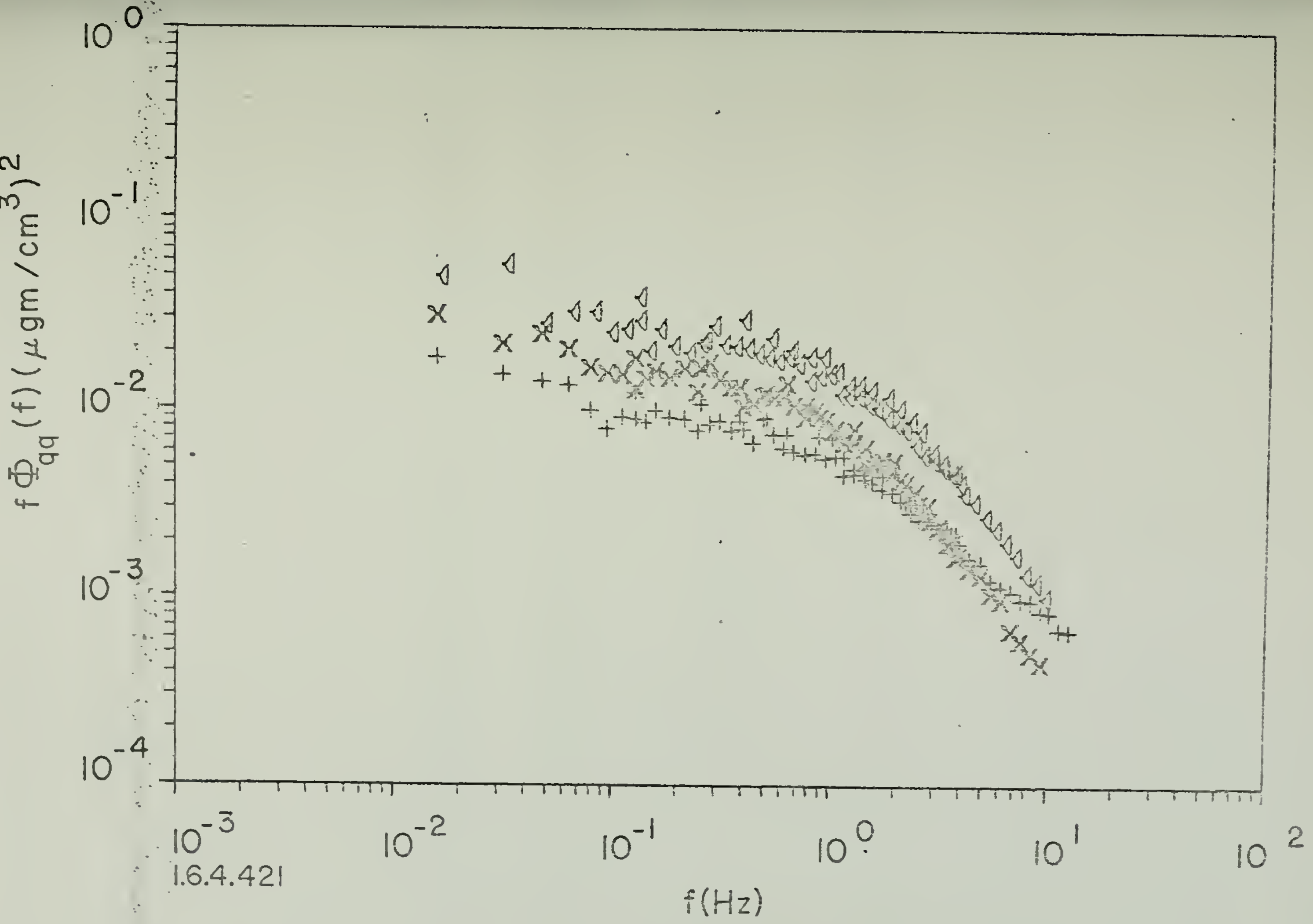
$f\Phi_{qq}(f)\,(\mu gm/cm^3)^2$
10^0
10^{-1}
10^{-2}
10^{-3}
10^{-4}
10^{-3}
10^{-2}
10^{-1}
10^0
10^1
10^2
1.6.4.421
f(Hz)

FIGURE 30

MITOS I humidity spectra plotted versus frequency

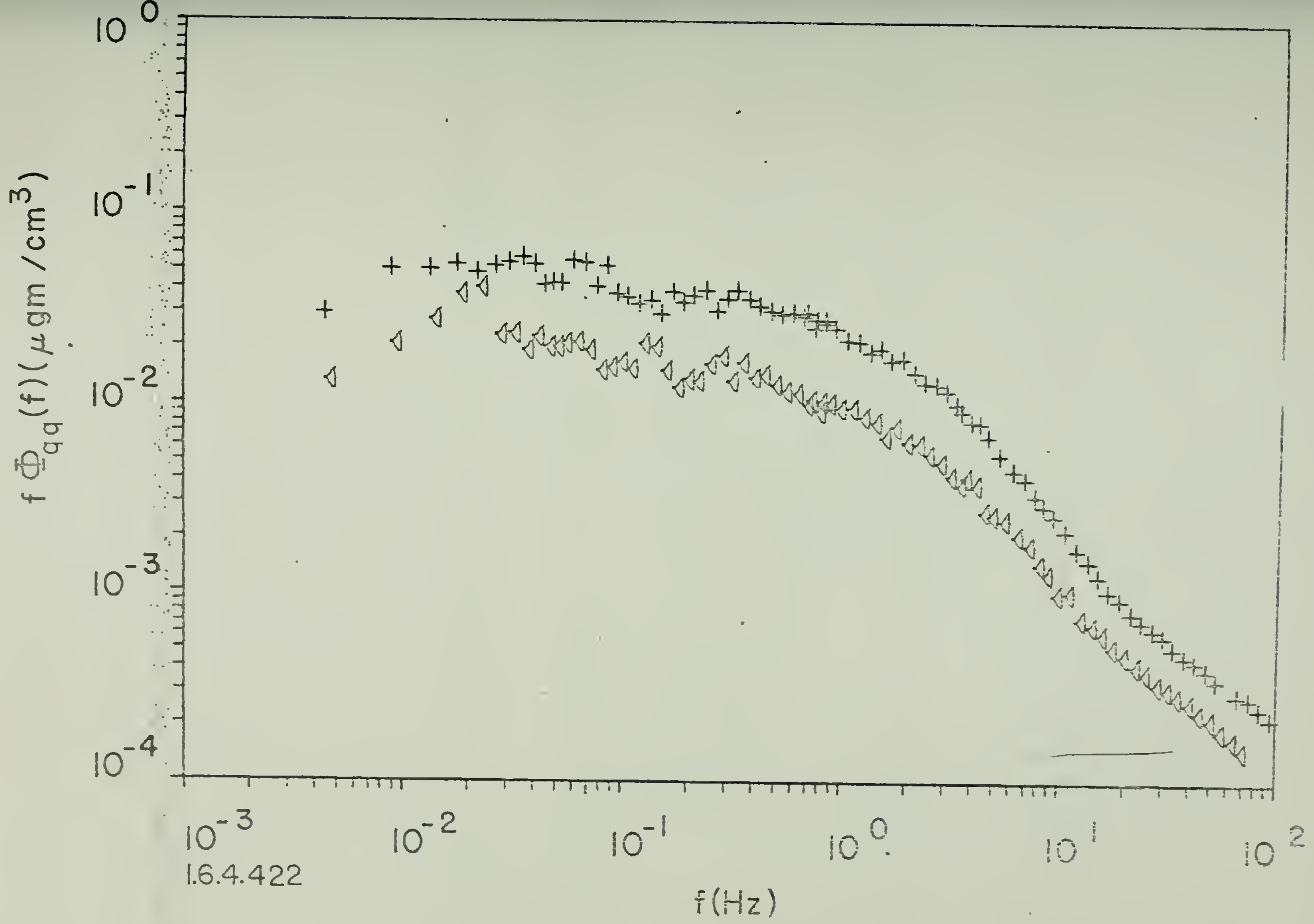
$f\,\Phi_{qq}(f)\,(\mu gm/cm^3)$
10^0
10^{-1}
10^{-2}
10^{-3}
10^{-4}
10^{-3}
10^{-2}
10^{-1}
10^0
10^1
10^2
1.6.4.422
f(Hz)

FIGURE 31

MITOS III and OWAX humidity spectra plotted versus frequency

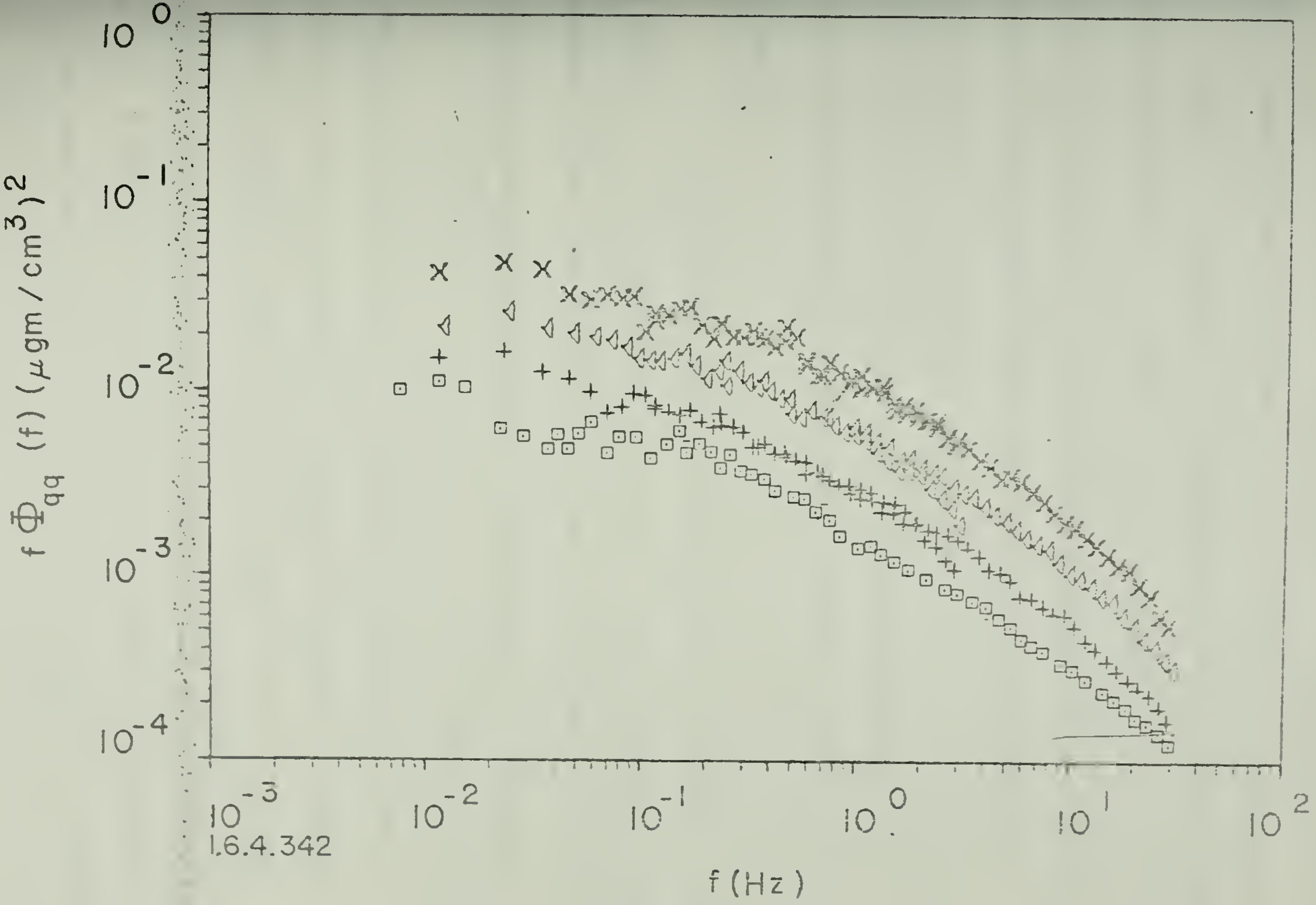
$f\,\Phi_{qq}\,(f)\;(\mu gm/cm^3)^2$
10^0
10^{-1}
10^{-2}
10^{-3}
10^{-4}
10^{-3}
10^{-2}
10^{-1}
10^0
10^1
10^2
1.6.4.342
f (Hz)

The temperature spectra of MITOS I appear to exhibit a high frequency peak at 0.8 Hz for run 1 and at $f \approx 1.5$ Hz for run 7. Temperature spectra from BOMEX presented by Leavitt[11] and Phelps and Pond[10] also exhibit a high frequency peak for $0.25 < f < 0.9$ Hz for 8 meter data. The temperature spectra from MITOS III and OWAX 4 do not exhibit similar peaks and also do not follow the predicted $f^{-2/3}$ inertial subrange behavior for $1 < f < 100$ Hz. It is difficult to ascertain the behavior of the thermistor spectra for $f > 1$ Hz since above that frequency the spectra roll-off due to thermistor response.

The humidity spectra from all cruises are similar and appear to follow a $f^{-2/3}$ behavior for $f > 0.8$ Hz and do not exhibit any high frequency peak. The MITOS III humidity spectra obtained at 1250 cm exhibit the most pronounced inertial subrange for $f \gtrsim 0.2$ Hz.

Differences between temperature and humidity spectra and between individual runs for the temperature spectra are shown in figures 32 and 33 which present average temperature and humidity spectra normalized with T_*^2 and q_*^2 plotted versus z/L. The humidity spectra collapse quite well and exhibit a $f_N^{-2/3}$ behavior for $f_N > 0.3$. The temperature spectra do not collapse and only the MITOS I temperature data exhibit a $-2/3$ behavior for $f_N > 2$. The temperature spectra of MITOS III and OWAX appear to follow a $-1/4$ slope

FIGURE 32

Average temperature spectra normalized with T_*^2 plotted versus normalized frequency

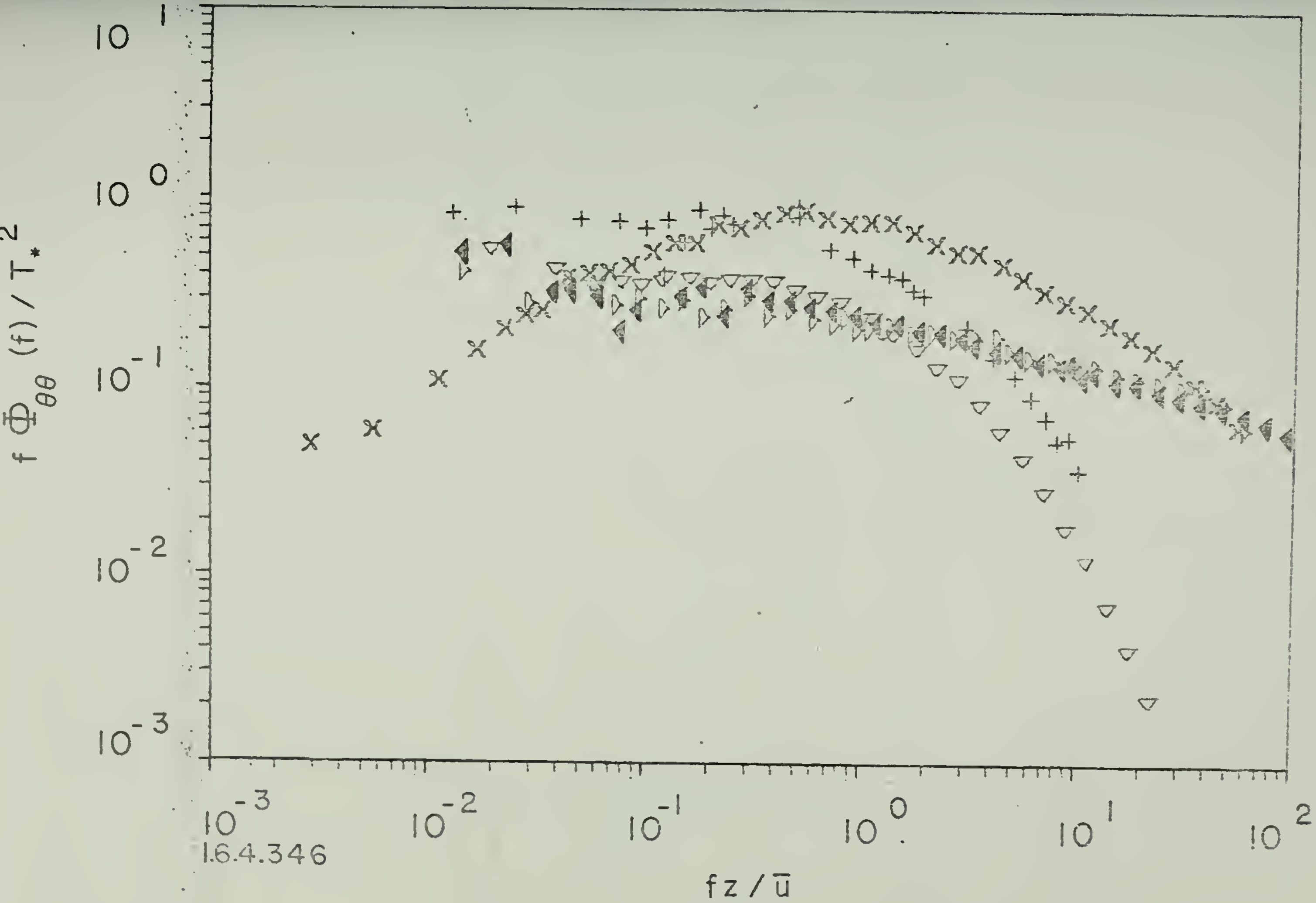
$f\,\Phi_{\theta\theta}(f)/T_*^2$
10^1
10^0
10^{-1}
10^{-2}
10^{-3}
10^{-3}
10^{-2}
10^{-1}
10^0
10^1
10^2
1.6.4.346
$fz/\bar{u}$

FIGURE 33

Average humidity spectra normalized with q_*^2 plotted versus normalized frequency

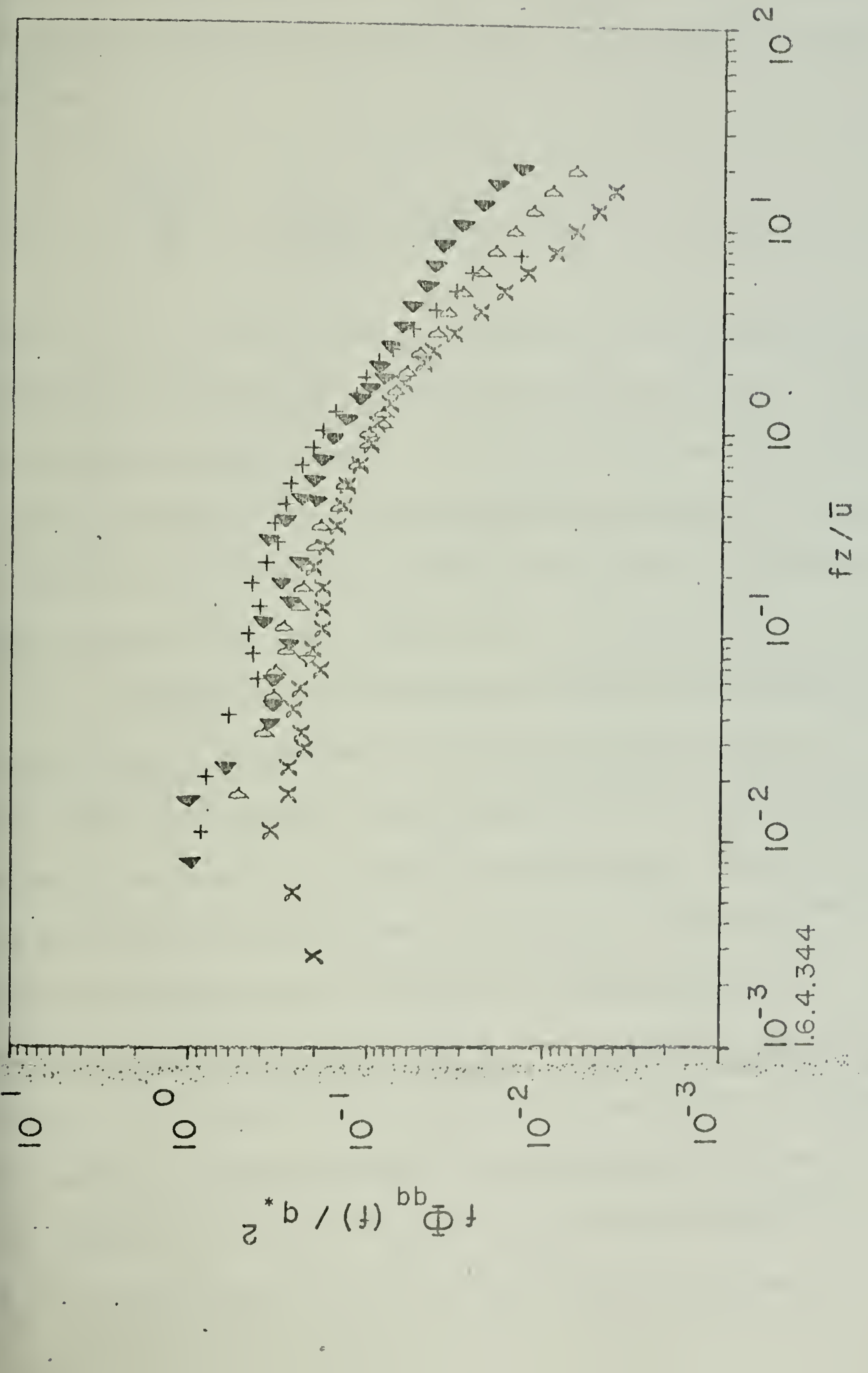
10^{1}
10^{0}
10^{-1}
10^{-2}
10^{-3}
$f\,\Phi_{qq}(f)\,/\,q_*^{2}$
10^{-3}
10^{-2}
10^{-1}
10^{0}
10^{1}
10^{2}
$fz\,/\,\overline{u}$
16.4.344

over 2 1/2 decades for $f_N > 0.5$. The expression for the temperature and humidity spectra in the inertial subrange given by Eq. (12) can be rewritten as

$$\frac{f\Phi_{\gamma\gamma}(f)}{\gamma_*^2} = \frac{\beta_\gamma}{(2\pi k)^{2/3}} \Phi_H \Phi_\epsilon^{-1/3} f_N^{-2/3} \qquad (49)$$

where $\gamma = T$ or q, Φ_H is the dimensionless scalar production given by Eq. (19), β_γ the scalar subrange constant, and $K = 0.4$. The dimensionless scalar production of temperature and humidity variance has been assumed equal and in balance with the dimensionless scalar dissipation given by Eqs. (30) and (33) for temperature and humidity. This assumption may not be valid as will be discussed in Section 4.7.

Figures 34 and 35 show the averaged temperature and humidity spectra normalized as in Eq. (49) and plotted versus f_N. Also shown in these figures are the temperature and humidity spectra of Phelps and Pond[10] and Leavitt[11] for BOMEX data, Phelps and Pond[10] for pre-BOMEX (San Diego) data, and Wyngaard[58] and Kaimal[56] for Kansas temperature data, normalized in a similar manner. Data from this work has been normalized with $\Phi_H = (1-16\ z/L)^{-1/2}$ and $\Phi_\epsilon^{-1/3} = [(1-16\ z/L)^{-1/4} - z/L]^{-1/3}$ as were used by Leavitt[11] for his normalized spectra. This normalization is not significantly different from that employed by Wyngaard[58] who used $\Phi_H = 0.74\ (1-9\ z/L)^{-1/2}$, $\Phi_{\epsilon_2}^{-1/3} = (1 + 0.5|z/L|^{2/3})^{-1/2}$, and $K = 0.35$. The Kaimal[56] and

FIGURE 34

Average temperature spectra normalized with T_*^2, Φ_H (dimensionless temperature gradient) and $\Phi_\epsilon^{-1/3}$ plotted versus normalized frequency

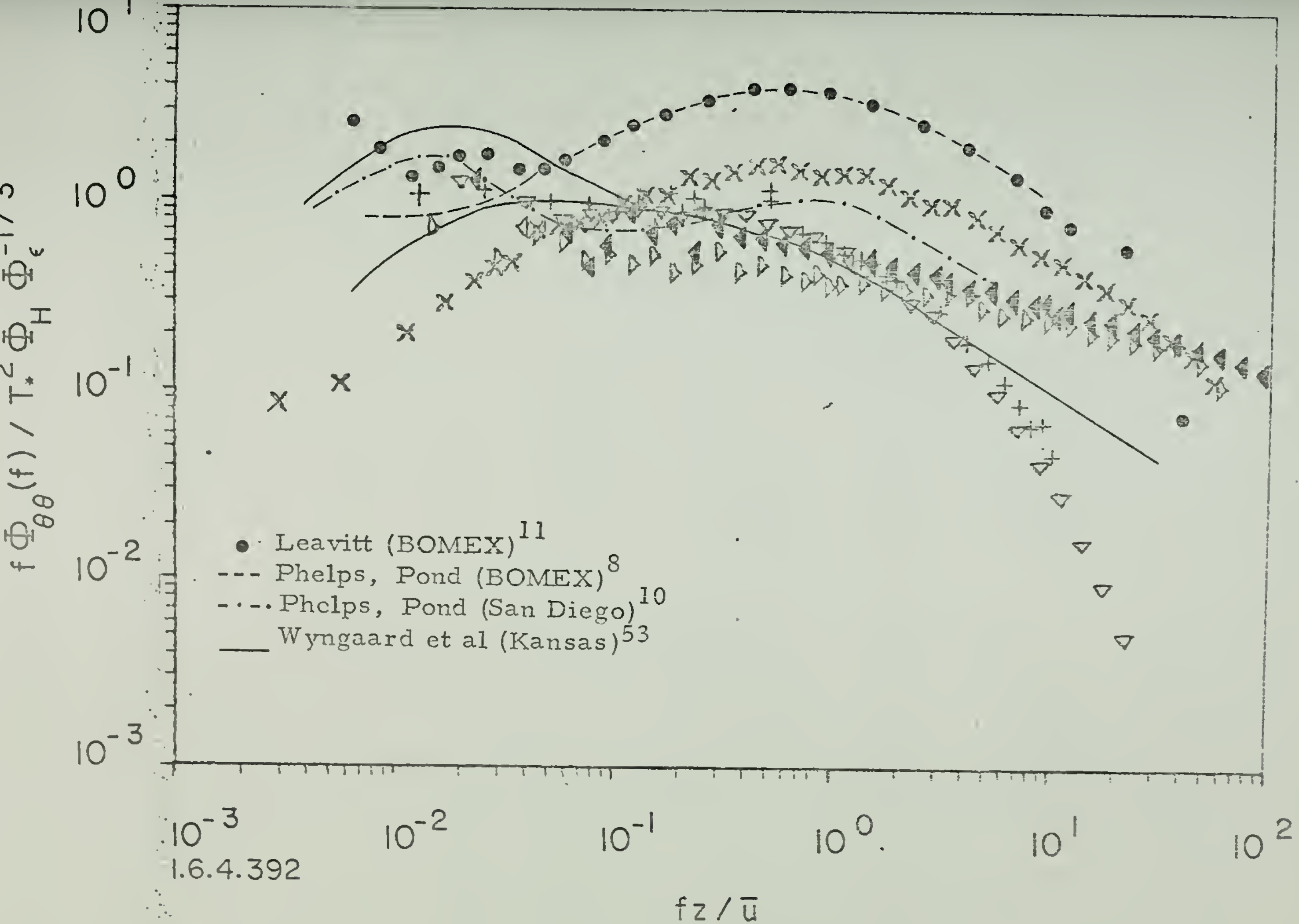
$f\,\Phi_{\theta\theta}(f)\,/\,T_*^2\,\Phi_H\,\Phi_\epsilon^{-1/3}$
10^1
10^0
10^{-1}
10^{-2}
10^{-3}
10^{-3}
10^{-2}
10^{-1}
10^0
10^1
10^2
$fz/\bar{u}$
● Leavitt (BOMEX)11
--- Phelps, Pond (BOMEX)8
-·-· Phelps, Pond (San Diego)10
—— Wyngaard et al (Kansas)53

1.6.4.392

FIGURE 35

Average humidity spectra normalized with q_*^2, Φ_E (dimensionless humidity gradient) $\Phi_\epsilon^{-1/3}$ plotted versus normalized frequency

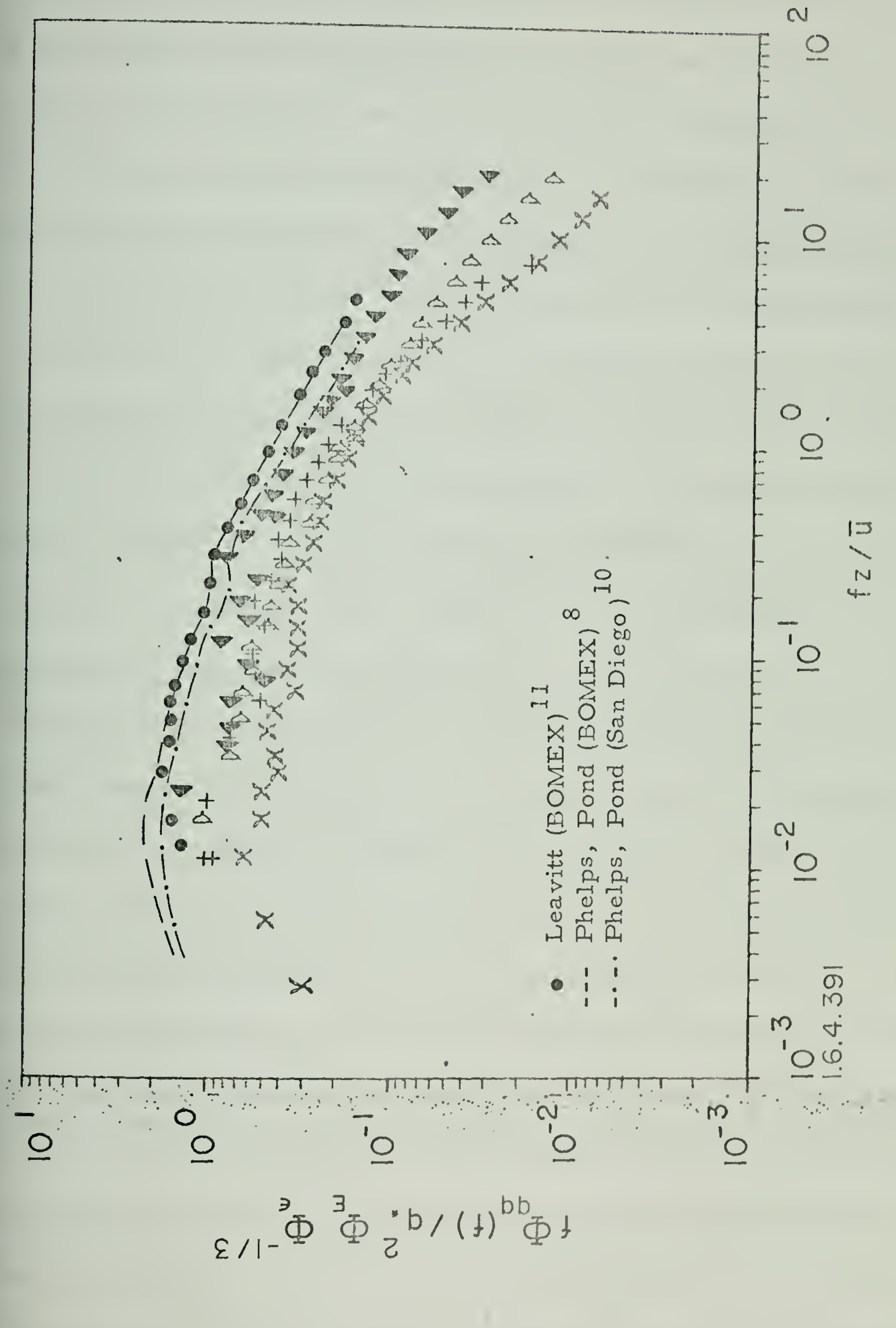
$f\Phi_{qq}(f)/q_*^2\,\Phi_m\,\Phi_e^{-1/3}$
10^{1}
10^{0}
10^{-1}
10^{-2}
10^{-3}
10^{-3}
10^{-2}
10^{-1}
10^{0}
10^{1}
10^{2}
fz/ū
● Leavitt (BOMEX)[11]
--- Phelps, Pond (BOMEX)[8]
-·-·- Phelps, Pond (San Diego)[10]
1.6.4.391

Wyngaard[58] Kansas data, represented by the solid line in figure 34, if normalized with the expressions in this work and K = 0.4 would be approximately 3% lower (based on $-z/L = 0.2$) than shown. The temperature and humidity spectral data for BOMEX and pre-BOMEX cruises shown in figure 34 and 35 was obtained by fairing a mean line through Phelps and Pond's[10] spectral results. Since their results were normalized with σ_θ^2 and σ_q^2, the normalization of figure 34 was calculated based on average $\sigma_\theta^2/T_*^2 = 4.23$ for pre-BOMEX and 6.63 for BOMEX (this includes correction for K in their definition of $T_* = \overline{w\theta}/Ku_*$), σ_q^2/q_*^2 of 4.84 for pre-BOMEX and 5.25 for BOMEX, and average $-z/L$ values of 0.165 (pre-BOMEX) and 0.195 (BOMEX) to calculate the values of T_*^2, q_*^2, Φ_H and $\Phi_\epsilon^{-1/3}$. The expressions for Φ_H and $\Phi_\epsilon^{-1/3}$ used to normalize the Phelps and Pond[10] data were the same as those used by Leavitt.[11] The Phelps and Pond[10] and Leavitt[11] BOMEX temperature and humidity spectra shown in figures 34 and 35 agree for $f_N > 0.05$ and are higher than San Diego data of Phelps and Pond[10] and spectra from this work. The normalized humidity spectra of Phelps and Pond[10] differ by 10% due to the different conversion factors. This difference is greater by as much as 25% for $f_N > 0.2$, probably caused by low pass filtering of the San Diego data at a lower frequency than the BOMEX data as noted by Phelps and Pond.[10] The 10% difference in the normalized average humidity spectra of Phelps and Pond[10] may be due to scatter

in the Phelps and Pond[10] spectra but appears to be real when compared to the humidity spectra of this work.

The general trend in the normalized temperature spectra is for the warmer more humid BOMEX and MITOS I data to be higher than the Kansas land (dry) spectra and the less humid San Diego spectra. The temperature spectra from MITOS III and OWAX 4 do not follow the predicted $f_N^{-2/3}$ behavior for $f_N > 10$ as shown by the Kansas data. The MITOS I temperature spectra have the same shape as the BOMEX data and follow the predicted $f_N^{-2/3}$ behavior for $f_N > 10$. The San Diego thermistor data of Phelps and Pond[10] does not extend beyond $f_N \simeq 8$ and has the same shape as the thermistor spectra of the SOMA and OWAX 2 and 3 runs. The Phelps and Pond[10] data do not extend beyond $f_N = 10$ and Leavitt's[11] average temperature spectra shows scatter and response limitations above $f_N = 10$, so that any comparison of spectra for $f_N > 10$ is tenuous.

The normalized temperature spectra of figure 34 are higher in spectral level than the corresponding normalized humidity spectra of figure 35 for $f_N > 1$. No attempt was made to average all the temperature and humidity spectra for comparison of the two on one plot due to the large spread of the individual spectra from different cruises. Comparison of the constant β_θ and β_q which can be obtained from Eq. (49) will be made in Section 4.7a.

4.6 Cospectra

Results of cospectral analysis are presented in this section. Cospectra from the four cruises are presented in a manner similar to the presentation of power spectra, with averages and plot symbols remaining the same unless otherwise noted. Two realizations for each cospectral computation were made at the two lowest sampling frequencies shown in Table 6 for each run. Since the correlations between the variables being compared in the cospectral analysis are less than unity, cospectral estimates will have larger uncertainties than spectral estimates at the same frequency, particularly for low frequency estimates. Uncertainties in the cospectral levels at lower frequencies have been minimized by the long averaging periods. The number of estimates of the lowest frequency cospectral points at $f = 0.004$ Hz is between 170 for the OWAX 3 run and 32 for the MITOS III data.

The cospectra from the MITOS III and OWAX cruises have been corrected for internal misalignment of the sonic anemometer (OWAX only), instrument pitch, and wave induced FLIP motion using the procedures discussed in Section 4.3. The uncorrected $w\gamma$ cospectra from the MITOS I and SOMA cruises are also presented, since scalar flux cospectra are less sensitive to motion effects than the uw cospectra. The momentum flux cospectra from MITOS I and SOMA are not presented since no pitch angle was available to obtain pitch corrected

uw cospectra, and the (uw) cospectral estimates are sensitive to drift of the x-wires experienced during the two cruises.

4.6a Cospectra of momentum (uw)

Absolute (uw) cospectra from MITOS III and OWAX plotted versus frequency (f) are shown in figure 36. In the frequency range $0.01 < f < 0.1$ Hz used to determine the value of the spectral correlation coefficient $R_{uw}(f)$, the spectra exhibit a broad, fairly constant peak. No cospectral estimates were made below 0.001 Hz. Cospectra of momentum flux presented by Leavitt[11] and extending to 0.0001 Hz exhibited considerable scatter and negative values in the frequency interval $0.0001 < f < 0.001$ Hz, so that there are only small (< 5%) contributions to the uw covariances below 0.001 Hz.

The averaged uw cospectrum of OWAX and the MITOS III cospectrum normalized with u_*^2 and plotted versus $\log f_N$ are shown in figure 37. Wyngaard and Coté[61] predict an inertial subrange behavior for the uw cospectra given by the expression

$$\frac{-f_N \Phi_{uw}(f_N)}{u_*^2} = \alpha_{uw} \, G(z/L) \, f_N^{-4/3} \tag{50}$$

where the function $G(z/L) = 1.0$ determined empirically from Kansas data by Kaimal et al[56] for $-2 \leq z/L \leq 0$, with a predicted value of the constant $\alpha_{uw} = 0.048$. The cospectral curve predicted by Wyngaard and Coté[61] is shown by the dark line in figure 37 where the divergence

FIGURE 36

MITOS III and OWAX momentum flux (uw) cospectra (corrected for pitch) plotted versus frequency

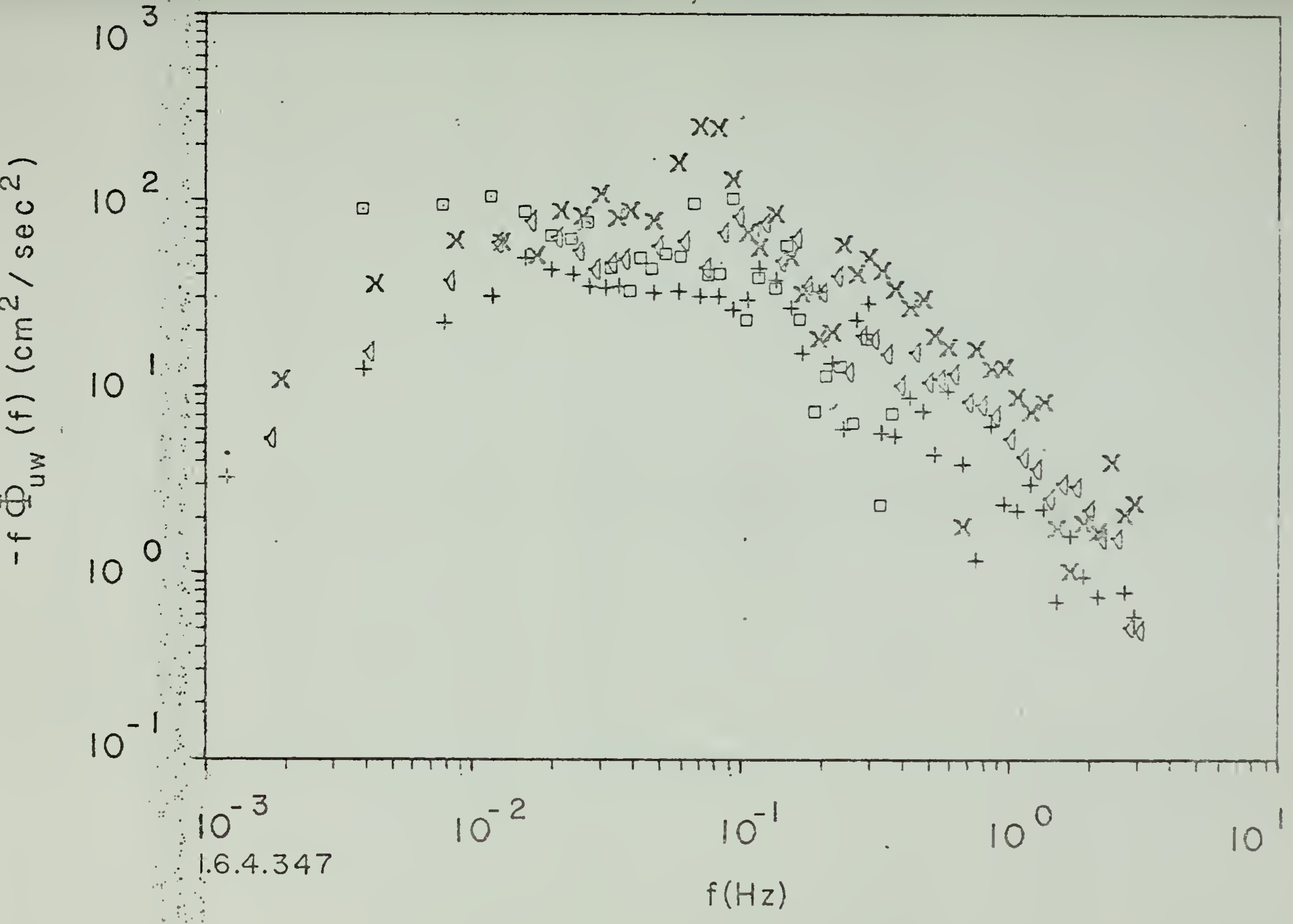
$-f\,\Phi_{uw}(f)\ (cm^2/sec^2)$
10^3
10^2
10^1
10^0
10^{-1}
10^{-3}
10^{-2}
10^{-1}
10^0
10^1
1.6.4.347
f(Hz)

FIGURE 37

Average uw cospectra normalized with u_*^2 plotted versus normalized frequency (comparison with other results)

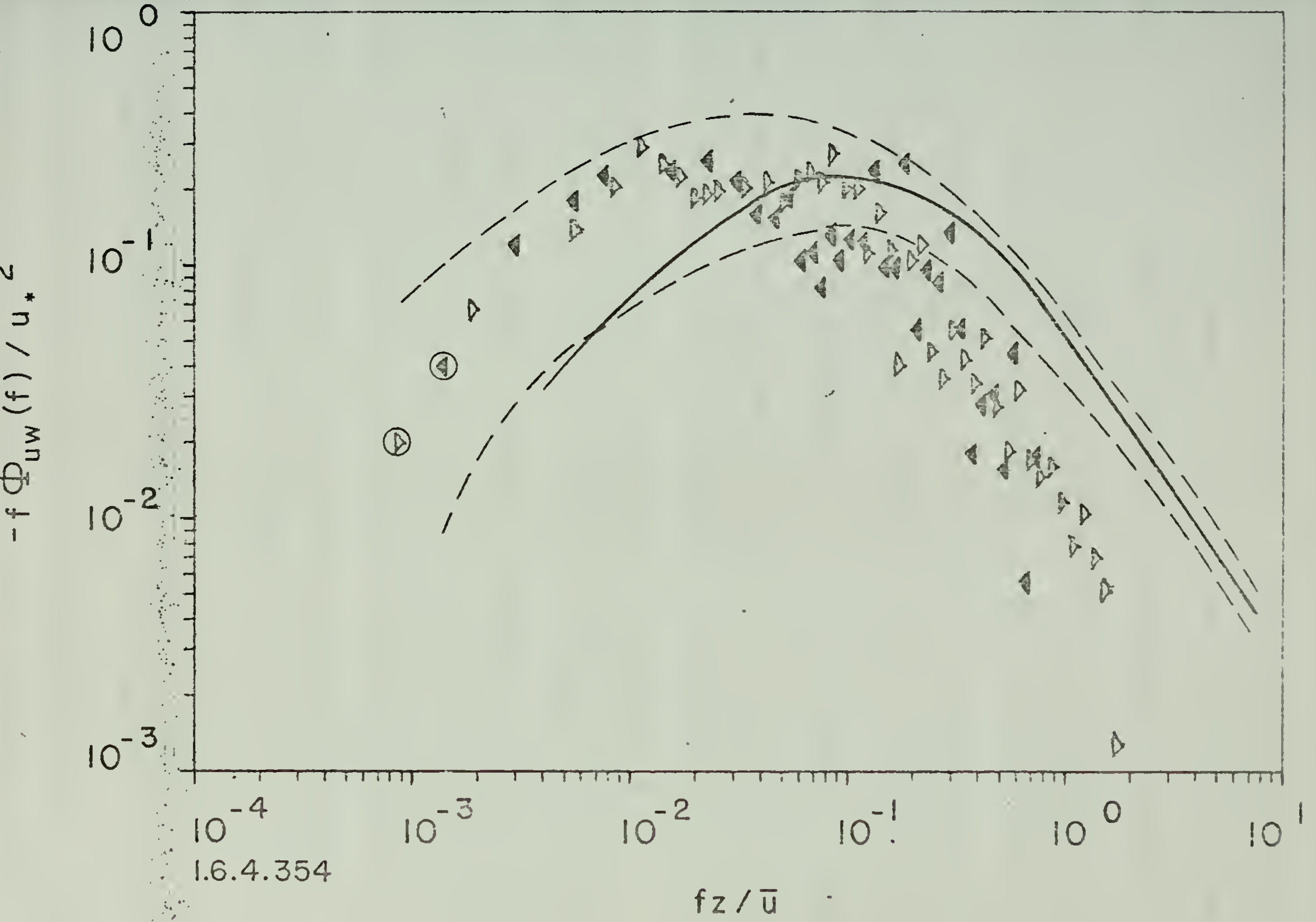
$-f\Phi_{uw}(f)/u_*^2$
10^0
10^{-1}
10^{-2}
10^{-3}
10^{-4}
10^{-3}
10^{-2}
10^{-1}
10^0
10^1
1.6.4.354
$fz/\bar{u}$

of the curves for $f_N < 0.4$ represents different low frequency shapes for unstable conditions $(-2 \leq z/L < 0)$. The results of Pond et al[8] from BOMEX are represented by the envelope defined by the dashed lines of Figure 37. Pond's[8] data had to be converted by a factor of $\sigma_w^2/u_*^2 = 1.74$ since the data were presented normalized with σ_w^2.

The cospectra of MITOS III and OWAX follow the predicted $f_N^{-4/3}$ behavior for $f_N > 0.2$, but are lower in cospectral level than the Kaimal et al[56] or Pond et al[8] cospectra. The value of $\alpha_{uw} = 0.01 \pm 0.002$ for this data also illustrates the lower cospectral levels. Lower cospectral levels for $f_N > 0.2$ for the MITOS III and OWAX data cannot be completely explained by spatial averaging errors. The two cospectra collapse on one another and exhibit a $f_N^{-4/3}$ behavior over nearly a decade in the range $0.2 < f_N < 2$, below $f_N = 2.8$, where the effects of spatial averaging occur for the OWAX data. The pitch corrections applied to data of Pond et al[8] using an assumed R_{uw} value are much larger than equivalent corrections applied to cospectra of this work, but the corrections are only significant at low frequencies $(f < 0.1 \text{ Hz})$.

Normalized uw cospectra of Leavitt[11] for 30 m data also exhibit lower cospectral levels above $f_N = 0.7$ than the 8 m data, however, the fall-off in the 30 m data is greater than $f_N^{-4/3}$ and was attributed to noise in one channel of the 30 m sonic anemometer. Although no excessive noise was observed in the u or w signals of

FIGURE 38

Average uw cospectra normalized with u_*^2 plotted linearly versus normalized frequency (comparison with other results)

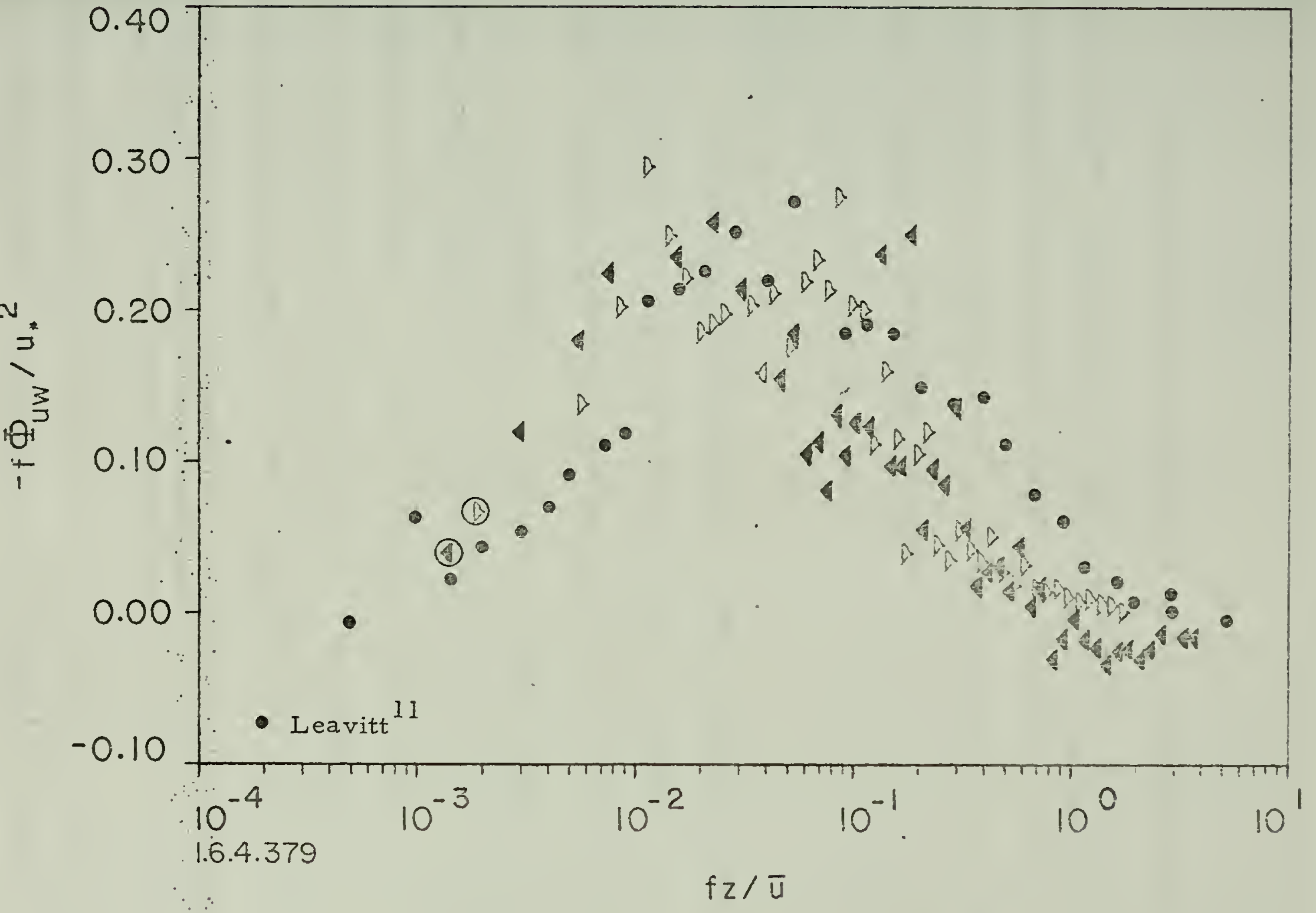
$-f\Phi_{uw}/u_*^2$
0.40
0.30
0.20
0.10
0.00
-0.10
10^{-4}
10^{-3}
10^{-2}
10^{-1}
10^{0}
10^{1}
$fz/\bar{u}$
● Leavitt[11]
1.6.4.379

the sonic anemometers used during the OWAX and MITOS III cruises, noise in a single channel may have contributed to the faster roll-off in the cospectra. The behavior of the uw cospectra at higher frequencies ($f_N > 0.2$) may be due to effects other than spatial averaging and high frequency noise. Both normalized cospectra from the MITOS III and OWAX compare with one another and have the same shape as the uw cospectra obtained by Kaimal et al[56]. The spectra appear to be shifted to lower frequencies, suggesting that production of kinetic energy may occur at larger scales over the ocean than over land under certain conditions.

A correction was applied to the OWAX cospectra for the internal misalignment of the vertical sensing path, however, this distortion may have contributed to lower cospectral levels for $f_N > 1.0$.

The normalized uw cospectra are shown plotted linearly versus log f_N in figure 38 and compared with Leavitt's[11] averaged uw cospectrum (circles). Leavitt[11] obtained a value of $\alpha_{uw} = 0.07 \pm 0.02$ from the 8 m normalized cospectra. The cospectra from this work are lower than Leavitt's[11] data for $f_N > 0.2$ and show evidence of possible high frequency noise contamination with positive high frequency cospectral values for the MITOS III data above $f_N = 0.7$. The low frequency cospectral levels ($f_N < 0.01$) are, in general, slightly higher than results of Leavitt,[11] probably due to the difference in pitch correction procedure.

4.6b Cospectra of heat and water vapor flux ($w\theta$, wq)

$w\theta$ Cospectra

Dimensional $w\theta$ cospectra are shown in figure 39 - SOMA, 40 - MITOS I, and 41 - MITOS III and OWAX. The SOMA $w\theta$ cospectra do not exhibit similar shapes; possible reasons for this behavior have been proposed earlier and include the low $w\theta$ covariance values indicating near neutral conditions and suggesting effects of non-stationarity, uncertainties in the w and θ calibrations, and lack of pitch corrections. The SOMA data also have the shortest averaging time and only extend to a low frequency cut-off of 0.015 Hz so that uncertainties in the calculation of cospectral levels are equivalent to the other cruise data.

The MITOS I $w\theta$ cospectra have a peak at $f \simeq 0.5$ Hz and exhibit a shape similar to the shape of the BOMEX $w\theta$ cospectra shown in figures 42 and 43. The dimensional $w\theta$ cospectra of MITOS III and OWAX corrected for pitch are different than the MITOS I $w\theta$ cospectra and exhibit a broad peak in the frequency interval $0.01 < f < 0.3$ Hz , similar to the peak observed in the MITOS III and OWAX uw cospectra. The cospectra are not greatly affected by FLIP induced motion, with only one averaged cospectral estimate from the OWAX 2 run at $f \simeq 0.1$ Hz significantly lower than other estimates (corrected for in the integration). The cospectral points circled at $f \simeq 0.002$ Hz were used to extend the integration to 10^{-3} Hz as discussed in

FIGURE 39

SOMA heat flux $(w\theta)$ cospectra plotted versus frequency

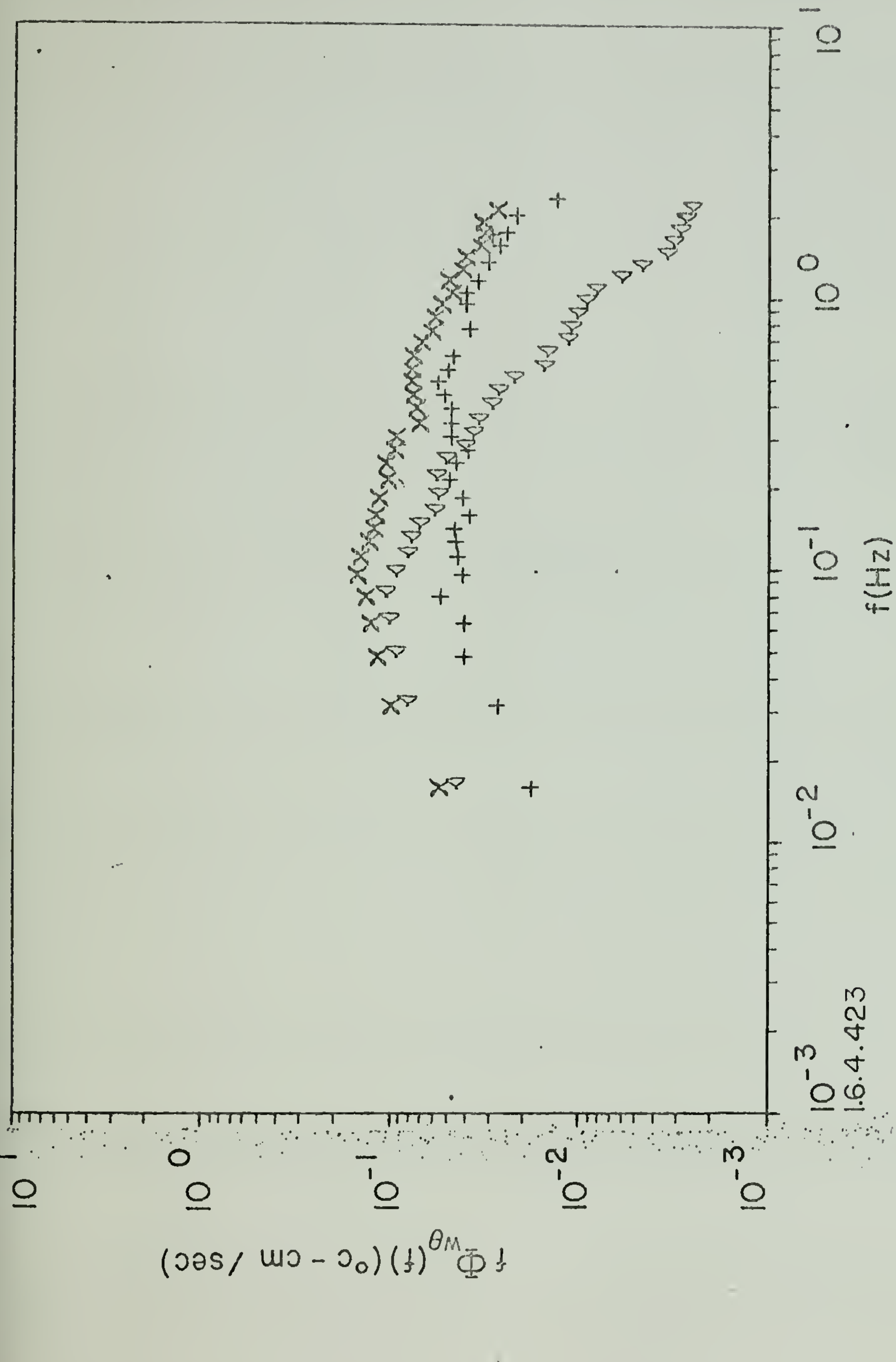
10^-3
10^-2
10^-1
10^0
10^1
f(Hz)
10^1
10^0
10^-1
10^-2
10^-3
f Φ_wθ(f) (°c - cm /sec)
1.6.4.423

FIGURE 40

MITOS I $w\theta$ cospectra plotted versus frequency

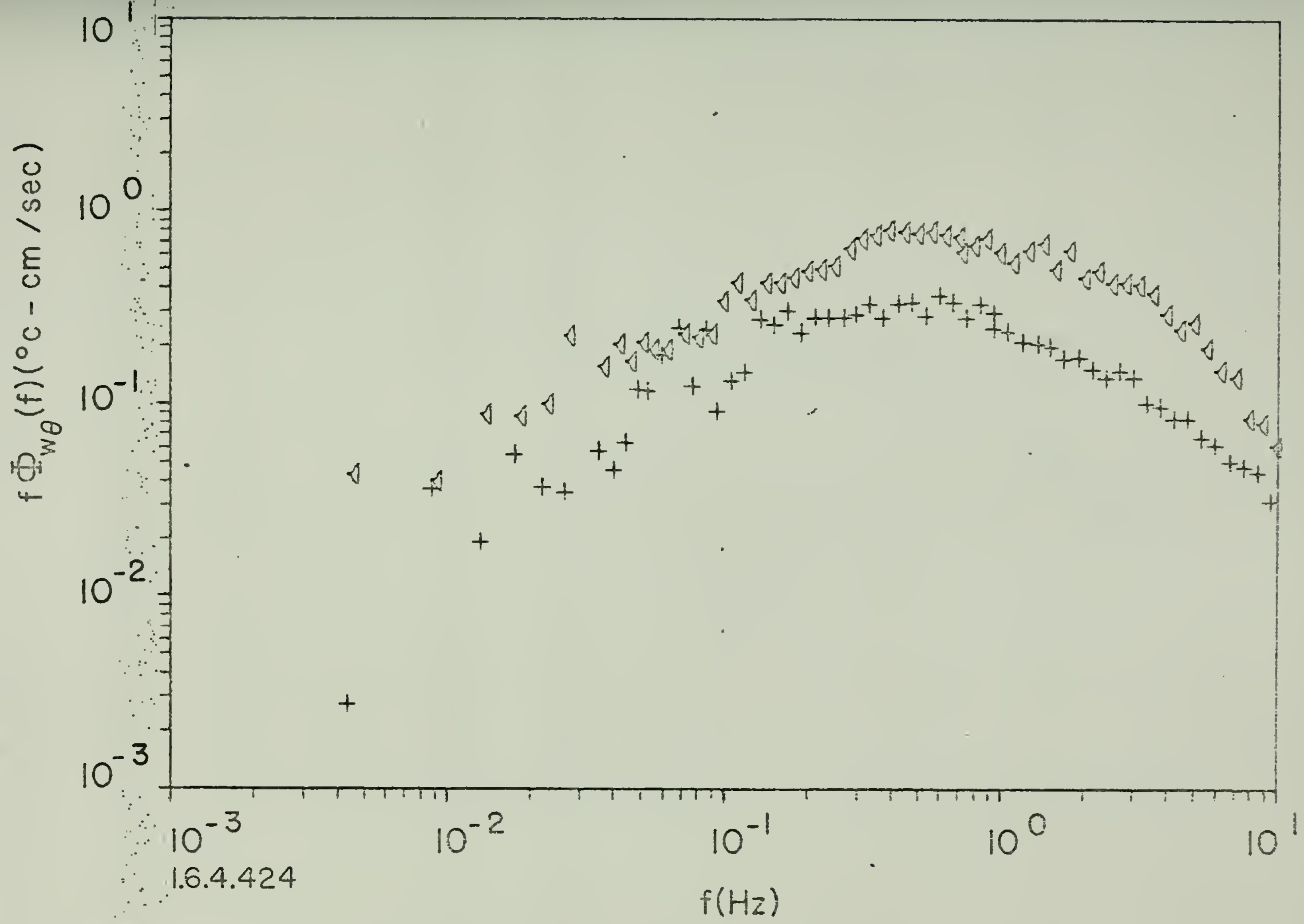
$f\Phi_{w\theta}(f)(°c - cm / sec)$
10^{1}
10^{0}
10^{-1}
10^{-2}
10^{-3}
10^{-3}
10^{-2}
10^{-1}
10^{0}
10^{1}
1.6.4.424
f(Hz)

FIGURE 41

MITOS III and OWAX $w\theta$ cospectra plotted versus frequency corrected for pitch

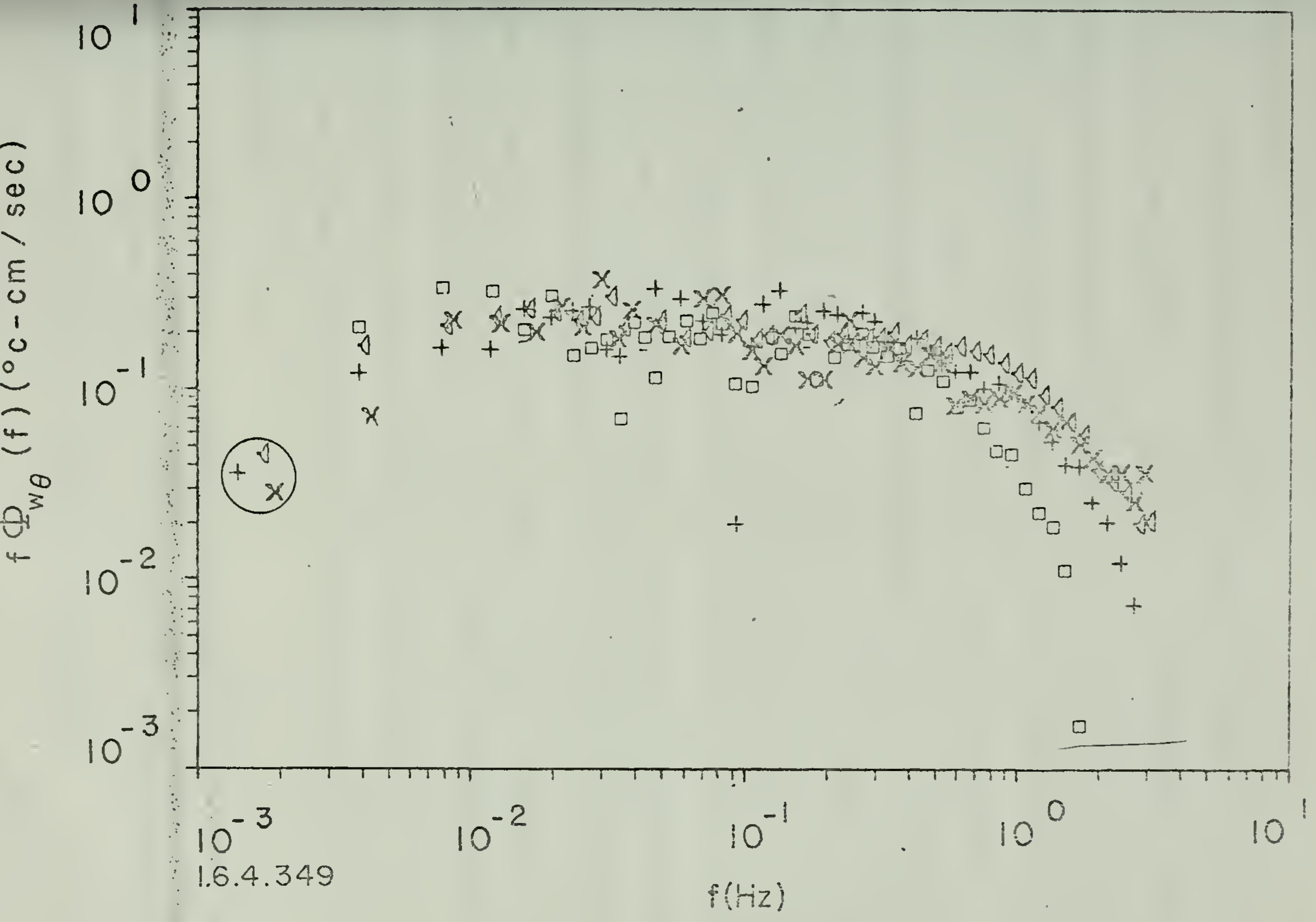
$f\,\Phi_{w\theta}(f)$ (°c-cm / sec)
10^{1}
10^{0}
10^{-1}
10^{-2}
10^{-3}
10^{-3}
10^{-2}
10^{-1}
10^{0}
10^{1}
1.6.4.349
f(Hz)

Section 4.2. For subsequent cospectral plots, those assumed points will also be circled.

Figures 42 and 43 show averaged $w\theta$ cospectra from all the cruises normalized with $u_*\theta_*$ the negative heat flux ($= -\overline{w\theta}$) plotted logarithmically and linearly vs log f_N. Differences between the MITOS I and MITOS III and OWAX data include an apparent shift of the MITOS I data to higher f_N values than the MITOS III and OWAX cospectra and a narrower peak in the MITOS I cospectra and lower cospectral levels for $f_N < 0.05$. The averaged SOMA data also exhibit a peak at $f_N \cong 0.03$, probably not real since the cospectra were not corrected for pitch effects which are most pronounced for low frequencies. The peak in the MITOS I data is probably real and is comparable to the BOMEX results of Pond et al[8] shown in figure 42 (envelope shown by hatched lines) and the results of Leavitt's[11] averaged $w\theta$ normalized cospectra shown in figure 43 (circles). An estimated average of Pond's et al[8] pre-BOMEX (San Diego) results for $w\theta$ are also shown in figure 42 and agree well with the $w\theta$ cospectra of MITOS III and OWAX

The prediction of Wyngaard and Cote'[61] for inertial subrange $w\theta$ cospectra behavior, using arguments similar to those used to obtain Eq. (50) for the uw cospectra, is written as

$$\frac{-f_N \Phi_{w\theta}(f_N)}{u_*\theta_*} = \alpha_{w\theta} H_w(z/L) f_N^{-4/3} \qquad (51)$$

FIGURE 42

Average $w\theta$ cospectra normalized with u_*T_* plotted versus normalized frequency (comparison with other results)

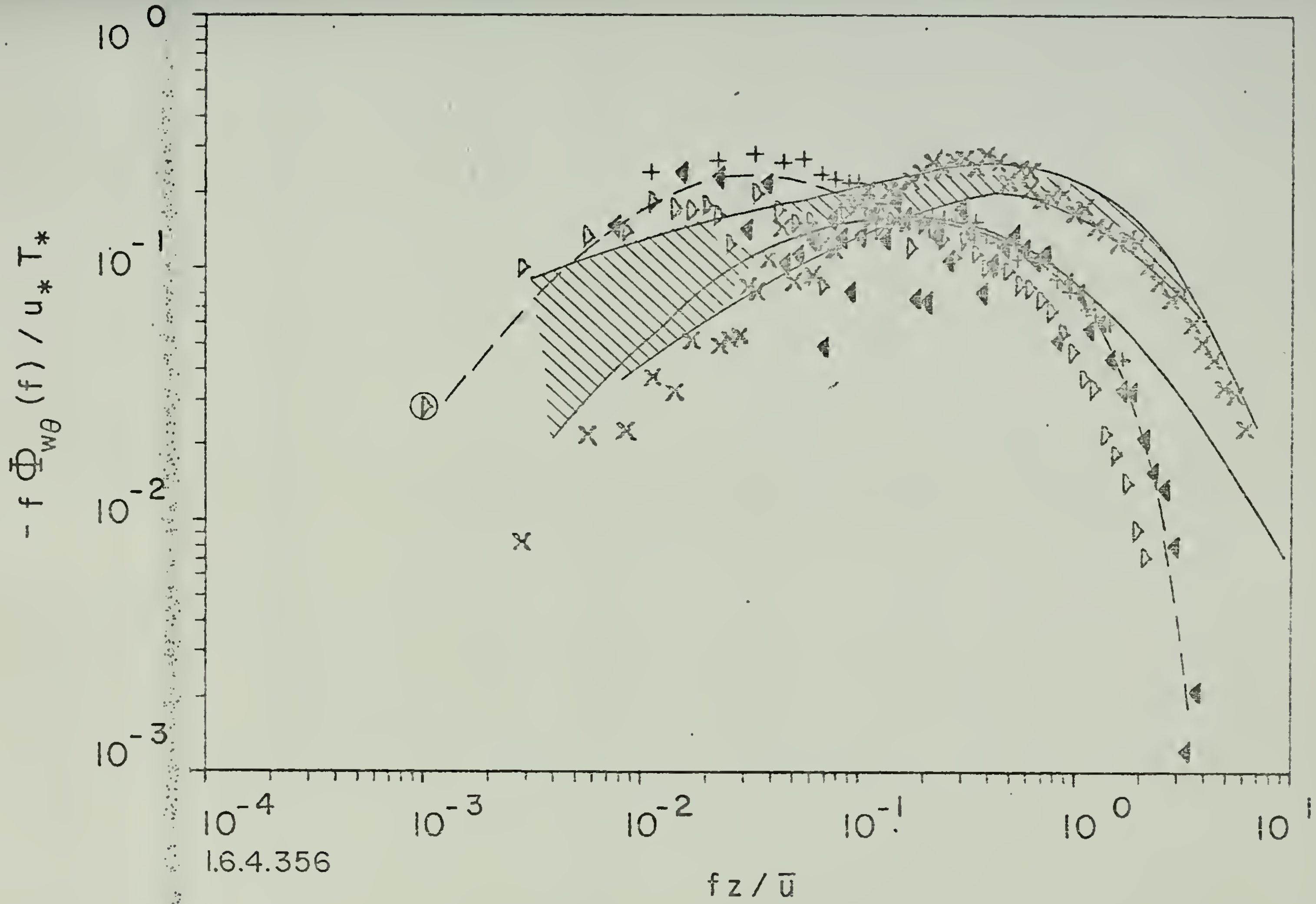
- f $\Phi_{w\theta}$ (f) / u_* T_*
10^0
10^{-1}
10^{-2}
10^{-3}
10^{-4}
10^{-3}
10^{-2}
10^{-1}
10^0
10^1
fz / $\bar{u}$
1.6.4.356

FIGURE 43

Average $w\theta$ cospectra normalized with u_*T_* plotted linearly versus normalized frequency (comparison with other results)

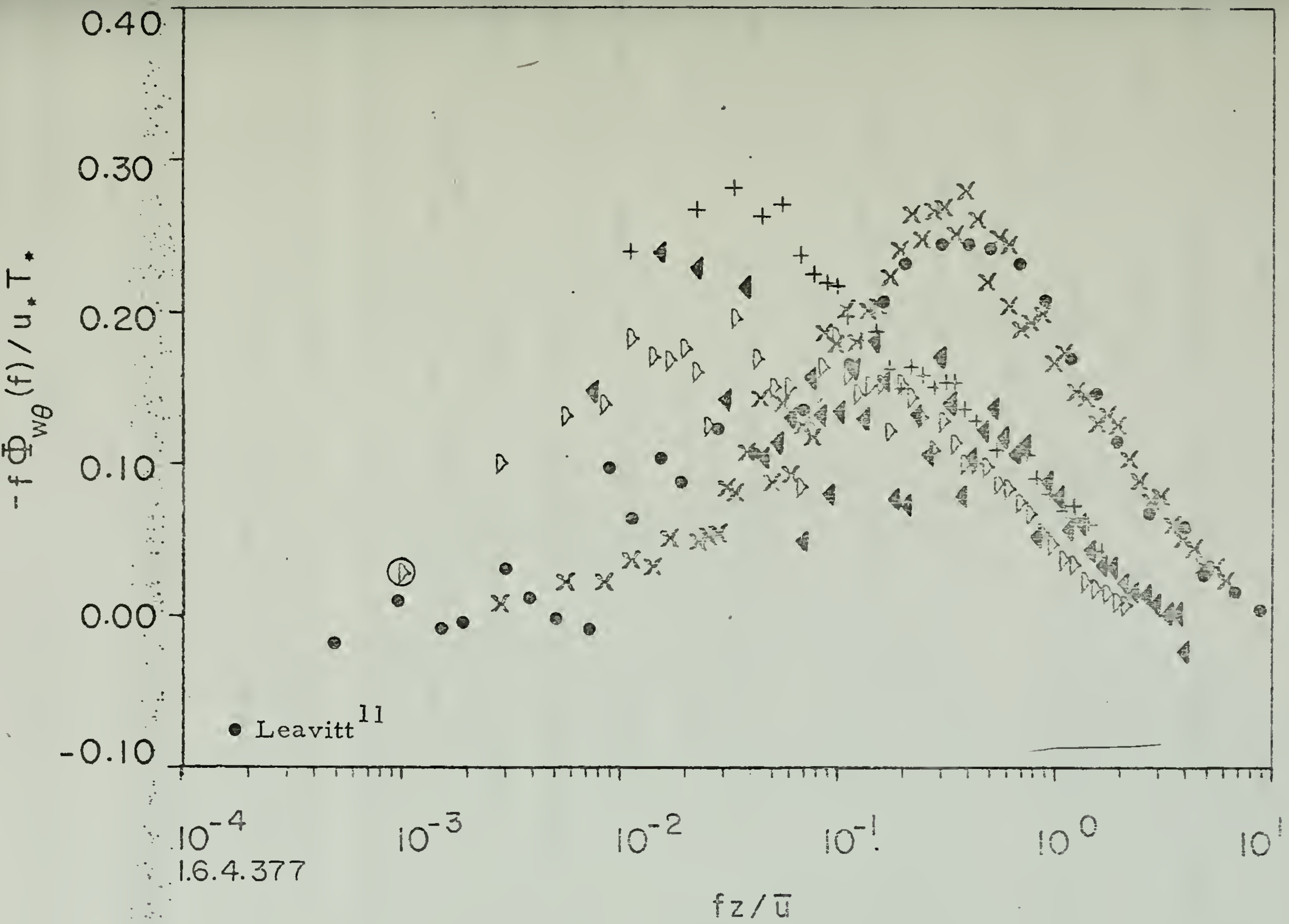
$-f\Phi_{w\theta}(f)/u_*T_*$
0.40
0.30
0.20
0.10
0.00
-0.10
● Leavitt[11]
10^{-4}
10^{-3}
10^{-2}
10^{-1}
10^{0}
10^{1}
1.6.4.377
$fz/\overline{u}$

where $H_w(z/L) = 1.0$ for $-2 \leq z/L \leq 0$, and the constant $\alpha_{w\theta} = 0.14$ from results of Kaimal et al.[56] The $w\theta$ cospectra curve suggested by Kaimal et al[57] is shown (dark line) in figure 42, with the divergence in the predicted curve for $f_N < 2$ representing the variation of low frequency shapes for different unstable conditions; the lower line is for $z/L = 0$ and the upper line is for $z/L = -2$.

The cospectra of MITOS I exhibit a $f_N^{-4/3}$ behavior for $f_N > 2$, with $\alpha_{w\theta} = 0.29 \pm 0.04$, larger than the $\alpha_{w\theta}$ of Kaimal et al[56] by a factor of 2, but comparable to Leavitt's[11] result of $\alpha_{w\theta} = 0.30 \pm 0.08$. The low frequency cospectral points of the MITOS I data for $0.012 < f_N < 0.03$ are lower than those of Leavitt[11] since no pitch correction was applied to the MITOS I data. This difference in the cospectra may also be due to uncertainties in the low frequency cospectral estimates of spectra from this work and Leavitt's[11] cospectra.

The MITOS III and OWAX pitch corrected $w\theta$ cospectra agree well with predicted curve of Kaimal et al[56] for Kansas data and the San Diego results of Pond et al,[8] except at higher frequencies, where there is evidence of spatial averaging effects and possible high frequency noise effects above $f_N = 1.3$ for the MITOS III data, and above $f_N = 0.3$ for the OWAX data. Contributions to the $w\theta$ covariance are not greatly affected by the falloff, illustrated by plotting the normalized cospectra linearly vs $\log f_N$ in figure 43.

The MITOS III value of $\alpha_{w\theta} = 0.06 \pm 0.02$ also indicates that the high frequency cospectral levels are low when compared to the results of Kaimal et al.[56] The $w\theta$ cospectral levels are higher than the uw cospectra for $f_N > 0.2$, and lower than the uw cospectral levels for $f_N < 0.2$. This is particularly true for the MITOS I $w\theta$ cospectra when compared to the predicted uw cospectra of Kaimal et al[56] and the MITOS III and OWAX cospectra. Assuming $\alpha_{uw} = 0.05$, the vertical transport of heat is 6 times more efficient than momentum for MITOS I and only slightly more efficient for the MITOS III data for smaller eddies $(f_N > 1)$. The difference in cospectral shapes between the MITOS I $w\theta$ cospectra and the predicted and calculated uw cospectra implies that the vertical transport of heat for MITOS I conditions is much less efficient than the transport of momentum for larger eddies $(f_N < 1.0)$. The difference in the MITOS III and OWAX $w\theta$ cospectra and uw cospectra at low frequencies is not as pronounced as the MITOS I $w\theta$ cospectra.

wq Cospectra

Cospectra of water vapor flux (wq) in absolute units for the four cruises are shown in figures 44-SOMA, 45-MITOS I, and 46-MITOS III and OWAX. The wq cospectra from all the cruises have similar shapes and exhibit a broad peak over the frequency range $0.01 < f < 0.3$ Hz, the same interval as the peak in the MITOS III and OWAX $w\theta$ cospectra, and broader than the peak of the uw

FIGURE 44

SOMA water vapor flux (wq) cospectra plotted versus frequency

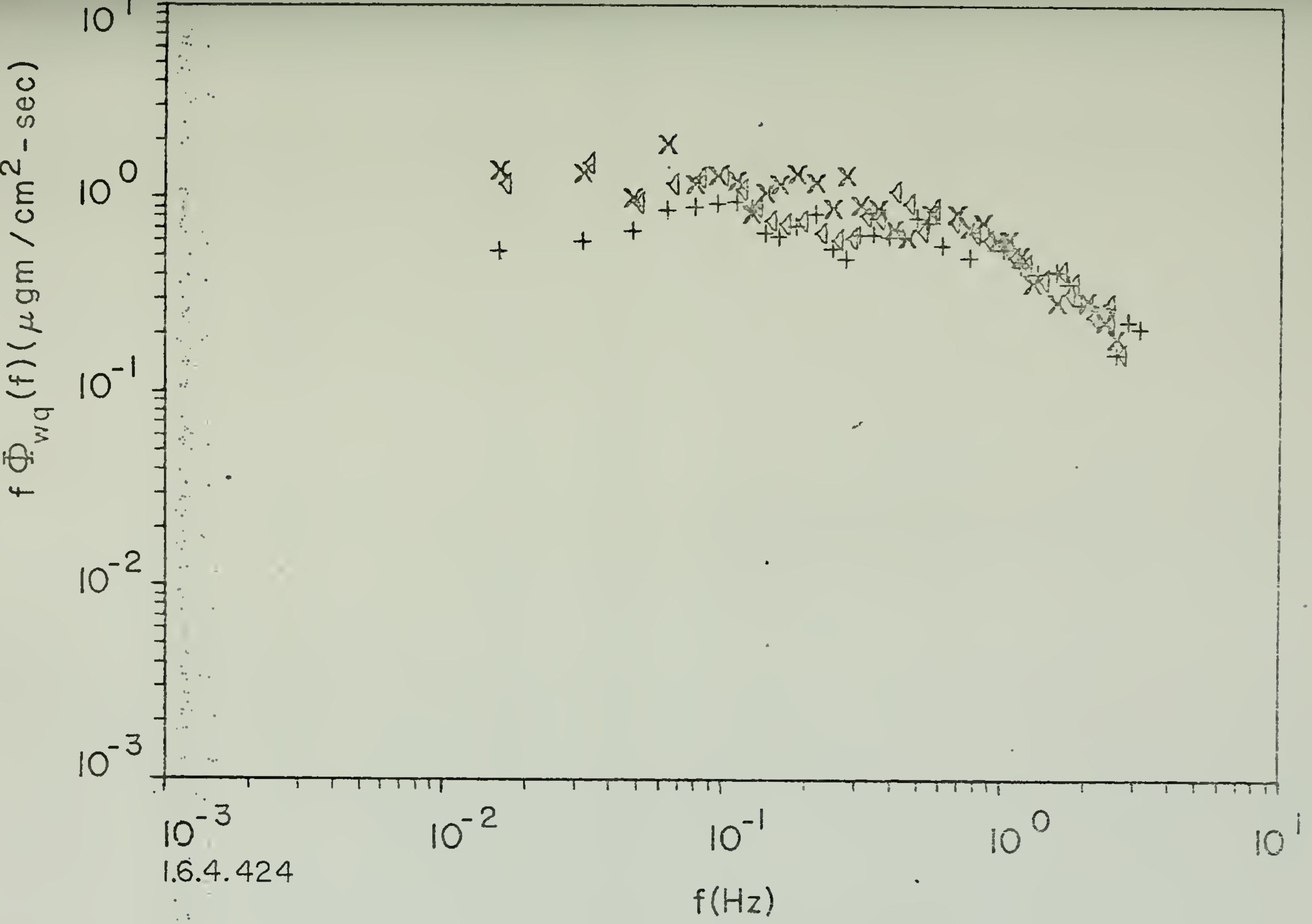
$f\,\Phi_{wq}(f)\,(\mu gm/cm^2\text{-}sec)$
10^1
10^0
10^{-1}
10^{-2}
10^{-3}
10^{-3}
10^{-2}
10^{-1}
10^0
10^1
1.6.4.424
f(Hz)

FIGURE 45

MITOS I wq cospectra plotted versus frequency

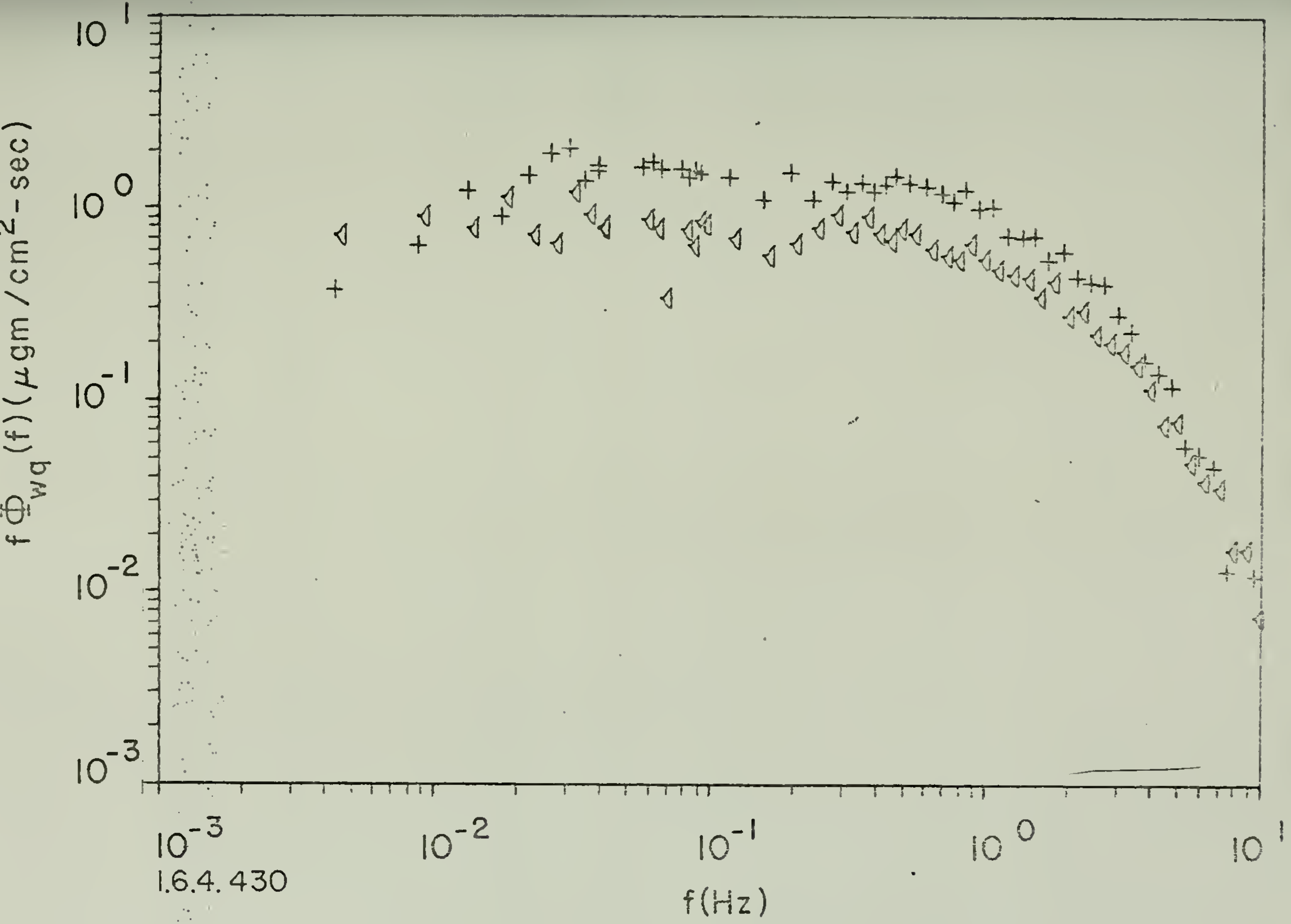
$f\Phi_{wq}(f)\,(\mu gm/cm^2\text{-}sec)$
10^1
10^0
10^{-1}
10^{-2}
10^{-3}
10^{-3}
10^{-2}
10^{-1}
10^0
10^1
1.6.4.430
f(Hz)

FIGURE 46

MITOS III and OWAX wq cospectra plotted versus frequency (corrected for pitch)

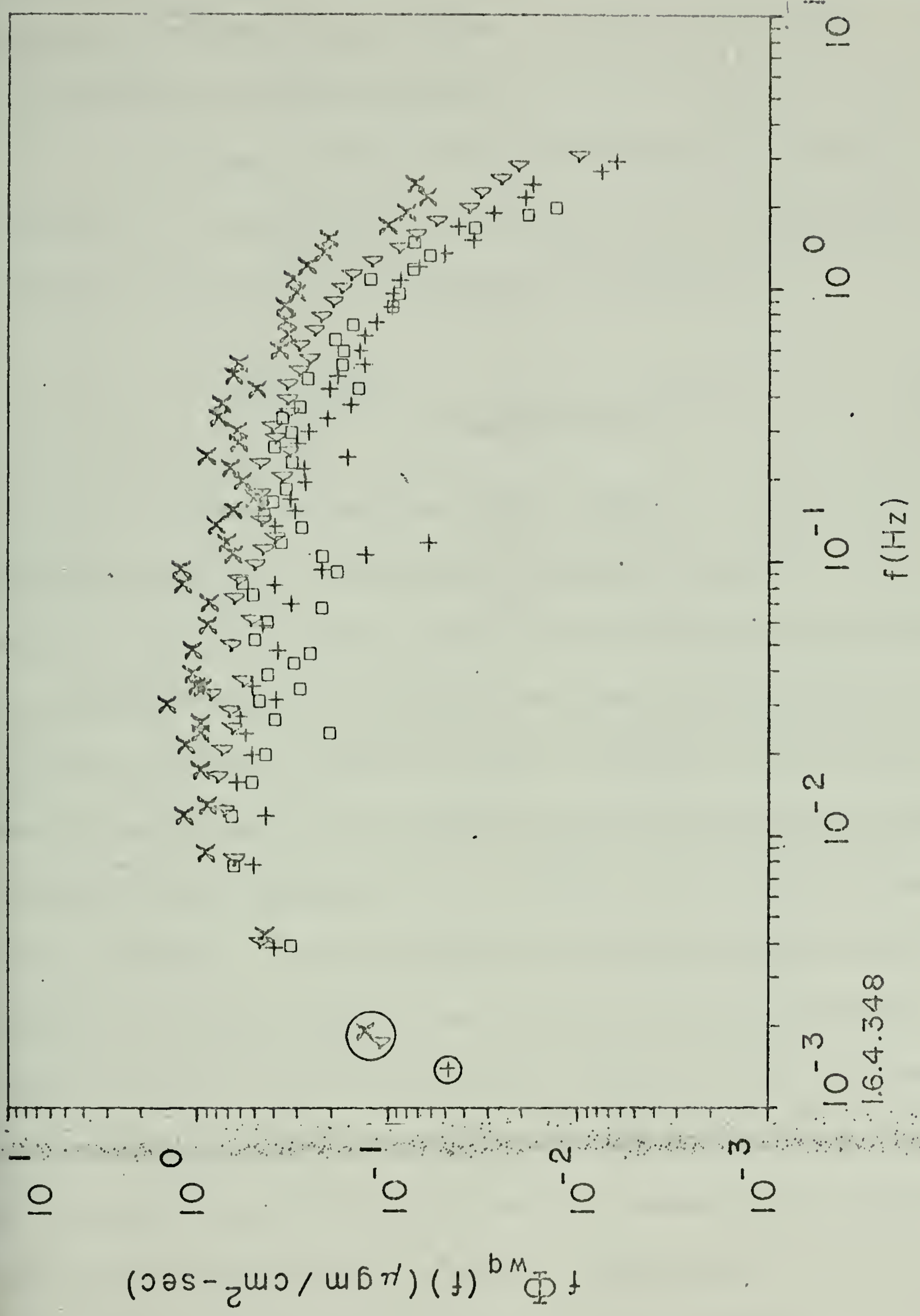
$f\Phi_{wq}(f)$ (μgm / cm^2-sec)
10^1
10^0
10^{-1}
10^{-2}
10^{-3}
f(Hz)
10^{-3}
10^{-2}
10^{-1}
10^0
10^1
16.4.348

cospectra. There is evidence of wave induced FLIP motion in the wq cospectra, with low cospectral points occurring at $f \simeq 0.1$ Hz (corrected for prior to integration).

The expression for the inertial subrange form of the normalized wq cospectrum derived using the same procedures as were done for the uw and $w\theta$ cospectra is written as

$$\frac{-f_N \Phi_{wq}(f_N)}{u_* q_*} = \alpha_{wq} M_w(z/L)\, f_N^{-4/3} \quad . \qquad (52)$$

where it is assumed the function $M_w(z/L) \simeq H_w(z/L) \simeq 1$ for unstable conditions, and α_{wq} is the cospectral·subrange constant. This expression was also used by Leavitt[11] for presentation of normalized wq cospectral results. Normalized wq cospectra from all the cruises are shown in figures 47 and 48 plotted as $\log f\,\Phi_{wq}(f)$ versus $\log f_N$ and linearly versus $\log f_N$; the negative sign in the normalized cospectra results from the definition of q_* , so that $u_* q_* = -\overline{wq}$, the negative water vapor flux. The normalized wq cospectra collapse with the exception of the high frequency end of the OWAX wq cospectrum. Reasons for this behavior of the OWAX cospectrum have been proposed in the previous section. It should be noted that the high frequency end of the MITOS III and MITOS I cospectra are similar, indicating that only the OWAX cospectra are affected by high frequency noise or sensor separation errors. The subrange constant determined from the data

FIGURE 47

Average wq cospectra normalized with $u_* q_*$ plotted versus normalized frequency (comparison with other results)

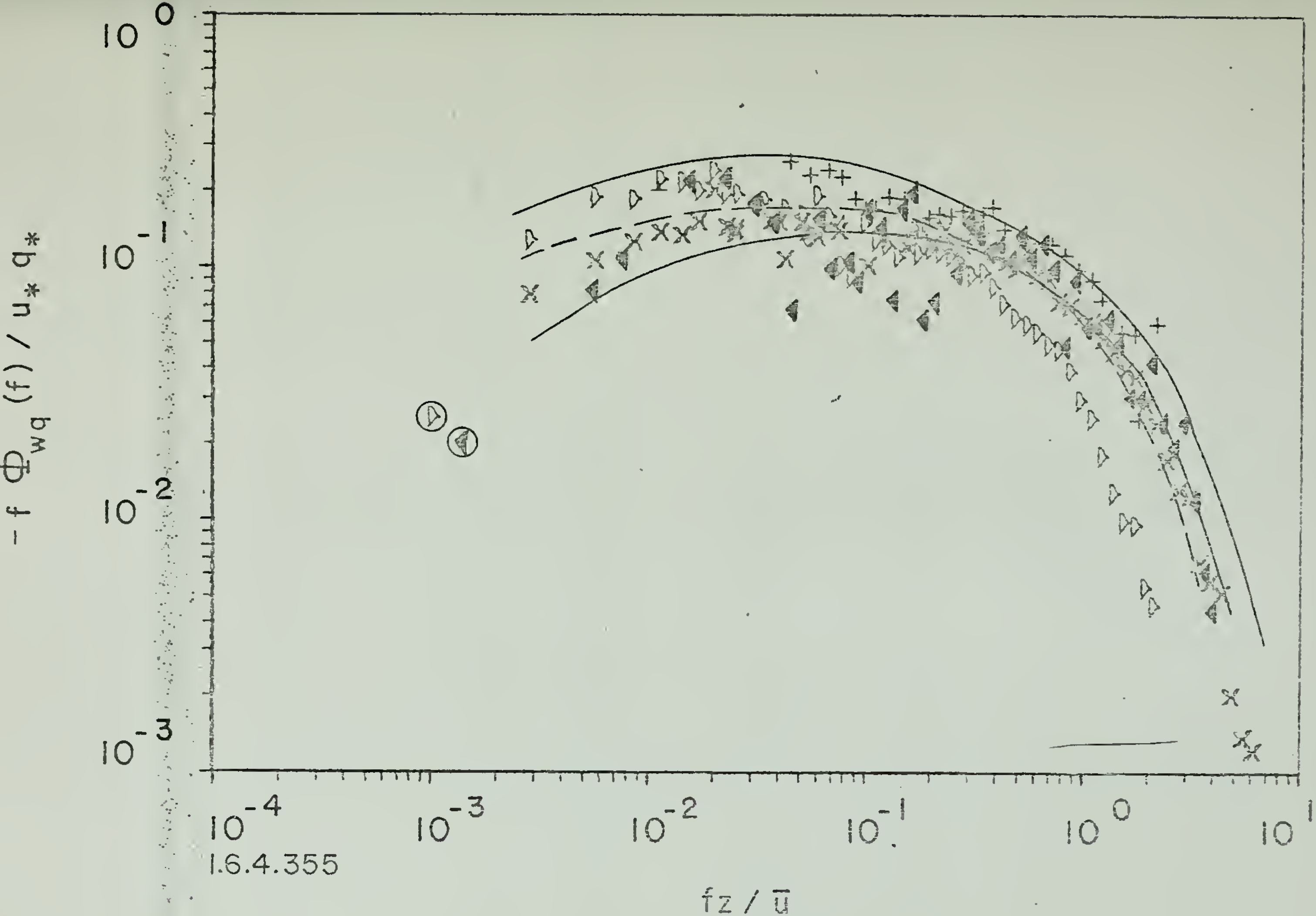
10^0
10^-1
10^-2
10^-3
- f Φ_wq (f) / u_* q_*
10^-4
10^-3
10^-2
10^-1
10^0
10^1
1.6.4.355
fz / ū

FIGURE 48

Average wq cospectra normalized with u_*q_* plotted linearly versus normalized frequency (comparison with other results)

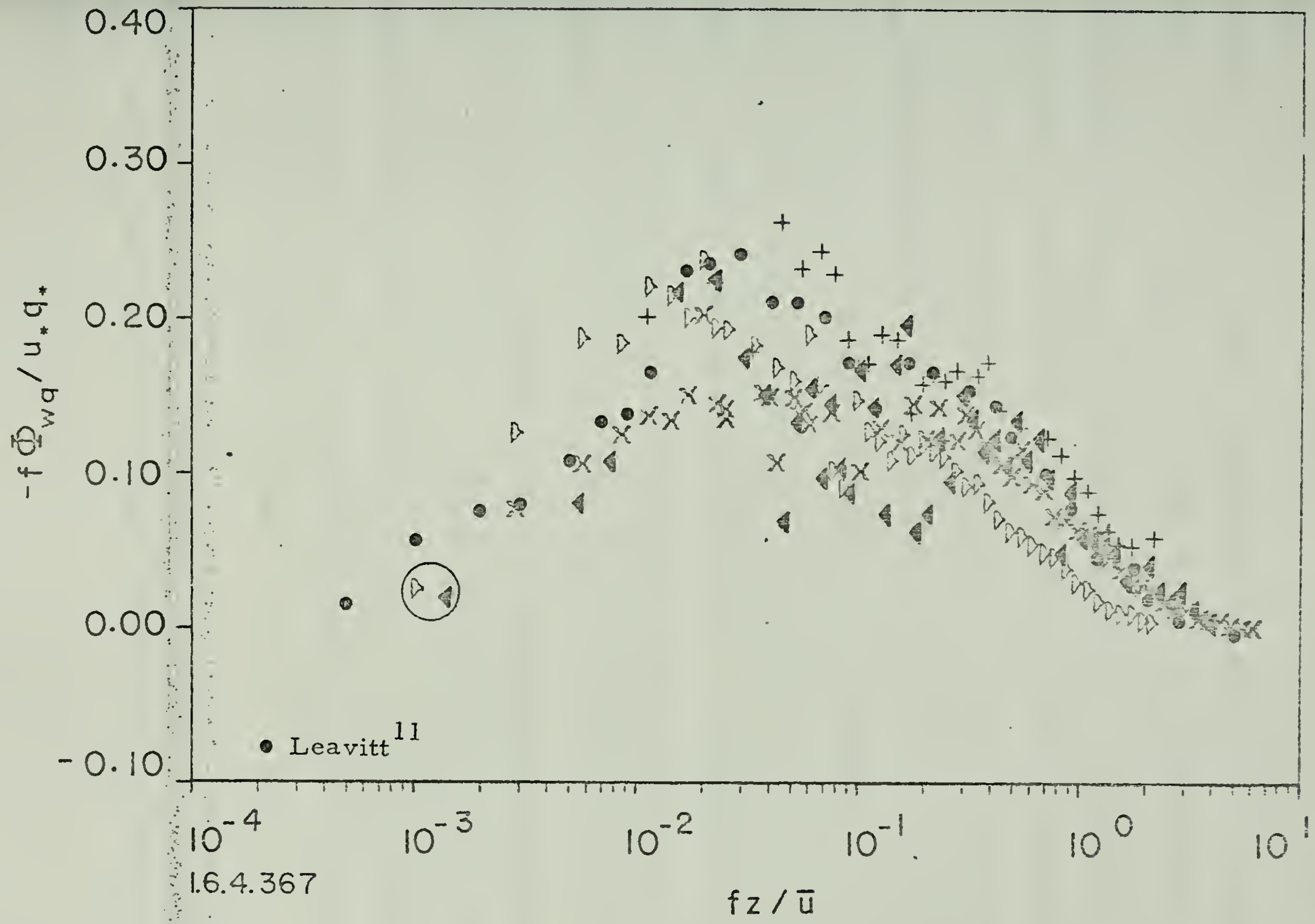
0.40
0.30
0.20
0.10
0.00
-0.10
$-f\Phi_{wq}/u_*q_*$
● Leavitt[11]
10^{-4}
10^{-3}
10^{-2}
10^{-1}
10^{0}
10^{1}
$fz/\overline{u}$
1.6.4.367

(excluding OWAX) is $\alpha_{wq} = 0.08 \pm 0.02$. This value of α_{wq} is higher than $\alpha_{uw} = 0.01$ obtained from the MITOS III and OWAX uw cospectra, and $\alpha_{uw} = 0.048$ suggested by Kaimal et al.[56] Leavitt[11] obtains a value of $\alpha_{wq} = 0.11 \pm 0.02$, higher but not significantly different from the α_{wq} for this work. Leavitt's[11] wq cospectra also exhibit a sharp fall-off at $f_N \simeq 1$ for 8 m data so that the values of α_{wq} may be slightly underestimated, but are much lower than the $\alpha_{w\theta}$ values for MITOS I (0.29) and BOMEX (0.30).

The wq cospectra of Pond et al[8] for BOMEX and San Diego data are shown in figure 47; Leavitt's[11] average wq cospectrum from BOMEX results is shown in figure 48 (circles). No attempt was made to average the BOMEX results presented by Pond et al,[8] and the cospectra are represented by the envelope of the two unbroken curves in figure 47. The pre-BOMEX results are approximated by the dashed curve of figure 47. All the normalized wq cospectra agree, with the exception of the OWAX cospectra for $f_N > 0.3$. All the cospectra may be somewhat underestimated at high frequencies $(f_N > 2)$ because of noise effects and instrument response.

Following the results of Leavitt,[11] the cospectral constants $\alpha_{w\theta}$ and α_{wq} are related to the spectral constants β_θ and β_q by the equation

$$\frac{\beta_\theta}{\beta_q} \simeq [\alpha_{w\theta}/\alpha_{wq}]^2 \qquad (53)$$

if it assumed that $H(z/L) = M(z/L)$ and $\Phi_H = \Phi_E$. Using the values from the MITOS I results, $\alpha_{w\theta}/\alpha_{wq} = 3.6$, implies $\beta_\theta \simeq 13\ \beta_q$. Leavitt's[11] result for $\alpha_{w\theta}/\alpha_{wq} = 2.7$ implies that $\beta_\theta = 7.3\ \beta_q$. The high frequency fall-offs of the $w\theta$ and wq cospectra make this relationship between β_θ and β_q somewhat uncertain. A more sensitive test of the relationship between the scalar spectral constants will be made in Section 4.7.

The $w\theta$ and wq normalized cospectra are not significantly different with the exception of the MITOS I cospectra. The MITOS I data suggest that under certain conditions heat is transported vertically more efficiently than water vapor at smaller scales, and less efficiently than water vapor at larger scales. The crossover point at $f_N \simeq 0.1$ corresponds to a scale size of 42 meters using an average height of 42 meters for the MITOS I cruise.

The α_{wq} values indicate that the vertical transport of water vapor is relatively more efficient than the transport of momentum for smaller scales $(f_N > 0.2)$, although the difference is not as pronounced as the vertical transport of heat and momentum.

If the high frequency behavior $(0.2 < f_N < 2.0)$ of the OWAX $w\theta$ and wq cospectra is real, it suggests that the production of temperature and humidity variance occurs at larger scales for colder, less humid conditions, than for the warm humid conditions of MITOS I and BOMEX.

4.6c Cospectra of horizontal heat and water vapor flux ($u\theta$, uq)

The dimensional $u\theta$ cospectra from the MITOS I and MITOS III and OWAX cruises are shown in figures 49 and 50. Corresponding dimensional uq cospectra are shown in figures 51 and 52. The MITOS III and OWAX $u\theta$ cospectra and the uq cospectra from all runs exhibit a broad peak in the frequency interval $0.01 < f < 0.1$ Hz and have similar shapes. The MITOS I $u\theta$ cospectra have a different shape than the other cospectra and exhibit a peak in the frequency interval $0.1 < f < 0.4$ Hz for the MITOS I-1 run, and between $0.2 < f < 0.7$ Hz for the MITOS I-7 run. The $u\theta$ and uq cospectra have not been extended to 0.001 Hz since the low frequency behavior of the cospectra is not established over the ocean, and few measurements of horizontal heat and water vapor flux cospectra have been made. The $u\theta$ and uq cospectra presented by Pond and Phelps[19] and the Kansas results of Kaimal et al[56] for $u\theta$ are referred to in this section for comparison of results.

Average $u\theta$ and uq cospectra from the three cruises have been normalized with $u_* \theta_*$, and $u_* q_*$ and plotted as $\log f \Phi_{u\theta}(f)$ versus $\log f_N$ in figures 53 and 54, and plotted linearly versus $\log f_N$ in figures 55 and 56. The expression for the inertial subrange behavior of the normalized $u\theta$ cospectrum following the prediction of

FIGURE 49

MITOS I horizontal heat flux $(u\theta)$ cospectra plotted versus frequency

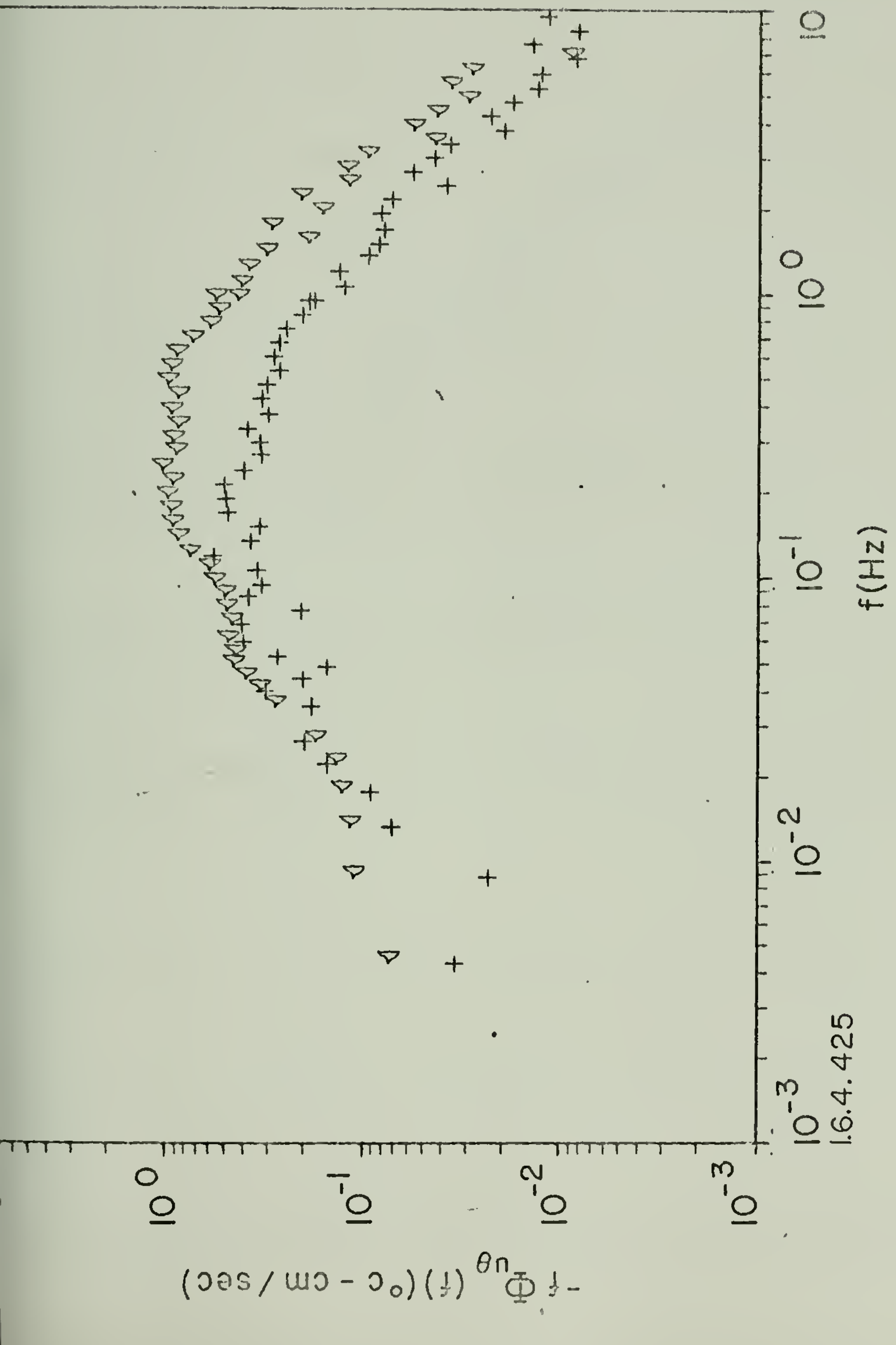
$-f\,\Phi_{u\theta}(f)$ (°C - cm / sec)
10^{0}
10^{-1}
10^{-2}
10^{-3}
10^{-3}
10^{-2}
10^{-1}
10^{0}
10^{1}
f(Hz)
16.4.425

FIGURE 50

MITOS III and OWAX $u\theta$ cospectra plotted versus frequency

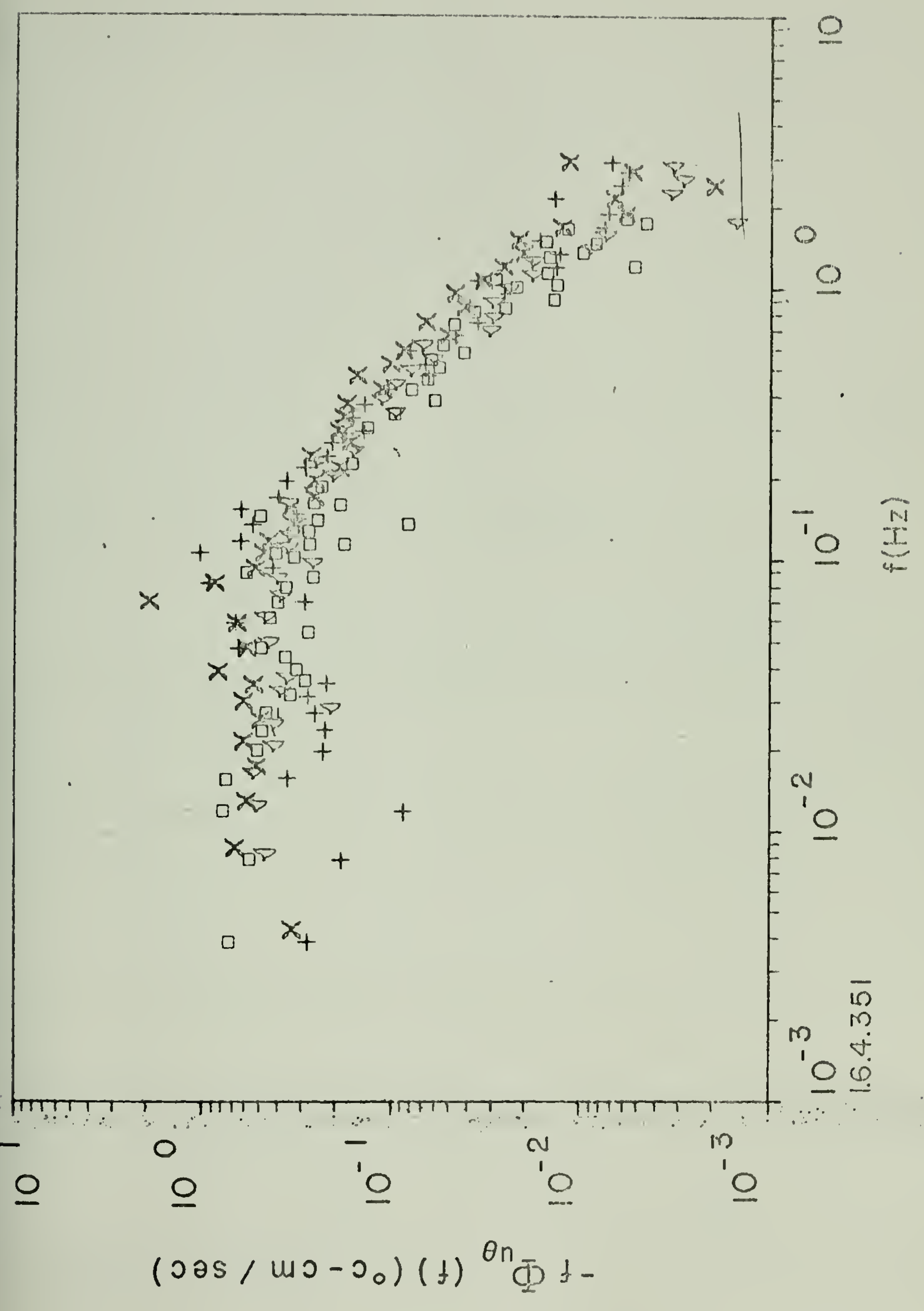
10^{-3}
10^{-2}
10^{-1}
10^{0}
10^{1}
f(Hz)
16.4.351
10^{1}
10^{0}
10^{-1}
10^{-2}
10^{-3}
$-f\ \bar{\Phi}_{u\theta}(f)$ (°c-cm / sec)

FIGURE 51

MITOS I horizontal water vapor flux (uq) cospectra plotted versus frequency

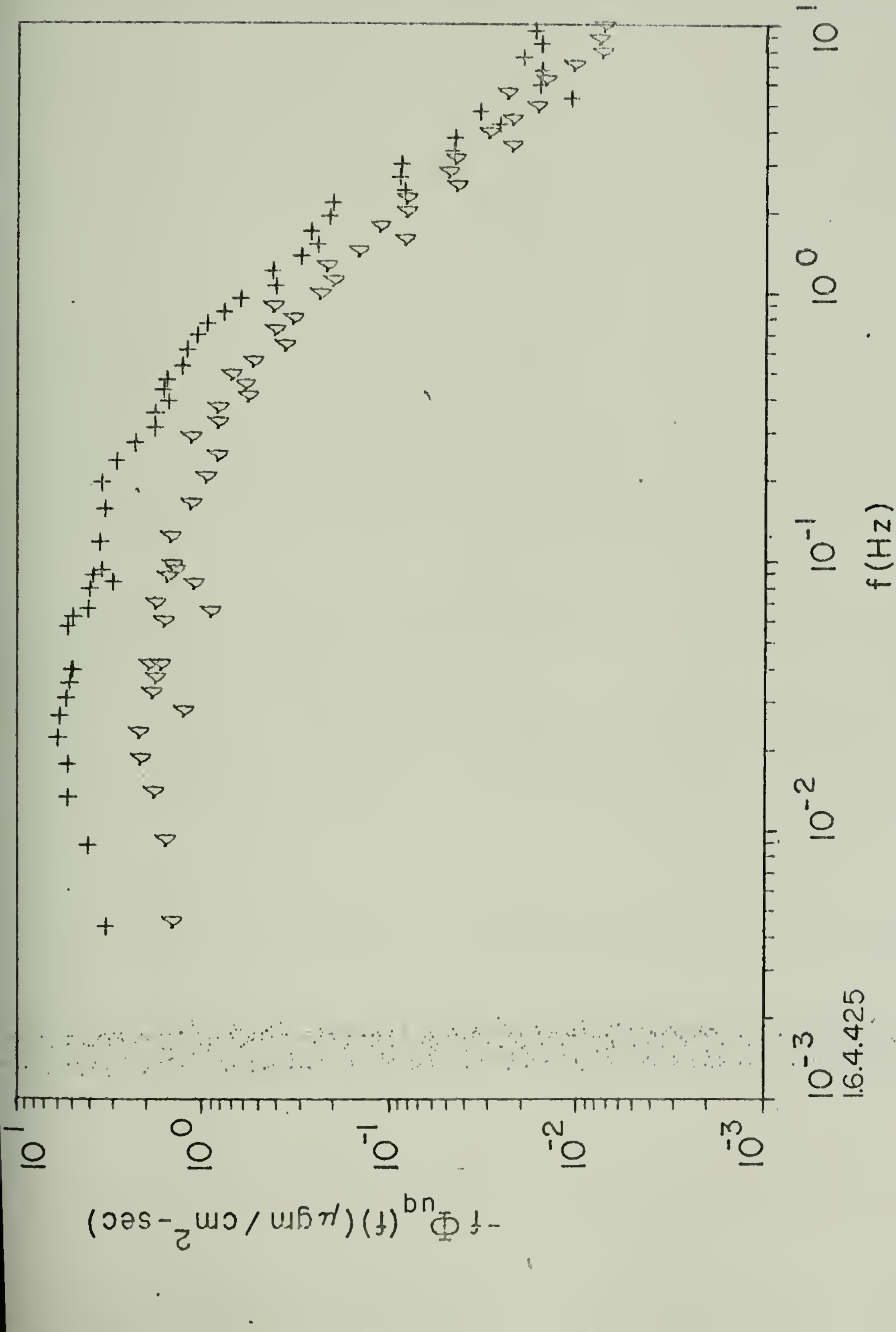
f(Hz)
10^-3
10^-2
10^-1
10^0
10^1
-f Φ_uq(f) (μgm / cm²-sec)
10^1
10^0
10^-1
10^-2
10^-3
16.4.425

FIGURE 52

MITOS III and OWAX uq cospectra plotted versus frequency

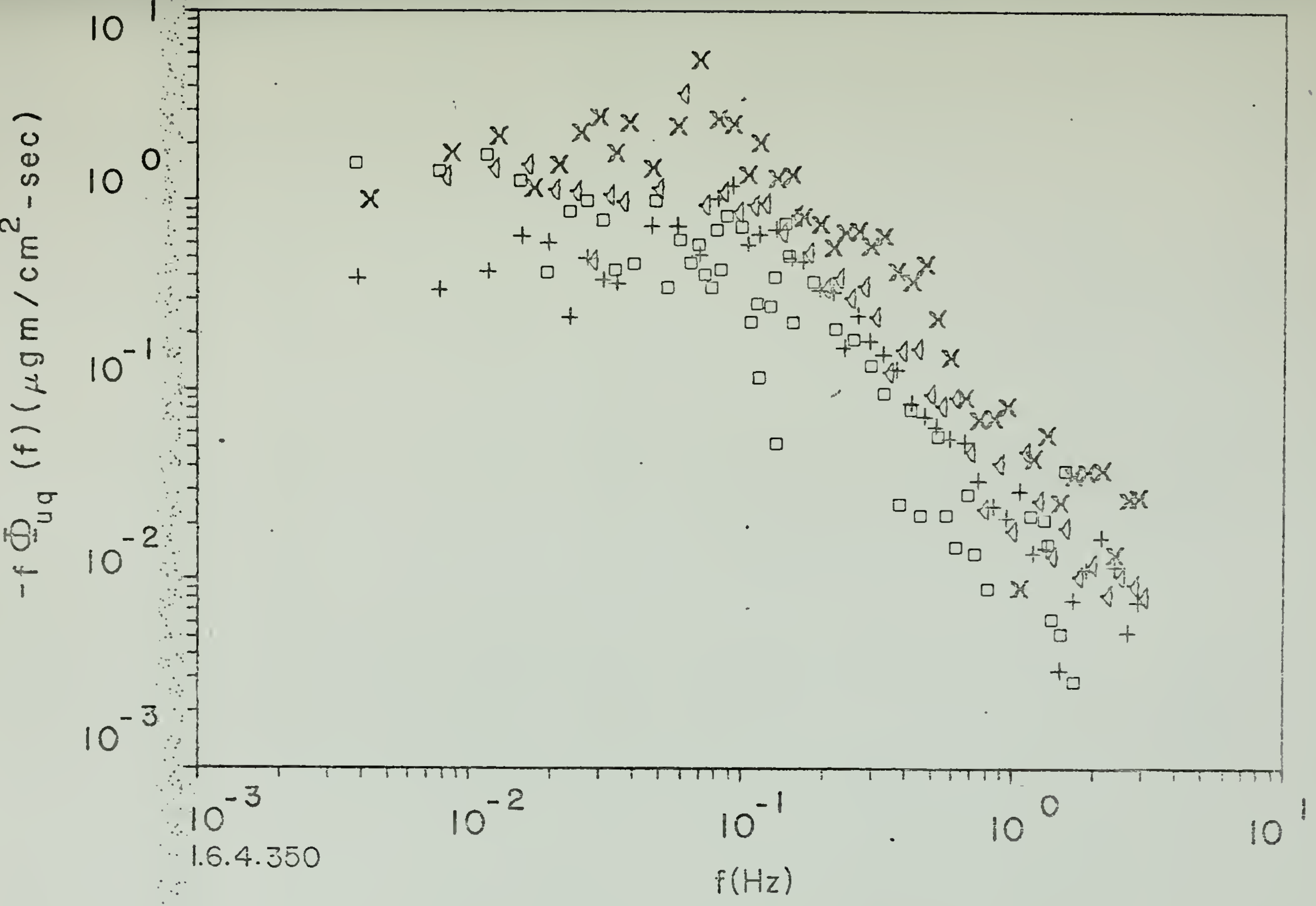
$-f\,\Phi_{uq}(f)\,(\mu gm/cm^2\text{-}sec)$
10^{1}
10^{0}
10^{-1}
10^{-2}
10^{-3}
10^{-3}
10^{-2}
10^{-1}
10^{0}
10^{1}
1.6.4.350
f(Hz)

Wyngaard and Cote'[61] is given by the expression

$$\frac{f_N \Phi_{u\theta}(f_N)}{u_* \theta_*} = \alpha_{u\theta} H_u(z/L) f_N^{-3/2} \tag{54}$$

where $H_u(z/L) = 1$ for $-2 \leq z/L \leq 0$, and $\alpha_{u\theta}$ is the cospectral subrange constant. Kaimal et al[56] suggest a value of $\alpha_{u\theta} = 0.035$. The $-3/2$ cospectral slope is not as well defined for the $u\theta$ cospectra as for the $w\theta$ cospectra. Wyngaard and Cote'[61] predict a slope of -3 for the inertial subrange of the $u\theta$ cospectra from similarity arguments. A slope of $-3/2$ appears to fit the $u\theta$ cospectral behavior at high frequencies of the three cruises and is used to calculate the $\alpha_{u\theta}$ values for comparison with Kaimal et al[56] results. The MITOS I normalized cospectrum exhibits higher cospectral levels for $f_N > 0.2$ than the MITOS III and OWAX cospectra, and lower cospectral levels than the other two cospectra for $f_N < 0.03$. The cospectra have different subrange levels, also shown by the subrange constants for each cruise: $\alpha_{u\theta} = 0.08$ (MITOS I), $\alpha_{u\theta} = 0.04$ (MITOS III), and $\alpha_{u\theta} = 0.012$, with uncertainities of $\sim 20\%$ in the estimates. The differences may in part be due to spatial averaging effects and high frequency noise, however, the differences amounting to factors of 2, extend over nearly half a decade between $0.3 < f_N < 1.3$. The normalized $u\theta$ cospectra of Phelps and Pond[10] is represented by the envelope of the hatched area in figure 53. The results of Kaimal

FIGURE 53

Average $u\theta$ cospectra normalized with $u_* T_*$ plotted versus normalized frequency (comparison with other results).

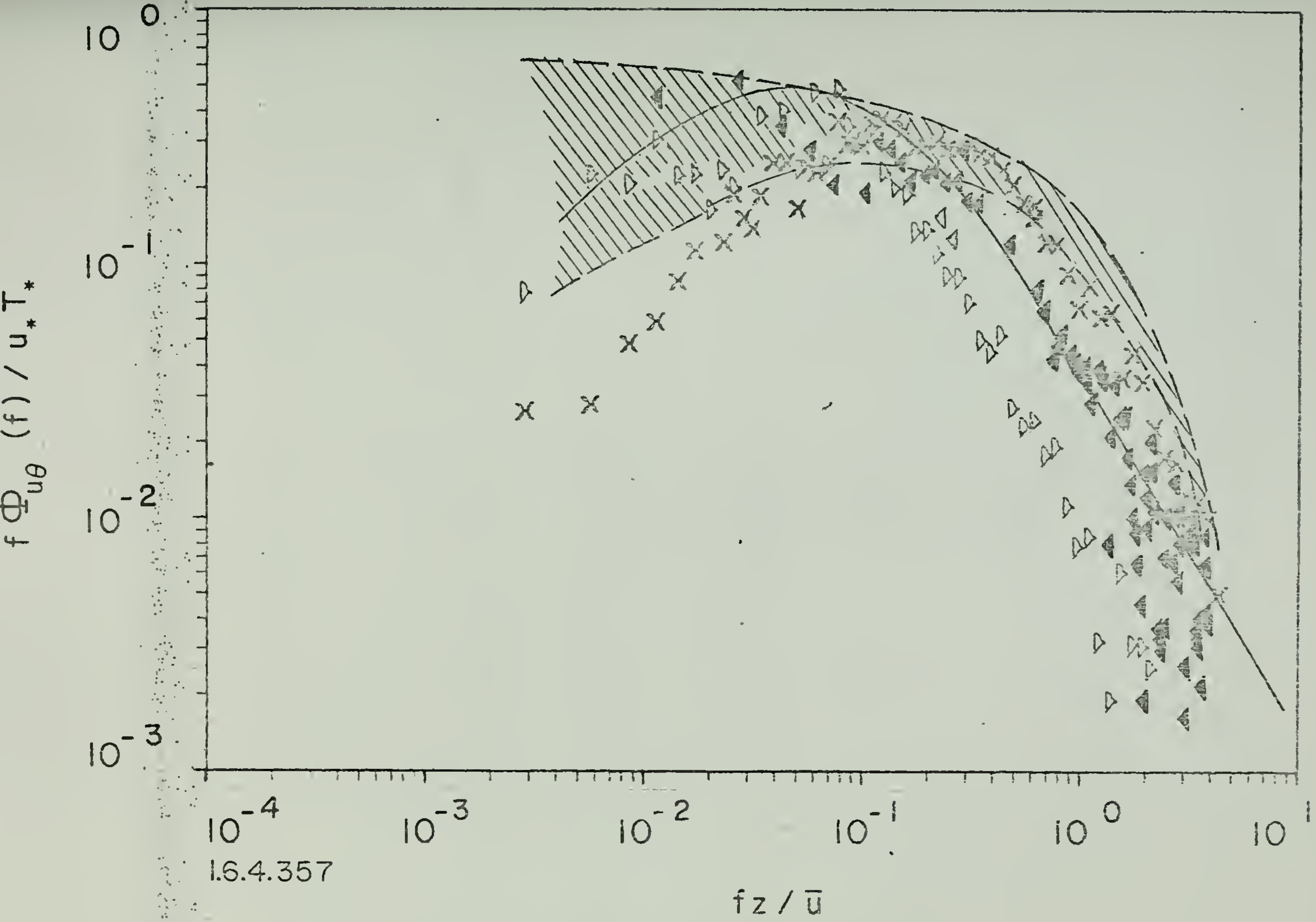
10^0
10^{-1}
10^{-2}
10^{-3}
$f\Phi_{u\theta}(f)/u_*T_*$
10^{-4}
10^{-3}
10^{-2}
10^{-1}
10^0
10^1
1.6.4.357
$fz/\overline{u}$

FIGURE 54

Average uq cospectra normalized with $u_* q_*$ plotted versus normalized frequency (comparison with other results)

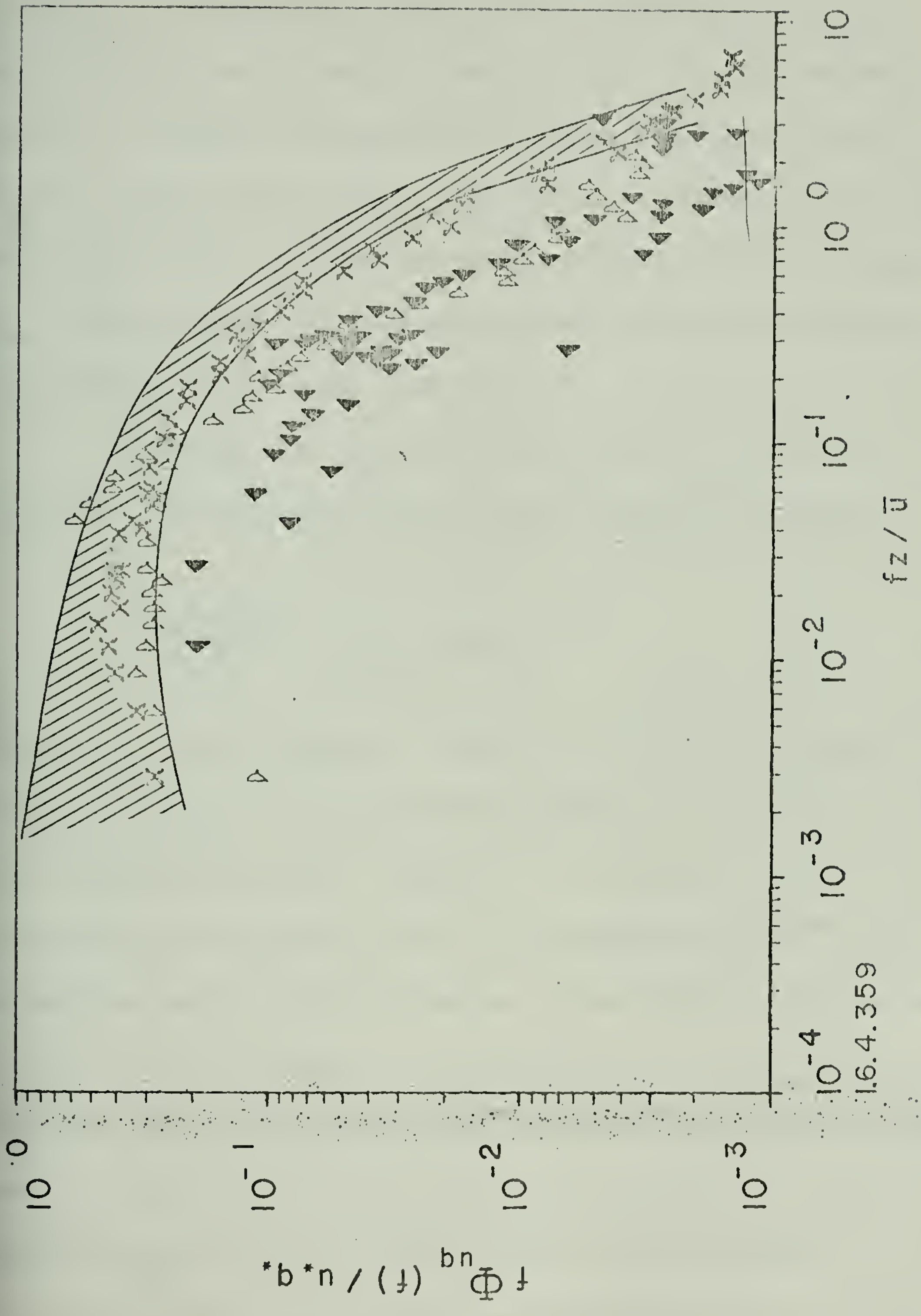
10^{0}
10^{-1}
10^{-2}
10^{-3}
$f\Phi_{uq}(f)/u_*q_*$
10^{-4}
10^{-3}
10^{-2}
10^{-1}
10^{0}
10^{1}
$fz/\overline{u}$
16.4.359

et al[56] are shown by the solid curve. The Phelps and Pond[10] cospectra are comparable to the MITOS I cospectrum for $f_N > 0.04$ and are higher than the MITOS I data for $f_N > 0.6$. The indicated value of the cospectral constant for the Phelps and Pond[10] data is $\alpha_{u\theta} \simeq 0.1$ for a slope of $-3/2$. The cospectra of Kaimal et al[56] do not significantly differ from the MITOS III cospectra. The trend in the $\alpha_{u\theta}$ values suggests relatively more efficient horizontal heat flux transport for warm humid conditions.

Assuming a similar behavior for the normalized uq cospectra, the expression for the inertial subrange is given by

$$\frac{f_N \Phi_{uq}(f_N)}{u_* q_*} = \alpha_{uq} M_u (z/L) f_N^{-3/2} \qquad (55)$$

where α_{uq} is the cospectral constant and it is assumed that the function $M_w = M_u \simeq 1$ for unstable conditions $(-2 \leq z/L \leq 0)$. The uq cospectra also appear to follow a $-3/2$ slope for $f_N > 0.3$ so the slope value is retained for Eq. (55). The Phelps and Pond[10] data is represented by the envelope of the two curves of figure 54. The uq cospectra also exhibit differences in the interval $0.3 < f_N < 1.3$ similar to the differences in the $u\theta$ cospectra. The subrange constants determined for each cruise are $\alpha_{uq} = 0.022$ (MITOS I) and $\alpha_{uq} = 0.008$ (MITOS III and OWAX) with uncertainties of 20% and 30% respectively. The constant determined from the Phelps and Pond[10]

FIGURE 55

Average $u\theta$ cospectra normalized with $u_* T_*$ plotted linearly versus normalized frequency

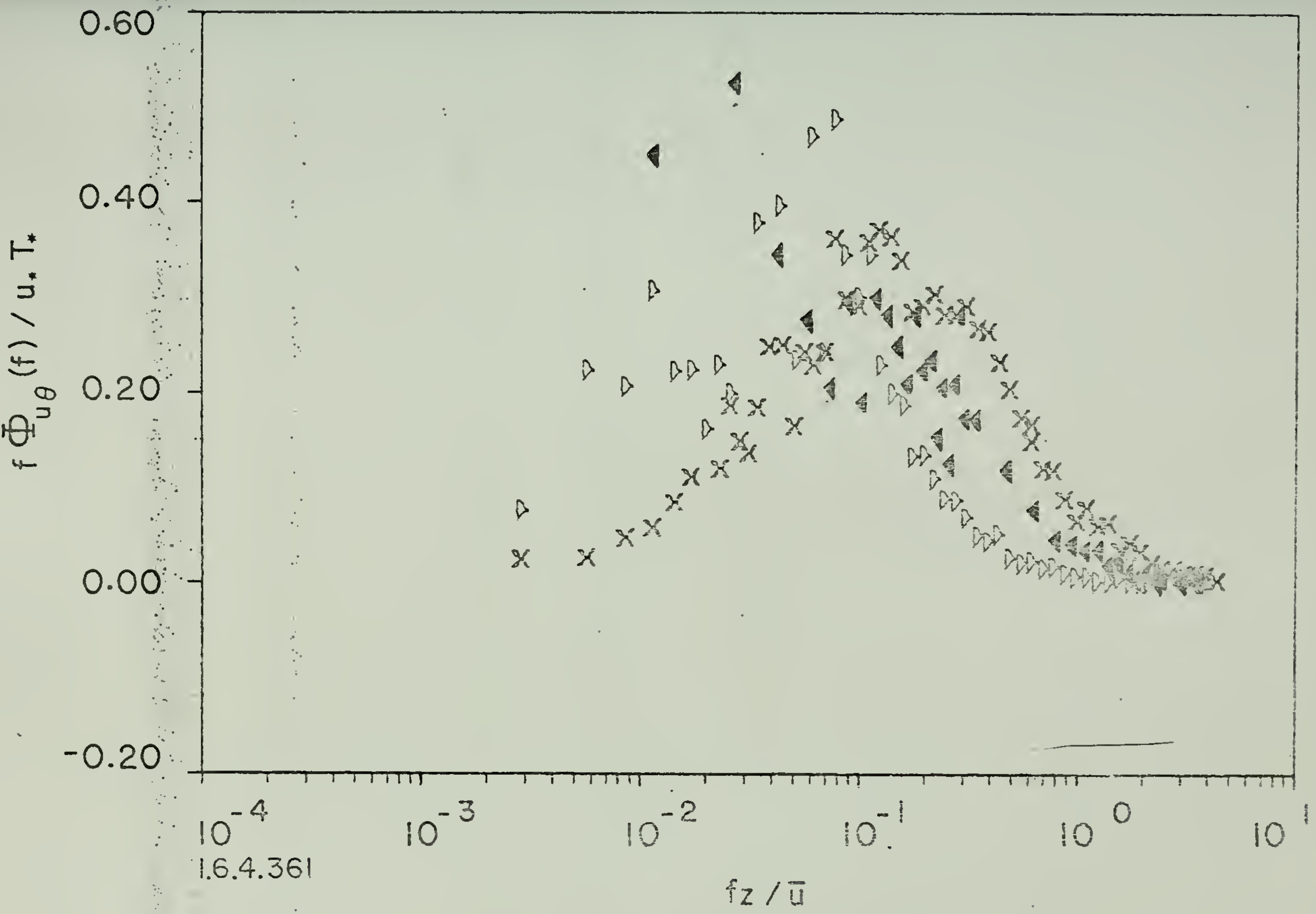
0.60
0.40
0.20
0.00
-0.20
$f\Phi_{u\theta}(f) / u_* T_*$
10^{-4}
10^{-3}
10^{-2}
10^{-1}
10^{0}
10^{1}
1.6.4.361
$fz / \overline{u}$

FIGURE 56

Average uq cospectra normalized with $u_* q_*$ plotted linearly versus normalized frequency

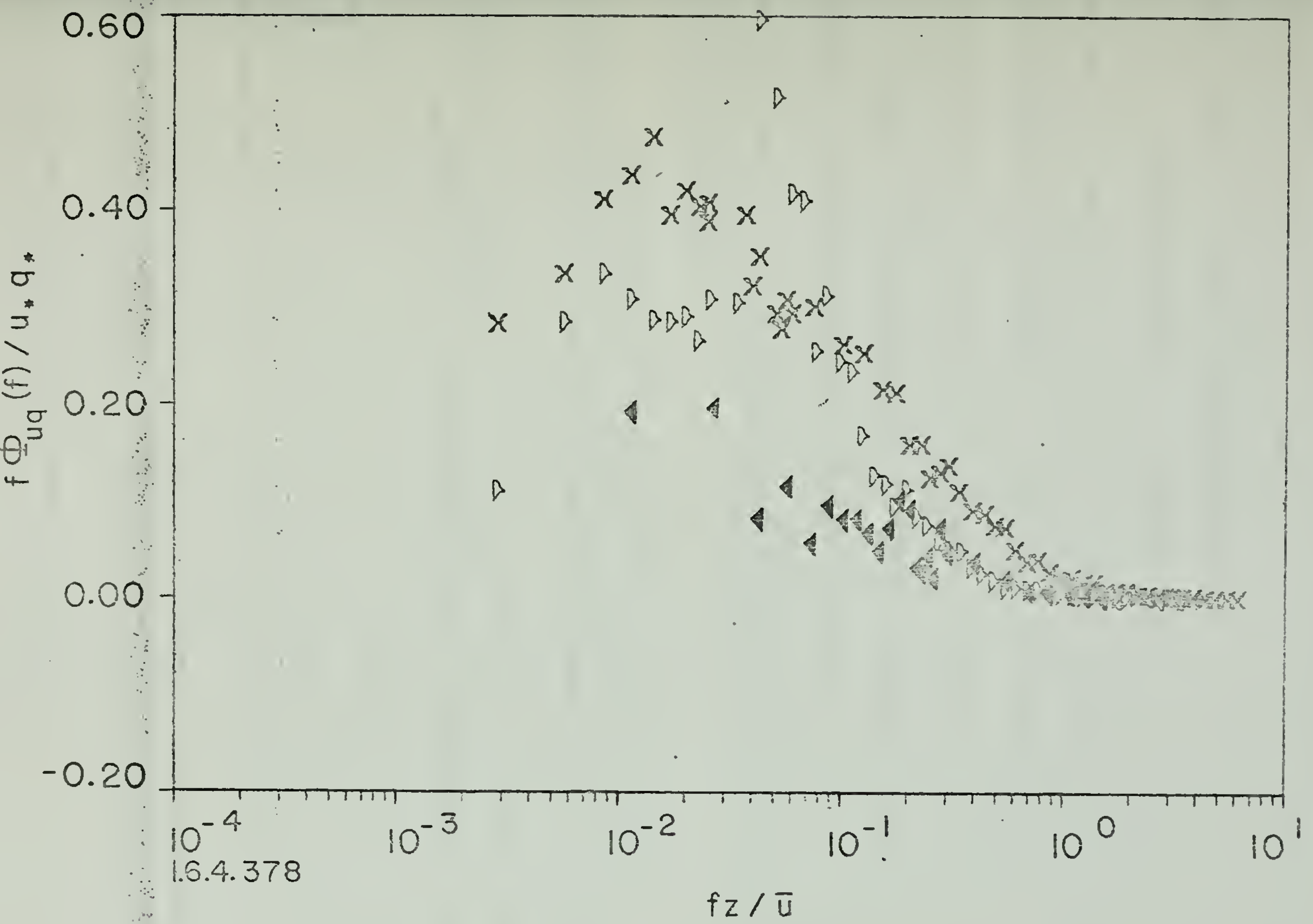
0.60
0.40
0.20
0.00
-0.20
$f\Phi_{uq}(f)/u_* q_*$
10^{-4}
10^{-3}
10^{-2}
10^{-1}
10^{0}
10^{1}
1.6.4.378
$fz/\overline{u}$

data is $\alpha_{uq} \simeq 0.033$. The trend in the α_{uq} values suggest a relatively more efficient transport of horizontal water vapor flux at small scales for warm, humid conditions.

The normalized uq cospectra have lower cospectral levels than the $u\theta$ cospectra for $f_N > 0.1$, most pronounced for the MITOS I cruise which also has higher uq cospectral levels than the $u\theta$ cospectra for $f_N < 0.1$ corresponding to a scale of 50 meters for $z = 5$ meters. This suggests that horizontal transport of heat is relatively more efficient than the horizontal transport of water vapor for small scales. Conversely, for the MITOS I cruise the opposite is true for large scales.

The relative efficiency of the horizontal and vertical transport of heat and water vapor can be estimated from the ratios $\alpha_{u\theta}/\alpha_{w\theta}$ and α_{uq}/α_{wq}. The $\alpha_{u\theta}/\alpha_{w\theta}$ ratios for the three cruises are 0.27 (MITOS I), 0.36 (MITOS III) and 0.27 (OWAX); the α_{uq}/α_{wq} ratios are 0.27 (MITOS I), 0.1 (MITOS III) and 0.27 (OWAX). These results suggest that the vertical transport of heat and water vapor is always more efficient than the horizontal transport for small ($f_N > 0.2$) scales. Kaimal et al[56] suggest this behavior for horizontal and vertical heat transport for conditions over land; the reverse is also true for larger scales ($f_N < 0.2$).

4.6d Cospectra of temperature and humidity (θq)

The dimensional cospectra of temperature and humidity are presented in figures 57 - SOMA, 58 - MITOS I, and 59 - MITOS III and OWAX. The θq cospectra of SOMA, MITOS III and OWAX have similar shapes. The θq cospectra of the MITOS I cruise are not so typical and exhibit a narrow peak at the frequency interval $0.5 < f < 1.0$ Hz, similar to the peak in the MITOS I $w\theta$ cospectra.

The θq cospectra have been normalized with $T_* q_*$, consistent with the normalization of the cospectra presented in Sections 4.6a, b, and c. The expression for the normalized θq cospectra may be written as

$$\frac{f_N \Phi_{\theta q}(f_N)}{T_* q_*} = \alpha_{\theta q} H_{\theta q}(z/L) f_N^{-5/3} \qquad (56)$$

as suggested from the previous cospectral results. The z/L variation of $H_{\theta q}$ is not known and is assumed equal to 1 for unstable conditions as was done for the previous cospectral stability functions. The choice of the $-5/3$ slope for the θq cospectral subrange is based on similarity arguments and dimensional analysis by Wyngaard (personal communication to C. Friehe and G. Dreyer, 1972). The normalized θq cospectra are shown plotted as $\log f\Phi_{\theta q}(f)/T_* q_*$ versus $\log f_N$ in figure 60, and linearly versus $\log f_N$ in figure 61. The normalized θq cospectra exhibit differences in the θ-q relationship at high and

FIGURE 57

SOMA temperature-humidity (θq) cospectra plotted versus frequency

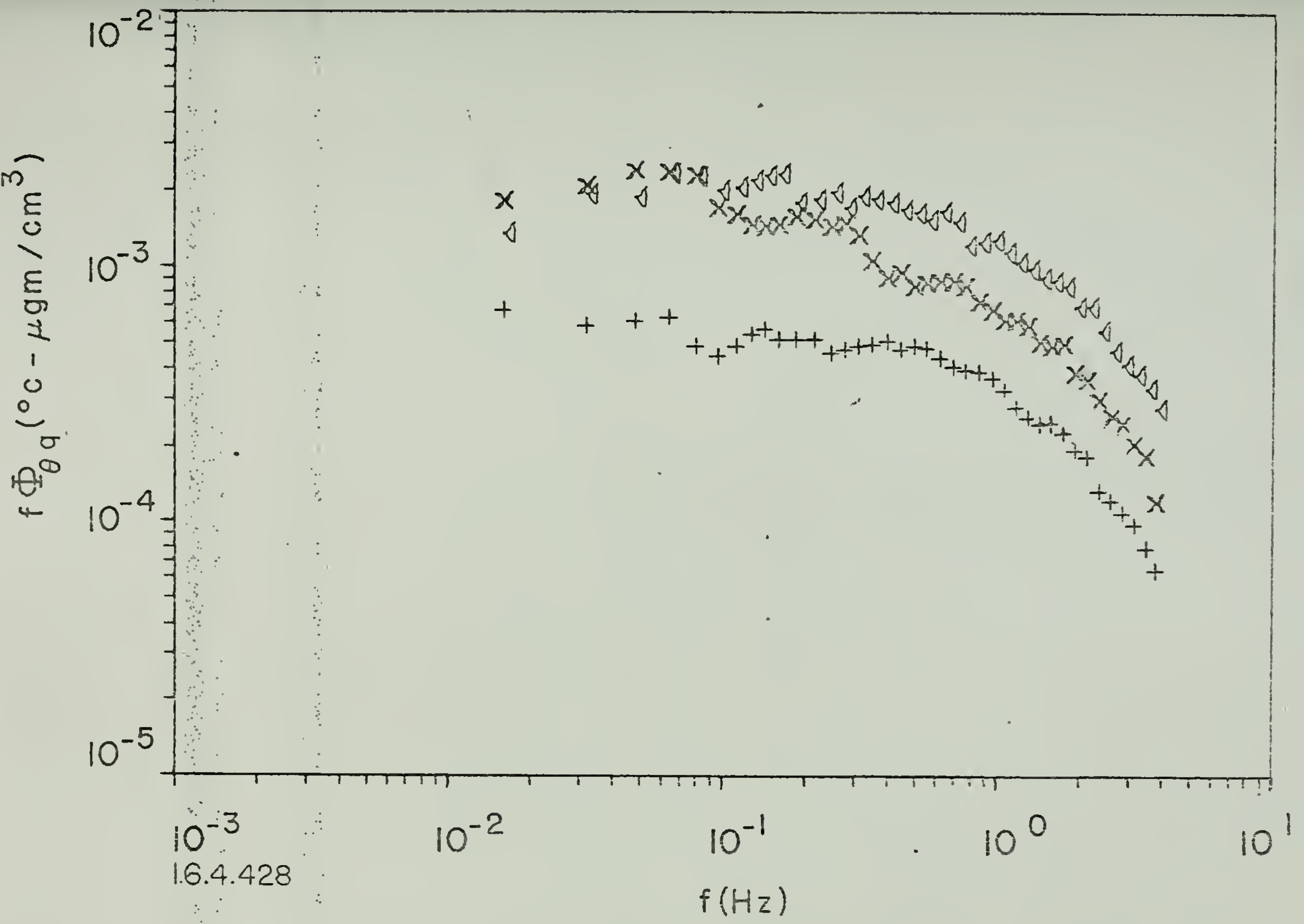
$f\Phi_{\theta q}$ (°c - μgm / cm^3)
10^{-2}
10^{-3}
10^{-4}
10^{-5}
10^{-3}
10^{-2}
10^{-1}
10^{0}
10^{1}
f (Hz)
1.6.4.428

FIGURE 58

MITOS I θq cospectra plotted versus frequency

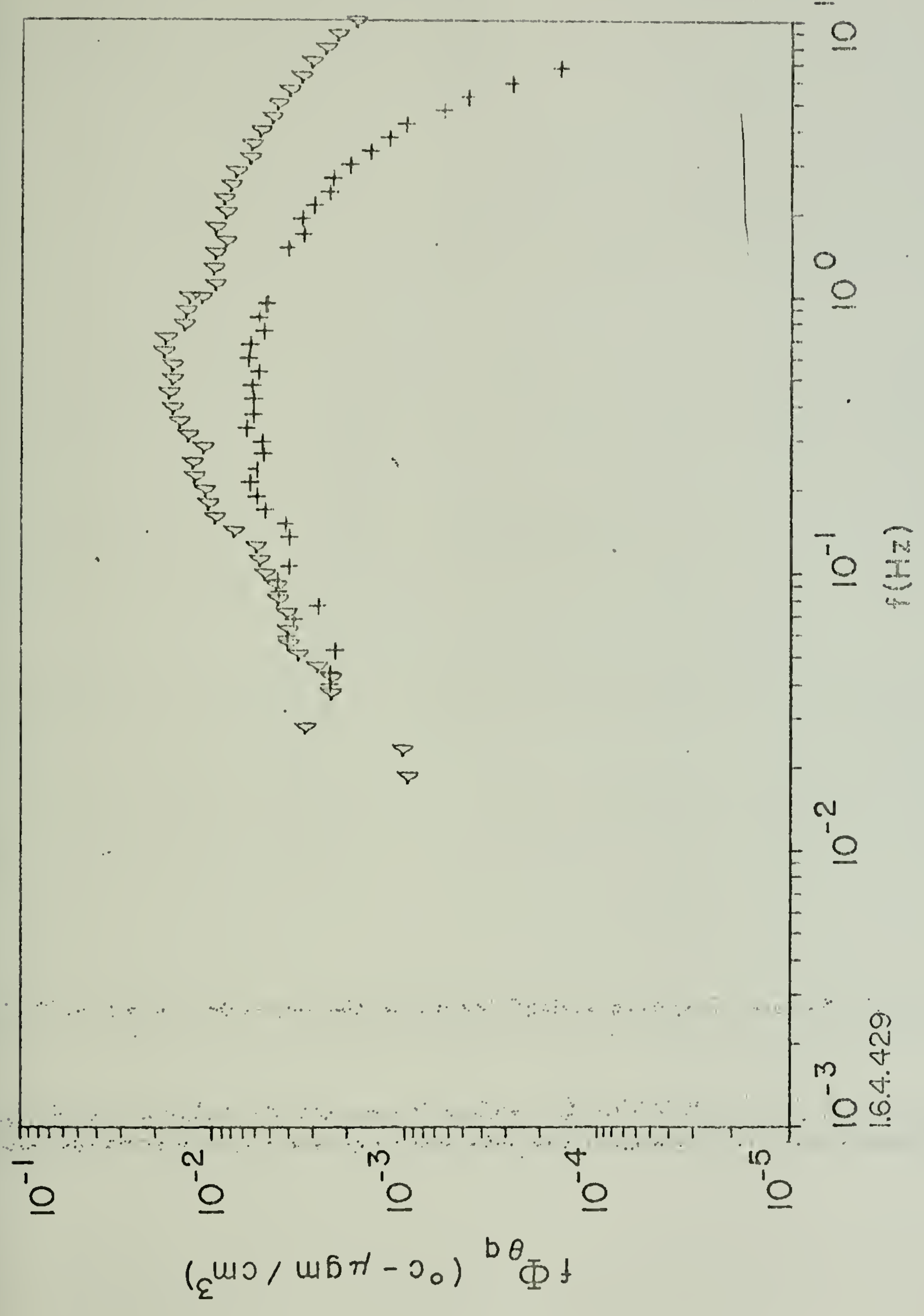
f Φθq (°c - μgm / cm³)
10⁻¹
10⁻²
10⁻³
10⁻⁴
10⁻⁵
10⁻³
10⁻²
10⁻¹
10⁰
10¹
f (Hz)
1.6.4.429

FIGURE 59

MITOS III and OWAX θq cospectra plotted versus frequency

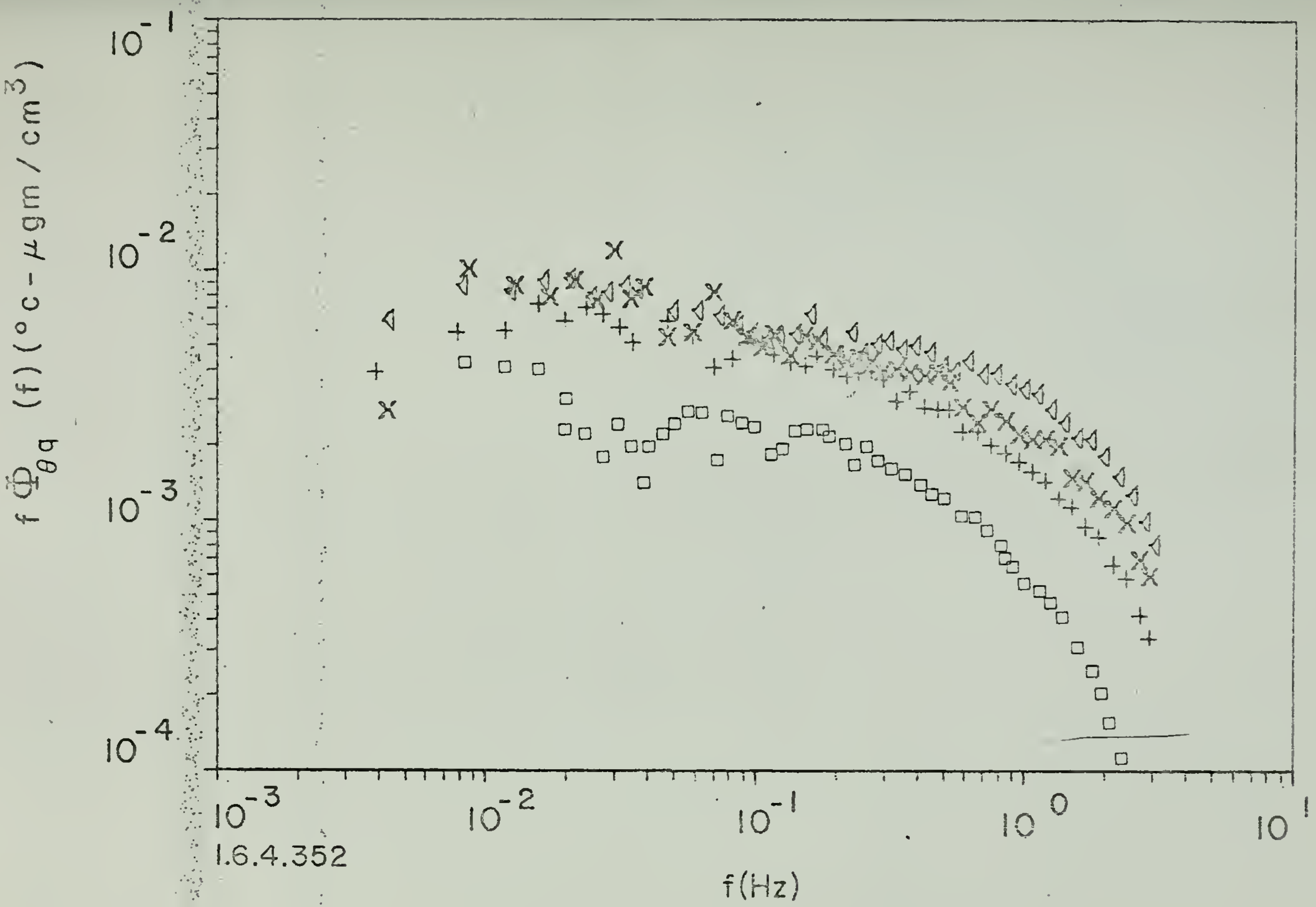
$f\,\Phi_{\theta q}$ (f) (°c - μgm / cm^3)
10^{-1}
10^{-2}
10^{-3}
10^{-4}
10^{-3}
10^{-2}
10^{-1}
10^{0}
10^{1}
1.6.4.352
f(Hz)

FIGURE 60

Average θq cospectra normalized with $T_* q_*$ plotted versus normalized frequency

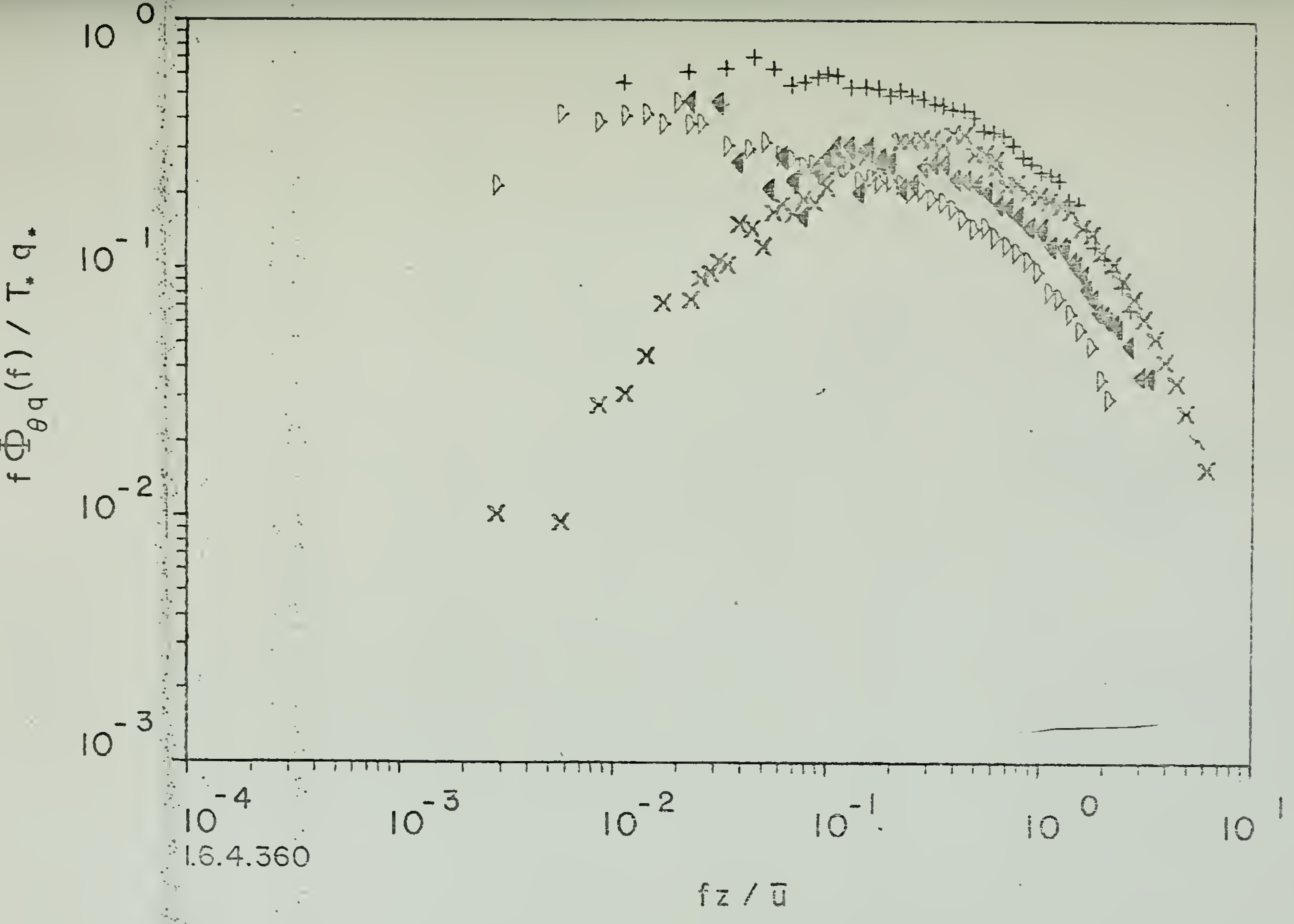
$f\Phi_{\theta q}(f) / T_* q_*$
10^0
10^{-1}
10^{-2}
10^{-3}
10^{-4}
10^{-3}
10^{-2}
10^{-1}
10^0
10^1
1.6.4.360
$fz / \overline{u}$

FIGURE 61

Average θq cospectra normalized with $T_* q_*$ plotted linearly versus normalized frequency

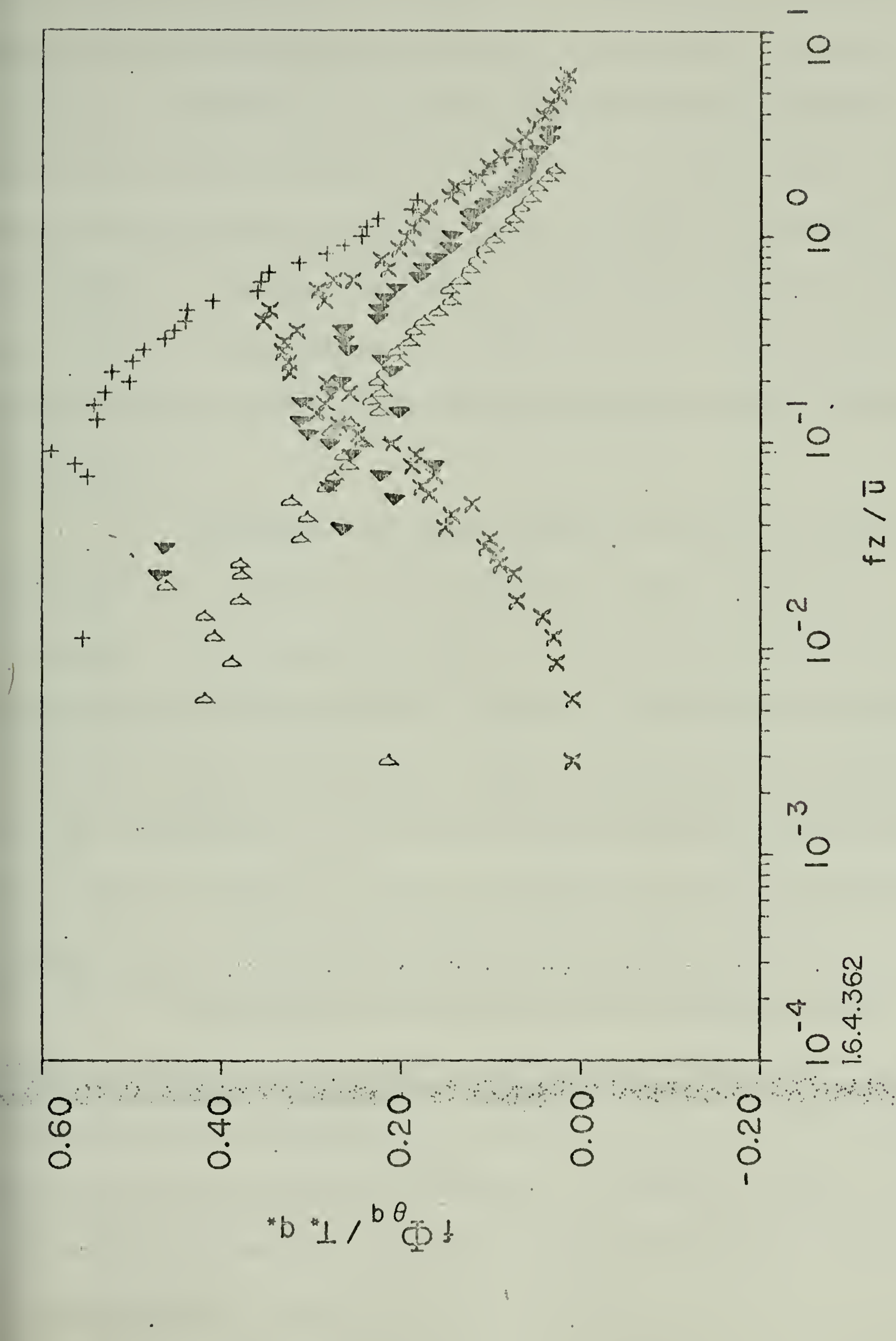
0.60
0.40
0.20
0.00
-0.20
$f\Phi_{\theta q} / T_* q_*$
10^{-4}
10^{-3}
10^{-2}
10^{-1}
10^{0}
10^{1}
$fz / \overline{u}$
16.4.362

low frequencies between the MITOS I cruise and the other cruises, similar to the differences observed in the normalized $w\theta$ and $u\theta$ cospectra. Since the θq cospectra are presented in this manner, uncertainties in the assumed and calculated u_* values will also affect the cospectral levels, but will not change the shape of the cospectra. The SOMA θq cospectra may also be affected by temperature calibration errors and uncertainties in the $\overline{w\theta}$ estimates used to calculate T_*, due to x-wire (w) drift and possible non-stationarity effects discussed in Section 4.2.

The highest normalized cospectral levels are exhibited by the SOMA θq cospectra reflecting the lower values of the $\overline{w\theta}$ covariance. The shape of the SOMA θq cospectrum is similar to the shape of the MITOS III and OWAX cospectra, indicating that the differences in the SOMA $w\theta$ cospectra shapes is probably due to not correcting for pitch effects. The "crossover" point exhibited by the $w\theta$ and $u\theta$ cospectra of MITOS I is also well defined for the θq cospectra of MITOS I at $f_N = 0.15$ (~30-50 meters scale size).

The MITOS III and OWAX cospectra appear to exhibit a slight low frequency peak at f_N values of 0.023 and 0.015 respectively, corresponding to a scale size of 230 m for the OWAX data and 540 m for the MITOS III data. A slight peak in the 8 m θq correlation presented by Leavitt[11] is also apparent at $f_N \sim 0.01$ corresponding to a mean scale size of 530 m.

TABLE 7 - Cospectral Subrange Constants

	α_{uw}	$\alpha_{w\theta}$	α_{wq}	$\alpha_{u\theta}$	α_{uq}	$\alpha_{\theta q}$
MITOS I	-	0.29	0.08	0.08	0.025	0.19
MITOS III	0.01	0.06	0.08	0.04	0.008	0.12
OWAX	0.01	0.03	0.03	0.008	0.008	0.09
Leavitt[11]	0.07	0.30	0.11	-	-	-
Kaimal et al[56] and Wyngaard and Coté[61]	0.048	0.14	-	0.035	-	-

The trend in the normalized $w\theta$, $u\theta$, wq, and uq normalized cospectra for the colder, less humid runs to show small contributions to the covariance at higher frequencies is also exhibited by the normalized θq cospectra. Differences in cospectral level occur for $f_N > 0.15$, the "crossover" point. A slope of approximately $-5/3$ is exhibited by all the normalized θq cospectra in the interval $0.4 \lesssim f_N \lesssim 1.5$. The subrange constants for the last three cruises were MITOS I, $\alpha_{\theta q} \simeq 0.19$; MITOS III, $\alpha_{\theta q} \simeq 0.12$; and OWAX, $\alpha_{\theta q} \simeq 0.09$. The uncertainty in the subrange constants determined from figure 60 was 10-20%.

Although no information concerning the phase relationships between temperature and humidity were obtained for this work, it should be noted that for their BOMEX θq data, Leavitt[11], and Phelps and Pond[10] show only small negative phases at lower frequencies than the BOMEX θq phases. The negative phases indicate that the temperature leads the humidity.

A summary of the cospectral subrange constants is given in Table 7.

4.7 $k^{5/3}$ Spectra and Comparison of Flux Techniques

In this section comparisons are made between the different flux estimation techniques discussed in Section 2. The assumptions invoked to simplify the budget equations of kinetic energy and scalar variances are also examined. The directly calculated fluxes of momentum,

sensible and latent heat used as a basis for the comparison have been presented in Tables 2 and 4, and discussed in Sections 4.3 and 4.4.

4.7a Comparison of eddy correlation and inertial dissipation techniques

Momentum Flux

Two basic assumptions invoked for estimation of momentum flux by the inertial dissipation technique are that the budget equation for kinetic energy may be simplified to the forms given by Eqs. (24) or (25), and that the one-dimensional horizontal velocity spectra is represented by a -5/3 power law behavior as shown in Eq. (11). Eqs. (24) and (25) suggest two forms for the dimensionless viscous dissipation giben by

$$\Phi_{\epsilon_1} = (1-16\ z/L)^{-1/4} - z/L \tag{57}$$

$$\Phi_{\epsilon_2} = (1 + 0.5\,|z/L|^{2/3})^{3/2} \tag{58}$$

The expression for Φ_{ϵ_1} is derived from the assumption that total production (mechanical + buoyant) is equal to dissipation of mechanical energy. Wyngaard and Coté[37] have obtained the expression for Φ_{ϵ_2} from Kansas data as discussed in Section 2.6.

The velocity power spectral relation of (11) can be rewritten as

$$\frac{k^{5/3}\,\Phi_{uu}(k)\,(Kz)^{2/3}}{u_*^2\,\Phi_\epsilon^{2/3}} = \alpha_u \tag{59}$$

where k is the radian wavenumber determined from the relation $k = 2\pi f/\overline{U}$ by Taylor's hypothesis, $K = 0.4$, Φ_ϵ given by Eq. (57) or (58), and $u_*^2 = -\overline{uw}$.

In figures 62 and 63, average velocity spectra from all the cruises are normalized as given by Eq. (58) divided by α_u, and plotted logarithmically versus $\log k$, the radian wavenumber in units cm^{-1}. The u_*^2 values for the SOMA and MITOS I spectra have been calculated based on an assumed $C_D = 1.3 \times 10^{-3}$, and those for the MITOS III and OWAX directly measured and corrected for pitch as discussed in Section 4.3. In figure 62, Φ_{ϵ_1} from Eq. (57) is used in the normalization, and in figure 63, Φ_{ϵ_2} from Eq. (58). The value of the subrange constant used in the normalization is $\alpha_u = 0.53$ from direct dissipation measurements to be presented in the next section. Also shown in figures 62 and 63 is the hot-film velocity spectrum from OWAX 4 for comparison with the average sonic anemometer spectra. A constant value of 1 for the spectra indicate a slope of $-5/3$ and agreement between the direct and inertial dissipation methods. It should be noted that a value of 1 (one) is not an exact agreement between the two methods since the directly calculated u_*^2 values were used to calculate the values of Φ_ϵ.

FIGURE 62

$k^{5/3}$ average horizontal velocity spectra normalized with $\alpha_u u_*^2 \Phi_{\epsilon_1} (Kz)^{-2/3}$ plotted versus radian wavenumber (ordinate represents agreement between direct covariance and inertial dissipation estimates of u_*^2)

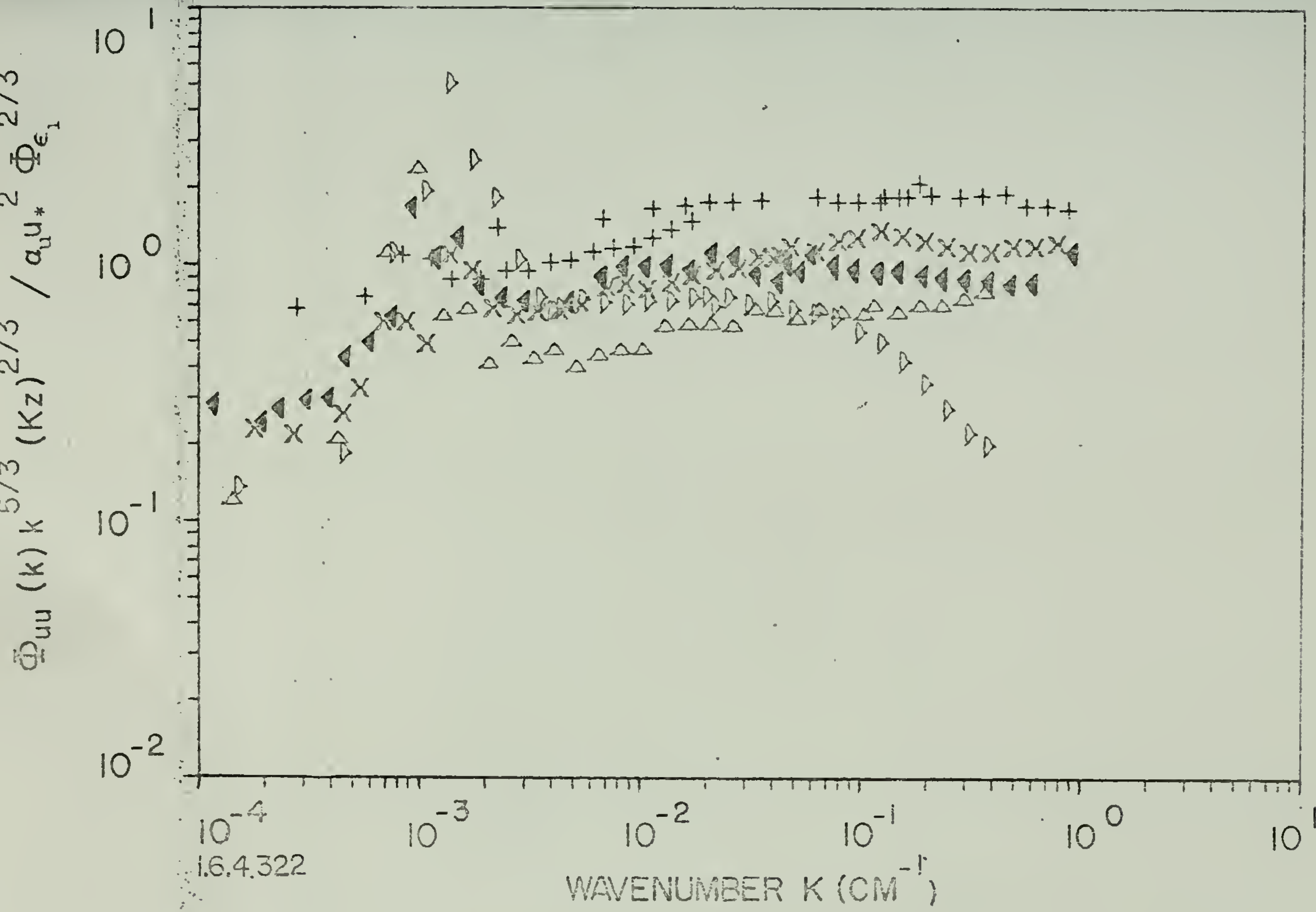
$\Phi_{uu}(k)\,k^{5/3}\,(Kz)^{2/3}\,/\,a_u u_*^{2}\,\Phi_{\epsilon_1}^{2/3}$
10^{1}
10^{0}
10^{-1}
10^{-2}
10^{-4}
10^{-3}
10^{-2}
10^{-1}
10^{0}
10^{1}
1.6.4.322
WAVENUMBER K (CM^{-1})

FIGURE 63

$k^{5/3}$ average horizontal velocity spectra normalized with $\alpha_u u_*^2 \Phi_{\epsilon_2} (Kz)^{-2/3}$ plotted versus radian wavenumber (ordinate represents agreement between direct covariance and inertial dissipation estimates of u_*^2)

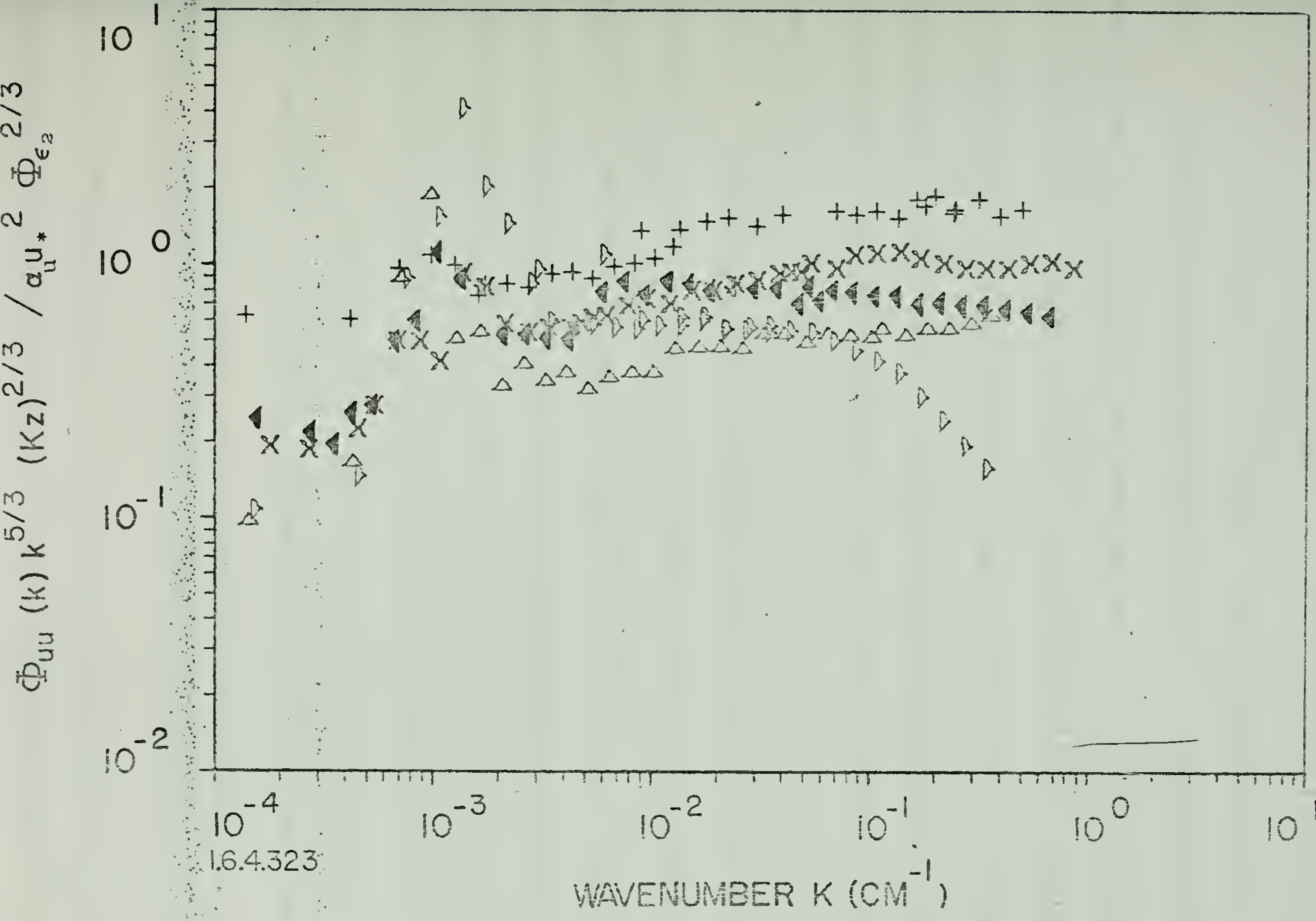
$\Phi_{uu}(k)\,k^{5/3}\,(Kz)^{2/3}\,/\,\alpha_u u_*^{2}\,\Phi_{\epsilon_2}^{2/3}$
10^{1}
10^{0}
10^{-1}
10^{-2}
10^{-4}
10^{-3}
10^{-2}
10^{-1}
10^{0}
10^{1}
1.6.4.323
WAVENUMBER K (CM^{-1})

From figure 62 the constant spectral levels and the corresponding interval for the spectra are SOMA (1.7) and MITOS III (0.93) for $0.02 < k < 0.8\ \mathrm{cm}^{-1}$; OWAX (0.75) for $0.02 < k < 0.5\ \mathrm{cm}^{-1}$; and MITOS I (1.2) for $0.1 < k < 1\ \mathrm{cm}^{-1}$. From figure 63 the constant spectral levels over the same intervals are SOMA (1.3), MITOS I (0.94), MITOS III (0.73), and OWAX (0.58). The MITOS I velocity spectrum exhibits the narrowest inertial subrange; all the spectra have a gradual approach to an inertial subrange behavior for $k < 0.02\ \mathrm{cm}^{-1}$, and exhibit effects of wave induced FLIP motion in the interval $0.001 < k < 0.003\ \mathrm{cm}^{-1}$.

The high values of subrange spectral levels for the SOMA and MITOS I data as compared to the OWAX and MITOS III spectra, suggest that the assumed value of $C_D = 1.3 \times 10^{-3}$ may be low. Another source of error in the normalized spectral levels of SOMA and MITOS I spectra is x-wire drift. As discussed in Section 4.5a this drift in the MITOS I data was corrected for by matching x-wire calibrations to cup anemometer measurements and using the mean of before and after run calibrations. It was not possible to completely correct all the SOMA data so the spectral levels are probably inordinately high.

Matching the MITOS I x-wire to cup anemometer results may have also introduced an error contributing to high spectral levels. From analysis of the OWAX sonic and cup anemometer mean velocity

measurements, the mean velocities agree within 4% except for the OWAX 3 run which indicated 5-7% cup over-speeding. Analysis of the MITOS III hot-film and cup data indicated up to 15% cup over-speeding. This over-speeding for MITOS III may be high since the hot-film was mounted horizontally with respect to the flow field instead of vertically as was done for the OWAX 4 hot-film. Wyngaard and Coté[37] used a 10% correction for cup over-speeding for their Kansas velocity data based on analysis of the Kansas cup anemometer measurements by Izumi and Barad (1970).[62] Hyson (1972)[63] and Kondo et al (1971),[64] suggest that cup over-speeding is 1% or less, however, Kondo et al[64] indicate that up to 4-7% cup over-speeding over land may occur in the daytime. If a value of $C_D = 1.5 \times 10^{-3}$ and a 10% cup over-speeding correction is applied to the MITOS I data, the subrange spectral levels would be 0.8 (figure 62) and 0.61 (figure 63). This correction does not include the effect on $\Phi_\epsilon^{2/3}$ due to changes in the z/L values but the differences are not significant (<5%).

Using the corrected values for the MITOS I spectra and the MITOS III and OWAX result, the average spectral level for figure 62 is 0.83 ± 0.07 and for figure 63 is 0.64 ± 0.004. The confidence limits only reflect differences in the average corrected spectral levels and as such are probably low. Better confidence limits for the spectral levels would be ~ 30% referring to the confidence limits on u_*^2 in

Table 4.

The trend in the values indicates that for this work the inertial dissipation method underestimates the value of u_*^2. The underestimation is more pronounced using the Φ_{ϵ_2} expression proposed by Wyngaard and Coté.[37] Pond et al[8] obtain good agreement between directly measured u_*^2 values (corrected for pitch by the "$R_{uw}(f) = -0.5$" method) and the inertial dissipation method using an $\alpha_u = 0.55$ and the expression

$$u_*^2 = [K(\epsilon - B)z]\,\Phi_m^{-2/3} \tag{60}$$

derived from Eq. (22) assuming no flux divergence, where $B = g\left(\frac{\overline{w\theta}}{\overline{T}} + \frac{\overline{T}}{273} \times 0.47 \times 10^{-3}\,\overline{wq}\right)$ (equivalent to the second term in Eq. (22). Pond et al,[8] however, do not include the effects of stability on the mean velocity profile (Φ_m) in their calculations. Including the Φ_m dependence in their calculations would increase the u_*^2 values obtained by the inertial dissipation method by 25%.

For near neutral conditions ($-z/L < 0.1$) Miyake et al (1970)[33] apply the inertial dissipation technique with the assumption that production and dissipation are in equilibrium (Eq. (3)) and obtain higher values of u_*^2 than those obtained by the eddy correlation technique. From measurements over land Hicks and Dyer (1972)[36] obtain a value of $\alpha_u = 0.54$ using the relationship given by Eq. (56) with the u_* values obtained by the eddy correlation technique and confining the estimates

of α_u to conditions of $u_* > 20$ cm/sec and $H_S > 10$ mw/cm^2.

The subrange spectral levels of figures 62 and 63 are also an indication of the ratio of dissipation of mechanical energy to production (including stability effects for production). Using the inertial dissipation technique to obtain the dimensionless dissipation and (Φ_m -z/L) to obtain the dimensionless shear production, Leavitt[11] finds a 7% difference (production greater) between the two for $\alpha_u = 0.53$ (a value of ~0.96 on figure 61). Leavitt[11] also finds the dimensionless turbulent transport to be approximately half of that found by Wyngaard and Coté.[37] If this additional correction were applied to Leavitt's[11] results on figure 62 it would correspond to a value of approximately 0.80 (average of 0.96 and 0.64) in agreement with the value obtained for the results from figure 62. It should be noted that if a similar correction were applied to data from this work the results would be lower than those obtained from figure 62.

Heat and water vapor flux

The assumptions required for estimation of heat and water vapor flux by the inertial dissipation technique are similar to those employed for estimation of momentum flux when applied to the scalar variance equations and spectral relations. Also required are the assumptions that the eddy transfer coefficients for heat and momentum, and water vapor and momentum are equal and the dimensionless scalar gradients for temperature (Φ_H) and humidity (Φ_E) are equal.

The expressions for the temperature and humidity spectra from Eq. (12) can be rewritten as

$$\frac{k^{5/3}\,\Phi_{\theta\theta}(k)\,(Kz)^{2/3}}{2T_*^2\,\Phi_H\,\Phi_\epsilon^{-1/3}} = \beta_\theta \qquad (61)$$

and

$$\frac{k^{5/3}\,\Phi_{qq}(k)\,(Kz)^{2/3}}{2\,q_*^2\,\Phi_E\,\Phi_\epsilon^{-1/3}} = \beta_q \qquad (62)$$

where the starred quantities are calculated by Eq. (6) using directly measured covariances, $\Phi_H \simeq \Phi_E = (1-16\,z/L)^{-1/2}$, and Φ_ϵ as by Eq. (54). The difference between Φ_{ϵ_1}, and Φ_{ϵ_2} will not be significant for comparison of the temperature and humidity results.

Estimates of β_θ vary considerably from values of 0.40 (Pond et al[8]), Wyngaard and Coté[37], Pacquin and Pond (1971),[65] to values of 1.0 or larger suggested by the results of Leavitt[11] of $\beta_\theta \simeq 3.0$; Stegen et al (1973),[14] and Gibson et al[47] obtain $\beta_\theta \simeq 1.2$ using the direct dissipation technique. Boston and Burling (1972)[66] and Boston (1970)[67] suggest $\beta_\theta = 0.8$ for direct dissipation measurements over a mud flat. Values of β_θ from direct dissipation measurements for this work are presented in the next section and vary from 0.7 to 2.4. There is a dearth of values of β_q in the literature from open ocean measurements and include estimates of $\beta_q = 0.4$ by Pacquin

and Pond[65] and Pacquin (1972)[68] using second and third order structure functions, and $\beta_q = 0.25$ suggested by Leavitt[11] from flux profile measurement results of Paulson et al which imply $\Phi_E = \Phi_m \neq \Phi_H$. the β_θ and β_q values given above are based on the definitions of scalar variance dissipation from Eqs. (30) and (33).

Temperature and humidity spectra from the cruises normalized in the manner of Eqs. (61) and (62) are shown in figures 64 and 65, plotted versus $\log k(\mathrm{cm}^{-1})$. A constant value of the spectra indicates a spectral slope of $-5/3$. Due to the variation of β_θ and β_q estimates as discussed above, the normalized cospectra have not been divided by the subrange constants as was done for the momentum flux comparison. The value of the spectral levels thus represent the implied β_θ or β_q required for agreement between the inertial dissipation estimate of T_*^2 or q_*^2, and the value determined from direct covariance measurements. Since directly measured covariances are used to calculate Φ_H and Φ_ϵ the implication is not exact. For given values of β_θ and β_q, the spectral levels divided by those values represent the ratio of scalar dissipation by the inertial dissipation technique to the scalar production assuming $\Phi_E = \Phi_H = (1-16\, z/L)^{-1/2}$.

The normalized temperature spectra of figure 64 exhibit considerable differences. The thermistor temperature spectra from the SOMA cruise and OWAX 2 and 3 runs exhibit a roll-off in spectral

FIGURE 64

$k^{5/3}$ average temperature spectra normalized with $2\,T_*^2\,\Phi_H \Phi_\epsilon^{-1/3}\,(Kz)^{-2/3}$ plotted versus radian wavenumber (ordinate represents β_θ required for agreement between direct covariance and inertial dissipation estimates of T_*^2)

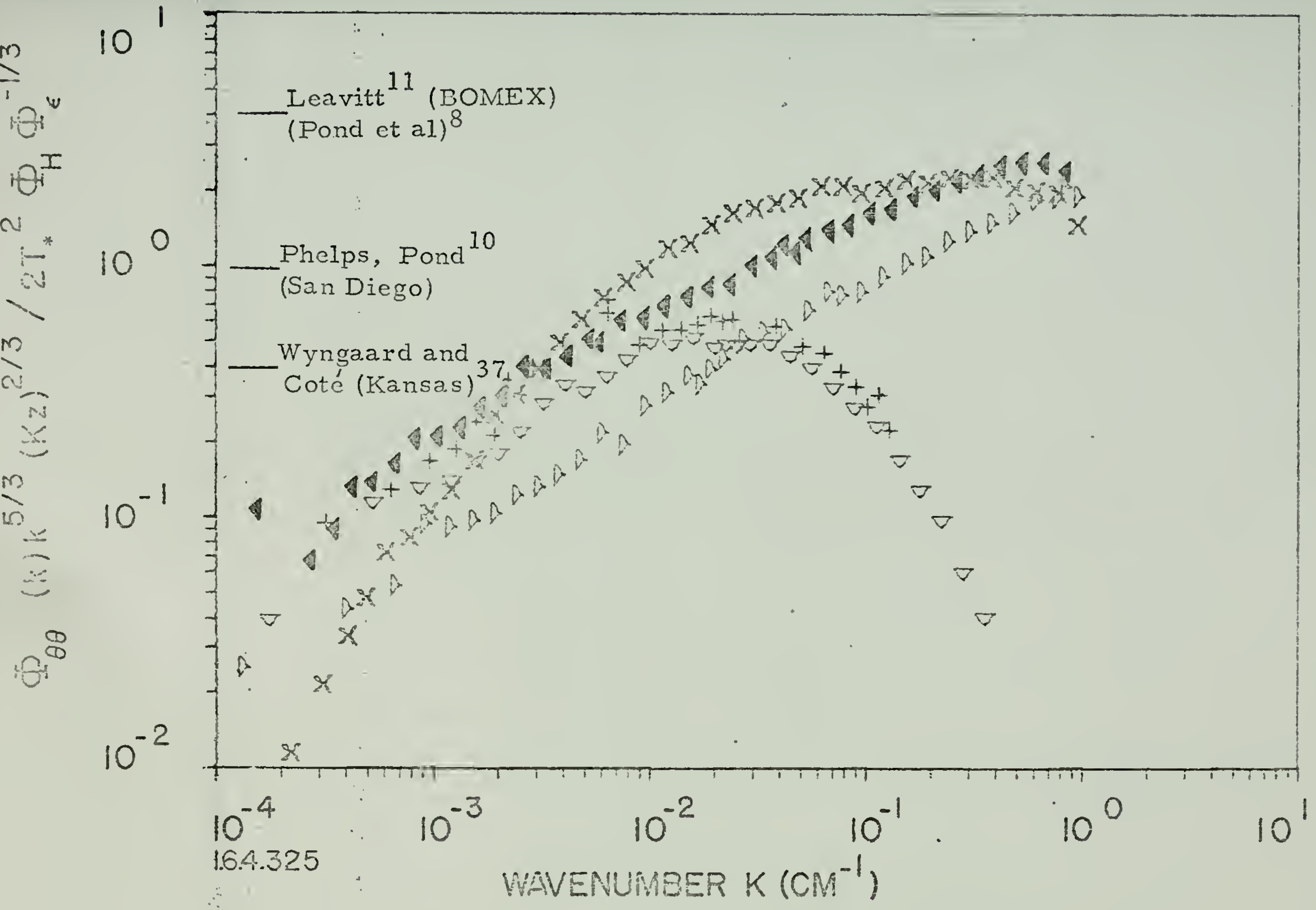
Leavitt[11] (BOMEX)
(Pond et al)[8]
Phelps, Pond[10]
(San Diego)
Wyngaard and Coté (Kansas)[37]
$\Phi_{\theta\theta}(k)k^{5/3}(Kz)^{2/3}/2T_*^2\,\Phi_H\,\Phi_\epsilon^{-1/3}$
10^1
10^0
10^{-1}
10^{-2}
10^{-4}
10^{-3}
10^{-2}
10^{-1}
10^0
10^1
164.325
WAVENUMBER K (CM^{-1})

FIGURE 65

$k^{5/3}$ average humidity spectra normalized with $2\, q_*^2\, \Phi_E \Phi_\epsilon^{-1/3}\, (Kz)^{-2/3}$ plotted versus radian wavenumber (ordinate represents β_q required for agreement between direct covariance and inertial dissipation estimates of q_*^2)

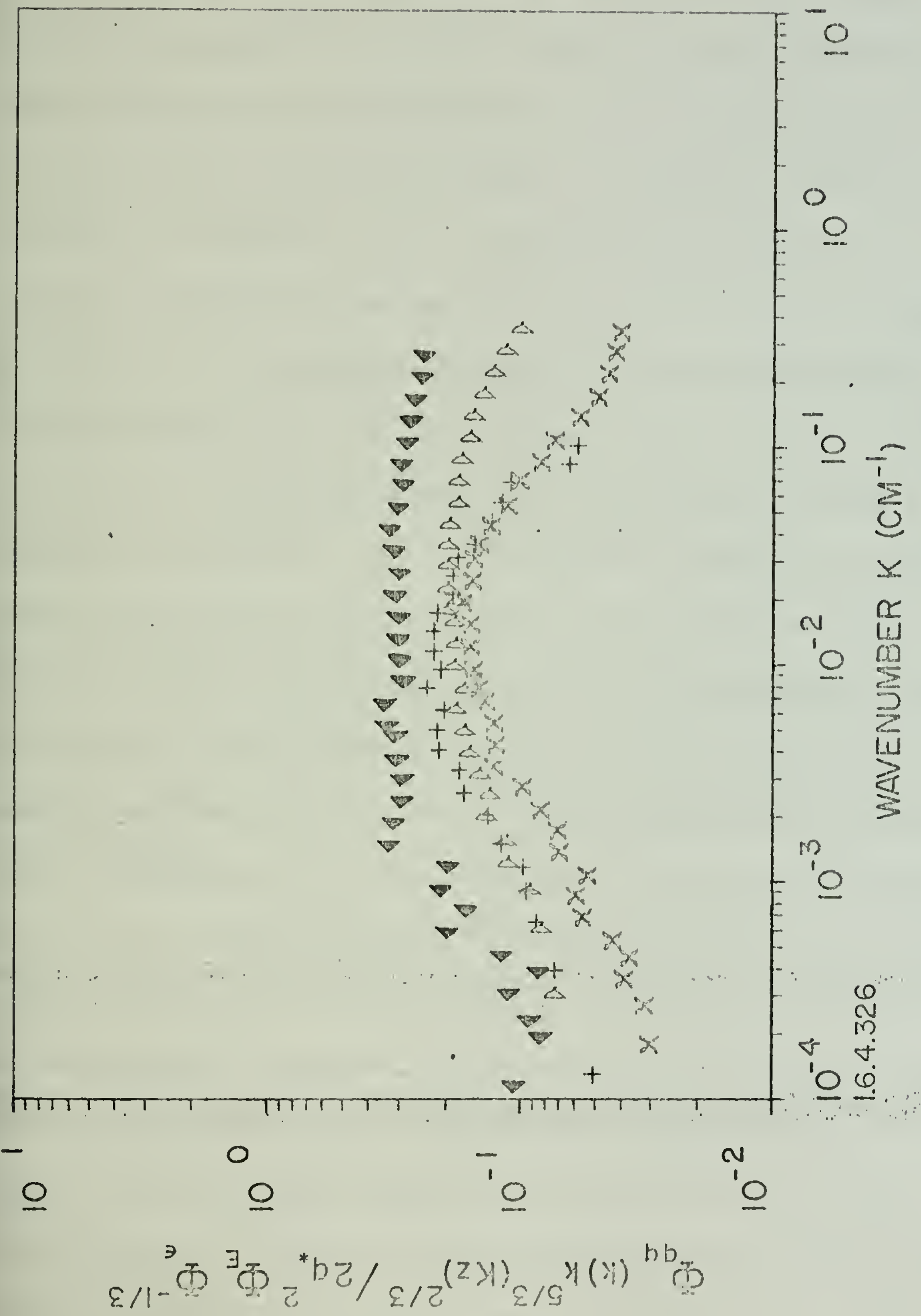
$\Phi_{qq}(k)\,k^{5/3}(kz)^{2/3}/2q_*^2\,\Phi_E\,\Phi_\epsilon^{-1/3}$
10^{1}
10^{0}
10^{-1}
10^{-2}
10^{-4}
10^{-3}
10^{-2}
10^{-1}
10^{0}
10^{1}
WAVENUMBER K (CM^{-1})
16.4.326

level for $k > 0.03\ \mathrm{cm}^{-1}$ due to instrument response. The cold wire spectra are still increasing, however, and do not exhibit constant spectral levels below $k = 0.8\ \mathrm{cm}^{-1}$ with the exception of the MITOS I data. The MITOS I spectrum exhibits a constant spectral level of 2.1 ± 0.2 (implied β_θ) over the range of wavenumbers $0.06 < k < 1.0\ \mathrm{cm}^{-1}$ for a slope of $-5/3$. The MITOS III spectrum has a narrower subrange in the interval $0.3 < k < 1.0\ \mathrm{cm}^{-1}$ with an implied $\beta_\theta = 2.5 \pm 0.2$. An inertial subrange for the OWAX 4 spectrum is nearly nonexistent. The OWAX 4 spectral level for $0.7 < k < 1.0\ \mathrm{cm}^{-1}$ is 1.7 ± 0.2. The slopes exhibited by the MITOS III and OWAX 4 spectra for $k < 0.3\ \mathrm{cm}^{-1}$ are $-4/3$ and $-5/4$ respectively, instead of the inertial subrange slope of $-5/3$. If the assumed value of $C_D = 1.3 \times 10^{-3}$ were increased to 1.5×10^{-3} for the MITOS I data as discussed for the momentum flux comparison, the implied β_θ would be increased to a value of 2.5, comparable to the MITOS III result. The implied β_θ values of Leavitt[11] and Pond et al[8] for BOMEX data (4.2 ± 1), Phelps and Pond[10] for San Diego data (~ 1.0), and Wyngaard and Coté[61] and Kaimal et al[56] (0.4 ± 0.05) are shown at the left-hand side of figure 64. The Phelps and Pond[10] results from San Diego are based on spectra obtained from measurements of temperature using a thermocouple with frequency response out to ~3 Hz (3db point), and may not sufficiently reflect the temperature behavior at smaller scales. The Kansas result of Kaimal et al[56] and

Wyngaard and Cote'[61] was obtained from measurements of the production and turbulence transport of temperature variance and assuming the imbalance between production and transport equaled dissipation using 20 cm fine platinum wire thermometers corrected for spatial resolution effects.

The spectra shown in figure 64 indicate that large errors (overestimation) may result when estimating the sensible heat flux by the inertial dissipation technique. A value of $\beta_\theta \simeq 2.0$ is required for estimates of $\overline{w\theta}$ comparable to the direct covariances using this technique over the ocean, in conjunction with temperature measurements out to scales as small as 6 cm in wavelength. The results also imply that dissipation of temperature variance may exceed production by a factor of 2 or more (for $\beta_\theta \simeq 1$). Direct dissipation measurements presented in the next section also appear to support this implication.

The normalized humidity spectra from the four cruises are shown in figure 65. The spectra exhibit constant spectral values over the interval $0.01 < k < 0.04$ cm^{-1}. The MITOS III spectrum has a constant value of implied $\beta_q = 0.29 \pm 0.03$ over a considerably wider range ($0.002 < k < 0.1$ cm^{-1}) than the other spectra. The SOMA and OWAX values are the same with an implied $\beta_q = 0.20 \pm 0.03$. The lowest spectral levels are exhibited by the MITOS I spectra in the same

interval as the OWAX and SOMA spectra with the implied $\beta_q = 0.13 \pm 0.02$ (0.15 for $C_D = 1.5 \times 10^{-3}$). The lower spectral values for $k \geq 0.04$ cm^{-1} are due to instrument response. The high spectral levels of the MITOS III data for $k > 0.04$ cm^{-1} may be due to high frequency noise in the humidity signal at lower frequencies than the filter cut-off (Nyquist frequency). The average implied β_q for this work is 0.21 ± 0.05, which is lower than the value obtained by Pacquin and Pond,[65] and Pacquin[68] of 0.41. The value of $\beta_q = 0.25$ suggested by Leavitt[11] is comparable with the value of β_q from figure 65, and suggests $\Phi_E = \Phi_m$, if production and dissipation of humidity variance are equal. This implies water vapor is transported more nearly like momentum than heat.

Referring to the results of Section 4.6 and the expression for $\alpha_{w\theta}/\alpha_{wq}$ given by Eq. (53), the ratio of the cospectral constants for heat and water vapor flux implied $\beta_\theta \simeq 13\,\beta_q$. Using average values of $\beta_\theta \simeq 2.24$ and $\beta_q \simeq 0.21$, the result is $\beta_\theta \simeq 11\,\beta_q$ not significantly different than the result predicted by the cospectral subrange constants.

4.7b Comparison of eddy correlation and direct dissipation techniques

Estimation of the fluxes of momentum and sensible heat by the direct dissipation technique have been made from measurements of

the mean square time derivatives of velocity and temperature. The mean viscous dissipation $(\overline{\epsilon})$ and mean dissipation of temperature variance $(\overline{\chi_\theta})$, calculated using Eqs. (13) and (14) from the MITOS I, MITOS III and OWAX 4 data are given in Table 8. No corrections for Hekstad's (1965)[69] modification of Taylor's hypothesis have been applied as was done by Wyngaard and Coté[37], since the corrections are typically $< 2\%$.

The $\overline{\epsilon}$ and $\overline{\chi}_\theta$ estimates for MITOS I were obtained by Steve McConnell[51] by matching high frequency spectra of velocity and temperature time derivatives to the converted velocity and temperature spectra $(\Phi_{\theta\theta}(f) \times f^2/(2\pi)^2)$ shown in figures 14 and 28. The χ_θ values for MITOS III-2 and OWAX 4 from McConnell[51] are calculated for shorter time periods than the direct covariances but are representative values for the runs. The MITOS III $\overline{\epsilon}$ value is an average from three estimates at the beginning, middle and end of the run, and the OWAX 4 (McConnell)[51] value is from the beginning of the run. All the $\overline{\epsilon}$ and $\overline{\chi}_\theta$ values have confidence limits of approximately 20% or better.

The α_u and β_θ values shown in Table 8 were calculated using the directly measured $\overline{\epsilon}$ and $\overline{\chi}_\theta$ estimates and employing the relations

$$\Phi_{\dot{u}\dot{u}}(k) = \alpha_u \overline{\epsilon}^{2/3} k^{1/3} \qquad (63)$$

TABLE 8 - Direct Dissipation Results

		$\overline{\epsilon}$ (cm^2/sec^3)	$\overline{\chi}_\theta$ ($°C^2/sec$)	α_u	β_θ
MITOS I	1	117	8.6×10^{-4}	0.53	2.4
	7	108	8.6×10^{-3}	0.50	1.9
MITOS III	2	21.2	6.3×10^{-4}	0.53	0.68
OWAX	4	43.3	2.6×10^{-3}	0.54	0.67

$$\Phi_{\dot{\theta}\dot{\theta}}(k) = \beta_{\theta}\, \overline{\chi}_{\theta}\, \overline{\epsilon}^{\,-1/3}\, k^{1/3} \qquad (64)$$

where $\dot{u}$ and $\dot{\theta}$ are spatial derivatives by Taylor's hypothesis. Velocity and temperature derivative spectra from MITOS I-1 and 7, and OWAX 4 are shown in figure 66, 67 and 68 (from McConnell).[51] The spectra are normalized with $\overline{\epsilon}^{\,-2/3}$ (velocity) and $\overline{\chi}_{\theta}\, \overline{\epsilon}^{\,-1/3}$ (temperature) and multiplied by $k^{-1/3}$ so that the spectral levels plotted linearly represent α_{u} and β_{θ}, and a constant value indicates a + 1/3 slope. The abscissa is given as log $(\eta\, k)$ where η is the Kolmogorov microscale $(\nu^{3}/\overline{\epsilon})^{1/4}$, and 10 $(\eta\, k) \simeq k$ (for reference to figures 62 through 65). The derivative spectra exhibit a subrange behavior similar to that shown by the velocity and temperature spectra of figures 62 through 65, with the MITOS I temperature derivative spectra exhibiting an extensive inertial subrange and the OWAX 4 temperature derivative spectra having only a narrow subrange. The β_{θ} values from the MITOS I derivative spectra are comparable to the implied β_{θ} values. The MITOS III (Table 8) and OWAX 4 β_{θ} values are much lower (by a factor of 3) than the implied β_{θ} values. The $\overline{\chi}_{\theta}$ values determined by the direct dissipation technique do not require the assumption that production is equal to dissipation. The direct β_{θ} values are mainly dependent on the shape (area) of the $\dot{\theta}$ -spectrum and the direct $\overline{\chi}_{\theta}$ and $\overline{\epsilon}$ values. Since the $\dot{\theta}$ -spectrum

FIGURE 66

MITOS I-1 and 7 $k^{-1/3}$ velocity derivative spectra normalized with $\epsilon^{2/3}$ plotted linearly versus normalized wavenumber (ηk) (ordinate represents α_u from direct dissipation estimate) (from McConnell,[50] 1974)

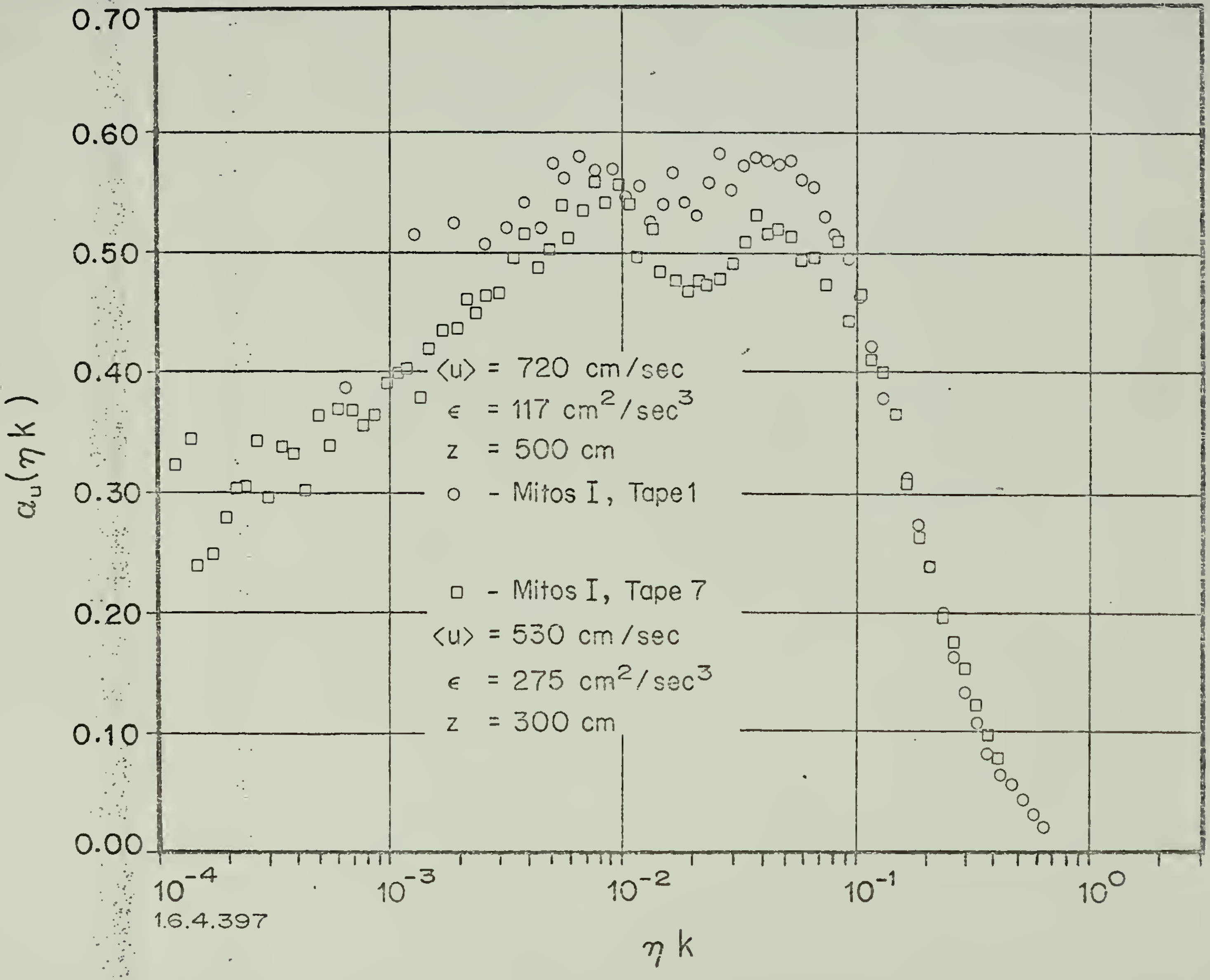
0.70
0.60
0.50
0.40
0.30
0.20
0.10
0.00
$a_u(\eta k)$
10^{-4}
10^{-3}
10^{-2}
10^{-1}
10^{0}
ηk
1.6.4.397
$\langle u \rangle$ = 720 cm/sec
ϵ = 117 cm^2/sec^3
z = 500 cm
○ - Mitos I, Tape1
□ - Mitos I, Tape 7
$\langle u \rangle$ = 530 cm/sec
ϵ = 275 cm^2/sec^3
z = 300 cm

FIGURE 67

MITOS I-1 and 7 $k^{-1/3}$ temperature derivative spectra normalized with $\chi_\theta \epsilon^{-1/3}$ plotted linearly versus normalized wavenumber (ηk) (ordinate represents β_θ from direct dissipation estimate) (from McConnell,[50] 1974)

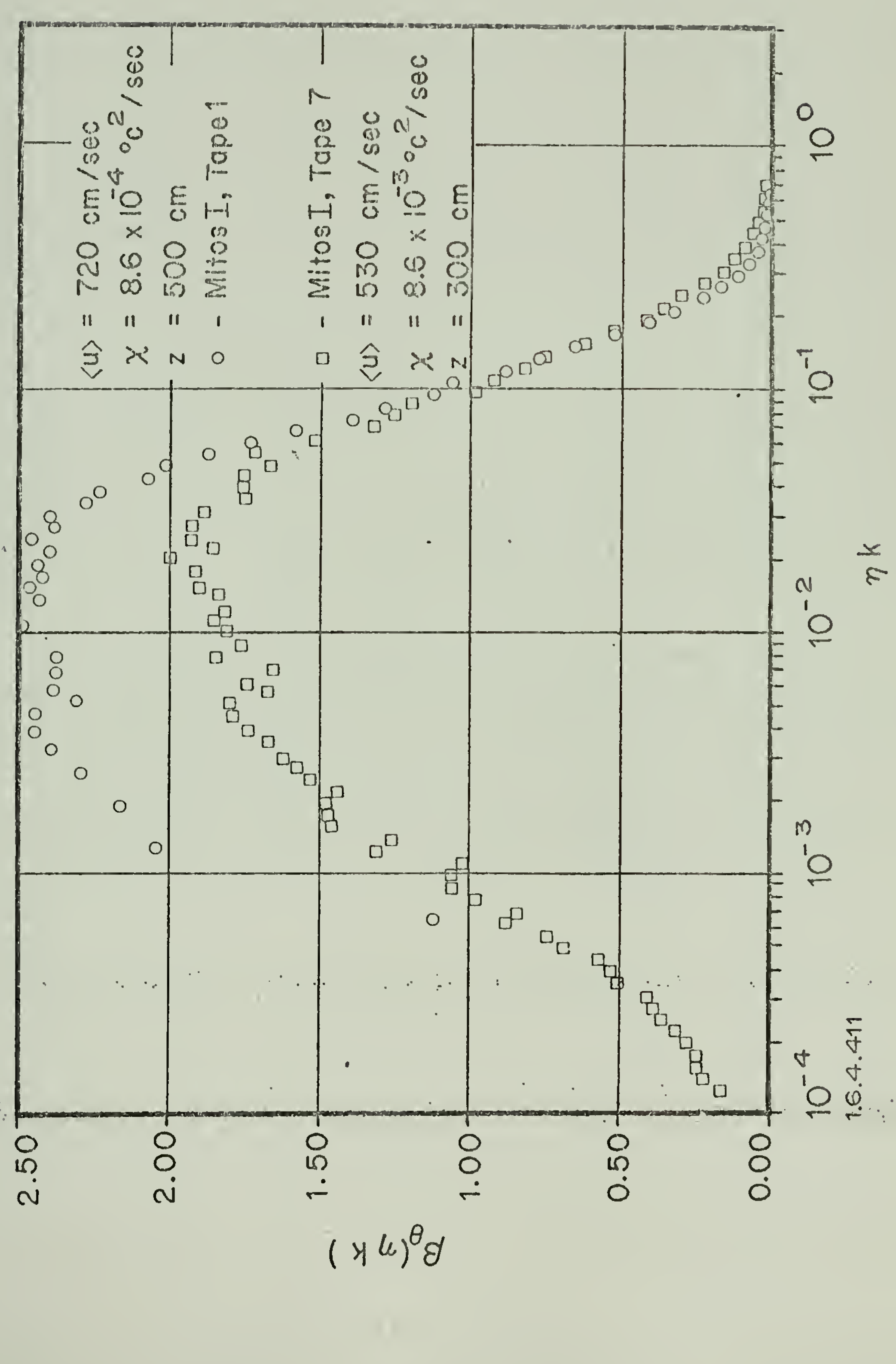
⟨u⟩ = 720 cm/sec
χ = 8.6 x 10^-4 °c^2/sec
z = 500 cm
○ - Mitos I, Tape 1
□ - Mitos I, Tape 7
⟨u⟩ = 530 cm/sec
χ = 8.6 x 10^-3 °c^2/sec
z = 300 cm
10^-4
10^-3
10^-2
10^-1
10^0
ηk
2.50
2.00
1.50
1.00
0.50
0.00
Bθ(ηk)
1.6.4.411

FIGURE 68

OWAX-4 $k^{-1/3}$ velocity and temperature derivative spectra normalized with $\epsilon^{2/3}$ (velocity) and $\chi_\theta \epsilon^{-1/3}$ (temperature) plotted linearly versus normalized wavenumber (ηk) (ordinate represents α_u or β_θ from direct dissipation estimate) (from McConnell,[50] 1974)

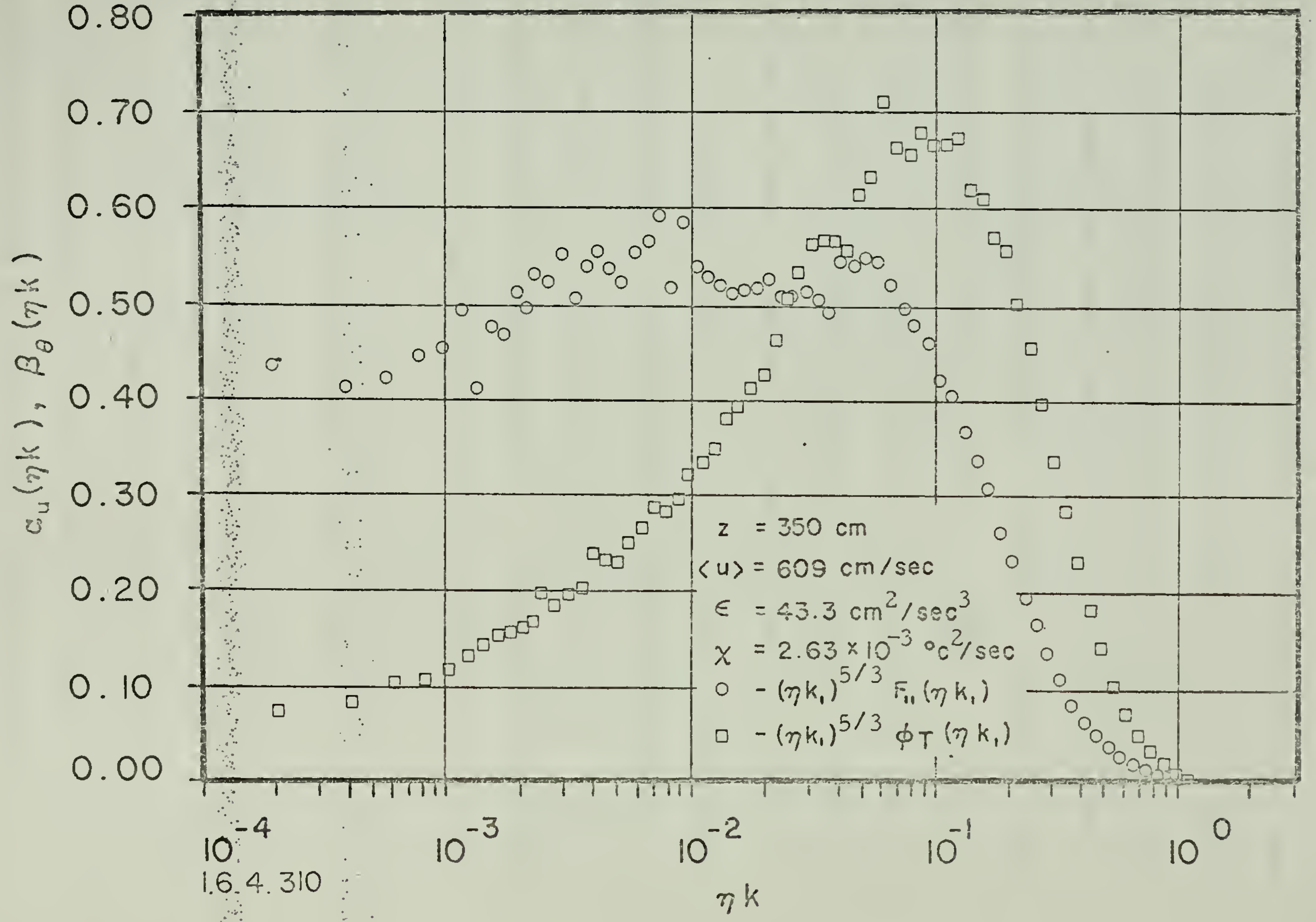
0.80
0.70
0.60
0.50
0.40
0.30
0.20
0.10
0.00
$c_u(\eta k)$, $\beta_\theta(\eta k)$
10^{-4}
10^{-3}
10^{-2}
10^{-1}
10^{0}
ηk
1.6.4.310
z = 350 cm
⟨u⟩ = 609 cm/sec
ϵ = 43.3 cm^2/sec^3
χ = 2.63 × 10^{-3} °c^2/sec
○ - $(\eta k_1)^{5/3}\, F_{11}(\eta k_1)$
□ - $(\eta k_1)^{5/3}\, \phi_T(\eta k_1)$

for OWAX 4 is displaced to the right of the $\dot{u}$ - spectrum, a larger relative area is obtained to determine $\overline{\chi}_\theta$ which results in a smaller value of β_θ as compared to the MITOS I $\dot{\theta}$ - spectra and β_θ values.

Gibson et al[13] obtained a value of $\beta_\theta = 1.17$ from BOMEX data using the same procedure as used above to calculate β_θ. At the time, the β_θ value was considered high, and two possible explanations for the high value were suggested. The first explanation was that an anisotropic temperature field (estimated by $S\left(\frac{d\theta}{dx}\right)$, skewness of $\dot{\theta}$) would enhance vertical temperature gradients if positive skewness values were observed, resulting in higher β_θ estimates. Skewness values for the temperature spectral derivative (from McConnell)[50] averaged 0.81 for the MITOS I data and 0.84 for the OWAX 4 data, not significantly different. Both skewness results indicate similar anisotropic conditions. The second explanation was that β_θ would increase with increasing intermittency of ϵ, estimated by the factor $\left(\frac{1}{3} K\right)^{1/3}$, where K is the kurtosis of du/dx. Kurtosis of du/dx (also from McConnell)[50] from MITOS I and OWAX 4 were ~ 19 and 23 respectively, so that the higher kurtosis values did not correspond to the higher β_θ values. The higher β_θ values from this work may be due to the effects of anisotropy of the temperature field when compared to similar measurements over land (dry conditions), however, other effects besides anisotropy and ϵ intermittency are required to explain differences in the β_θ values from the different cruises.

Results of calculation of momentum flux and sensible heat flux by the direct dissipation method for MITOS I, MITOS III, and OWAX 4 are shown in Table 9 for comparison to the directly measured covariances. The direct dissipation estimates of u_*^2 and $\overline{w\theta}$ were calculated using Eqs. (7) and (8), rewritten to include corrections for stability effects as

$$u_*^2 = \left(\frac{Kz\epsilon}{\Phi_\epsilon}\right)^{2/3} \tag{65}$$

$$\overline{w\theta} = \left[\frac{\chi_0 Kz u_*}{2\,\Phi_H \Phi_\epsilon^{-1/3}}\right]^{1/2} \tag{66}$$

For Eq. (65) the two expressions for Φ_ϵ given in Section 4.7a are also compared. The u_* values used in Eq. (66) are the direct dissipation estimates for $z/L = 0$. The expression for Φ_{ϵ_1} was used in Eq. (66).

The direct dissipation estimates of u_*^2 for MITOS I are all higher than the calculated direct covariances suggesting the assumed values of $C_D = 1.3 \times 10^{-3}$ is low. If a value of $C_D = 1.5 \times 10^{-3}$ is used and a 10% cup over-speeding correction is applied (as in Section 4.7a) to the direct dissipation estimates, the results for MITOS I are comparable to those from MITOS III and OWAX 4. It should be noted that the confidence limits for the direct covariances are ± 25% and for the direct $\overline{\epsilon}$ estimates ± 20% so that comparisons between the two methods will only refer to trends using the values of Table 9. The

TABLE 9

Comparison of Eddy Correlation and Direct Dissipation Techniques

Momentum Flux (cm^2/sec^2)

				$u_*^2 = (Kz\epsilon/\Phi_\epsilon)^{2/3}$	
		$u_*^2 = -\overline{uw}$	$u_*^2 = (Kz\epsilon)^{2/3}_{(z/L=0)}$	$\Phi_{\epsilon_1}^{2/3} = (\Phi_m - z/L)^{2/3}$	$\Phi_{\epsilon_2}^{2/3} = 1 + 0.5\lvert z/L\rvert^{2/3}$
MITOS I	1	(642)	818	887	723
	7	(365)	611	654	514
MITOS III	2	455	482	514	395
OWAX	4	343	332	359	289

Sensible Heat Flux (°C - cm/sec)

		$w\theta$	$w\theta = \left(\frac{X_\theta K z u_*}{2}\right)^{1/2}_{(z/L=0)}$	$w\theta = \left(\frac{X_\theta K z u_*}{2\Phi_H \Phi_\epsilon^{-1/3}}\right)^{1/2}$
MITOS I	1	1.19	1.57	2.06
	7	3.10	3.85	5.76
MITOS III	2	1.46	1.86	2.91
OWAX	4	1.20	1.82	2.58

same is true for the $\overline{w\theta}$ estimates with better confidence limits on the values obtained from the two methods.

Best agreement between the values of u_*^2 is obtained using $z/L = 0$ for the direct dissipation calculations. Including the MITOS I results corrected as suggested above, the u_*^2 estimates using Φ_{ϵ_1} are an average of 12% higher than the direct covariances, and the estimates using Φ_{ϵ_2} are an average of 13% lower. The results indicate that the dimensionless turbulent transport is approximately half of that suggested by Wyngaard and Coté[33], and in agreement with the results of Leavitt[11] for turbulent transport from BOMEX measurements.

The direct dissipation estimates of $\overline{w\theta}$ are significantly higher than the direct covariance measurements. If the 10% cup over-speeding correction is applied to the MITOS I $\overline{w\theta}$ estimates, the direct dissipation results for all the data are higher than the direct covariances by an average of 30% for $z/L = 0$, and 77% when stability corrections are included. Differences between the $\overline{w\theta}$ values for the two methods cannot be accounted for by uncertainties in the pitch corrected covariances and the $\overline{\chi_\theta}$ and $\overline{\epsilon}$ estimates, particularly when stability corrections are included in the direct dissipation calculations. The results support the evidence from the previous section that dissipation of temperature variance may exceed production by a factor of 2 or more.

Stegen et al (1973)[14] used the direct dissipation technique to estimate momentum flux and sensible heat flux from high frequency hot-wire and cold-wire velocity and temperature measurements. Using the stability expression Φ_{ϵ_2} to correct the direct dissipation estimates of u_*^2, Stegen et al[14] obtain an average value of shear stress of $\sim$ 0.39 dynes/cm^2, somewhat lower than the eddy correlation results reported by Pond et al[8] of 0.49 (Univ. of British Columbia result) and 0.44 (Oregon State Univ. result) dynes/cm^2. If the results of Stegen et al[14] for 6.7 m. $(-z/L \simeq .26)$ were corrected for stability effects using the expression Φ_{ϵ_1} (Eq. (57), the estimated stress would be 0.39 dynes/cm^2, in better agreement with the direct covariance results. It should also be noted that the direct covariance results were corrected for pitch using the $R_{uw} = -0.5$ technique to estimate the rotation angle. The analysis of Section 4.3 suggested that this method may tend to overestimate the correction under certain conditions, however, not necessarily applicable to the BOMEX results.

Stegen et al[14] did not apply stability corrections to the direct dissipation estimate of the sensible heat flux since the variability in the $\overline{\chi_\theta}$ estimates were considered greater than the errors due to neglecting stability effects. As a result, a value of $H_S = 0.74$ mw/cm^2 was obtained, lower than the results reported by Pond et al[8] of 1.0 (OSU) and 1.3 (UBC) mw/cm^2 from direct covariance measurements, also using the $R_{uw} = -0.5$ correction. If stability

effects are included in the calculation of Stegen et al[14] (using 6.7 m and - z/L = 0.26), the resultant H_S = 1.25 mw/cm^2, in agreement with the direct covariance measurements. This result is much lower than the OSU inertial dissipation estimate of H_S = 2.8 mw/cm^2 using a β_θ = 0.4 ; for β_θ = 1. Better agreement is obtained with a corrected value of H_S = 1.1 for the OSU inertial dissipation estimate of the sensible heat flux. Although there appears to be agreement between the direct dissipation estimate of H_S when stability effect are included and the direct covariance measurement, the absolute spectral levels for the OSU, UBC, and UW (Univ. of Washington - Leavitt)[11] temperature spectra did not overlap with the low frequency portion of the UCSD (Stegen et al)[14] temperature spectra (personal communication, Leavitt, Friehe). Differences between the two sets of spectra may have been due to spatial resolution effects at the high end of the low frequency spectra (OSU, UBC and UW), and high pass filtering effects (below ~ 2 Hz) at the low end of the high frequency (UCSD) temperature spectra.

As was mentioned earlier, the MITOS I cruise had conditions similar to those of BOMEX, and the high frequency temperature spectra (McConnell)[51] used to obtain $\overline{\chi_\theta}$ estimates were matched to the temperature spectra presented in Section 4.5b so that any differences due to calibrations would be eliminated.

4.7c Scalar variance budgets reexamined

A basic assumption common to both the inertial and direct dissipation techniques used to estimate the fluxes of heat and water vapor, is that production of temperature and humidity variance is equal to dissipation (Eq. (4)). For open ocean measurements, this assumption may not be valid. Production and dissipation of temperature variance were calculated for the cold wire runs and the results are given in Table 10. The $\overline{\chi_\theta}$ values obtained by McConnell (1974)[50] and given in Table 8 were used to calculate the dissipation. Production was calculated from the relationship derived by combining Eqs. (4), (6), (8) and (19) and written as

$$- \overline{w\theta} \cdot \frac{d\overline{T}}{dz} = \frac{T_*^2 \, u_*}{\alpha \, Kz} \; \Phi_H \quad . \tag{67}$$

Similar results for humidity were not obtained since $\overline{\chi_q}$ could not be determined from humidity measurements, due to the limited frequency response of the Lyman-Alpha humidiometer. Calculations of production of temperature variance were based on $\alpha = 1.0$ ($K_H = K_m$), $K = 0.4$, $\Phi_H = (1-16\, z/L)^{-1/2}$, and T_* and u_* from direct covariance measurements (MITOS I u_* from an assumed C_D). Ratios of dissipation to production are also given in Table 10.

For all the cold wire runs, dissipation of temperature variance is greater than production. The smallest ratios for dissipation to production from MITOS I of 2.6 would be increased to

TABLE 10

Production and Dissipation of Temperature Variance

		Production ($^{\circ}C^{2}$/sec)	Dissipation ($^{\circ}C^{2}$/sec)	$\frac{\text{Dissipation}}{\text{Production}}$
MITOS I	-1	1.7×10^{-4}	4.3×10^{-4}	2.6
	-7	1.7×10^{-3}	4.3×10^{-3}	2.6
MITOS III-2		0.83×10^{-4}	3.2×10^{-4}	3.8
OWAX	4	2.9×10^{-4}	1.3×10^{-3}	4.6

$$\text{Production} = -\overline{w\theta}\,\frac{d\overline{T}}{dz} = \frac{T_*^2\,u_*}{\alpha K z}\,(1 - 16\,z/L)^{-1/2}$$

$$\text{Dissipation} = \frac{\overline{\chi_\theta}}{2}$$

about 3 if a 10% cup over-speeding correction is included in the calculation of $\overline{\chi_\theta}$. The values of production for the MITOS I runs would not be significantly affected by an increase in u_* if a value of $C_D = 1.5 \times 10^{-3}$ were used, since Φ_m would also increase, and the increase in Φ_m and u_* would be balanced by a comparable decrease of T_*^2.

Although dissipation of humidity variance was not directly measured, results of Section 4.7a indicate that production of humidity variance may be larger than dissipation. Using a value of $\beta_q = 0.4$, and $\Phi_H = \Phi_E$, Leavitt[11] obtained equal production and dissipation rates for humidity variance. The average implied $\beta_q \simeq 0.21$ from comparison of the direct covariances and estimates of the inertial dissipation technique, suggests that for a given $\beta_q = 0.4$, production is greater than dissipation. If the expression for $\Phi_E \neq \Phi_H$ and $\Phi_E \simeq \Phi_M$ as suggested by Leavitt's[11] flux profile analysis, the implied β_q would be more nearly equal to 0.4 if production equals dissipation.

From the direct and inertial dissipation results for temperature and the inertial dissipation results for humidity, a reconsideration of the assumptions used to simplify the scalar variance budgets seems appropriate. Eqs. (29) and (32) were obtained by assuming horizontal homogeneity and stationarity. To test the assumption of horizontal homogeneity for the temperature variance

budget, the term $-\overline{u\theta}\,\frac{dT}{dx}$ has to be considered. For the OWAX 4 run, a horizontal temperature gradient of approximately 5° C per 100 m. would be required to balance production and dissipation. This gradient is far greater than would be expected over the ocean or seen in the OWAX 4 time series of Section 4.1. Although non-stationarity may have affected the temperature results for the SOMA cruise due to the small heat fluxes measured, non-stationarity effects for the other cruises can be expected to be small as noted by Wyngaard and Coté[37] for over-land temperature measurements.

Two terms which appear in the temperature variance budget and not included for humidity are the heat transfer due to radiation, $\overline{2\theta R'}$, and the heat transfer due to viscous heating, $\overline{2\theta\epsilon}/C_p$. Effects of the terms were considered in Section 2.4. From the previous discussion it appears that the viscous heating term may be neglected. Effects of radiative heating/cooling for BOMEX conditions have been discussed by Leavitt,[11] Phelps and Pond,[10] and Pond et al.[8] Phelps and Pond[10] suggest that absorption of longwave radiation by the increased water vapor concentrations in BOMEX would tend to produce a more homogeneous temperature structure and cause suppression of large scale temperature fluctuations. This would not explain the larger differences between dissipation and production for the less humid OWAX cruise. As mentioned in Section 2.4, maximum destruction of $\overline{\theta^2}$ occurs at small scales (dissipation scales) for

internal radiative transfer (Townsend, 1958).[42] If $\overline{2\theta R'}$ were included as a dissipative term for this case, the difference between production and dissipation would be increased.

Leavitt[11] suggests that the effects of cooling by radiative flux divergence measured during BOMEX may account for differences between the temperature and humidity signals, the spectra and the cospectra. Leavitt[11] also suggests that the cooler air at heights between 50 and 400 m (as evidenced in the BOMEX potential temperature gradient) due to radiative cooling, descends by negative buoyancy adjacent to the backs of warm plumes and causes the "cold spikes". As shown in figures 7 and 9, the same phenomenon (cold spikes) are also observed for both the warm, humid conditions of MITOS I, and the cold, less humid conditions of OWAX 4. From the OWAX 4 production-dissipation results, radiative cooling alone could not account for the differences between production and dissipation for both types of conditions.

The scalar flux divergence terms for the temperature and humidity budget may amount to 25% and 10% of the production as suggested by the results of Leavitt,[11] and Wyngaard and Cote'[37] (temperature). The magnitude of temperature flux divergence is not sufficient to account for the differences between production and dissipation. If a humidity flux divergence of 10% of the production is assumed, it would result in a decrease of the implied β_q values and

lend more support to the suggestion of Leavitt[11] that $\Phi_E = \Phi_m$. Temperature profile results of Paulson et al[44] implied $\Phi_H = 0.4 (1 - 16\ z/L)^{1/2}$. This expression for Φ_H would result in a greater difference between dissipation and production than obtained using $\Phi_H = (1 - 16\ z/L)^{-1/2}$, to balance the production and dissipation results would require $\Phi_H \simeq 4\ (1 - 16\ z/L)^{-1/2}$, highly unlikely.

The remaining terms in the scalar variance budgets are the source/sink terms, S_θ and S_q, which represent contributions or losses to the variances due to interaction or possible effects of spray on the temperature and humidity fields. It is proposed that the evaporation of spray can account for differences between production and dissipation of temperature variance. Evaporation of spray in conjunction with the ramp model proposed by Gibson et al[51] can explain the ramplike structure of the temperature and humidity time traces, and can also explain the cold spikes in the temperature signal and the associated behavior of the humidity signal. Upon careful examination of the temperature and humidity time traces, they may be represented as shown in figure 69. The associated vortex structure shown below the temperature and humidity signal representations is an end view of the horizontal roll vortices of the Gibson[51] model. The wavelength of the ramps is shown as 100 meters representing the large scale ramps in figures 7, 8 and 9. The 5 m. ramps shown by Gibson et al[51] are not inconsistent with the fine scale structure shown

FIGURE 69

Ramp model for temperature and humidity over the ocean

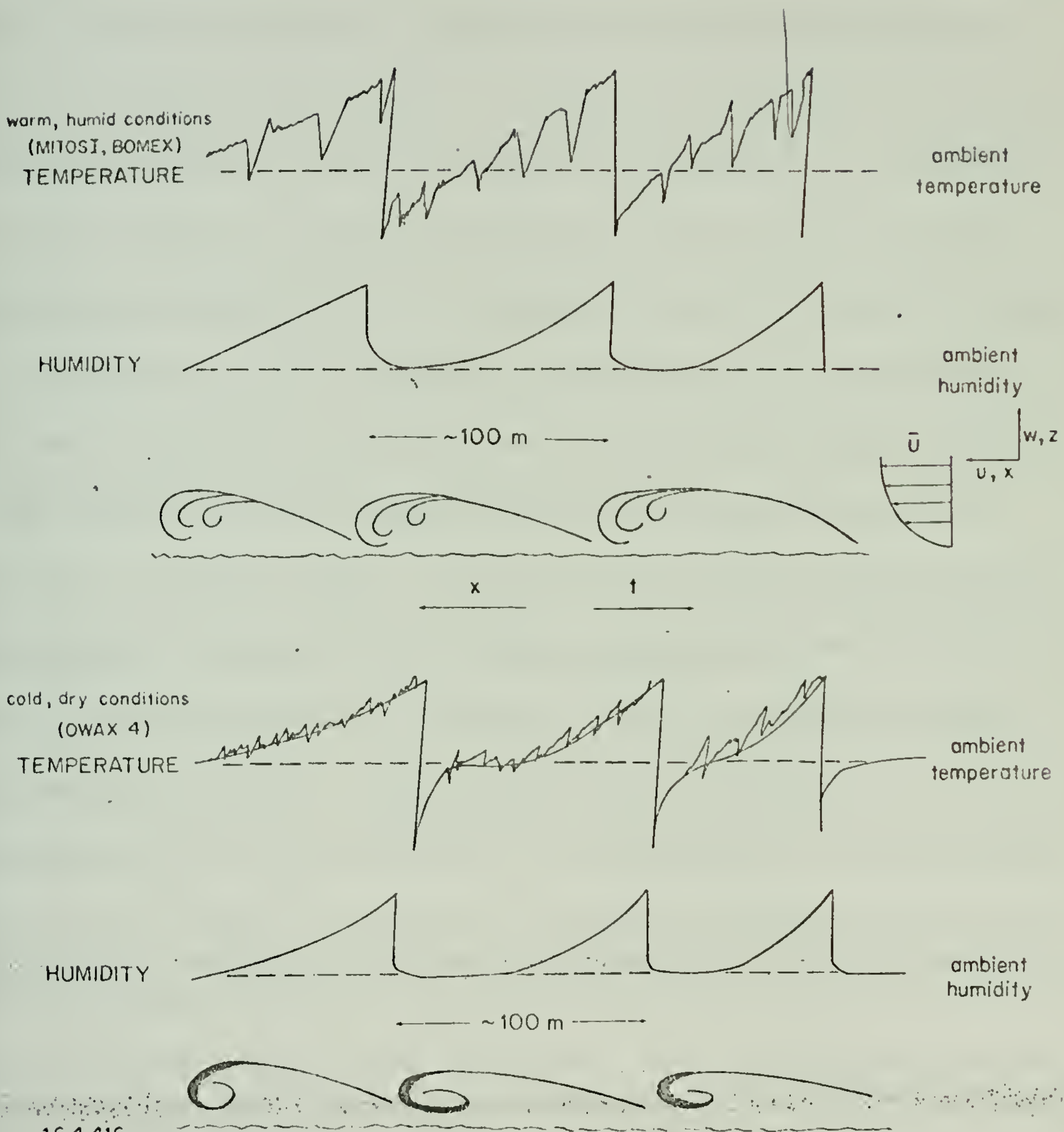
warm, humid conditions
(MITOSI, BOMEX)
TEMPERATURE
ambient temperature
HUMIDITY
ambient humidity
~100 m
Ū
w, z
u, x
x
t
cold, dry conditions
(OWAX 4)
TEMPERATURE
ambient temperature
HUMIDITY
ambient humidity
~100 m

1.6.4.416

in the magnifications of figures 7 and 9.

Water droplets of spray accumulated in fine sheets along the interfaces of the roll vortices evaporate, causing the "cold spikes" of the temperature signals. The additional source of evaporation which increases the temperature variance can account for the difference between calculated values of production and dissipation of temperature variance. Since the air above the vortex is dryer than the air within the vortex, evaporation occurs on the outer edge of the vortex cooling the overlying air. The maximum accumulation of air cooler than the ambient temperature will then be forced down at the leading interface of the vortex due to the negative buoyancy of the cooler air and the structure of the roll vortex. The descending cooler air at the leading edge of the vortex causes a cold spike, and the excess water vapor due to evaporation causes a "rounding" of the corresponding humidity minima at the interface. The small amount of "smoothing" of the humidity signal at the lower part of the ramp interface may also be due to the Lyman-Alpha humidiometer measuring a combination of water vapor and spray which has accumulated at the vortex leading edge or effects of frequency response limitations. The amount of water vapor required to account for the difference between production and dissipation is small due to the high value of the latent heat of vaporization. Similarly, the amount of water droplets required would also be small. Differences between the temperature time traces for the two

cruises will be discussed in detail in Section 5.

From a laboratory study conducted by Wu (1973)[70], the concentration of water droplets measured at velocities above 8 m/sec indicate that less than 10 droplets per m^2 (mean diameter ~ 150 μ) occur at heights between 5 and 20 cm in a wind wave tank (14 m x 1.5 m) for wind velocities less than 8 m/sec. Although it is fairly well established (Wu, 1973,[70] Krauss, 1967[71]) that droplet concentration decreases exponentially with height above the sea surface, absolute droplet concentration for a given height and wind velocity is not known.

For the OWAX 4 run, a value of $S_\theta = -1 \times 10^{-3}$ °C/sec is required to account for the difference between production and dissipation. If $\dot{S}$ (μgm/cm^3 - sec) is used to represent the adiabatic rate of evaporation, then S_θ may be written as

$$S_\theta = \frac{L_v}{\rho\, C_p} \overline{(\dot{S}\theta)} \tag{68}$$

where $\dot{S} = \overline{\dot{S}} + \dot{s}$ (the mean and fluctuating evaporation rates). If it is assumed that $\dot{s}$ and θ are perfectly anti-correlated ($r_{\dot{s}\theta} = \frac{\overline{\dot{s}\theta}}{\sigma_{\dot{s}}\,\sigma_\theta} = -1$, an increase of $\dot{s}$ results in a decrease of θ), then $\sigma_{\dot{s}}$ may be estimated from the relation

$$S_\theta \simeq \frac{L_v}{\rho\, C_p} (\sigma_{\dot{s}}\,\sigma_\theta) \tag{69}$$

For $S_\theta = -1.0 \times 10^{-3}$ °C^2/sec and $\sigma_\theta = 0.1$ °C , a value of $\sigma_{\dot{s}} = 4.0 \times 10^{-3}$ μgm/cm^3 sec is obtained. To determine if this value of $\sigma_{\dot{s}}$ is reasonable, an examination of the time series is required. If an average ΔT of 0.1 °C for the "cold spike" portion of the temperature ramp interface is assumed, the time required for evaporation to occur may be calculated from the relation.

$$\Delta t \simeq \frac{\Delta T}{L \Delta \dot{s}} \rho C_p \qquad (70)$$

obtained by integrating the time rate of change of the species concentration equation (for $T \rho C_p$ - sensible heat) and assuming the evaporation source term produces the entire temperature change (0.1 °C). For $\Delta \dot{s} = \sigma_{\dot{s}} \simeq 4 \times 10^{-3}$ μgm/cm^3 - sec , the Δt required is ~ 10 sec . For the OWAX 4 run ($\bar{U} \sim 5$ m/sec) this represents 50 meters, approximately half a ramp wavelength. For $|r_{\dot{s}\theta}| < 1$ or $\Delta T > 0.1$ the time and/or distance would be larger. Assuming that evaporation occurs along a considerable portion of the vortex interface, this result does not seem unreasonable. The resulting Δq due to evaporation is 4×10^{-2} μgm/cm^3 , much smaller than the mean water vapor concentration and yet possibly enough to cause a smoothing of the humidity minima at the ramp interface. As mentioned previously, due to effects of frequency response limitations of the Lyman-Alpha and possible sensing of water droplets, this smoothing may be

instrumental.

For the MITOS I and BOMEX conditions, the evaporation of droplets may also be occurring in conjunction with radiative cooling as suggested by Leavitt.[11] The combination of the two phenomenon could account for the imbalance of the temperature variance budget for the MITOS I data and the difference in the temperature signals of the MITOS I and OWAX cruises. Radiative cooling in the air above the roll vortices combined with evaporation would tend to break up the ramp structure and lengthen the "cold spike" as shown in figure 69 and in figures 7, 7a, 7a1, and 7a2. The difference between the two time series can also explain shape of the temperature spectra and the $w\theta$ and $u\theta$ cospectra from MITOS I. The spectral and cospectral results are discussed in Section 5.

4.8 Application of the Bulk Aerodynamic Technique for Estimation of the Turbulent Heat Fluxes

The bulk aerodynamic method relates mean wind speed and sea-air temperature and humidity differences to the fluxes of latent and sensible heat by the relations

$$\begin{aligned} H_S &= \rho C_p C_{w\theta} \overline{U} \Delta T \\ H_L &= L_v C_{wq} \overline{U} \Delta q \end{aligned} \tag{71}$$

where ΔT is the difference between sea surface temperature and air temperature at a specific height, and Δq is the corresponding absolute humidity difference (saturated at the sea surface temperature). Roll[2] has suggested that the constants $C_{w\theta} = C_{wq} = C_D$ for near neutral conditions. To include the effects of stability on the mean wind shear, and temperature and humidity profiles, the expressions of (71) may be rewritten as

$$H_S \simeq \rho \, C_p \, C_{w\theta} \, \overline{U} \, \Delta T \, \Phi_B$$

$$H_L \simeq L_v \, C_{wq} \, \overline{U} \, \Delta q \, \Phi_B \, . \qquad (72)$$

where

$$\Phi_B = \left(1 - \frac{(\sigma_H/2) + \xi}{\ell n \, (z/z_o)} \, . \, z/L\right) \quad . \qquad (73)$$

The constants $\sigma_H/2$ and ξ result from linearization of the dimensionless scalar gradient $\Phi_H (= \Phi_E)$, and the dimensionless wind shear Φ_m. The constant z_o represents the "roughness" height and will be assumed equal to one for the bulk aerodynamic calculations. Using values of $\sigma_H = 16$ and $\xi = 3.5$ (Krause, (1967)[71], and Lumley and Panofsky (1964)[19]), values of $\overline{U} \, \Delta T \, \Phi_B$ and $\overline{U} \, \Delta q \, \Phi_B$ were calculated for each run and are given in Table 11. Also given are the corresponding $\overline{w\theta}$ and $\overline{wq}$ values by the direct covariance technique, and the $C_{w\theta}$ and C_{wq} required for agreement

TABLE 11 - Bulk Aerodynamic Results

		Latent Heat Flux (μgm/cm^2 - sec)			Sensible Heat Flux (° C - cm/sec)		
		$\overline{U}\,\Delta q\,\Phi_B \times 10^{-3}$	$\overline{wq}$ direct	$C_{wq} \times 10^{-3}$	$\overline{U}\,\Delta T\,\Phi_B \times 10^{-3}$	$w\theta$	$C_{w\theta} \times 10^{-3}$
SOMA	1	3.20	3.52	1.10	1.35	0.22	0.16
	2	3.77	5.46	1.45	1.33	0.28	0.21
	3	3.43	5.99	1.75	1.07	0.42	0.39
MITOS I	1	4.99	10.08	2.02	1.85	1.19	0.64
	7	5.21	6.12	1.17	6.18	3.10	0.50
MITOS III	2	3.48	2.96	0.85	0.70	1.46	2.10
OWAX	2	2.59	2.46	0.95	0.68	1.32	1.94
	3	3.40	3.65	1.07	0.77	1.43	1.85
	4	4.09	5.11	1.25	0.82	1.20	1.45

between the bulk aerodynamic method and the direct estimates.

The average value of C_{wq} is $(1.29 \pm 0.36) \times 10^{-3}$, in agreement with the value suggested by Pond et al[8] of $(1.20 \pm 0.24) \times 10^{-3}$ for BOMEX results. For the pitch corrected covariances (MITOS III and OWAX), $C_{wq} = 1.03$, suggesting $C_{wq} < C_D$, similar to the result of Pond et al[8] for pitch corrected covariances using estimated pitch angles.

The large range of the $C_{w\theta}$ values suggests that the bulk aerodynamic method is not useful in estimating the sensible heat flux. Trends in the data indicate that for warm humid conditions the bulk aerodynamic method over-estimates the sensible heat flux, and under-estimates the flux for colder, less humid conditions. Similar results were obtained by Pond et al[8] with regard to lack of agreement between the direct and bulk aerodynamic techniques, however, the sense of the disagreement was reversed.

Results of this work and those of Pond et al[8] indicate that estimates of total heat flux (sensible + latent) based on one flux measurement by the bulk aerodynamic method and an average BOWEN ratio should employ the latent heat flux instead of the sensible heat flux to estimate the total heat flux.

5. SUMMARY AND CONCLUSIONS

The primary objectives of this work were to measure the turbulent fluxes of momentum, sensible and latent heat by the direct covariance method corrected for instrument motion, and compare the direct measurements to estimates of the fluxes by the inertial and direct dissipation techniques. Stability corrections were applied to the estimates of the fluxes by the dissipation techniques.

5.1 Momentum Flux

Directly measured $\overline{uw}$ covariances, corrected for internal sensor alignment and instrument tilt using measured pitch angles, had an average uncertainty of ± 25%. Sources of errors were discussed in Section 4.3. The corrected covariances were compared to the $\overline{uw}$ values which would have been obtained using two different methods of estimating the mean pitch angle in lieu of actually measuring the angle. Results of the comparison suggest that for small pitch angles $(< 2^\circ)$ with small variations $(\sigma_\varphi < 0.5\,\overline{\varphi})$; corrections based on $\varphi = \sin^{-1} \overline{W}_m / \overline{U}_m$ tend to underestimate the pitch correction, and those based on $R_{uw}(f) = -0.5$; for $0.01 < f < 0.1$ Hz, tend to overestimate the pitch correction. The value of the spectral correlation coefficient for the measured pitch angle corrected covariances was $R_{uw}(f) = -0.32 \pm 0.08$. For the MITOS III uw covariance with $\sigma_\varphi > \overline{\varphi} < 1^\circ$, the instantaneous pitch correction applied to the data gave a uw value

comparable to results of the other two methods. The estimated pitch angles, however, were higher than the measured pitch angle.

The measured $\sigma_u/u_* = 2.8 \pm 0.5$, was comparable with the results of Leavitt[11] from similar open ocean velocity measurements using estimated pitch angle corrections, and Mitsuta and Fujitani[55] using inertial reference frame corrections for ship motion. Pitch corrected σ_w/u_* results followed the predicted $(-z/L)^{1/3}$ behavior and were comparable with the results of Leavitt[11] and Pond et al.[8] Values of σ_w/u_* for this work were higher than the results of Wyngaard et al[58] obtained over land.

Vertical velocity fluctuations over the open ocean may have more low frequency energy containing eddies than over land as suggested by the scalar ramp model and associated horizontal roll vortices shown in figure 69. Discussion of the time series in Section 4.1 included the observation that warm, humid air was associated with upward vertical velocity and negative horizontal velocity changes, with the opposite also being true for colder, less humid air. The associated anisotropy of the velocity field due to the large eddy structure which determines the scalar field structure is supported by the results of Gibson et al,[51] who found positive skewness values of about 0.5 for $(\partial w/\partial x)$ when conditionally sampled (i. e. when $\overline{w} \sim 0$), as compared to the isotropic value of zero.

The average correlation coefficient for the pitch corrected results was $r_{uw} = -0.26 \pm 0.08$, also in agreement with the results of

Leavitt[11] and Pond et al.[8] To remove possible stability dependence of the correlation coefficient, the r_{uw} values were normalized with the expression for the non-dimensional dissipation of kinetic energy. Using $\Phi_{\epsilon_1}^{2/3} = (\Phi_m - z/L)$, the resultant normalized value was $\tilde{r}_{uw} = -0.25 \pm 0.06$, comparable to the result of Miyake et al[33] for near neutral conditions.

Velocity f_N - spectra, normalized to include stability effects agreed within the given uncertainties of the u_*^2 values with the results of Leavitt[11] and Kaimal et al,[56] and followed the predicted $f_N^{-2/3}$ inertial subrange behavior. Values of 0.29 ± 0.06 (horizontal velocity spectra) and 0.40 ± 0.09 (vertical velocity spectra) for the f_N - spectral constants were in better agreement with the predicted constants using the dimensionless dissipation expression for Φ_{ϵ_1} (as above). Lower values of the constants were obtained using the form of $\Phi_{\epsilon_2}^{2/3} = (1 + 0.5|z/L|^{2/3})$ suggested by Wyngaard and Coté.[37] Scatter in the spectral results for the first two cruises was attributed to x-wire drift, possible cup over-speeding errors, and uncertainties in the calculated u_* values from an assumed $C_D (1.3 \times 10^{-3})$. Spatial averaging effects and distortion of the vertical sensing path of the sonic anemometer (OWAX) caused a steeper roll-off in the high frequency end of the u and w spectra for the last two cruises than the first two cruises using x-wire anemometers.

The normalized pitch corrected momentum flux f_N - cospectra

were similar to uw cospectra obtained by Leavitt[11] and Pond et al.[8] The uw cospectra subrange constant for this work, $\alpha_{uw} \cong 0.01$, was lower than comparable estimates of α_{uw} by Leavitt[11] (0.07) and Kaimal et al[56] (0.05). The lower α_{uw} value may be due to a combination of high frequency noise in the uw cospectra and possible distortion of the sonic anemometer (vertical path) as mentioned above. However, the high frequency behavior of the cospectra followed the predicted $f_N^{-4/3}$ subrange slope over nearly a decade for $f_N > 0.1$. This indicates the lower α_{uw} value may be real and suggests that production of kinetic energy may occur at larger scales over the open ocean than over land under certain conditions. A shift of production of kinetic energy to larger scales is consistent with the ramp model, with well defined horizontal roll vortices for the colder, less humid conditions as shown in the bottom portion of figure 69.

Comparison between estimates of the momentum flux by the direct covariance and inertial dissipation techniques was made using a $k^{5/3}$ spectral representation of the data, illustrating the approach and agreement with the predicted $k^{-5/3}$ power law behavior required for application of the inertial dissipation technique. Agreement was obtained between direct covariance estimates of momentum flux, and inertial and direct dissipation estimates within the uncertainties of the direct estimates, applying the assumption that total production of kinetic energy (mechanical + buoyant) was equal to dissipation (Φ_{ϵ_1}).

Lower estimates of momentum flux were obtained by the dissipation techniques using the expression suggested by Wyngaard and Coté (Φ_{ϵ_2}). The average value of the velocity inertial subrange constant from the direct dissipation technique was $\alpha_u = 0.53 \pm 0.03$. Trends in the direct dissipation estimates of momentum flux suggest that turbulent transport cannot be neglected in the marine boundary layer and may be approximately half of the estimates of dimensionless turbulent transport over land (Wyngaard and Coté[37]).

5.2 Latent Heat Flux

The pitch corrected $\overline{wq}$ covariances had an average uncertainty of $\sim \pm 10\%$. Larger uncertainties could be attributed to the uncorrected $\overline{wq}$ direct estimates which were probably determined within $\pm 25\%$. Values of σ_q/σ_* for this work followed the predicted $(-z/L)^{-1/3}$ behavior with $C_q \simeq 0.95$. Values of σ_q/q_* were lower than corresponding σ_θ/T_* values, and were lower than the σ_q/q_* results of Phelps and Pond[10] and Leavitt[11] for BOMEX data. The average correlation coefficient for the water vapor flux results was $r_{wq} = 0.43 \pm 0.11$, with a trend in the r_{wq} values from the colder, less humid cruises to be higher than results from the warm, humid cruises. To remove trends due to stability effects, normalized correlation coefficients ($\tilde{r}_{wq}$) were calculated, using $\Phi_H^{1/2}\,\Phi_\epsilon^{1/6}$ for the normalization. The trend remained in the $\tilde{r}_{wq}$ values and may be due to the better defined ramp and associated vortex structure shown at

the bottom of figure 69 for the colder, less humid conditions, as compared to the warm, humid conditions. Values of r_{wq} and r_{uq} for the warm, humid conditions were comparable to results of Phelps and Pond[10] from BOMEX measurements.

Normalized humidity f_N - spectra and water vapor flux cospectra collapsed well and were similar to velocity spectra and cospectra. Humidity spectra followed the predicted $f_N^{-2/3}$ behavior. Normalized wq and wθ cospectra from the colder, less humid conditions were also similar, reflecting the similarities in the temperature and humidity ramp structure for those cruises, as compared to the warm, humid conditions. Normalized water vapor flux cospectra exhibited an $f_N^{-4/3}$ subrange behavior with an average value of the cospectral subrange constant of $\alpha_{wq} = 0.08 \pm 0.02$. The results did not include the OWAX value of $\alpha_{wq} \simeq 0.03$. Comparison of α_{wq} and α_{uw} values suggested the vertical transport of water vapor is similar to transport of momentum for small and large scales, especially true for the colder, less humid conditions. Normalized horizontal water vapor flux cospectra exhibited an $f_N^{-3/2}$ subrange behavior with a trend in the α_{uq} values suggesting relatively more efficient transport of horizontal water vapor flux at small scales for warm, humid conditions. This result is also consistent with the ramp model shown in figure 69, where the smaller scales are more pronounced for the warm, humid conditions (upper portion of figure 69). Comparison of the α_{wq} and α_{uq} results

indicated vertical transport of water vapor is always more efficient than the horizontal transport for smaller scales.

A normalized $k^{5/3}$ spectra representation was used for comparison of latent heat flux estimates by the direct covariance and inertial dissipation techniques. Due to uncertainty of the actual value of the humidity subrange constant β_q, the spectra were plotted to represent the implied β_q required for agreement between the two estimates of the latent heat flux. An average $\beta_q = 0.21 \pm 0.05$ was required for agreement. The direct dissipation technique was not applied to estimates of latent heat fluxes since the frequency response of the Lyman-Alpha humidometer, used to measure humidity fluctuations, was not sufficient for direct estimates of dissipation of humidity variance. The implied β_q was lower than $\beta_q = 0.41$ obtained by Pacquin and Pond[65] from measurements of 2nd and 3rd order structure functions. For $\beta_q = 0.41$, the $k^{5/3}$ humidity spectra results suggest $\Phi_E = \Phi_M$ for production of humidity variance equal to dissipation, or production greater than dissipation for $\Phi_E = \Phi_H$. The β_q for this work is comparable to $\beta_q = 0.25$ suggested by Leavitt[11] based on the flux-profile results of Paulson et al,[44] and also comparable to the results of Smedman-Högström (1972),[72] who obtained a value of $\beta_q = 0.29 \pm 0.10$ from measurements over land in Northern Sweden, assuming production equaled dissipation.

5.3 Sensible Heat Flux

Directly measured $\overline{w\theta}$ direct covariances, corrected for pitch effects, were determined with uncertainties of ~ ±10%. Uncorrected direct $\overline{w\theta}$ values for the SOMA cruise were subject to x-wire drift (in w), temperature calibration uncertainties, and possible effects of non-stationarity for near neutral stability conditions. The average SOMA and MITOS I direct $\overline{w\theta}$ values are probably estimated within ± 25%, although this uncertainity may be higher for the SOMA cruise. Values of σ_θ/T_* for the MITOS I, MITOS III and OWAX cruises follow the predicted $(-z/L)^{-1/3}$ behavior with $C_T = 0.95$ as suggested by Wyngaard et al.[58] The σ_θ/T_* values for the warm, humid cruises are higher than σ_q/q_* and more comparable to BOMEX results of Leavitt,[11] and Phelps and Pond[10] than the results of the colder, less humid cruises. High values of σ_θ/T_* for the SOMA cruise were attributed to uncertainties in u_* values (from an assumed C_D) and possible effects of non-stationarity.

Significant differences were exhibited between average values of the correlation coefficient, $r_{w\theta}$, for the colder, less humid cruises corrected for pitch ($r_{w\theta} = 0.48 \pm 0.04$), and the warm, humid cruises (0.16 ± 0.11), not accounted for by lack of pitch corrections for the warm, humid cruises. The $r_{w\theta}$ correlation coefficients were normalized in the same manner as was done for the r_{wq} values to remove any trends due to stability effects. Normalized correlation

coefficients, $\tilde{r}_{w\theta}$ exhibited similar trends as the non-normalized values, however, less pronounced. The higher values of $r_{w\theta}$ and $\tilde{r}_{w\theta}$ for the colder, less humid cruises can be attributed to the well defined ramp structure for those cruises, illustrated in the bottom portion of figure 69. The average value of the normalized correlation coefficients was $\tilde{r}_{w\theta} = 0.21 \pm 0.1$, comparable to the result of Miyake et al[59] ($r_{w\theta} = 0.24 \pm 0.2$) for near neutral conditions. No significant trend in the $r_{u\theta}$ values were observed.

Normalized temperature f_N - spectra from different cruises with different meteorological conditions did not compare with one another, and were not similar to humidity or velocity spectra. Normalized sensible heat flux cospectra exhibited similar differences, however, the $w\theta$ cospectra from the colder, less humid cruises were somewhat similar to the corresponding wq cospectra. Temperature spectra from the warm, humid MITOS I cruise exhibited a $f_N^{-2/3}$ behavior and were similar to temperature spectra obtained by Leavitt,[11] and Phelps and Pond[10] for BOMEX data. Temperature spectra from the colder, less humid cruises appeared to follow a -1/4 power law behavior over nearly 2 1/2 decades of normalized frequency above $f_N \simeq 0.5$. The normalized temperature spectra from the warm, humid cruises in general exhibited higher spectra levels than the spectra from colder, less humid cruises. If it is assumed that evaporation of spray is contributing to the suppression of low frequency temperature

fluctuations (discussed in the next section), spectra obtained at heights farther from the surface should have higher normalized low frequency spectral levels than spectra from lower heights. Evidence of this effect can be observed by comparison of the $k^{5/3}$ temperature spectra (figure 63) from MITOS III (12. 5 m.) and OWAX (3. 5 m.) for the colder, less humid conditions, and comparison of 8 m. and 30 m. temperature spectra obtained by Leavitt.[11] In both cases, spectra obtained at greater heights above the ocean surface exhibit more pronounced low frequency energy. Leavitt[11] suggested that the higher low frequency 30 m. spectral levels may be due to radiational heating of the thermocouples, however, he noted that not all periods of daylight showed the low frequency fluctuations.

Normalized $\overline{w\theta}$ cospectra exhibited an $f_N^{-4/3}$ behavior, with higher values of $\alpha_{w\theta}$ associated with warm, humid conditions. The shape of the normalized $\overline{w\theta}$ cospectra and the $\alpha_{w\theta}$ values indicated that production of temperature variance is shifted to smaller scales for the warm, humid conditions, and that under these conditions the vertical transport of heat can be 6 times more efficient than momentum for smaller scales. The temperature ramp structures represented in figure 69 indicate more small scale activity for the warm, humid conditions supporting the cospectral evidence. Normalized horizontal heat flux cospectra exhibited differences similar to the $w\theta$ cospectra. The $u\theta$ cospectra followed the predicted

$f_N^{-3/2}$ inertial subrange behavior with values of $\alpha_{u\theta}$ which indicated that horizontal transport of heat was also shifted to smaller scales under warm, humid conditions. The "cross-over" point of the $w\theta$, $u\theta$ and θq cospectra was that value of f_N above or below which the cospectra from the warm, humid conditions exhibited higher $(> f_N)$ or lower $(< f_N)$ cospectral levels than cospectra from the colder, less humid conditions. The value of f_N at the cross-over point represents approximately 50 meters, which corresponds to half a ramp wavelength as shown in figure 69. For larger scales than 50 meters temperature is less correlated with velocity or humidity for the warm humid conditions, and the reverse true for scales smaller than 50 meters. The "cold spike" of the warm humid conditions is not as sharp as the "cold spike" for the colder, less humid conditions, reducing the similarities between temperature and humidity (and velocity presumably) for scales larger than half a ramp wavelength. Smaller scales in the temperature field are more pronounced for the warm humid conditions as illustrated in the top portion of figure 69, associated with a "breaking-up" of the roll vortices as shown. The break-up of the roll vortices and associated ramp structure may be due to combined effects of evaporation (less pronounced for warm, humid conditions) and descending overlying cool air due to radiative cooling as suggested by Leavitt[11] for BOMEX conditions. The $\alpha_{u\theta}$ and $\alpha_{w\theta}$ results also suggested that vertical transport of heat is always more efficient than

the horizontal transport for smaller scales as found by Kaimal et al[56] over land; the reverse was also true for larger scales.

Comparison of the inertial dissipation and direct covariance techniques for estimating sensible heat flux was made in the same manner as was done for latent heat flux. For agreement between the two techniques a value of the inertial subrange constant for temperature of $\beta_\theta \simeq 2$ was required. The $k^{5/3}$ temperature spectra indicated that under colder, less humid condition over the ocean, temperature may not exhibit an inertial subrange (slope -5/3) for scales corresponding to $k < 0.3\ \mathrm{cm}^{-1}$. Temperature measurements should be made out to scales as small as 6 cm in wavelength when applying the inertial dissipation technique. As mentioned above, lack of an inertial subrange for temperature, under cold, dry conditions may be due to evaporation of spray. The inertial subrange of temperature is most pronounced for the warm, humid-conditions, even with a shift of larger production scales toward the diffusive scales. The subrange only extends to the point where the production scales of the associated $w\theta$ cospectra (warm, humid conditions) no longer are dominant ($w\theta$ cospectral levels go to zero).

Estimates of $\overline{w\theta}$ by the direct dissipation technique were higher than direct covariance estimates by a factor of 2 or more. Corresponding estimates of the inertial subrange constant for temperature, β_θ, varied from 0.7 ± 0.07 to 2.4 ± 0.2. From

direct estimates of the dissipation of temperature variance $(\overline{\chi}_\theta/2)$ and sensible heat flux $(\overline{w\theta})$, with uncertainties of ± 20% and ± 10% respectively, dissipation of temperature variance was found to be higher than production $(-\overline{w\theta}\,\frac{dT}{dz})$ by as much as a factor of 4. The differences could not be accounted for by uncertainties in the direct estimates, or by temperature flux divergence which may be as much as 25% of production (Leavitt[11]). Differences between production and dissipation of temperature variance could be accounted for by consideration of sources of production usually neglected in the temperature variance budget and attributed to the combined effects of ocean spray evaporation and radiative cooling.

The high β_θ values from the direct dissipation technique (which does not require the assumption of production equal to dissipation of temperature variance) may be due to the effect of internal radiative transfer (Townsend[42]) which tends to destroy $\overline{\theta^2}$ at diffusive scales or spray droplets (more likely for the warm, humid conditions with higher β_θ values) hitting the cold wire probes and reducing the high frequency response. There is evidence that spray can hit probes since the x-wire probes for the MITOS I and SOMA cruises (warm, humid) were affected by salt contamination which produced drift in the calibrations. Both of the above effects would reduce the high frequency area under the θ - spectra and increase the estimate of β_θ.

From the inertial and direct dissipation results, use of the

dissipation techniques for estimation of sensible heat flux over the open ocean is somewhat tenuous due to the inapplicability of the assumption that production equals dissipation of temperature variance, and the possible lack of an inertial subrange.

5.4 Model of the Atmospheric Surface Layer Over the Ocean

In Section 4.7c a model of the structure of the atmospheric surface layer over the ocean was proposed consisting of horizontal roll vortices with axis aligned perpendicular (or nearly so) to the mean flow, influenced by the combined effects of evaporation of ocean spray and radiative cooling. The structure of the roll vortices is determined by the characteristics of the wind shear which brings up warm, moist positively buoyant air, balanced by the negative bouyancy of cooler overlying air due to evaporation and/or radiative cooling (inversion layer). For cold, dry conditions, evaporation of spray droplets entrained in the vortex interfaces is enhanced, resulting in a more organized vortex structure, exhibited by the well-defined ramp structure in both the temperature and humidity signals. Under these conditions, the signals are more intermittent, with relatively more quiescent periods. Larger production scales of temperature and humidity variance are dominant. The roll vortices are stretched out since the negative buoyancy of cool air at the vortex interface due to evaporation acts as a cohesive agent. Cold spikes are well defined and of short duration since only a relatively small amount of mixing of warm and cold (humid and dry) air takes place at the leading (down

wind) vortex interface. The temperature and humidity signals are well correlated. Relatively large $\overline{\chi}_\theta$ values are obtained and corresponding lower β_θ values due to the existence of well defined dissipative scales. The β_θ estimates are higher than over land due to antisotropy in the small scales. There is not a pronounced inertial subrange in the temperature spectrum since the intermediate (transfer) scales are damped by the effects of evaporation. Under these conditions, as the height above the sea surface increases, the effects of spray evaporation will be less pronounced since spray concentration decreases exponentially with height.

Under warm conditions, with higher absolute humidity levels, the vortex structure and associated ramp structure of the scalars begin to break-up. Less evaporation of spray occurs and effects of radiative interaction with the temperature field due to increased water vapor concentrations tends to produce a more homogeneous temperature structure and cause suppression of large production scales. Radiative cooling in the overlying air (inversion layer) also contributes to the break-up of the vortex structure and associated temperature and humidity signals. Cold spikes are of longer duration and more spread out due to better mixing within the vortex structure. This results in less correlation between temperature and humidity (and velocity) at larger scales, and a shift of production to smaller scales. Relatively smaller $\overline{\chi}_\theta$ values are obtained and corresponding higher β_θ values

due to the suppression of both large scales (long wave radiative transfer) and diffusive scales (internal radiative transfer). Suppression of the small diffusive scales may also be due to frequency response degradation of the cold wire probes due to increased water droplet concentration. The intermediate inertial scales are more pronounced resulting in a well defined inertial subrange for temperature. The imbalance between production and dissipation of temperature variance can thus be attributed to effects of evaporation and combined effects of long and short-wave radiative transfer.

The exact effects of evaporation and radiative transfer on production and dissipation of humidity variance is not known since no direct dissipation measurements could be made. There appears to be a slight shift to smaller scales of humidity for warm, humid conditions with radiative transfer. Conversely, the larger scales are more pronounced with relatively higher rates of evaporation occurring under cold, dry conditions. From measurements over land (flat alluvial plain), Martin (1972)[73] suggests that at heights from 2-4 m. large scale fluctuations contribute more to humidity variance than temperature variance, and that the characteristic scale of the humidity field may be larger than that of temperature by about a factor of two.

The model proposed above for lower levels of the marine does not appear to be in conflict with recent models of the marine boundary

layer. Within the last few years, studies of the structure of the marine boundary layer have become highly sophisticated with the development and application of ultra sensitive radar, reliable low level aircraft observations, and fine scale measurements of velocity, temperature and humidity. From aircraft measurements of momentum, sensible and latent heat fluxes during Operation BOMEX, Grossman and Bean (1973)[74], and Bean et al (1972)[75] (water vapor flux only) have suggested that the structure of the marine boundary layer at the 18-150 m. level consists of a combination of linear, buoyant, convective plumes or horizontal roll vortices at large and small scales, and random cellular convective elements. Work of Konrad (1970)[76] and Lemone (1972)[77], based on radar soundings and aircraft data, appear to support the model of Grossman and Bean[74], however, Lemone[77] suggests that the horizontal structures observed at wavelengths from 1.5 to 6.5 km.(near neutral conditions) may coexist with other scales of motion (large and small) with increasing instability. Bean et al[75] suggest that from humidity measurements (at 18-125 m.) smaller scales are observed on crosswind runs, indicating more than one scale may be dominant in the marine boundary layer. Their humidity time series exhibit the ramp (sawtooth) structure for along wind runs (along wind is that measured from FLIP), and a "top hat" structure is observed on crosswind runs. Gibson et al[51] note that buoyant plumes may produce the distinctive sawtooth behavior but that they are only a sufficient and

not a necessary condition for ramps to exist.

Lemone[77] has suggested that the horizontal roll vortices axes may be between -5° and 20° to the left of the geostrophic wind. Leavitt[11] suggests ~ 10° axes orientation and a wavelength of ~ 1.4 km for the roll vortices during BOMEX. The MITOS I and OWAX time series (figures 7-9) suggest that different scales can coexist within an individual ramp structure, from wavelengths of 100-200 m, down to scales comparable to those of the Gibson et al[51] model or smaller. It seems reasonable to expect that scales from 1-6 km (Lemone[77]) may also contain smaller scales.

Results of the MITOS I and OWAX cospectra analysis suggest that the dominant scale size governing the transport of heat can vary according to the meteorological conditions. The scale sizes can also vary with height as suggested by comparison of the MITOS III and OWAX $w\theta$ and $u\theta$ results for cold, dry conditions, and by comparison of Leavitt's[11] 8 m and 30 m temperature spectra and sensible heat flux cospectra. In both cases (not as pronounced for the cospectra), the larger scales ($f_N < 0.01$) have more energy (normalized) for Leavitt's[11] 30 m data than for the 8 m. Leavitt[11] suggests the low frequency enhancement may be due to radiational warming of thermocouples, however, he also states that not all periods of daylight exhibited the low frequency fluctuations.

Leavitt[11] has suggested that air-sea temperature differences

and sea surface temperature fluctuations may also contribute to differences between temperature and humidtiy measured in a cold, dry environment as compared to warm humid conditions. The air-sea temperature differences for MITOS I and OWAX were comparable suggesting that this is not a significant factor. Possible coupling between internal wave events, low frequency sea surface temperature fluctuations, and air temperature fluctuations, however, may be affecting the temperature structure in at low levels in the atmospheric surface layer.

Measurements of temperature over land as compared to results over the ocean indicate that the positive buoyancy generated by humidtiy differences (enhanced by sensible heat transfer) can sustain a vortex structure (ramp structure) much better when only evaporation occurs. Boston and Burling's[66] result of $\beta_\theta = 0.8$ over a semi-moist flat suggests that additional buoyancy of water vapor and corresponding evaporation may account for the higher β_θ value due to the anisotropy of the temperature field with a ramp structure. The positive buoyancy and lack of evaporation over dry land (ex. Kansas) may not be sufficient to sustain roll vortices when coupled with more severe surface roughness condition, although Haugen et al[25] have suggested that buoyant plumes can effect the heat transport process over land.

In conclusion it appears that the temperature spectra (and β_θ values) and sensible heat flux cospectra do not follow universal

similarity over the ocean. The humidity spectra and cospectra may require modified scaling than what is normally used now to follow similarity predictions and the influence of evaporation and radiative transfer on the spectra and cospectra is not clear. Differences between production and dissipation of temperature variance, and the behavior of the temperature spectra and sensible heat flux cospectra could be accounted for by consideration of other sources of production usually neglected in the temperature variance budget, and attributed to the combined effects of ocean spray evaporation and radiative heating/cooling in light of the model proposed for the lower levels of the marine boundary layer.

5.5 Recommendations for Further Study

Application of the dissipation technique for estimation of sensible and latent heat and the bulk aerodynamic technique for estimation of sensible heat requires further study. A quantitative evaluation of the influence of evaporation of ocean spray on both the temperature and humidity variance budgets and the spectra and cospectra is desirable. This would include extension of the laboratory work conducted by Wu[70] to field experiments over the ocean to determine droplet concentrations, variations with height, and rate of evaporation for various meteorological conditions. The possible problem of water droplet discrimination of the Lyman-alpha sensor should be investigated. This could be done in conjunction with simultaneous laser spray

measurements. A dynamic frequency response calibration of the cold wire probes is needed; this work currently is underway in the research group at UCSD.

The influence of sea surface temperature fluctuations and coupling between internal wave events, sea surface temperature fluctuations, and air temperature fluctuations also requires further study. The temperature cold spikes and ramp structure may also be associated with the above phenomena, and also correlated with surface waves.

The influence of radiation on both the temperature and humidity fields also require further study. A promising laboratory investigation is currently underway at the large water-wave facility at the Institut de Mechanique Statistique de la Turbulence, in Marseille, France, (Coantic and Favre (1970)[78], (1973)[79]) to determine the effects of radiation, evaporation, water waves, and stability conditions on the transfer phenomenon under controlled conditions.

Application of various models of the marine boundary layer for the understanding of the physical processes occurring at the interface is indispensable. It appears that various proposed models may not be in conflict with one another and that different phenomena occurring simultaneously may account for the various model types.

Instantaneous corrections to the turbulent fluxes based on all components of motion relative to an inertial reference frame require further study. This work is currently underway at UCSD using outputs of a Litton inertial platform (see figure 3) and techniques similar to those employed by Mitsuta and Fujitani.[55] Recent work by Friche (1974)[80] indicates that fluxes determined by the direct covariance technique using a sonic anemometer to measure velocity, may be affected by contamination of the velocity measurements by temperature fluctuations. A major effect is on the shape of the cospectra, especially the horizontal heat flux cospectra. Effects of this contamination require further study.

REFERENCES

1. Taylor, G. I., "Some Early Ideas About Turbulence," J. Fluid Mech., 41, 3-11 (1970).

2. Roll, H. U., "Physics of the Marine Atmosphere," New York, Academic Press, 426 (1965).

3. Benton, G. S. (Chairman), "Report of Joint Panel on Air-Sea Interaction," Committee on Oceanography, National Academy of Sciences - National Research Council, Washington, D.C. (1962). (Also published in part in Bul. Amer. Met. Soc., 44, 1, 4-17 (1963).

4. Charney, J. (Chairman), "The Feasibility of a Global Observation and Analysis Experiment," Report of the Panel on International Meteorological Cooperation, Committee on Atmospheric Sciences, National Academy of Science - National Research Council, NAS Pub. 1290, 172 (1966).

5. Davidson, B., "The Barbados Oceanographic and Meteorological Experiment," Bul. Amer. Meteor. Soc., 49, 9, 928-934, (1968).

6. Kuettner, J. P. and J. Holland, "The BOMEX Project," Bul. Amer. Meteor. Soc., 50, 394-402 (1969).

7. Holland, J. F., "Comparative Evaluation of Some BOMEX Measurements of Sea Surface Evaporation, Energy Flux and Stress," J. Phys. Oceanogr., 2, 476-486 (1972).

8. Pond, S., G. T. Phelps, J. E. Pacquin, G. McBean and R. W. Stewart, "Measurements of the Turbulent Fluxes of Momentum, Moisture and Sensible Heat Over the Ocean," J. Atmos. Sci, 28, 901-917 (1971).

9. Phelps, G. T., "The fluxes of Latent and Sensible Heat in the Marine Boundary Layer," Ph.D. Thesis, Oregon State University, (1971).

10. Phelps, G. T. and S. Pond, "Spectra of the Temperature and Humidity Fluctuations and the Fluxes of Moisture and Sensible Heat in the Marine Boundary Layer," J. Atmos. Sci., 28, 918-928 (1971).

11. Leavitt, E., "Spectra Characteristics and Statistics of Surface Layer Turbulence Over the Tropical Ocean," Ph.D. Thesis, Univ. of Washington, 163 (1973).

12. Gibson, C. H. and R. B. Williams, "Turbulence Structure in the Atmospheric Boundary Layer Over the Open Ocean," AGARD CP #48, Nr. 5, 5-5-9 (1969).

13. Gibson, C. H., G. R. Stegen and R. B. Williams, "Statistics of the fine Structure of Turbulent Velocity and Temperature Fields Measured at High Reynolds Number," J. Fluid Mech., 41, 153-167 (1970).

14. Stegen, G. R., C. H. Gibson and C. A. Friehe, "Measurements of Momentum and Sensible Heat Fluxes Over the Open Ocean," J. Phys. Oceanog., 3, 86-92 (1973).

15. Smith, S. D., "Thrust-Anemometer Measurements of Wind Velocity Spectra and of Reynolds Stress Over a Coastal Inlet," J. Marine Res., 25, 239-262 (1967).

16. Weiler, H. S. and R. W. Burling, "Direct Measurements of Stress and Spectra of Turbulence in the Boundary Layer Over the Sea," J. Atmos. Sci., 24, 653-664 (1967).

17. Kaimal, J. C. and D. A. Haugen, "Some Errors in the Measurement of Reynolds Stress," J. Appl. Meteor., 8, 460-462 (1969).

18. Taylor, R. J., "A New Approach to the Measurement of Turbulent Fluxes in the Lower Atmosphere," J. Fluid Mech., 10, 449-458 (1961).

19. Lumley, J. L. and H. A. Panofsky, The Structure of Atmospheric Turbulence, New York, Interscience, 239p., (1964).

20. Kolmogorov, A. N., "The Local Structure of Turbulence in an Incompressible Viscous Fluid for Very Large Reynolds Number," Dokl. AN SSSR, 30, 301-305 (1941).

21. Obukhov, A. M., "Structure of the Temperature Field in a Turbulent Current," Izv. Akad. Nauk. SSSR, Ser. Geog. Geofiz., 13, #1, 58, (1949).

22. Corrsin, S., "On the Spectrum of Isotropic Temperature Fluctuations in an Isotropic Turbulence," J. Appl. Phys., 22, 469-473, (1951).

23. Obukhov, A. M., "Turbulence in an Atmosphere with Inhomogeneous Temperature," Tr. Inst. Teoret. Geofiz. Akad. Nauk. SSSR, 1, 95-115, (1946).

24. Monin, A. S. and Obukhov, A. M., "Basic Laws of Turbulent Mixing in the Surface Layer of the Atmosphere," Tr. Geofiz. Inst. Akad. Nauk. SSSR, 24(151), 163-187, (1954).

25. Haugen, D. A., J. C. Kaimal and E. F. Bradley, "An Experimental Study of Reynolds Stress and Heat Flux in the Atmospheric Surface Layer," Quart. J. Roy. Meteor. Soc., 97, 168-180, (1971).

26. Dyer, A. J. and B. B. Hicks, "The Spatial Variability of Eddy Fluxes in the Constant Flux Layer," Quart. J. Roy. Met. Soc., 98, 206-212, (1972).

27. Monin, A. S. and A. M. Yaglom, Statistical Fluid Mechanics, Vol. 1. Mechanics of Turbulence, MIT Press, Cambridge, Mass., 769 p., (1971).

28. Busch, N., H. Tennekes, H. A. Panofsky, "Turbulence Structure in the Planetary Boundary Layer," Pt. 1, B. L. Meteor. 4, 212-240, (1973).

29. Businger, J. A., J. C. Wyngaard, Y. Izumi and E. F. Bradley, "Flux-Profile Relationships in the Atmospheric Surface Layer," J. Atmos. Sci., 28, 181-189, (1971).

30. Paulson, C. A., "The Mathematical Representation of Wind Speed and Temperature Profiles in the Unstable Atmospheric Surface Layer," J. Appl. Meteor., 9, 857-861, (1970).

31. Badgley, F. I., C. A. Paulson, M. Miyake, *Profiles of Wind, Temperature, and Humidity Over the Arabian Sea,* The Univ. Press of Hawaii, 62 p., (1972).

32. Dyer, A. J. and B. B. Hicks, "Flux Gradient Relationships in the Constant Flux Layer," Quart. J. Roy. Meteor. Soc., *96,* 715-721, (1970).

33. Miyake, M., M. Donelan, G. McBean, C. Paulson, F. Badgley and E. Leavitt, "Comparison of Turbulent Fluxes Over Water Determined by Profile and Eddy Correlation Techniques," Quart. J. Roy. Meteor. Soc., *96,* 132-137, (1970).

34. Busch, N. and H. A. Panofsky, "Recent Spectra of Atmospheric Turbulence," Quart. J. Roy. Meteor. Soc., *94,* 132-148, (1968).

35. McBean, G. P., R. W. Steward and M. Miyake, "The Turbulent Energy Budget Near the Surface," J. Geophys. Res., *76,* 6540-6549, (1971).

36. Hicks, B. B., and A. J. Dyer, "The Spectral Density Technique for Determination of Eddy Fluxes," Quart. J. Roy. Meteor. Soc., *98,* #418, 838-944, (1972).

37. Wyngaard, J. C., and O. R. Coté, "The Budgets of Turbulent Kinetic Energy and Temperature Variance in the Atmospheric Surface Layer," J. Atmos. Sci., *28,* 190-201, (1971).

38. Coantic, M., and D. Leducq, "Turbulent Fluctuations of Humidity and Their Measurement," Radio. Sci., *4,* 1169-1174, (1969).

39. Plate, E. J., *Aerodynamic Characteristics of Atmospheric Boundary Layers,* US AEC Tech. Info. Center, Oakridge, Tenn., 180 p., (1971).

40. Friehe, C. A., "Generation of Temperature Fluctuations in the Atmospheric Boundary Layer," APS Bul., *18,* 1488, (1973).

41. Goody, R. M., *Atmospheric Radiation,* Oxford, Clarendon Press., 436 p., (1964).

42. Townsend, A. A., "The Effects of Radiative Transfer on Turbulent Flow of a Stratified Fluid," J. Fluid Mech., 4, 361-375, (1958).

43. Coantic, M., and B. Seguin, "On the Interaction of Turbulent and Radiative Transfers in the Surface Layer," B. L. Meteor., 1, 245-263, (1971).

44. Paulson, C. A., E. Leavitt, and R. G. Fleagle, "Air-Sea Transfer of Momentum, Heat, and Water Determined From Profile Observations During BOMEX," J. Phys. Oceangr., 2, 487-497, (1972).

45. Panofsky, H. A., "The Spectrum of Temperature," Radio Science, 4, 1143-1146, (1969).

46. Deardorff, J. W., "The Countergradient Heat Flux in the Lower Atmosphere and in the Laboratory," J. Atmos. Sci., 23, 503-506, (1966).

47. Gibson, C. H., "Digital Techniques in Turbulence Research," AGARD-AG-174, 1-26, (1973).

48. Phelps, G. T., S. Pond, and U. Garner, "Simultaneous Measurements of Humidity and Temperature Fluctuations," J. Atmos. Sci., 27, 343-345, (1970).

49. Clay, J., "Turbulent Mixing of Temperature in Water, Air and Mercury," Ph.D. Thesis, Univ. of Calif., San Diego, California, 184 p., (1973).

50. McConnell, S. O., "Anisotropy and Inertial Subrange Constants in High Reynolds Number Turbulence," Ph.D. Thesis, Univ. of Calif., San Diego, California, (1974).

51. Gibson, C. A., C. A. Friche, and S. McConnell, "Structure of Sheared Turbulent Scalar Fields," (submitted to J. Fluid Mech., Dec. 1973).

52. Deacon, E. L., and E. K. Webb, "Interchange of Properties Between the Sea and Air: Small Scale Interaction", The Sea, New York, Interscience, 43-87, (1962).

64. Kondo, J. C. G. Naito, and Y. Fujinawa, "Response of Cup Anemometer in Turbulence," J. Meteor. Soc. of Japan, 49, 63-74, (1971).

65. Pacquin, J. E. and S. Pond, "The Determination of the Kolmogorov Constants for Velocity, Temperature and Humidity Fluctuations From Second- and Third-order Structure Functions," J. Fluid Mech., 50, 257-269, (1971).

66. Boston, N., and R. W. Burling, "An Investigation of High Wavenumber Temperature and Velocity Spectra in Air," J. Fluid Mech., 55, 473-492, (1972).

67. Boston, N., "An Investigation of High Wavenumber Temperature and Velocity Spectra in Air," Ph. D. Thesis, Univ. of British Columbia, 113 p., (1971).

68. Pacquin, J. E., "A Comparison of Eddy Correlation and Dissipation Techniques for Computing the Fluxes of Momentum, Heat and Moisture in the Marine Boundary Layer," Ph. D. Thesis, Oregon State Univ., 71 p. (1972).

69. Hekestad, G., "A Generalized Taylor's Hypothesis with Application for High Reynolds Number Turbulent Shear Flows," J. Appl. Mech., 87, 735-739, (1965).

70. Wu, J., "Spray in the Atmospheric Surface Layer: Laboratory Study," J. Geophys. Res., 78, 511-519, (1973).

71. Krause, E. B., "Atmosphere-Ocean Interaction," Oxford University Press, 275 p., (1972).

72. Smedman-Högström, A., "Temperature and Humidity Spectra in the Atmospheric Surface Layer," B. L. Meteor. 3, 329-347, (1973).

73. Martin, H. C., "Humidity and Temperature Microstructure Near the Ground," Quart. J. Roy. Meteor. Soc., 98, 440-446, (1972).

74. Grossman, R. L., and B. R. Bean, "An Aircraft Investigation of Turbulence in the Lower Layers of the Marine Boundary Layer," NOAA Tech. Rep. ERL 291-WMPO4, 166 p., (1973).

53. Hasse, L., "On the Determination of the Vertical Transports of Momentum and Heat in the Atmospheric Boundary Layer at Sea," Tech. Rep. No. 188, Dept. of Oceanography, Oregon State University, 55 p., (1970).

54. Smith, S. D., "Thrust-Anemometer Measurements of Wind Turbulence, Reynolds Stress and Drag Coefficients Over the Sea," J. Geophyz. Res., 75, 6758-6770, (1970).

55. Mitsuta, Y. and T. Fujitani, "Direct Measurement of Turbulent Fluxes From a Crusing Ship," B. L. Meteor., 6, 203-217, (1974).

56. Kaimal, J. C., J. C. Wyngaard, Y. Izumi and O. Coté, "Spectral Characteristics of Surface Layer Turbulence," Quart. J. Roy. Meteor. Soc., 98, 563-589, (1972).

57. Monji, N., "Budgets of Turbulent Energy and Temperature Variance in the Transition Zone From Forced to Free Convection," Ph.D. Thesis, Univ. of Washington, 125 p., (1972).

58. Wyngaard, J. C., O. R. Coté, and Y. Izumi, "Local Free Convection Similarity and the Budgets of Shear Stress and Heat Flux," J. Atmos. Sci., 28, 1177-1182, (1971).

59. Miyake, M., Stewart, R. W., Burling, R. W., "Spectra and Cospectra of Turbulence Over the Water," Quart. J. Roy. Meteor. Soc., 96, 138-143, (1970).

60. Lai, R. J., and O. H. Shemdin, "Laboratory Investigation of Air Turbulence Above Simple Water Waves," J. Geophys. Res., 76, 7334-7350, (1971).

61. Wyngaard, J. C., and O. R. Coté, "Cospectral Similarity in the Atmospheric Surface Layer," Quart. J. Roy. Meteor. Soc., 98, 590-603, (1972).

62. Izumi, Y., and M. L. Barad, "Wind Speeds as Measured by Cup and Sonic Anemometer and Influenced by Tower Structure," J. Appl. Meteor., 9, 851-856, (1970.

63. Hyson, P., "Cup Anemometer Response to Fluctuating Wind Speeds," J. Appl. Meteor., 11, 843-848, (1972).

75. Bean, B. R., R. Gilmen, R. L. Grossman, R. McGavin, and C. Travis, "An Analysis of Airborne Measurements of Vertical Water Vapor Flux During BOMEX," J. Atmos. Sci., 29, 860-869, (1972)

76. Konrad, T. G., "The Dynamics of the Convective Process in Clear Air as Seen by Radar," J. Atmos. Sci., 27, 1138-1147, (1970).

77. LeMone, M. A., "The Structure and Dynamics of Horizontal Roll Vortices in the Planetary Boundary Layer," J. Atmos. Sci., 30, 1077-1091, (1973).

78. Coantic, M., and A. Favre, " Air-Sea Interactions Program and Facilities at I. M. S. T., Institut de Mechanique Statistique de la Turbulence, Marseille, France, Presented at 8th Symposium on Naval Hydrodynamics, C. I. T., Pasadena, Cal., (Aug. 1970).

79. Coantic, M., and A. Favre, "Activities in, and Preliminary Results of, Air-Sea Interactions Research at I. M. S. T.," Institut de Mechanique Statistique de la Turbulence, Marseille, France, Presented at 2nd IUTAM-IUGG Symposium, Charlottesville, Va., (Apr. 1973).

80. Friehe, C. A., "Effect of Temperature and Humidity Fluctuations on Sonic Anemometer Measurements," (Paper in progress (1974).

APPENDIX 1

NORMALIZED CORRELATION COEFFICIENTS

Correlation coefficients presented and discussed in Section 4.4 were normalized to remove any trends due to possible stability dependence of the correlations as suggested by Kaimal and Haugen.[17] The normalization may be derived from normalized variances and covariances by integration of the normalized spectra and cospectra of Sections 4.5 and 4.6 and applying the relation (from Eq. (2) and Sections 4.5 and 4.6)

$$(\sigma_x)^2 = \overline{x^2} = \int \Phi_{xx}(f)\, df = \int \Phi_{xx}(f_N)\, df_N \tag{A1}$$

and

$$\overline{xy} = \int \Phi_{xy}(f)\, df = \int \Phi_{xy}(f_N)\, df_N \quad . \tag{A2}$$

Normalized correlation coefficients are then defined as

$$\tilde{r}_{xy} = \frac{\widetilde{xy}}{\tilde{\sigma}_x \tilde{\sigma}_y} \tag{A3}$$

where

$$\widetilde{xy} = \int \Phi_{xy}(f_N)\, df_N / N_{xy} \tag{A4}$$

and

$$\tilde{\sigma}_x^2 = \int \Phi_{xx}(f_N)\, df_N / N_{xx} \tag{A5}$$

and similarly for $\tilde{\sigma}_y$. Using the expressions for the normalized forms of the spectra and cospectra of Sections 4.5 and 4.6 the normalized correlation coefficients are

$\underline{\tilde{r}_{uw}}$

$$\tilde{r}_{uw} = \frac{\widetilde{uw}}{\tilde{\sigma}_u \tilde{\sigma}_w} = \frac{\overline{uw} \; u_*^{-2} G^{-1} (z/L)}{(\sigma_u u_*^{-1} \Phi_\epsilon^{-1/3}) (\sigma_w u_*^{-1} \Phi_\epsilon^{-1/3})}$$

$$\tilde{r}_{uw} = \frac{\overline{uw} \; \Phi_\epsilon^{2/3}}{\sigma_u \sigma_w} \qquad \text{for } G(z/L) \simeq 1$$

$$(-z/L) > 0)$$

$\underline{\tilde{r}_{w\gamma} (\tilde{r}_{u\gamma})}$

$$\tilde{r}_{w\gamma} = \frac{\widetilde{w\gamma}}{\tilde{\sigma}_w \tilde{\sigma}_\gamma} = \frac{\overline{w\gamma} \; \gamma_*^{-1} u_*^{-1} K_w^{-1} (z/L)}{(\sigma_w u_*^{-1} \Phi_\epsilon^{-1/3}) (\sigma_\gamma \gamma_*^{-1} \Phi_H^{-1/2} \Phi_\epsilon^{1/6})}$$

$$\tilde{r}_{w\gamma} = \frac{\overline{w\gamma} \; \Phi_H^{1/2} \Phi_\epsilon^{1/6}}{\sigma_w \sigma_\gamma}, \quad \text{for } K_w (z/L) = 1$$

$$(-z/L > 0)$$

$$\Phi_E = \Phi_H$$

$\underline{\tilde{r}_{\theta q}}$

$$\tilde{r}_{\theta q} = \frac{\widetilde{\theta q}}{\tilde{\sigma}_{\theta} \tilde{\sigma}_{q}} = \frac{\overline{\theta q} \; q_{*}^{-1} \; T_{*}^{-1} \; H_{\theta q}^{-1} (z/L)}{(\sigma_{\theta} \; T_{*}^{-1} \; \Phi_{N}^{-1/2} \; \Phi_{\epsilon}^{1/6}) \; (\sigma_{q} \; q_{*}^{-1} \; \Phi_{\epsilon}^{-1/2} \; \Phi_{\epsilon}^{1/6})}$$

$$\tilde{r}_{\theta q} = \frac{\overline{\theta q} \; \Phi_{H} \; \Phi_{\epsilon}^{-1/3}}{\sigma_{\theta} \; \sigma_{q}} \quad , \text{ for } H_{\theta q}(z/L) = 1$$

$$(- z/L > 0)$$

$$\Phi_{H} = \Phi_{E}$$

152751

Thesis
D752

Dreyer

Comparison of momentum, sensible and latent heat fluxes over the open ocean determined by the direct covariance, inertial and direct dissipation techniques.

DISPLAY
DISPLAY
DISPLAY

3 OCT 74
6 SEP 74
26 SEP 74

152751

Thesis
D752

Dreyer

Comparison of momentum, sensible and latent heat fluxes over the open ocean determined by the direct covariance, inertial and direct dissipation techniques.

thesD752
Comparison of momentum, sensible and lat
3 2768 002 00687 6
DUDLEY KNOX LIBRARY